GEOLOGICA ULTRAJECTINA

Mededelingen van de
Faculteit Aardwetenschappen
der Universiteit Utrecht

No. 110

Experimental deformation of polyphase rock analogues

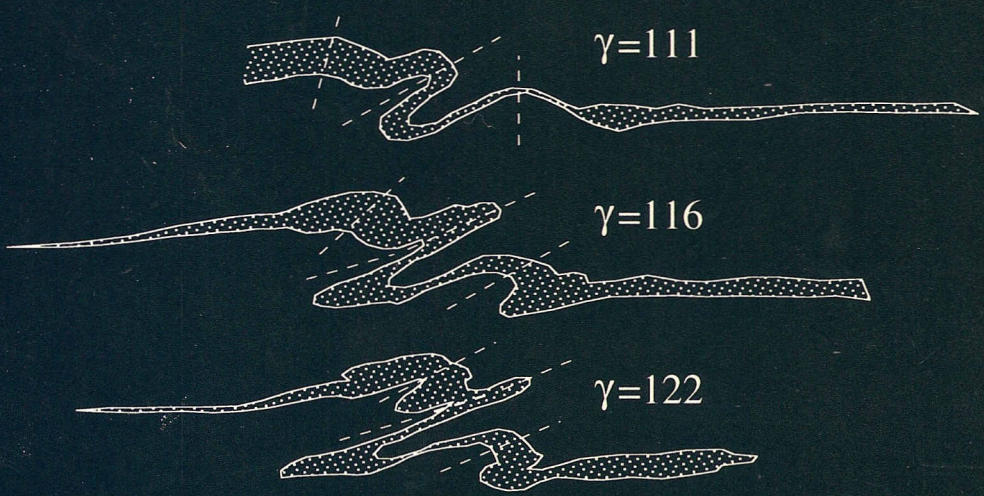

PAUL DIRK BONS

GEOLOGICA ULTRAJECTINA

Mededelingen van de
Faculteit Aardwetenschappen
der Universiteit Utrecht

No. 110

Experimental deformation of polyphase rock analogues

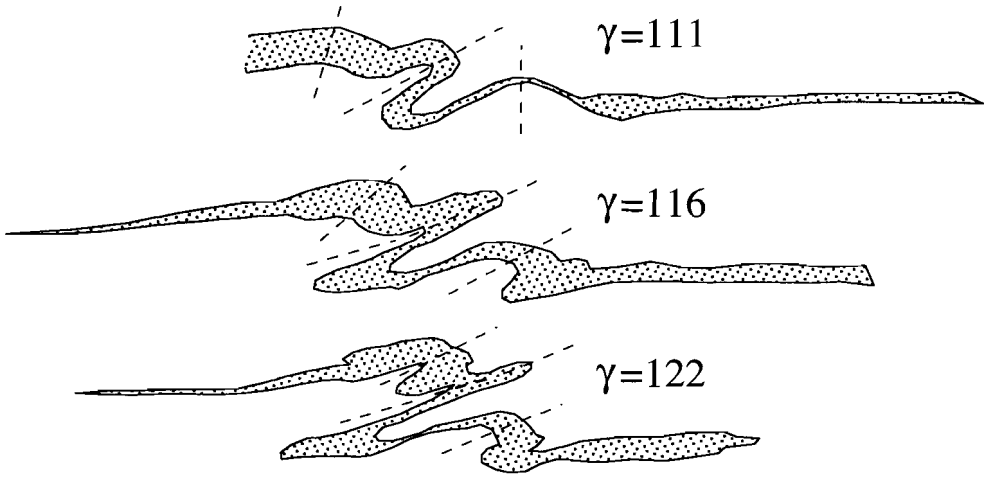

PAUL DIRK BONS

Experimental deformation of polyphase rock analogues

Experimentele deformatie van polyfase gesteente-analogen

(met een samenvatting in het Nederlands)

PROEFSCHRIFT

TER VERKRIJGING VAN DE GRAAD VAN DOCTOR AAN DE UNIVERSITEIT UTRECHT OP GEZAG VAN DE RECTOR MAGNIFICUS, PROF. DR J.A. VAN GINKEL, INGEVOLGE HET BESLUIT VAN HET COLLEGE VAN DECANEN IN HET OPENBAAR TE VERDEDIGEN OP WOENSDAG 22 SEPTEMBER 1993 DES OCHTENDS TE 10.30 UUR

DOOR

PAUL DIRK BONS

GEBOREN OP 20 FEBRUARI 1964 TE SYDNEY, AUSTRALIË

PROMOTOREN: PROF. DR S.H. WHITE
(FACULTEIT AARDWETENSCHAPPEN,
UNIVERSITEIT UTRECHT)
PROF. DR C.W. PASSCHIER
(INSTITUT FÜR GEOWISSENSCHAFTEN,
JOHANNES GUTENBERG-UNIVERSITÄT, MAINZ,
BONDSREPUBLIEK DUITSLAND)

CO-PROMOTOREN: DR J.L. URAI
(SHELL RESEARCH B.V., RIJSWIJK)
DR M.W. JESSELL
(DEPARTMENT OF EARTH SCIENCES, MONASH
UNIVERSITY, CLAYTON, AUSTRALIË)

Dit proefschrift werd mogelijk gemaakt met financiële steun van de Nederlandse Organisatie voor Wetenschappelijk Onderzoek (N.W.O.), c.q. de Stichting Aardwetenschappelijk Onderzoek Nederland (A.W.O.N.), projectnummer 751-353-021

CIP-GEGEVENS KONINKLIJKE BIBLIOTHEEK, DEN HAAG

Bons, Paul Dirk

Experimental deformation of polyphase rock analogues /
Paul Dirk Bons. - Utrecht: Faculteit Aardwetenschappen der Universiteit Utrecht. - (Geologica Ultraiectina, ISSN 0072-1026; no. 110)
Proefschrift Universiteit Utrecht. - Met lit. opg. - Met samenvatting in het Nederlands.
ISBN 90-71577-64-3.
Trefw.: deformatie / polyfase materialen / gesteente-analogen.

Some questions on polyphase materials:

How many strawberries, how large in the "charlotte aux fraises"? How to characterise their distribution?

How should one put the pears (aspect ratio, distribution ...) in the "charlotte aux poires"?

What are the internal stresses in the strawberries in the "charlotte aux fraises"?

What is the failure mode of the "millefeuille" at different temperatures?

(Y. Bréchet, 1993, NATO Advanced Research Workshop on Polyphase Polycrystal Plasticity, Palm Springs, California, U.S.A.)

Contents

Chapter 9.
Grain growth 147

Samenvatting

Veel gesteenten bestaan uit meer dan één mineraal met elk eigen rheologische eigenschappen. Hoewel reeds veel bekend is van de eigenschappen van monominerale gesteenten is de kennis van de rheologie van polyminerale gesteenten, of algemener: polyfase materialen, relatief gering. In deze studie is onderzocht wat de rheologische eigenschappen zijn van polyfase materialen en in het bijzonder hoe deze eigenschappen afhankelijk zijn van de materiaaleigenschappen, de microgeometrische verdeling en de volumefracties van de individuele componenten. Verder is onderzocht hoe de microgeometrie verandert gedurende deformatie en hoe dit weer de materiaaleigenschappen beïnvloedt. Een overzicht van de bestaande theorieën is gegeven in hoofdstuk 1.

De eerste benadering was het doen van experimenten met twee-fase composieten van de gesteente-analogen kamfer en octachloropropaan (OCP). Hoofdstuk 2 is aan de beschrijving van deze materialen gewijd. Het onderzoek naar mogelijke nieuwe gesteente-analogen heeft norcamphor als potentieel geschikt materiaal opgeleverd. De eerste waarnemingen van de microstructurele en rheologische eigenschappen zijn in hoofdstuk 2 beschreven.

Hoofdstuk 3 geeft een overzicht van de gebruikte technieken en apparatuur. Een nieuw deformatie-apparaat werd als deel van dit onderzoek ontworpen en gebouwd, speciaal voor deformatie tot zeer hoge schuifvervorming (γ=185). De methode om de vervorming in een monster in een doorzichtige deformatiecel te analyseren werd verbeterd. Een computerprogramma werd geschreven om deze analyse grotendeels automatisch uit te voeren. Hoofdstuk 4 beschrijft deze analyse.

De rheologische eigenschappen van kamfer en OCP werden bepaald met axisymmetrische verkortingsproeven, beschreven in hoofdstuk 5: beide zijn machtswet-materialen met spanningsexponenten van respectievelijk 3,3 en 4,5. Bij de gebruikte drukspanningen (0,2-1,2 MPa) vervormde OCP twee tot drie orden van grootte sneller dan kamfer. Mengsels van kamfer en OCP bleken ook machtswet-materialen te zijn onder de gegeven experimentele omstandigheden. De OCP vormde een matrix om de hardere kamferinsluitsels en kon de vervorming grotendeels opvangen. De eigenschappen van deze composieten kunnen, zelfs bij kleine volume fracties OCP, adequaat omschreven worden met modellen voor rigide insluitsels, omdat kamfer vrijwel rigide is ten opzichte van OCP.

Schuifexperimenten, het onderwerp van hoofdstuk 6, maken de waarneming mogelijk van microstructurele ontwikkelingen tot zeer hoge schuifvervorming en hun effect op de schuifsterkte van het gehele materiaal. Isotrope composieten van kamferinsluitsels in OCP vertoonden allereerst een vorming van een foliatie van kamferlenzen en lagen, gevolgd door plooiing van deze foliatie bij een totale schuifvervorming hoger dan 50-75. Plooiing vond plaats door het doorbuigen van de

kamferlagen, met assenvlakken die aanvankelijk een grote hoek (45-90°) maakten met het schuifvlak en vervolgens naar dit vlak roteerden terwijl de plooien zich sloten. De experimenten werden gedaan bij een constante schuifspanning en de respons in totale schuifvervormingsnelheid van het monster werd gemeten. Deze was eerst een toeneming van de snelheid, samenvallend met de foliatieontwikkeling, en vervolgens een afneming tegelijkertijd met de plooiing. In composieten van OCP-insluitsels in kamfer werd een sterke localisatie van de deformatie waargenomen in een smalle schuifzone, waarlangs de OCP-insluitsels verbonden waren.

Numeriek modelleren was de tweede benadering en wordt beschreven in hoofdstuk 7. Deze methode werd met name gebruikt om het effect van een anisotrope verdeling van de bestanddelen op de eigenschappen van een composiet te onderzoeken. De percolatiefractie van de hardste fase bleek van groot belang voor de eigenschappen van een composiet als geheel. Bij deze fractie wisselen de fasen van rol als matrix- en insluistelfase. De fractie waarbij dit gebeurt is afhankelijk van de geometrische verdeling van de fasen. De percolatiefractie bepaalt waar de eigenschappen van een composiet als geheel vallen tussen de Voigt- of constante vervorming(snelheid) grens en de Reuss- of constante spanning grens. In een grafiek met de spanning op de verticale as en de composietsamenstelling op de horizontale as, bepaalt de percolatie-fractie de relatieve horizontale afstand tussen deze grenzen. De methode wordt daarom de *Horizontale Afstand Schattingsmethode* (HAS) genoemd. Wanneer men de percolatiefractie en de eigenschappen van de bestanddelen en hun volumefracties kent, kan men zo een schatting maken van de composieteigenschappen.

In hoofdstuk 8 wordt de HAS vergeleken met bestaande modellen en met de experimentele resultaten van dit onderzoek. Aangtoond wordt dat de HAS toepasbaar is op suspensies van rigide insluitsels in zowel linear visceuze als machtswetkruip matrices. Ook worden enkele voorbeelden gegeven van geologische toepassingen.

De gebruikte organische analogen zijn zeer geschikt voor de bestudering van korrelgroei in een polykristallijn aggregaat. Korrelgroei en het effect ervan op de microstructuur vormen het onderwerp van hoofdstuk 9. Korrelgroei kan de vorming van een foliatie in een deformerend korrelaggregaat onderdrukken, waarbij het proces van het z.g. "buurman-verwisselen" een belangrijke rol speelt. Een computermodel werd geschreven om korrelgroei te simuleren. Met dit model kunnen microstructurele en topologische eigenschappen van een korrelaggregaat worden bepaald die indicatief zijn voor de voorgeschiedenis van het aggregaat. Processen zoals het vasthouden van de korrelgrenzen door kleine deeltjes en vervorming tijdens korrelgroei zijn verwerkt in het model.

Abstract

This thesis presents an investigation into the mechanical properties of ductile polyphase materials, which were studied by a number of different techniques.

The first approach was to do creep tests and transparent deformation cell experiments with two-phase composites of organic crystalline rock-analogues, camphor and octachloropropane (OCP). A deformation apparatus to deform these materials in simple shear to very high bulk shear strain (up to γ=185) was developed and built during this study. The method for the analysis of progressive deformation in the transparent deformation cell, using small marker particles, was improved and a computer program was written to perform this analysis. In the search for new rock analogues, norcamphor was found to be a promising material. First observations on its microstructural behaviour and rheological properties are presented.

The rheological properties of OCP and camphor at 28°C were determined: both are power-law creep materials with stress exponents of 4.5 and 3.3 respectively. The strain rate difference is two to three orders of magnitude within the experimental range of stresses (0.2-1.2 MPa). Mixtures of OCP and camphor are also power-law creep materials at these stresses. The soft phase OCP forms a matrix around the harder camphor inclusions and can accommodate most of the deformation. The properties of these mixtures can be described with matrix-rigid inclusion models, even at small volume fractions of OCP, because the camphor is virtually rigid compared to the OCP.

Simple shear experiments allowed the observation of microstructural developments to high finite shear strain. Isotropic composites of camphor inclusions in OCP showed the development of a foliation of camphor lenses and layers and finally (γ>50-75) folding of the foliation. Folding commenced with buckling of the camphor layers. Axial planes were initially at a high angle (45-90°) to the flow plane, and rotated towards it as the folds tightened. Experiments were done at a constant shear stress and the bulk shear strain rate response to these developments was an initial shear strain rate increase (softening) as the foliation formed and a subsequent shear strain rate decrease (hardening) at the onset of folding. Localisation of deformation into a narrow shear zone was observed in a composite of OCP inclusions in camphor at γ<1. The shear zone was formed by linking up of the OCP inclusions, which caused softening of the composite as a whole.

Numerical modelling was the second approach. This was used to investigate the effect of anisotropy of the phase distribution on bulk properties of a composite. It was observed that, for a given pair of phases, the bulk bulk properties of a composite are strongly related to the percolation fraction of the stronger phase. This is the fraction at which, with increasing concentration, this phase starts to form a connected framework, which is dependent on the geometrical distribution of the phases. The percolation fraction determines the horizontal distance of the composite properties between the Voigt or constant strain/strain rate bound and the Reuss or constant stress bound. Thus one can make an estimate of the composite properties if the percolation fraction is known, as well as the properties of the constituent phases and their volume fractions.

Grain growth and its effects on microstructure were also studied. Grain growth during deformation may suppress foliation development in a polycrystalline aggregate. Deformation induced neighbour switching was found to be an important mechanism for this. A computer model was written to model grain growth. With this model one can outline microstructural and topological features, such as grain shape, grain boundary curvature and the frequency distribution of size and number of sides of grains, which are indicative of the grain growth history of the grain aggregate. Drag by second phase particles and deformation during grain growth are incorporated in the model.

Chapter 1

Introduction

1.1 General background

Knowledge of the flow properties of rocks is of importance for modelling of rock deformation at all scales. Natural rocks are in general polymineralic and have a highly variable microstructure and - when deformed - show a wide range of finite strains. The major source of information for a geologist is the end product of a deformation history: the (micro-) structures. Flow properties of rock forming minerals at geological conditions are poorly constrained (e.g. Paterson 1987). Heterogeneous deformation in rock masses is a rule rather than an exception and a considerable part of deformation in the lower crust and mantle is thought to be accommodated by localised shear zones. With knowledge and models of how and why microstructures develop and how they may change the bulk flow properties of rocks one can try to outline which rocks are susceptible to strong strain weakening and possibly shear localisation.

Rocks, such as a granite, are usually polyphase materials that consists of two or more components (mineral species) that each occupy distinct regions within the composite material. Within each region the material can be described as one single continuum with the properties of the phase occupying the region. The shape and distribution of these regions define the microgeometry of the composite. At a larger scale, the composite can be treated as a single homogeneous and continuous material. The macroscopic mechanical properties and deformational behaviour of such composites is still poorly understood. This study concentrates on how these properties and deformational behaviour are related to

- the properties of the constituent phases,
- the internal geometry or microgeometry of the material (including the relative proportions).

In this study it is assumed that the properties of each constituent phase are independent of the presence of another phase. This is not necessarily true in rock deforming by diffusional mass transfer processes (Wheeler 1992). However, for intracrystalline, dislocation creep processes, that are thought to be important in the lower crust, our assumption is valid.

To investigate the effects of the different parameters on the properties of a composite one would ideally systematically vary each parameter. The possibility of doing so with natural rocks is limited. In most cases the composition of a rock and the microgeometry are strongly related. Experiments are therefore rather performed on artificial "rock-like" composites of minerals or rock-analogues (e.g. Burg & Wilson 1987; Jordan 1986, 1987, 1988; Ross *et al.* 1987). The advantage of the use of rock analogues, especially organic rock analogues, is that these materials are relatively soft at room temperature and low stresses and experiments can therefore done with relatively simple equipment and at high strain rates (Means 1980, 1981, 1989; Urai 1981, 1983) . The relative softness of these rock analogues make very high shear strain experiments possible, that cannot be done with real rocks.

Numerical modelling allows systematic investigation of the role of all parameters on the properties of a composite. This method was used in this study to investigate the effect of a preferred orientation of inclusions on the bulk properties of a composite.

The basic question asked in this study is:

- What are the rheological properties of a polyphase, polycrystalline material - especially a rock - deforming by crystal plastic deformation mechanisms?

Subquestions then are:

- What is the role of (i) the rheological properties of the constituent phases and (ii) the microgeometry of the material (including the relative proportions)?
- How does the microgeometry develop during deformation and how does this affect the bulk rheological properties of a composite?

1.2 Review of existing theories and models

There are several ways in which one can group the different theories, models and experimental results on polyphase materials. An overview and classification of the different theories and models is first given in this section, followed by a more detailed description of some of these models.

1.2.1 Classification

Estimates and bounds

Most theories aim to produce an estimate of the macroscopic properties of a polyphase material. The accuracy depends on the validity and sophistication of the theory and the knowledge and availability of the parameters. Another group is formed by the theories that do not produce one estimate, but two bounds. These two bounds define a range of possible values that can be expected for a particular case. Bounding theories, such as the Voigt&Reuss bounds (Reuss 1929; Voigt 1928) and the Hashin-Strickman bounds (Hashin & Strickman 1963) are useful when more accurate theories are lacking or cannot be used. They are also useful to test estimating theories, whose estimates must lie between the bounds. Bounding theories lose their value when bounds are too far apart.

Theoretical versus empirical models

Theories range from theoretical to empirical. Purely theoretical models are for instance the Self-Consistent Theory (SCT), Voigt&Reuss bounds (Reuss 1929; Voigt 1928), Hashin-Strikman bounds (Hashin & Strickman 1963). Experimental work has resulted in many empirical (flow) laws, as for instance the Krieger-Dougherty equation (Krieger & Dougherty 1959). These empirical laws often have a limited applicability. Experimental geology is on the whole largely in the early stages of this empirical approach, with experimental measurements of properties of polymineralic rocks (e.g. Westerly granite (Tullis & Yund 1977), aplite (Dell'Angelo & Tullis 1982), schists (Shea & Kronenberg 1993), but only few attempts to produce empirical laws (Handy 1989, 1992; Jordan 1988; Tullis *et al.* 1991).

Microgeometry

A third way of ordering theories is based on the way in which theories incorporate the internal geometry or microstructure of a polyphase material. The actual microscale geometry of a natural polyphase material (for instance a granite) is nowhere the same. The best one can achieve is to determine a statistical representative microstructure. Finite element modelling can then be used to calculate the properties for that particular microstructure (Horowitz *et al.* 1981; Tullis *et al.* 1991). One can also make an artificial microstructure as input for numerical modelling. The important point here is

that these models use the size(s), shape(s) of the regions occupied by the individual phases or "phase-particles" *and* their position in space, relative to other phase-particles.

Many theories only use the shape of phase particles and not their position (most SCT, suspension theory). This has the advantage that a calculation (of e.g. stress and/or strain (rate)) has to be done only once for each phase. This usually leads to a considerable simplification, which may make the problem more tractable mathematically, but may also lead to an over-simplification.

Several analytical or numerical solutions have been found for particular, often simple internal geometries, e.g. a cube of one phase with a sphere of a second in its centre (Eudier 1962; Tharp 1981; Tullis *et al.* 1991)). Here shape and position play a role, but there is only one shape and one position, which rarely corresponds to a natural microgeometry.

Finally we come to the theories that do not take shape or position into account. The Voigt&Reuss bounds fall in this group, as all internal geometries should give properties between these bounds. The Hashin-Strikman bounds can also be grouped here, although these bounds already assume some geometry: isotropy.

1.2.2 Models

Bounding models

The most elementary bounds, which are the limits of possible stress -strain (rate) values that can be attained at a given fraction for any microgeometry, are given by the Voigt and Reuss theory (Reuss 1929; Voigt 1928). These bounds were originally developed for elasticity, but can also be applied to viscosity, as is done here.

The Voigt bound is defined as the stress (σ) - strain (rate) ($\dot{\varepsilon}$) situation where *strain (rate) is constant* throughout the composite. The composite viscosity η_c^V (see Appendix C for a list of symbols) of a composite of two materials with viscosity η_1 and η_2 is then given by:

$$\dot{\varepsilon}_c = \dot{\varepsilon}_1 = \dot{\varepsilon}_2 \qquad \text{and} \qquad \sigma_c = F_1 \cdot \sigma_1 + F_2 \cdot \sigma_2 \tag{1.1\&2}$$

$$\Leftrightarrow \sigma_c = F_1 \cdot \eta_1 \cdot \dot{\varepsilon}_1 + F_2 \cdot \eta_2 \cdot \dot{\varepsilon}_2 = (F_1 \cdot \eta_1 + F_2 \cdot \eta_2) \cdot \dot{\varepsilon}_c \tag{1.3}$$

$$\Leftrightarrow \eta_c^V = (F_1 \cdot \eta_1 + F_2 \cdot \eta_2) \tag{1.4}$$

The viscosity of the composite is a linear function of the viscosities and the fractions (F_1, F_2) of the two components. The same linear relation holds for stiffness and flow stresses at a given strain rate (Fig. 1.1).

The Reuss bound is defined as the stress - strain (rate) situation where *stress is constant* throughout the composite. The viscosity η_c^R of a composite of two materials with viscosity η_1 and η_2 is then given by:

$$\sigma_c = \sigma_1 = \sigma_2 \qquad \text{and} \qquad \dot{\varepsilon}_c = F_1 \cdot \dot{\varepsilon}_1 + F_2 \cdot \dot{\varepsilon}_2 \tag{1.5\&6}$$

$$\Leftrightarrow \dot{\varepsilon}_c = F_1 \cdot \sigma_1/\eta_1 + F_2 \cdot \sigma_2/\eta_2 = (F_1/\eta_1 + F_2/\eta_2) \cdot \sigma_c \tag{1.7}$$

$$\Leftrightarrow \eta_c^R = (F_1/\eta_1 + F_2/\eta_2)^{-1} \tag{1.8}$$

Again the same relation holds for strain and strain rate at a given stress (Fig. 1.1).

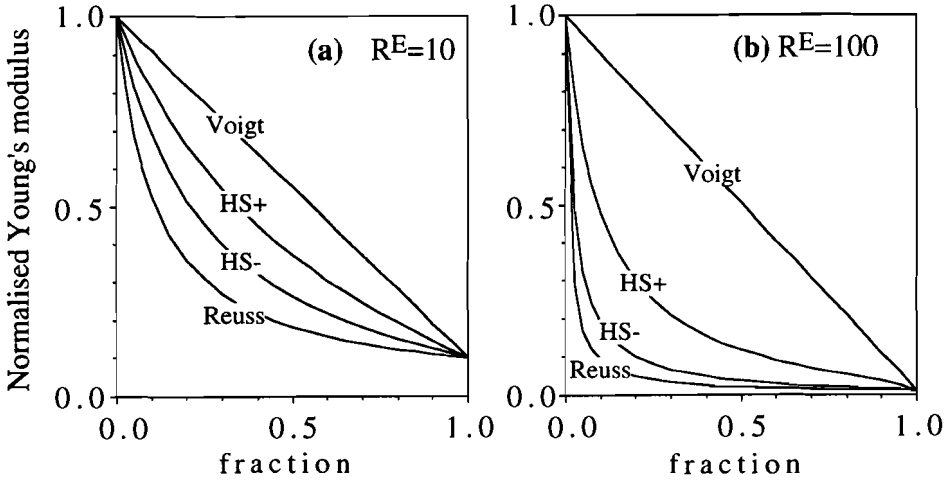

Fig. 1.1. The Voigt, Reuss, upper (HS^+) and lower (HS^-) Hashin-Strickman bounds on the normalised Young's modulus of a twophase composite of linear elastic materials with Poisson's ratio of 0.2 and Young's modulus ratio (R^E) of 10 (a) and 100 (b).

One can consider the two cases as resistors in series (Reuss) or parallel (Voigt) (Weijermars 1992). Several averaging procedures of the two bounds have been suggested (see discussion and references in Watt *et al.* 1976), such as $M_c=(M^R+M^V)/2$ (where M stands for the elastic modulus, either shear or bulk modulus).

Other well known bounds, especially in elasticity theory, are the Hashin-Strikman bounds (Hashin & Strickman 1963, and refs in Watt *et al.* 1976). These bounds constrain the possible (elastic) properties of a composite more than the Voigt and Reuss bounds (Fig. 1.1). For two-phase composites the two bounds are the solution for one particular microgeometry, namely that of a composite of composite spheres. Each sphere consists of a sphere of one phase surrounded by a shell of the other phase. The one bound then corresponds to the case where one phase forms the core,

the other bound where the other phase forms the core. The Hashin-Strickman bounds are valid for polyphase linear elasticity, however the same approach can be used for other (non-) linear material properties (Ponte Canstañeda 1991).

Matrix-inclusion models

Central in theories on suspension rheology and the Self-Consistent Theory (SCT) is that the polyphase material is modelled as consisting of inclusions embedded in a matrix. The properties of the composite are a function of the matrix properties and of the inclusion properties, the shape, orientation, distribution and fraction of the inclusions.

For suspensions it is clear that the matrix is formed by the suspending fluid and has the properties of this fluid. The inclusions are the suspended particles and are usually treated as relatively rigid, except for emulsion-type suspensions (Barnes *et al.* 1989). Eudier (1962) proposed a model for porous sintered steels, where the pores are modelled as inclusions in a steel matrix. The principle is not only applicable to polyphase materials with very high contrasts in properties between the phases (as in suspensions with rigid particles or porous aggregates) but also to composites where all phases are deformed significantly (Lee, & Mear 1991a&b; Weng 1990).

Suspensions & porous materials

One approach to estimate composite properties is the incremental or step-wise approach, where one starts with one pure phase and increases the fraction of the other phase incrementally. The effect of all particles in a suspension on the viscosity of a suspension can be taken as the sum of the effects of adding single particles to the suspension (Einstein 1906). If there is no interaction between the particles, i.e. the suspensions is infinitely dilute, then this can be written as the following equation:

$$\partial\eta/\partial F=c\cdot\eta \tag{1.9}$$

Where η stands for the viscosity of the suspension, F for the fraction of suspended particles and c a constant depending on the shape of the inclusions. Integration yields:

$$\eta=\eta_0(1+cF) \tag{1.10}$$

Here η_0 is the viscosity of the suspending medium and Einstein showed that for spheres in a dilute suspension c=2.5.

Equation (1.9) does not take into account the effect of interaction of particles in concentrated suspensions. The effect of adding one particle to a dilute suspension is

different to that of adding one to a concentrated suspension, since there is less space for the extra particle. Equation (1.9) then has to be replaced by:

$$\partial\eta/\partial F=c\cdot\eta/(1-KF) \qquad (1.11)$$

to take into account this so called "crowding effect" (Ball & Richmond 1980). Integration then yields:

$$\eta=\eta_0(1-KF)^{-c/K} \qquad (1.12)$$

At the maximum packing fraction F^m the suspended particles will all touch and form a framework. At this point the viscosity will rapidly increase to infinity. This maximum packing fraction is frequently used in suspension rheology and one can see that the constant K is equal to $1/F^m$. If we insert this in in equation (1.12) and replace c by $[\eta]$, which is the "intrinsic viscosity" (Krieger & Dougherty 1959), one gets the Krieger-Dougherty equation (shortened to K-D equation):

$$\eta=\eta o(1-F/F^m)^{-[\eta]/F^m} \qquad (1.13)$$

Equations of this type were also suggested for porous materials:

$$E=E_0\cdot(1-cF_p) \qquad \text{(1.14, Pohl (1969) in Tharp (1983))}$$

$$E=E_0\cdot c\cdot(1-F_p)^{3.4} \qquad \text{(1.15, Hirschhorn (1969) in Tharp (1983))}$$

$$\sigma=\sigma_0\cdot(1-cF_p^{2/3}) \qquad \text{(1.16, Eudier (1962) in Tharp (1983))}$$

(E, σ is Young's modulus or stress of porous material; E_0, σ_0 is Young's modulus or stress solid phase; F_p is porosity; c is a (material) constant).

If the contrast between material properties are very high (rigid clast and framework field in Handy (1989)), as in suspension of rigid particles or in porous materials, then the general equation relating the properties of the composite (P_c) and that of the matrix phase (either suspending fluid or solid phase in a porous material) P_0 is :

$$P_c = P_c(P_0,F_i) \qquad \text{(1.17, see also chapter 5)}$$

The composite properties (e.g. viscosity, Young's modulus) are only a function of the properties of the matrix phase and the fraction of the inclusion phase (F_i). This function itself depends on the microgeometry of the material (shape and distribution of inclusions) and the type of properties of the matrix phase (e.g. viscous or power-law fluid in a suspension or elastic solid phase in porous material). Equations (1.13-16) are all of this type.

Equations of the type of equation (1.17) are only valid for high contrasts between the material properties of a composite. They are also only valid for a limited range of compositions and distributions. The strength of a porous material will vanish when the porosity reaches a fraction that the material falls apart (porosity becomes matrix phase) and a suspension of rigid particles will become rigid when the rigid particles

effectively become the matrix phase. A model to estimate composite properties that is valid for the entire range of compositions would be of more use for geological applications.

Self-consistent models

Self-Consistent Theory approaches the subject in a similar way. Again, there is a matrix and an inclusion, but central to the SCT is that the properties of the matrix are equal to the macroscopic properties of the composite. A full mathematical treatment of the theory and the many ways of achieving a solution to the problem is beyond the scope of this thesis and only the basic principles (following Tóth *et al.* 1993) will be outlined below. The reader is referred to the following papers: Cleary *et al.* (1980), Hill (1965a&b), Kröner (1961), Molinari *et al.* (1987) and Watt *et al.* (1976).

The "self-consistency" of SCT is that both stress and strain rate (Σ_C and D_C) on the macroscale are the average of the stresses and strain rates ($\overline{\Sigma}$,$\overline{D}$) on the microscale. Assuming that the state of stress and strain rate is homogeneous within each phase (i), this can be written as:

$$\Sigma_C = \overline{\Sigma} = \sum(F_i\Sigma_i) \quad \text{and} \quad D_C = \overline{D} = \sum(F_iD_i) \qquad (1.18\&19)$$

The state of stress and strain rate within each phase can be determined when the relation between stress and strain rate for that phase are known and the interaction between inclusions of that phase and the matrix can be determined:

$$\Sigma_i - \overline{\Sigma} = \mu(\overline{D} - D_i) \qquad (1.20)$$

The interaction coefficient, μ, can be put in the form of a tensor of rank 1 to 3, depending on the parameters that are involved in the model. μ is a scalar for spherical inclusions and isotropic properties of the phases. The Voigt boundary corresponds to $\mu=\infty$ and the Reuss boundary to $\mu=0$. Equations (1.18-20) and the constitutive equations that describe the behaviour of the components can then be solved to obtain the composite stress and strain (strain rate) relation. SCT usually uses an ellipsoidal shape for the inclusions. The reason is that stress and strain(rate) are homogeneous in an ellipsoid lying in an infinite homogeneous matrix, with ideal coupling between matrix and inclusion, if deformation is homogeneous at infinity from the inclusions (Eshelby 1957). This assumption simplifies the mathematics of the SCT considerably and is used by most workers in the field.

SCT has been successfully applied to plasticity and elasticity in monomineralic aggregates (Hill 1965a; Molinari *et al.* 1987; Wenk *et al.* 1989, 1991). In this case the variety in stresses and strain rates within the material arises from the different

orientations of grains of one phase with anisotropic properties. The stresses and strain (-rates) are different in each grain, but have a continuous range of values around the average value for the composite. In a two-phase material there will be two stress and strain (-rate) value ranges, which may or may not overlap.

Basic SCT does not incorporate the effects of position of inclusions with respect to other inclusions, and usually one shape (ellipsoidal) is assumed for one or more of the phases. Molinari *et al.* (1987) described a method to incorporate spatial position and distribution of inclusions in the SCT. In standard SCT the interaction between the matrix, which has the properties of the bulk material, and an inclusion is determined, from which the stress / strain (-rate) state in an inclusion can be derived. This stress / strain (-rate) state in the inclusion is then again used to determine the properties of the bulk material. Instead of equating the matrix properties with the bulk properties, one can equate the matrix properties with the properties of the local environment. This refined SCT model resembles a finite element model in some ways.

SCT is not restricted to specific flow laws or elasticity laws of materials. Power-law stress-strain(rate) relations have been used by e.g. Ponte Canstañeda (1991), Willis (1991), Yoon & Chen (1990) and Wu & Chen (1992). These studies predict that a composite of two power-law creep materials with equal stress exponents is be a power-law creep material with the same stress exponent as the components. However, if the stress exponents of the components are not equal, then the composite is not a power-law creep material, that is, the stress exponent varies with stress or strain rate. This complicates the application of SCT to materials composed of components with different stress exponents. However, one can treat the composite as a power-law material within a small ranges of stresses or strain rates. A "local" or "effective" stress exponent of the composite, can be determined iteratively (Tóth *et al.* 1993).

The SCT is mathematically complex in its full generalisation, which limits its practical applicability. Consequently he author did not compare the different theories and approaches directly with the experimental results and numerical modelling. Tóth *et al.* (1993) put forward a simplified SCT-model for the creep behaviour composites of two phase power-law materials. This model has been tested on the creep data on OCP-camphor mixtures that are described in chapter 5. Stresses were calculated for isotropic mixtures of OCP and camphor at strain rates within the experimental range, using the experimentally determined flow laws for OCP and camphor and a scalar for the interaction coefficient (μ). The calculated stresses were in good agreement (within 7%) with the experimentally predicted stresses (Tóth *et al.* 1993). This suggests that

the SCT, even in simplified form, is a useful method to predict the properties of isotropic polyphase materials, even if the contrast in flow properties is high.

Yoon and Chen (1990) used the incremental approach (as in equations 1.9&11) and the self-consistency requirement to model the behaviour of a composite of power-law creep matrix with rigid inclusions, resulting in:

$$\dot{\varepsilon} = \dot{\varepsilon}_0 \cdot (1-F)^q \tag{1.21}$$

where $q = 1 + (k-1)n$ (1.22)

The factor k is the stress concentration factor for an isolated rigid inclusion in an infinite matrix and depends on the shape of the inclusion and the stress exponent (n) of the matrix phase. For equiaxed inclusions q is found to be:

$$q = 2 + n/2 \tag{1.23}$$

Equations for fibre shaped inclusions are also given in Yoon & Chen (1990) and Wu & Chen (1992).

It was argued by Kosheleva (1983) that one stress concentration coefficient does not suffice in the case of high concentrations of inclusions (>0.6) of spherical or cylindrical inclusions. It is also doubtful whether the SCT is physically valid when phases do not occur as spheroidal inclusions in a matrix, but form clusters. The model proposed by Yoon & Chen for instance only predicts complete rigidity of the composite if the fraction of the rigid inclusions is one. At smaller fractions, however, the rigid inclusions may form an interconnected framework (an infinite cluster), which makes the composite rigid as well. This effect is incorporated in the K-D equation by the maximum packing fraction. Clustering of the inclusions causes a variety in shape and size of the phase regions and the stresses and strains (-rates) will vary accordingly from cluster to cluster and within each cluster. Using one interaction coefficient probably oversimplifies the model when the connectivity of (both) phases plays a role (as mentioned by Watt *et al.* 1976).

Approaches from geology

A series of axisymmetric deformation experiments with limestone - halite composites are presented by Jordan (1986, 1987) and the results are compared with existing models (Jordan 1988). At small fractions of the softer phase halite, the composite strength follows the predictions of the Eudier-Tharp model for a limestone framework, with the constant c (equation 1.16) depending on internal geometry, strain hardening/-softening and strain. At higher fractions of halite, a transition is observed towards a stress-fraction relation (at constant strain rate) that is dominated by the halite. The limestone then behaved as essentially rigid compared to halite.

Stress values are very near to the the Reuss bound, with a rigid hard phase. Jordan (1988) suggests a modified version of the Reuss bound for a composite of a material with rigid clasts. Strain shadows exist on either side of a rigid clast. The volume of this strain shadow is a function of the angle δ (Fig. 1.2), which depends on the matrix properties. The effective fraction of the rigid phase now is the fraction of the rigid inclusions (F_i) plus the fraction of the strain shadows (F_{ss}). One can then modify the equation 8.8 for the Reuss boundary to:

$$\dot{\gamma}_c = (1 - F_i - F_{ss}) \cdot \dot{\gamma}_{matrix} \qquad (1.24)$$

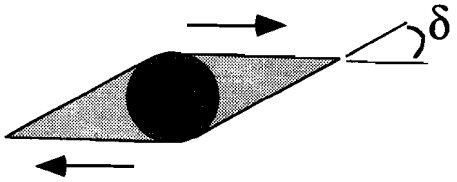

Fig. 1.2. The "rigid clast model" after Jordan (1988). A zero strain rate strain shadow exists on either side of a rigid clast. The volume of this strain shadow is determined by the angle δ.

It is doubtful whether this model has a wide applicability, since strain shadows do deform (see e.g. Masuda & Ando 1988) and it is also not clear how the angle δ can be determined for the (approximately zero-strain rate) strain shadow. In effect, the situation where this model applies is that of a suspension with rigid particles for which more elaborate models exist.

Another approach for rigid clasts in a deforming matrix is given by Handy (1989, 1992). Again there is a rigid phase (feldspar) occurring as inclusions in a weak phase matrix (quartz). The presence of the rigid inclusions causes a stress concentration in the weak phase, which can for instance be determined with paleopiezometric methods, and is found by Handy to be determined by the relative spacing (= fraction) of the inclusions. This stress concentration determines the average stress in the matrix phase and the overall stress - strain relation can then be determined with equation (1.8). The average strain rate in the matrix phase is used in this equation. The stress and strain rate in the matrix phase is however heterogeneous, especially when the relative distance between the inclusions is small (figure 6 in Handy 1989) and it then doubtful whether the use of an average strain rate is still valid (a problem that also holds for most SCT approaches).

Tullis *et al.* (1991) applied finite element modelling to the properties of diabase (pyroxene + plagioclase) and based an empirical flow law for twophase composites of power-law creep materials on it. This one-dimensional flow law is also of a

power-law type. For a power-law creep flow law of the type $\dot{\varepsilon} = A\exp^{-Q/RT}\sigma^n$, Tullis *et al.* proposed:

$$n_c = 10^{(F_1 \cdot \log n_1 + F_2 \cdot \log n_2)} \quad (1.25)$$

$$Q_c = \frac{Q_2 \cdot (n_c - n_1) - Q_1 \cdot (n_c - n_2)}{(n_2 - n_1)} \quad (1.26)$$

$$A_c = 10^{\{\log A_2 (n_c - n_1) - \log A_1 (n_c - n_2)\}/(n_2 - n_1)} \quad (1.27)$$

As pointed out by the authors, this is only applicable to low contrasts in flow-strength between the phases and a small difference in stress exponent. A composite of two power-law creep materials will only be a power-law creep material as well if (1) both phases have the same stress exponent and/or (2) the composite properties fall on the Voigt-bound and/or (3) one phase is effectively rigid / has effectively no strength compared to the other phase.

1.3 Set-up of this thesis

In this study, the main approach to investigate the rheology and microstructural developments in polyphase materials was the experimental deformation of two-phase organic rock analogues: octachloropropane and camphor. Part of this study was devoted to the search for and testing of possible new rock analogues. The compound norcamphor was found to be suitable as a rock analogue. The properties of OCP, camphor and norcamphor are described in chapter 2.

Experiments were carried out in a miniature axisymmetric gas apparatus, a bulk ring ring shear apparatus and transparent deformation cells. During this research, the bulk ring shear deformation apparatus was designed and built to deform samples in simple shear to very high shear strains (up to γ=185). The experimental procedure and equipment are described in chapter 3.

The distribution of strain during progressive deformation in a transparent deformation cell can be analysed with the aid of dispersed marker particles in a specimen. The existing method to do so was further refined and computerised to automatically perform the analysis. This is described in chapter 4.

Axisymmetric deformation experiments with composites of OCP and camphor are presented in chapter 5. The flow properties of the pure components were determined and compared with the flow properties of the composites. It was observed that the stress sensitivity of the strain rate is very similar to that of the soft component OCP, even at small fractions of OCP. This behaviour is explained by the microgeometry of the composites, where camphor occurred as inclusions in a matrix of OCP that accommodates virtually all deformation.

Simple shear experiments with the new bulk ring shear apparatus on OCP, camphor and their mixtures are described in chapter 6. In pure OCP, the measured bulk shear strain rate at a constant applied shear stress increases at the onset of deformation and reaches a steady state at a shear strain of almost 5. This steady state sets in when a steady state grain shape and crystallographic preferred orientation is reached. Experiments on initially isotropic composites of camphor (as inclusions) and OCP were performed, reaching bulk shear strains of up to 185. Initial increase of the bulk shear strain rate up to a bulk shear strain of about 50 was observed, coinciding with the development of a foliation, defined by the sheared camphor inclusions, and a compositional segregation. The bulk shear rate decreased at higher shear strains. Folding by buckling and subsequent shearing of the folds in the camphor layers and lenses set in at this stage. The development of the bulk shear strain rate can be explained in terms of the changing load carrying capacity of the hard camphor inclusions. This capacity decreases during the first stage of foliation development and is later on partially restored by folding. A composite of OCP inclusions in camphor localised deformation in a narrow shear zone by linking up of the OCP inclusions, that caused softening of the composite as a whole.

Numerical modelling, presented in chapter 7, was the second approach to investigate the flow properties of polyphase materials. Two finite element implementations were used, one to model 2-dimensional composites of isotropic linear elastic materials (HEL), and one to model 2-dimensional composites of isotropic incompressible power-law creep materials (BASIL). The effect of an anistropic distribution parallel or perpendicular to extension was studied with HEL. A method to make a first estimate for the stiffness of a composite is based on the results of modelling with HEL.

The results of the experiments and the numerical modelling are discussed in chapter 8. The estimation method developed in chapter 7 is further discussed and it is shown that it is also applicable to suspensions of rigid particles in viscous fluids. It is then shown how it can be applied on general 2-phase composites, such as some polymineralic rocks.

The final chapter 9 is dedicated to the subject of grain growth. A stage of static grain growth or annealing is an inevitable part of an experiment with organic rock analogues, since growth rates in these materials are high. This lead to an investigation into grain growth and the development of a model to simulate grain growth, especially grain growth contemporaneous with deformation. It is shown that grain growth during deformation may significantly reduce the development of a grain shape preferred orientation. The model provides quantitative indicators of, for instance, the maturity of a statically grown grain aggregate, grain growth during deformation and growth influenced by pinning of grain boundaries by second phase particles.

1.4 Published parts

Parts of this work have already been published or are in press or review. These articles have been included in this thesis unaltered, with the exception that the lay-out and figure numbers have been brought in line with the rest of the thesis. These articles are:

Bons P.D., M.W. Jessell & C.W. Passchier (1993) - Analysing the geometry of deformation in 2-D see-through experiments. *Journal Structural Geology,* 15 (3-5), 403-411 (Chapter 4)

Bons P.D. & J.L. Urai (1993) - Experimental deformation of 2-phase rock analogues. *Journal of Materials Science and Engineering,* submitted (Chapter 5)

Bons P.D. & J.L. Urai (1992) - Syndeformational grain growth: microstructures and kinetics. *Journal Structural Geology*, 14 (8-9), 1101-1109 (Chapter 9.1)

Parts of the chapters 6 and 7 have been used for the paper:

Bons P.D. & S.J.D. Cox (1993) - Analogue experiments and numerical modelling on the relation between microgeometry and flow properties of polyphase materials. *Journal of Materials Science and Engineering,* submitted

Data presented in chapter 5 have been used for the paper:

Tóth L.S., A. Molinari & P.D. Bons (1993) - Self consistent modelling of the creep behavior of twophase organic rock analogs. *Acta Metalurgica et Materiala,* submitted

Chapter 2

Rock analogues

2.1 Introduction

A rock analogue is a material that is used as a model material of a rock for experimental purposes. A requirement for selection of rock analogues is that the process studied is independent of scale or that the relevant properties of the analogues can be scaled to those of the materials that are modelled, the prototypes (Hubbert 1937; Wijermars & Schmeling 1986).

Processes such as folding, boudinage and rotation of inclusions are dependent on flow properties and (effective) viscosity-ratios, but independent of the actual deformation mechanisms of the materials. These processes can be modelled with materials such as clay, wax and putties, which are available as linear viscous or power-law creep materials (e.g. Hudleston 1973; Ildefonse, *et al.* 1992; Mancktelow 1991; Mandal & Karmakar 1989; Mandal & Khan 1991; Means 1989a; Passchier & Simpson 1986; Van Den Driessche & Brun 1987; Weijermars 1986).

Most grain-scale processes that occur during high pressure and temperature deformation of rocks, such as crystal plasticity, grain boundary migration, subgrain development and the development of shape and lattice preferred orientations depend on the structure of the material on the atomic to grain scale and the deformation mechanisms of the materials. Here the most accurately scaled model systems are from the same isomechanical group as the prototype (Frost & Ashby 1982; Poirier 1985). An example is the work of Tungatt & Humphreys (1984) on $NaNO_3$ as an analogue for $CaCO_3$. Both materials have the same crystal structure and type of bonding. Less perfectly scaled analogues however have shown their value by reproducing a smaller set of processes.

The analogues used in this study were used to model deformation in rock on the grain to multi-grain scale ($\approx$ μm - cm scale). The analogues had to be suitable for use in a transparent deformation cell (see Chapter 3.b).

The requirements for materials to be suitable for this purpose are:

1) Flow-properties have to be of the same type as for rocks that are modelled.
2) At low absolute temperature and stress, the material should be in the same field of the deformation-mechanism map as the prototype under the modelled conditions. For modelling of crystal plastic deformation in rocks this means that the analogue material must be crystalline, deforming by crystal plastic deformation mechanisms under the experimental conditions.
3) The materials have to be soft enough to deform according to requirements (1) and (2) at low stresses (up to $\approx$ 2 MPa), low temperature (up to $\approx$ 500 K) and at a practical strain rate ($\approx 1 \cdot 10^{-6}$ to $1 \cdot 10^{-3}$ s^{-1}).
4) The materials have to be transparent to enable observation of microstructures in thin sheets with an optical microscope.
5) Sample preparation must be easy and not dangerous.

Several materials fulfil these basic requirements. These can be inorganic compounds such as ice (e.g. Wilson 1986), sodium nitrate (Haggert *et al.* 1992; Tungatt & Humphreys 1984), bischofite and carnallite (Urai 1985, 1987), or organic molecular compounds such as octachloropropane, camphor, norbornene, naphtalene and wax. Means (e.g. Means 1989b) in particular made the use of organic crystalline compounds as rock analogues for the transparent deformation cell popular[§].

These rock analogues belong to the group of organic compounds referered to as "plastic crystals" (Gray & Winsor 1974). A short characteristic of the plastic crystals is given by Gray & Winsor: "This classification has usually been justified by the fact that their constituent molecules occupy mean positions at the points of a regular three-dimensional cubic lattice and to this extent they show order similar to that in solid crystals. However, the molecules undergo relatively free thermal rotatory motions about the lattice points so that there is complete long-range orientational disorder between them. In this respect, of all the mesophases, plastic crystals most closely resemble the amorphous liquid."

The organic compounds octachloropropane (abbreviated to "OCP"), camphor and norcamphor have been used in this study and their properties will be discussed below.

---

§ *Note that several of the organic rock analogues are (suspected to be) carcinogenic or neurotoxic. Future workers are warned to work in fume-cupboards or take other precautions.*

compound	formula	crystal system	T_m	features	references
octachloropropane (OCP)	C_3Cl_8	hexagonal	160°C	dynamic recrystallisation, subgrain formation, slip on basal and prismatic plane, twinning	Jessell (1986a, 1986b), Jessell & Lister (1991), McCrone (1949), McCrone & Cheng (1949), Means (1983, 1986, 1989), Means & Ree (1988), Ree (1990, 1991) Urai *et al.* (1986)
Camphor	$C_{10}H_{16}O$	rhombohedral <92°C cubic >92°C	179°C	Dynamic recrystallisation, twinning (?), kinking, slip on basal plane, strain localisation	Burg & Wilson (1987), Janssen (1991), Means (1989), Urai *et al.* (1980), Urai & Humphreys (1981)
Norcamphor	$C_7H_{10}O$	hexagonal (or trigonal)	93°C	dynamic recrystallisation, high grain boundary mobility, high static grain growth rate.	
adamantane	$C_{10}H_{14}$	cubic	209-212°C	relatively hard, can be mixed with several other materials (OCP, camphor, norcamphor)	Means, *pers. comm.*
Paradichlorobenzene	$C_6H_4Cl_2$	triclinic <32°C monoclinic >32°C	51°C	High grain boundary mobility, phase transition, twinning and kinking	Means (1980, 1986, 1989), Urai *et al.* (1986)
Norbornene (Norbornylene)	C_7H_{10}	hexagonal	44-46°	High grain boundary mobility, extremely odorous	Jessell & Lister (1991)
Biphenyl	$C_6H_5C_6H_5$	monoclinic LT <60°C, monoclinic HT >60°C	70°C	Undulose extinction, deformation lamellae & kinkbands	Means (1986, 1989)
Thymol	$CH_3C_3H_7C_6H_3OH$	hexagonal	52°C	dynamic recrystallisation	Means (1989)
Naphtalene	$C_{10}H_8$	monoclinic	80.5°C	grain boundary migration, subgrains, kink-bands	Blumenfeld & Wilson (1991), Burg *et al.* (1987)
Sodium nitrate	$NaNO_3$	rhombohedral	306°C	calcite-analogue	Haggert *et al.* (1992), Jessel & Cox (1992), Tungatt & Humphreys (1984), Means (1989)
Ice	H_2O	hexagonal	0°C	quartz-analogue	Burg *et al.* (1987), Means (1989), Wilson (1986) *and refs therein*

Table 2.1. Overview of known rock analogues that have been used in the transparent deformation cell, mainly based on literature and Fontein (1990).

2.2 Properties of OCP, camphor and norcamphor

In this section the analogues used in this study are described in detail and previous publications on these materials are reviewed. The emphasis lies on microstructural behaviour. Mechanical data obtained in this study are presented in chapter 5, except for data on norcamphor. Only three compounds were used as analogues in this study, but more were tried in an attempt to extend the range of suitable rock-analogues. A short overview of the crystalline rock analogues that have been used for experiments with the transparent deformation cell is given in table 2.1. A problem is that most of the known organic rock analogues form eutectic melts when mixed at room temperature (see table 2.2). A convenient two-phase system with the available organic rock analogues could only be made with camphor and OCP.

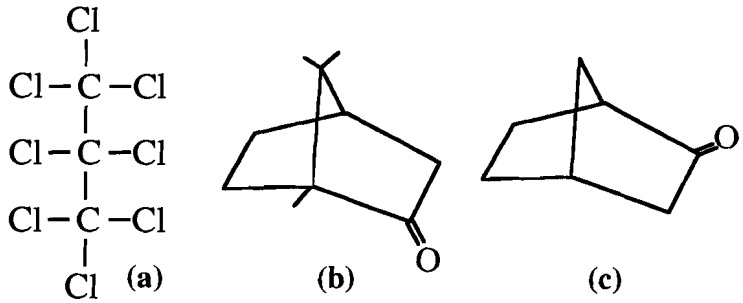

Fig 2.1. Molecular structure of (a) OCP, (b) camphor and (c) norcamphor.

	Biphenyl	Camphor	Paradichlorobenzene	Naphtalene	Norcamphor	OCP	Thymol
Biphenyl		+	+	+	-	-	+
Camphor	+		-	+	-	+	-
Paradichlorobenzene	+	-		+	-	-	+
Naphtalene	+	+	+		?	?	+
Norcamphor	-	-	-	?		-	-
OCP	-	+	-	?	-		-
Thymol	+	-	+	+	-	-	

Table 2.2. *Matrix showing whether two compounds form a eutectic melt when mixed at room temperature, after Fontein (1990). + = no eutectic melt forms, - = a eutectic melt forms, ? = not determined.*

2.2.1 Octachloropropane

Octachloropropane (C_3Cl_8, Fig. 2.1.a) is a soft, ductile material. The melting temperature (T_m) is 160°C (room temperature $\approx$ 0.7 T_m). It is optically uniaxial positive and has a low birefringence. Attempts for XRD determination of the OCP crystal structure were without results, because of the extremely weak reflections (Urai, *pers. comm.*). This is due to the relatively high degree of disorder, which causes plastic crystalls to give only a small number of reflections and considerable backgroud scattering (Winsor 1974).

OCP was first used for microstructural purposes as a material to study the kinetics of grain growth (McCrone 1949; McCrone & Cheng 1949). OCP is, together with ice, probably the most popular material to investigate microstructural developments in see-through experiments. Means (1983) was the first to recognise its applicability to study dynamic recrystallisation and its analogy with rock-forming minerals, especially quartz, in that respect. Its softness and high grain-boundary mobility at room temperature make it suitable for see-through experiments. Despite its popularity as a rock analogue, not much work has been done to determine its flow properties, with the exceptions of ter Haar *et al.* (1987 and Jessell (1986a).

One problem with OCP is that it is not commercially available. The OCP used in this study was donated by the SHELL Research Laboratory of Amsterdam and further refined with a vacuum sublimation-redeposition procedure by van Krieken in the laboratory at Utrecht University. The melting temperature of the refined OCP was determined (with a calorimeter) to be 160±2°C. OCP was also manufactured by van Krieken using a procedure described by Gerding and Rijnders (1946). This was done by chlorinating hexachloropropene (C_3Cl_6) dissolved in carbon tetrachloride (CCl_4) with chlorine (Cl2) under UV-radiation. The resulting mixture of OCP and C_3Cl_6 and CCl_4 must then be distilled several times to produce pure OCP. Both steps in the procedure are cumbersome and time consuming (van Krieken, *pers. comm.*). Grain boundary voids are reported to develop at temperatures above 60°C (0.8 T_m) by Ree (1992). This was not observed at these temperatures in the OCP used for this study. The OCP used by Ree was less pure which causes a partial melt to develop at temperature well below 160°C (Urai, *pers. comm.*).

Microstructures and deformation mechanisms

Deformation of OCP is characterised by grain boundary migration, subgrain development and the development of a crystallographic preferred orientation. Subgrains tend to form with initially straight boundaries perpendicular to the basal plane (Jessell (1986b) and Fig. 2.2.a). Grain boundaries are often serrated during deformation at room temperature (Fig. 18 in Urai *et al.* 1986) and remain more smoothly curved at higher temperatures (Ree (1991) and Fig. 2.2.a).

The development of a crystallographic preferred orientation in OCP has been studied by Jessell (Jessell 1986a, 1986b). A crystallographic preferred orientation with c-axes perpendicular to the flow plane develops during simple shear, which can lead to an almost single-crystal fabric at high shear strains (Fig. 2.2.b). Dislocation creep is the dominant deformation mechanism. The exact nature of the dislocations in the molecular lattice and the slip systems involved in creep is not known. The dominant slip systems are probably the basal plane and the prismatic planes (Jessell 1986a).

Kink-bands, or possibly twins, are observed during high strain rate and low temperature deformation (Jessell (1986a) and Fig. 2.2.c). Grain boundary sliding and diffusional mass transfer become significant at elevated temperature (Ree 1992). At lower temperatures these deformation mechanisms may operate as well, but are hard to observe (Means & Ree *pers. comm.*).

Fig 2.2. *Typical microstructures in deforming OCP. (a) OCP deforming in pure shear (E-W shortening) with smoothly curved grain boundaries ($T \approx 80°C$, $\dot{\varepsilon} \approx 1 \cdot 10^{-5}\ s^{-1}$). (b) Steady state microstructure in sinistral simple shear (circular shear zone). Most grains (light grey) have their basal plane parallel to the flow plane, forming an almost "single grain texture". Small dark grains have c-axes in the flow plane. Grain boundaries are serrated and highly mobile ($T \approx 70°C$, $\dot{\gamma} \approx 7 \cdot 10^{-4}\ s^{-1}$). (c) Kink-bands in two of the larger OCP grains deforming in simple shear (circular shear zone). (room temperature, $\dot{\gamma} \approx 7 \cdot 10^{-4}\ s^{-1}$). Dashed lines are edge of piston (a) frosted grips (b,c) and arrows indicate movement direction of piston/grips. Width of view 3.5 mm.*

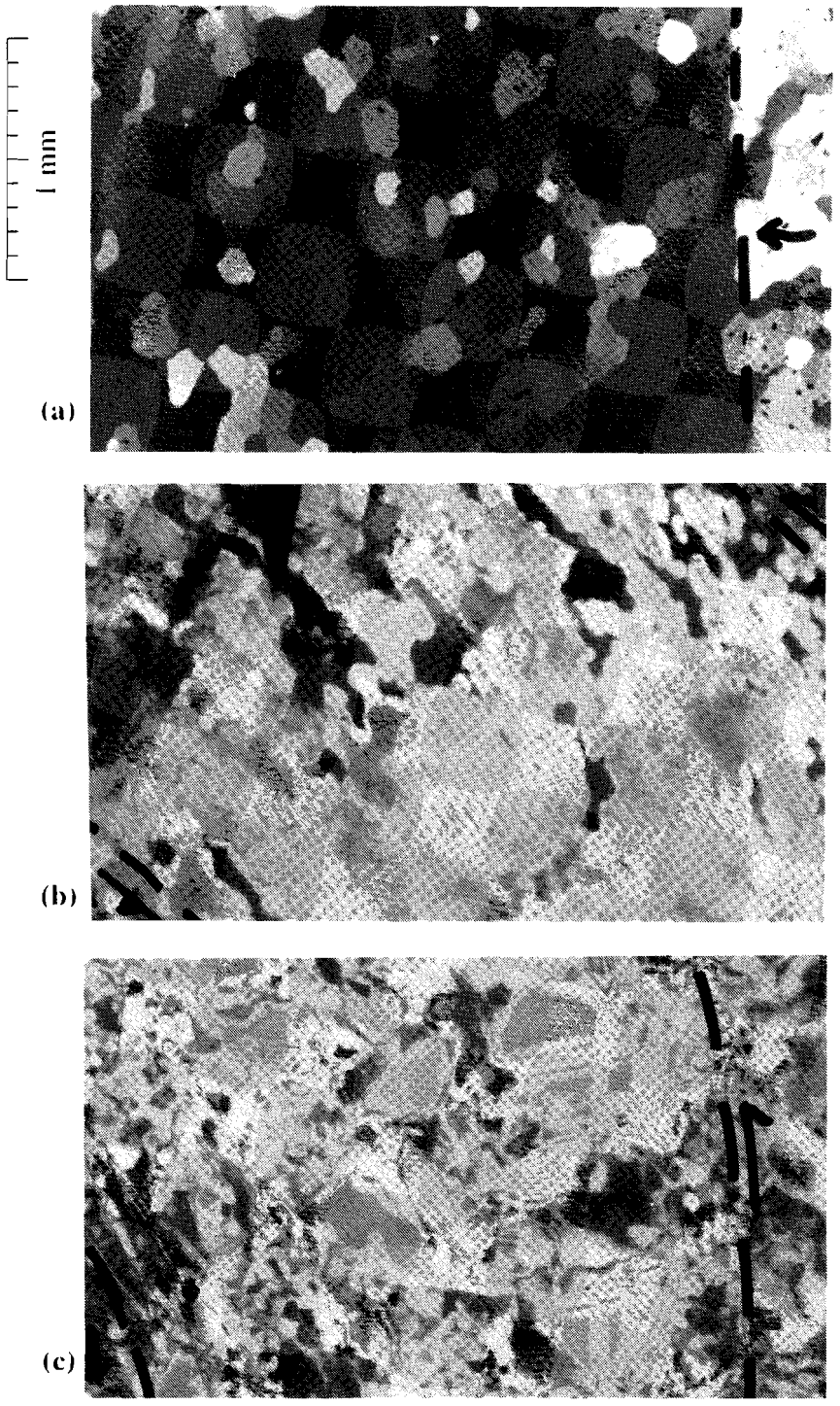
1 mm
(a)
(b)
(c)

Classification into microfabric regimes

The fabrics or microstructures that develop in deforming OCP are strongly dependent on the relative contributions of the different processes, which depend primarily on temperature and strain rate. One can roughly distinguish four "macrofabric regimes" with increasing temperature and decreasing strain rate (Fig. 2.3). The boundaries between the different regimes are not sharp. The microfabric regimes are defined by the observed characteristics in microstructure (after Schmid *et al.* 1987).

I. "Augen regime" (low temperature, high strain rate). Grain size is rapidly reduced as subgrains become independent grains through ongoing rotation of the lattice. Highly undulose large grains can remain as augen, sometimes with mechanical twins (Fig. 2.2.c).

II. "Serrated regime" (low to intermediate temperature and strain rate). Grain boundaries are typically serrated. Most grains show undulose extinction and sub-grains (Fig. 2.2.b).

III. "Foam regime" (intermediate to high temperature, low strain rate). Grain boundaries remain smoothly curved during deformation as in a foam texture Straight kinks develop in grains in one or more crystallographically determined orientations, sometimes dividing grains into "blocky" subgrains (Fig 2.2.a).

IV. "Partial melt / void regime" (temperature above 60-100° (depending on purity). Vapor or melt filled voids develop between grains, especially at triple-junctions. Diffusional creep and grain-boundary sliding become significant. Grain boundaries are smoothly curved. Low-angle straight subgrain boundaries develop.

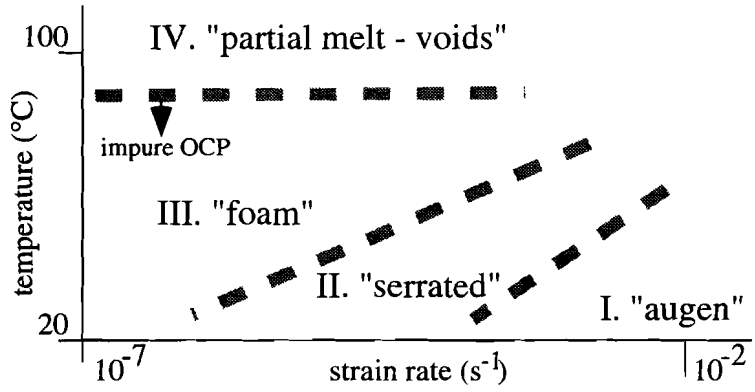

Fig 2.3. *Schematic "fabric map", showing the predominance of the four texture types discussed in the text as a function of temperature and strain rate. Boundaries are not sharp.*

Static grain growth

OCP pressed at room temperature to a thin sheet has a grain size in the order of 10 μm. A coarse (100-500 μm) foam texture develops within hours or days, depending on temperature. Usually some of the statically grown grains will have one or more straight low-angle grown-in sub-grain boundaries. Grains in the foam-texture are essentially equidimensional. It therefore seems that growth-rates are independent of lattice orientation (McCrone 1949).

2.2.2 Camphor

Camphor ($C_{10}H_{16}O$, Fig. 2.1.b) is rhombohedral, optically uniaxial negative, with a low birefringence below 92±7°C. At higher temperatures, up to its melting temperature of 179°C, it has a f.c.c. lattice. Deformation of camphor is characterised by the formation of sharp kink-bands, dynamic recrystallisation, development of a crystallographic preferred orientation and a tendency to localise strain (Urai *et al.* 1980; Urai & Humphreys 1981). The description below will be restricted to low-temperature behaviour, because all experiments in this study were done at about 300 K.

There are two isomers of camphor, d- and l-isomers, with slightly differing properties. A mixture of d&l-isomers was used for this study, purchased from Merck (Germany). Purity and melting temperature of this batch were not determined.

Slip and kinking

The basal plane seems to be the only significant slip plane (Urai 1980) in camphor. This leads to strongly inhomogeneous strain distribution between grains with different orientations of the basal plane (with respect to the applied stress). Deformation usually leads to bending of the lattice, followed by the development of mobile kink boundaries. Sharply bounded regular arrays of kink-bands or possibly twins occur at low strain (a few percent shortening, Fig. 2.4.). The kink-bands can occur as broad pointed "flames" or as sets resembling albite type twins in plagioclase.

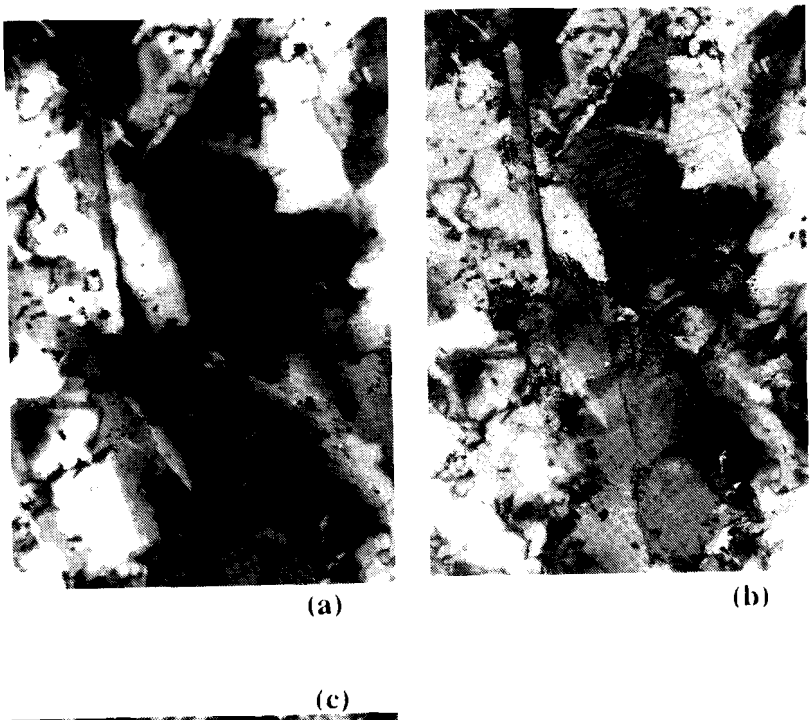

Fig 2.4. *Deforming camphor. (a) starting material, (b) 1.8% shortening (+3 mins.), (c) 4.7% shortening (+8 mins.), (d) 7.7% shortening (+13 mins.), (e) 14% shortening (+23 mins.), (f) 23% shortening (+38 mins) and (h) 31% shortening (+53 mins.). Thin kink lamellae develop in the dark grain on the left. Recrystallisation of the kinkboundaries is visible from (d) and at (f) the grain is completely recrystallised. Broader kinks develop in the large grain on the right. T=30°C, shortening and crossed niccols in NW-SE direction,* $\dot{\varepsilon} \approx 1 \cdot 10^{-4}\ s^{-1}$. *Width of view 2.6 mm.*

(d)

(e)

(f)

(g)

Dynamic recrystallisation

Arrays of kink-bands are the most conspicuous intragranular microstructures in a coarse grained camphor aggregate deforming at low temperature. Kink-boundaries rapidly become unstable and develop irregularities, leading to the division of the kink-bands into many smaller (sub-) grains. The combination of kinking and subsequent recrystallisation of the twins and kinks is an efficient mechanism to reduce the grain size to a few tens of microns. This can be seen in figure 2.4, where a large grain is divided up into a few thousand (sub-) grains after ≈15% strain. Sub-grain formation and grain boundary migration also reduce the grain size, irrespective of the presence of kinks.

It is not certain what the dominant deformation mechanism is at such a small grain size, as the grains are smaller than the thickness of the specimen and are therefore difficult to distinguish. There is a marked strain rate dependency on the grain size and vice versa, already observed by Urai (Urai *et al.* 1981, see also chapter 5). Strain tends to be localised in regions with the smallest grain size and with the strongest crystallographic preferred orientation. This grain size dependency of the strain rate was also observed with the mechanical tests (Chapt. 5). It is possible that diffusional creep and grain boundary sliding become important at a small grain size. Diffusional creep as one of the deformation mechanisms was also suggested by Burg & Wilson (1987).

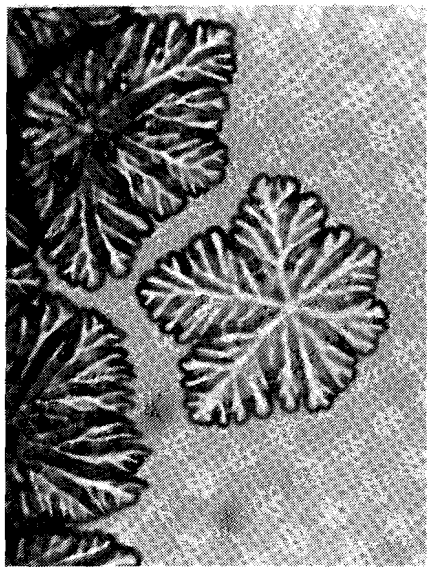

Fig 2.5. *Vapour grown (at 40°C) dendritic crystals of norcamphor showing hexagonal symmetry. Width of view 0.2 mm.*

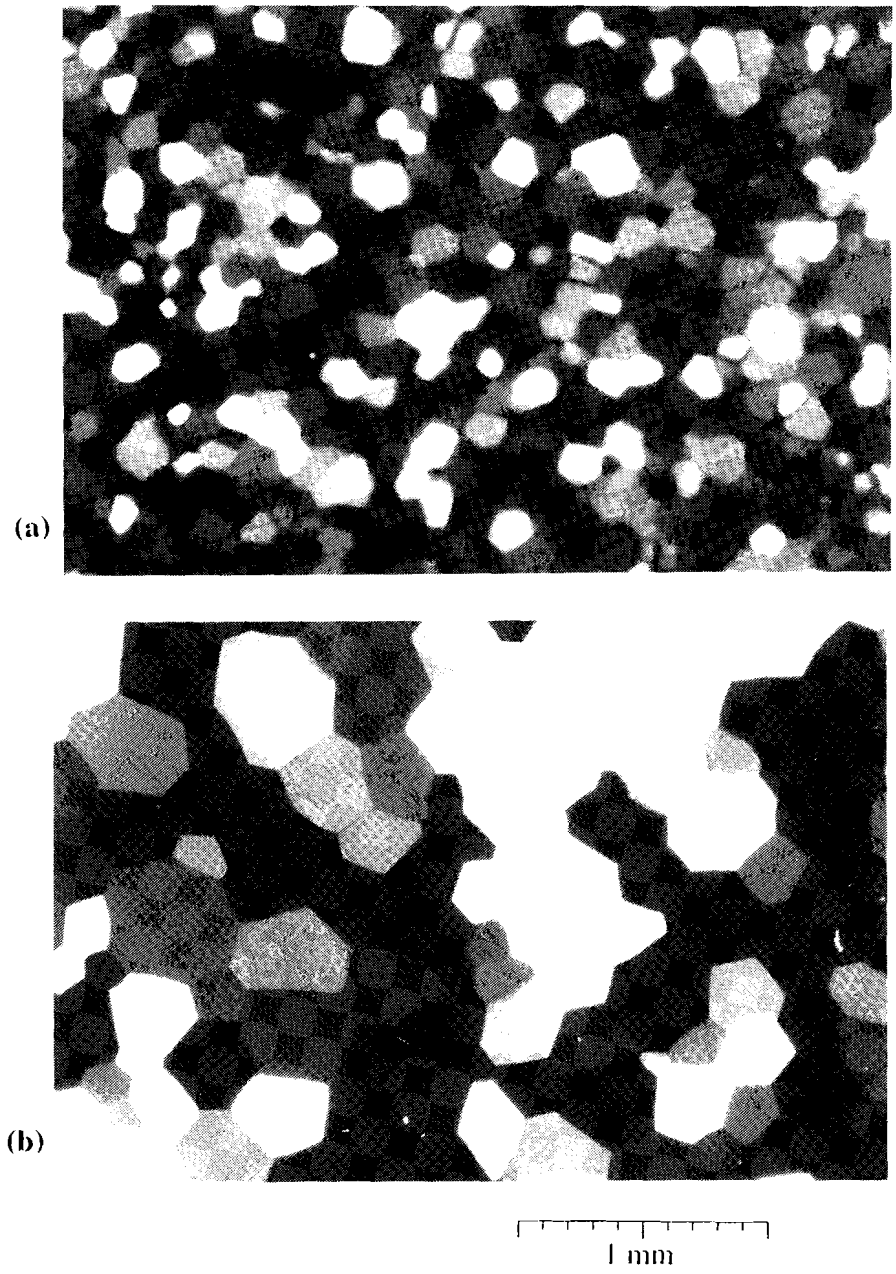

Fig 2.6. Static grain growth at 40°C. (a) Material shortly after cold pressing and (b) after 4 hours. Width of view 3.5 mm.

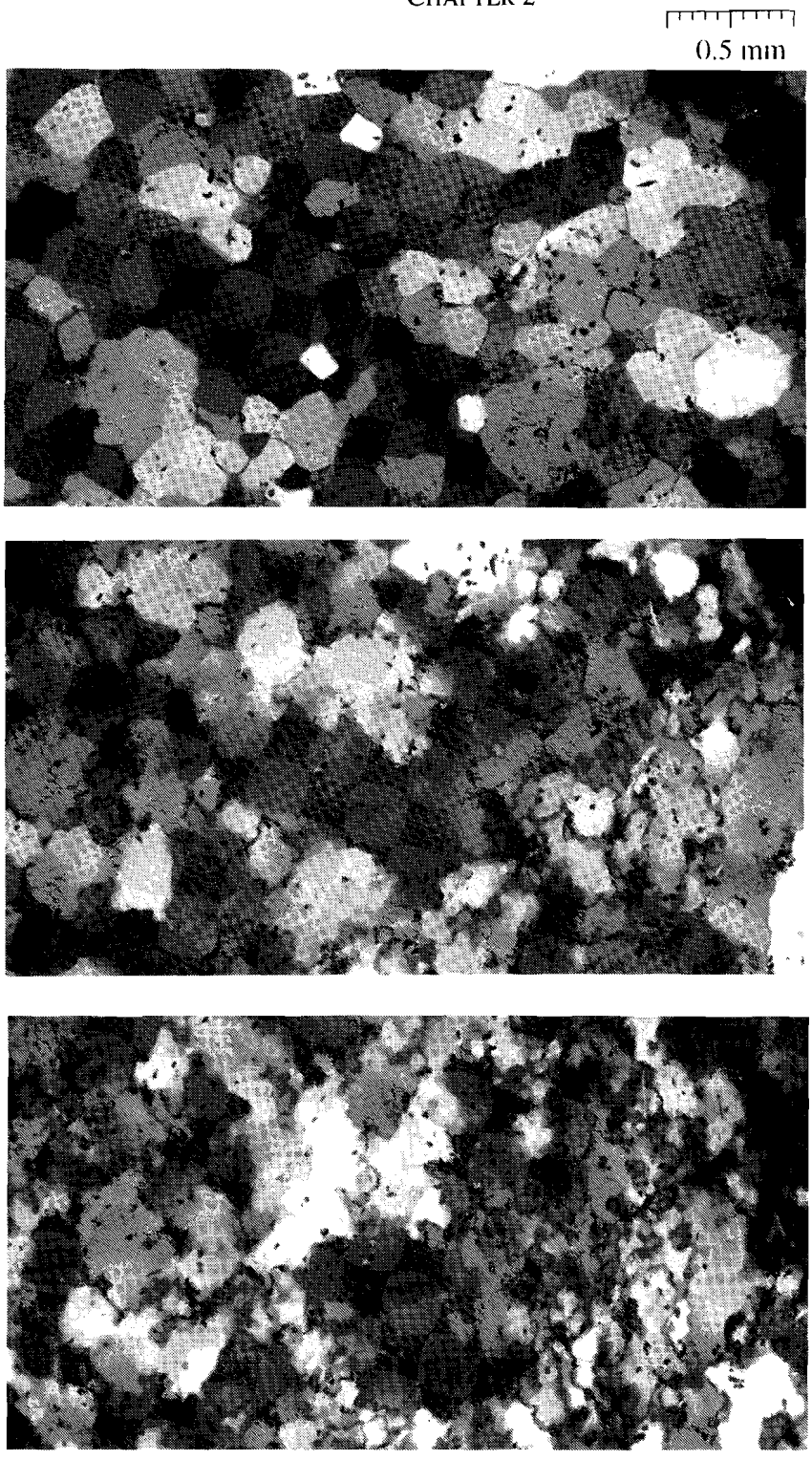
0.5 mm
(a)
(b)
(c)

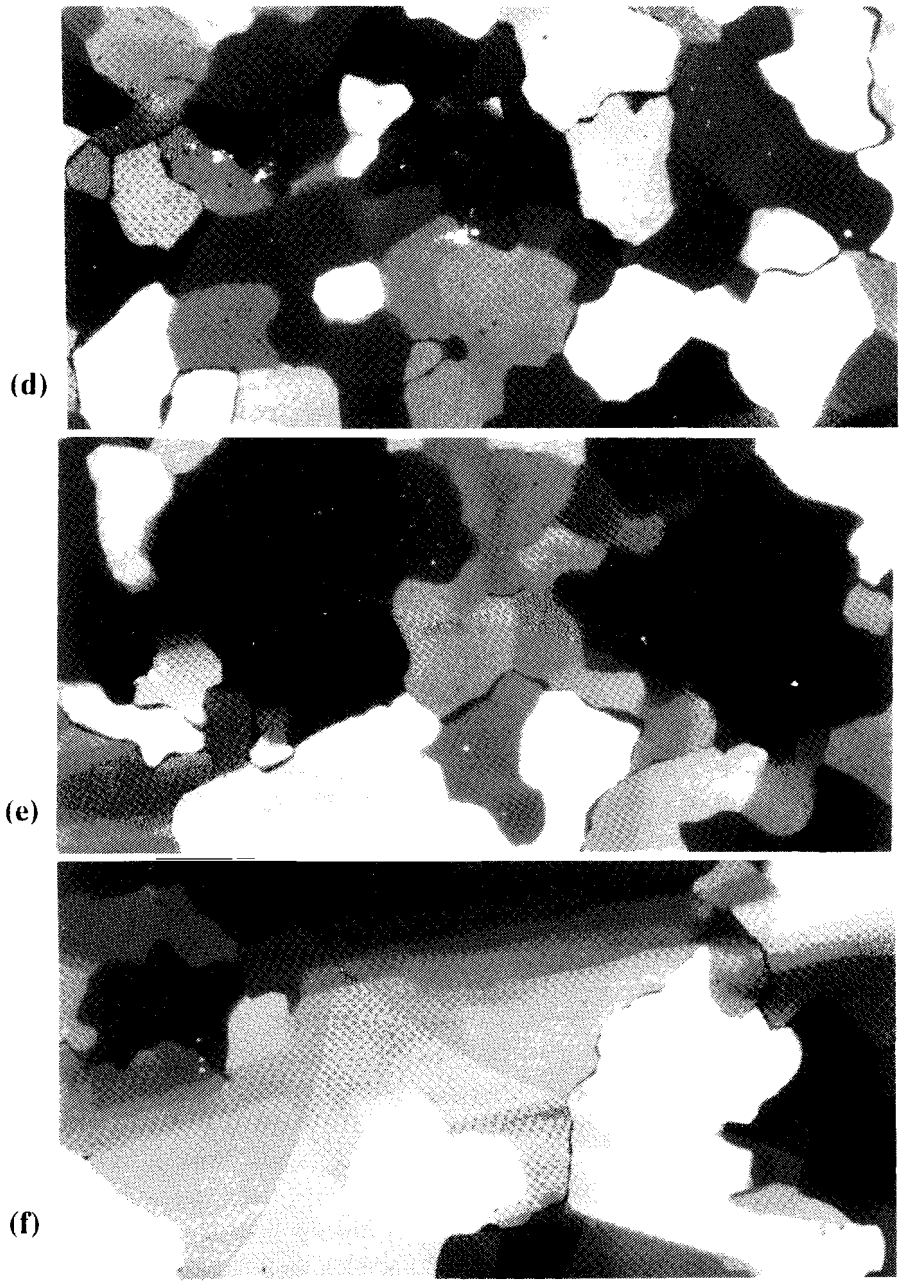

Fig 2.7. Microstructures in deforming norcamphor (a-c) low temperature (40°C, $\dot{\varepsilon}$= 1·10^{-6} s^{-1}). (a) Starting material, (b) 21% shortening (+33 mins.) and (c) 39% shortening (+66 mins.), (e-f) high temperature (360 K, strain rate 1.5·10^{-5} s^{-1}). Pure shear with shortening in E-W direction. (e) Starting material, (f) 15% shortening (+ 190 mins.) and (g) 25% shortening (+ 270 mins.). Width of view 3.5 mm, E-W shortening.

2.2.3 Norcamphor

Properties and microstructures

Norcamphor ($C_7H_{10}O$, Fig. 2.1.c), with a melting point of 94°C, is a material not previously used as a rock analogue. It was introduced by A.M. Wassenaar. The norcamphor used in this study has a purity of 98% and was purchased from Sigma-Aldrich (Belgium). Norcamphor seems to pose no special health hazards, but the physical and toxicological properties have not been thoroughly investigated (Sigma-Aldrich Material Safety Data Sheet). Norcamphor is relatively soft at room temperature (easy to deform plastically by hand) and the rate of recrystallisation is high, allowing deformation experiments at relatively high strain rate (up to 10^{-2} s^{-1}). Sample preparation is easy because of its softness. A sample with a course grained foam texture can be prepared within hours because of its high grain growth rate. It is slightly odorous and sublimates rather quickly, necessitating a sealed deformation cell (e.g. with grease). Its softness, ease of handling, high recrystallisation rate and safety make norcamphor very suitable for research and teaching purposes. Norcamphor forms eutectic melts when mixed at room temperature with most other known organic rock analogues (Table 2.2).

Norcamphor is uniaxial negative. Precipitation from vapour on glass surfaces produces dendritic crystals that have a trigonal symmetry (Fig. 2.5), similar to OCP-precipitate. A hexagonal or trigonal symmetry is inferred from this observation. Birefringence is 0.005-0.01. This makes norcamphor unsuitable for very thin (< 50 μm) samples.

Static grain growth is rapid at room temperature, compared to other known organic rock analogues, except norbornene. A thin specimen with an average grain size of less than 10 μm will develop a foam texture in a few hours (grain size ≈ 0.1 mm, Fig. 2.6).

Microstructures in norcamphor deforming in pure shear are shown in figure 2.7. At low temperature (near room temperature) the microstructure is characterised by serrated grain boundaries, undulose extinction, subgrains, a grain shape preferred orientation and a lattice preferred orientation. The grain boundaries remain more straight or smoothly curved at temperatures near the melting point. Subgrains form by progressive rotation and their boundaries are straight and subgrains are long and narrow or "blocky". The grain size increases during deformation, in the example shown in figure 2.7 to mm-size. The dominant deformation mechanisms is inferred to be dislocation creep. In pure shear the basal planes rotate towards an orientation approximately 45° to the shortening direction, whereas in simple shear the basal planes rotate towards the flow plane. The exact deformation mechanisms remain to be determined. A role of diffusional creep is possible.

Creep tests

Three creep tests were done with a miniature triaxial gas apparatus (see Chapter 3 for procedure and description of equipment). Cylindrical specimens with a diameter of 10 mm and a length of 15 mm were deformed under a constant load at a confining pressure of 0.8±0.1 MPa and a temperature of 28±1°C. The samples were pressed in a die at room temperature to virtually zero posrosity and not annealed prior to deformation. The creep curves are shown in figure 2.8.a-c. Differential stress ($\sigma=\sigma_1-\sigma_3$) - shortening rate ($\dot{\varepsilon}$) values measured at 5, 10 and 15% shortening were used to make a best fit for a power-law flow law:

$$\dot{\varepsilon} = 0.6^{+1.2}_{-0.4}\cdot\sigma^{7.8\pm0.9} \qquad (2.1)$$

The $\log(\dot{\varepsilon})$-$\log(\sigma)$ data are shown in figure 2.8.d, together with data for OCP and camphor for comparison (see Chapter 5). These first measurements suggest that the stress exponent is much higher for norcamphor than for OCP (4.5±0.3) and camphor (3.3±0.3). More experiments are needed to determine the flow properties accurately.

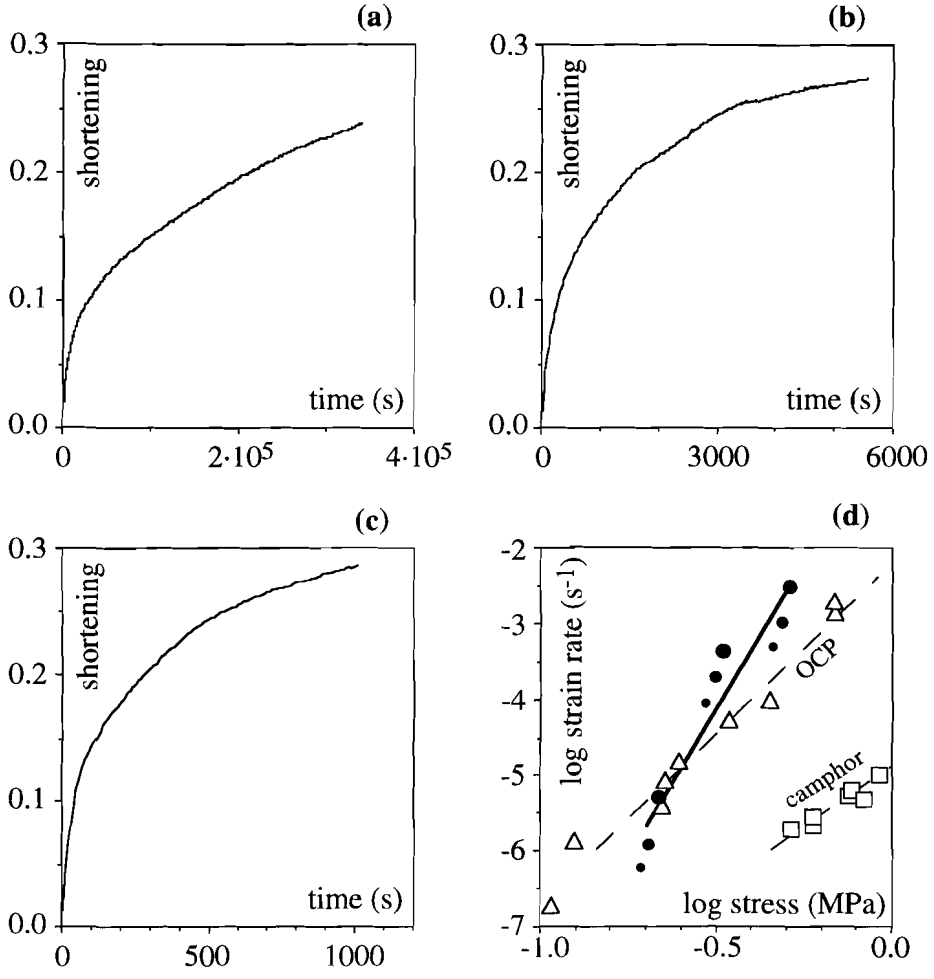

Fig 2.8. Results of creep tests. (a-c) Shortening versus time graphs for three constant load experiments at and T=28°C and initial differential stress of (a) 0.23 MPa, (b) 0.35 MPa and (c) 0.54 MPa. (d) Log(σ)-log(ε̇) graph with best fit for a power law stress-strain rate relation. Circles represent values obtained from the constant load tests at 5% (large circles), 10% (medium size circles) and 15% (small circles). Data for OCP (triangles) and camphor (open squares) are added for comparison.

Chapter 3

Equipment and experimental method

Two types of experiments were done in this study:
1) bulk deformation experiments, and
2) experiments with a transparent deformation cell

The first, discussed in section 3.a., is mainly aimed at obtaining rheological data. Possibilities to observe the specimen are limited, usually to the initial and final state. The second, discussed in section 3.b., is especially aimed at observing a deforming specimen in transmitted light during deformation. This type of experiments is suited for the study of microstructural development, but less suited for the collection of rheological data. The two types of experiments complement each other.

3.1 Bulk deformation experiments.

The basic experimental approach is to take a representative sample of the material of interest and subject it to controlled conditions of stress and strain (-rate). The relation between stress and strain rate can then be determined by systematically varying the controlling parameters. In this study two types of bulk deformation experiments were done:
1) axisymmetric compression (pure shear)
2) ring shear (simple shear)

3.1.1 Axisymmetric compression

The axisymmetric deformation geometry is technically the most simple and is widely used in rock mechanics research (e.g. Tullis & Tullis 1986a). In a typical experiment a cylindrical sample is held and compressed between two pistons. Deformation is coaxial, with the largest principal stress parallel to the axis of the sample. Using servo control or dead loading, one can either apply a force on the pistons and measure the rate at which the sample shortens, or one can move the pistons towards each other at a constant rate and measure the force needed to do this.

The deforming sample retains its cylindrical shape if lubrication at the contact between the pistons and the sample is perfect and if there is no tendency to localise

strain. If there is friction along this contact, the sample tends to deform into a barrel shape. Deformation and stress distribution then become increasingly heterogeneous during shortening and reliable stress - strain rate measurements are limited to low finite shortening (less then about 25% shortening in this study).

A miniature axisymmetric gas apparatus (Urai 1983) was used in this study. The apparatus is especially designed for deformation experiments with rock analogues such as camphor and OCP. It is described below and the results of experiments with this apparatus are presented in chapter 5. Calibrations are given in Appendix B.a.

specimen size:	diameter	10.0 mm
	length	15-20 mm
confining pressure: compressed air, maximum 5 MPa.		
Utrecht:	0.6 ± 0.05 MPa (all experiments except below)	
Melbourne:	0.8 ± 0.1 MPa (norcamphor & OCP+quartz tests)	
Heater element 250 Watt. Temperature range 0 - ≈300°C Temperature controller type CAL-9000 (CAL Controls Inc., Libertyville, Illinois, USA) with one 250 Watt heater element, power setting at 40% of maximum.		
LVDT: H.F. Jensen, Denmark, type UCA 5 C		
Maximum load 150 N with present set-up, higher loads possible.		
Jacketing: rubber jackets, Uritemp BV, Apeldoorn, The Netherlands		

Table 3.1. *specifications of the axisymmetric gas apparatus*

The apparatus

A schematic drawing and a photograph of the apparatus is given in fig. 3.1 fig. 3.2 and specifications in table 3.1.

The apparatus consists of a vertical piston-sample assembly in a steel pressure vessel. A cylindrical sample (10 mm in diameter, 15-20 mm in length) is placed between the upper and lower piston and jacketed with rubber. A confining pressure is applied on the sample by pressurising the vessel with compressed air, typically 0.6 MPa. The maxiumum confining pressure is 5 MPa. Seals are low friction - low clearance metal-to-metal ones that allow a small amount of air to leak during operation. The sample is loaded via a compensated piston assembly (see fig. 18 in Tullis & Tullis 1986) with a dead weight (fig. 3.1.b). All load applied on the upper piston by the dead weight, calibrated for the friction of the piston in its shaft, produces the vertical differential stress on the sample. We will refer to this as the "stress" or σ ($=\sigma_1-\sigma_3$) for the rest of this thesis. The relative displacement of the

upper piston is measured with an LVDT (Linear Variable Displacement Transducer) and logged on a personal computer. The strain (ε) is defined as the change in length relative to the undeformed sample length. The strain rate ($\dot{\varepsilon}$) is defined as the rate of change in length relative to the current sample length. A coiled heater element surrounds the piston assembly within the vessel and temperature is measured with a thermocouple (K-type) near the sample. Temperature was 28 °C for all experiments presented in chapter 5. Temperature was calibrated by inserting a second thermocouple through a hollow piston into a dummy sample of camphor. This showed that temperature variations over time and space were within ±1 °C at a set temperature of 28 °C.

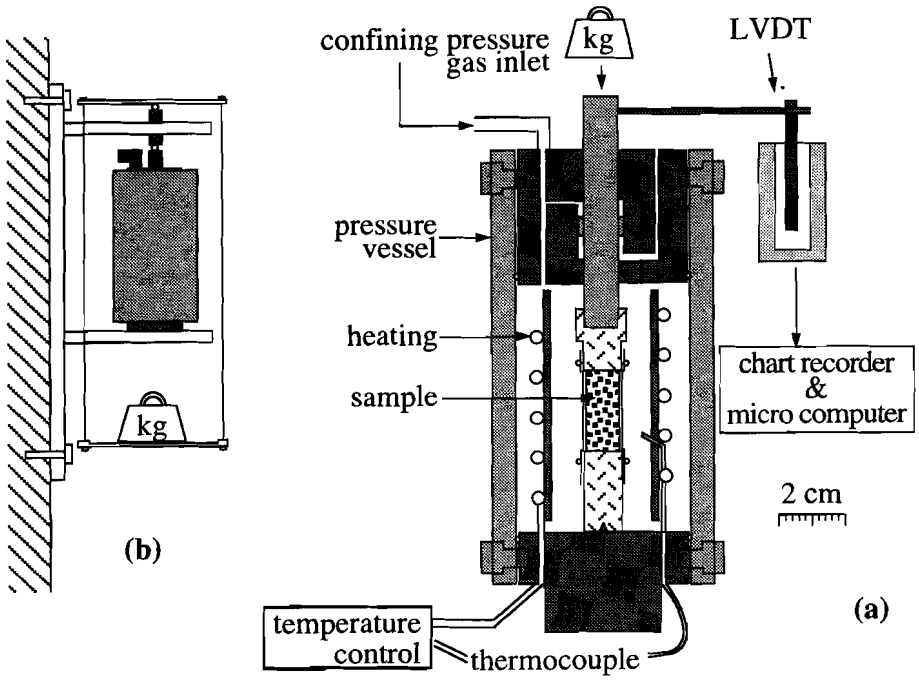

Fig. 3.1. (a) Schematic cross-section of the miniature axisymmetric gas apparatus. (b) The apparatus with its frame and the dead weight tray.

The error in stress measurements is about ±0.01 MPa (≈1-5%) due to variation in friction along the upper piston. With increasing strain the error increases as the sample deforms into a barrel shape (usually with a maximum diameter of about 13 mm, and a minimum diameter of 11-12 mm). Some experiments were done with a piston of 10 mm diameter, but most with 12 mm diameter. In this case the piston has a slightly greater diameter than the sample, which avoids wrapping of the sample

around the pistons. The friction at the piston - sample contact was reduced with silicon oil lubrication. The stress is corrected by assuming a constant volume and a cylindrical shape of the sample during the experiment. The error of the LVDT is less than ±0.01 mm and the errors in measurement of the length of the sample before and after deformation about 0.1 mm. The error in strain and strain rate values is therefore less than about ±2%.

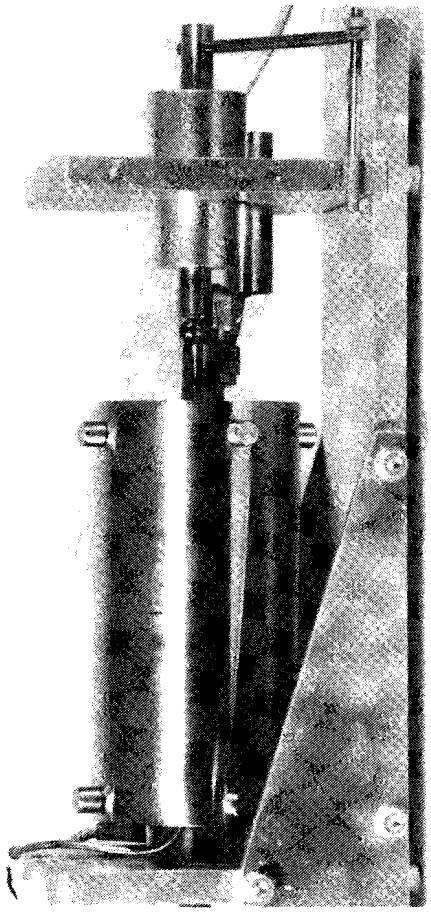

Fig. 3.2. *Photograph of miniature axisymmetric gas apparatus in its frame.*

3.1.2 Non-coaxial deformation

Non-coaxial progressive deformation to high finite shear strain is common in the earth's crust. Experimental non-coaxial deformation of strong materials, especially the end member type simple shear, is unfortunately in general technically more difficult than coaxial deformation. The main difficulty lies in producing a homogeneous stress field in the specimen and in making a reliable seal. Seven experimental configurations designed to produce non-coaxial deformation are listed and described by Price and Torok (1989, *and refs. therein*). These configurations are applied to soils, rocks and rock-analogues, such as clays and putties. A new design is added by Price and Torok (1989).

In the simplest design, a specimen is wedged between two parallel platens or grips that are forced to move parallel to each other (fig. 3.3.a) to deform the specimen in simple shear (e.g. Harris & Cobbold 1984). The specimen is welded or glued to the platens or the platens are made of the same or a similar material as the specimen to ensure a complete coupling (Franssen & Spiers 1990; Ross *et al.* 1987, and fig. 3.3.b). A disadvantage of (b) is that the boundary of the deforming region is not planar and the distribution of stress and deformation is therefore heterogeneous. Another possibility to avoid slip at the platens is to apply a normal force on the specimen (fig. 3.3.c). A disadvantage of this method is that the deformation type is not a simple shear, but a general non-coaxial deformation. The main advantage of (c) is that deformation can be applied by converging pistons in a cylindrical piston-sample column. A "conventional" axisymmetric deformation apparatus can then be used (e.g. Borradaile & McArthur 1990; Dell'Angelo & Tullis 1989; Jordan 1987; Schmid *et al.* 1987).

Stress or displacement is only applied on one side of the sample (top and bottom) in the experimental configurations described above. The specimen can be confined laterally (plane of view in fig. 3.3) to impose plane strain deformation. Another approach is to apply the deformation in two sides (top & bottom, left and right side), with an array of pistons (fig. 3.3.d), a flexible membrane (fig. 3.3.e) or rotating shafts (e.g Ildefonse *et al.* 1992; Passchier & Simpson 1986; Price *et al.* 1989; Treagus 1988; Treagus & Sokoutis 1992; Van Den Driessche & Brun 1987, and fig. 3.3.f).

Unconfined sides of the specimen cause a distortion of the applied stress field and a change of shape of the specimen during deformation enhances this distortion. Only a relatively small finite deformation can be achieved, although in general more than with the axisymmetric configuration.

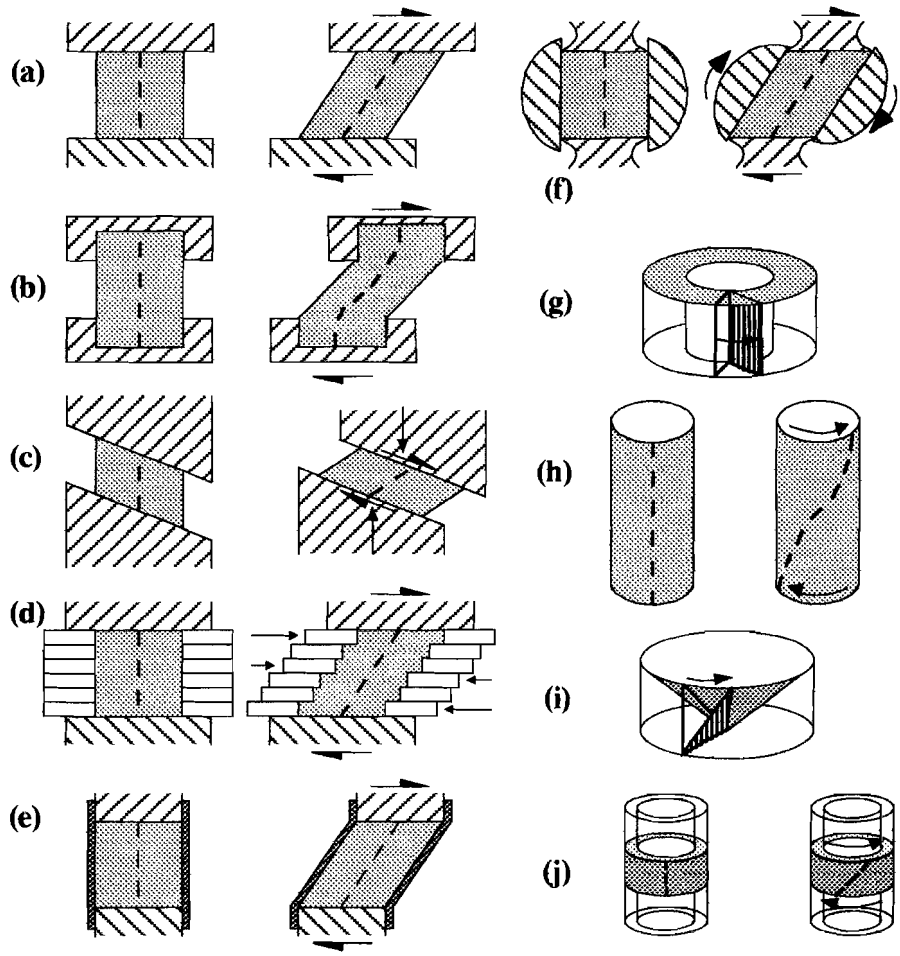

Fig. 3.3. Experimental configurations for non-coaxial deformation (see text for explanation)

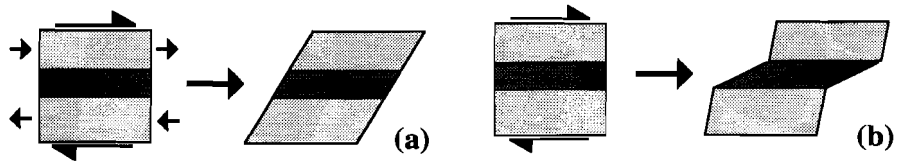

Fig. 3.4. Response of an anisotropic material to different boundary constraints. (a) simple shear deformation is imposed on the outer shape of the specimen and (b) shear stress or shear displacement is only applied on the top and bottom side of the sample. Heterogeneties in deformation are uninhibited.

Cylindrical shear configuration

A special group of configurations are the cylindrical deformation configurations. The main advantage of this configuration is that deformation does not change the outer shape of the specimen. Deformation therefore does not change the geometry of the applied stress and very high shear strains can be achieved.

There are two basic types of cylindrical deformation: Couette and torsional deformation. Couette deformation is the deformation between two coaxial cylinders (fig. 3.3.g), such that the shear plane is cylindrical as well (Passchier & Sokoutis 1993). A disadvantage of Couette flow is that the stress distribution is heterogeneous in the specimen: shear stress increases towards the centre of the apparatus (centre of rotation). In the torsional deformation configuration the two ends of a cylindrical specimen (rod) are rotated with respect to each other (fig. 3.3.h). In this case the shear plane is perpendicular to the axis of rotation. Shear strain in a specimen is linearly dependent on the radial distance from the centre of rotation. A special case of this configuration is the cone-and-plate configuration, commonly used in viscometers to determine the rheology of fluids (e.g. Barnes *et al.* 1989, fig. 3.3.i). The advantage of this configuration is that the shear strain and -rate are independent of the radial distance from the centre of rotation. Another approach to reduce the differences in bulk shear strain (-rate) in the torsional configuration is to use a "hollow cylinder" (Handin *et al.* 1960) and fig. 3.3.j). The hollow cylinder configuration is mostly used in soil mechanics (e.g. Saada & Townsend 1981) and has been used by Tullis & Weeks (1986) to study frictional sliding in rocks.

Boundary constraints and anisotropic materials

In the methods described in the previous section the change in outer shape of the sample is prescribed on all sides of the sample (d,e,f), or only one or two of the sides are constrained (a,b,c). Heterogeneties in the direction perpendicular to the shear plane are suppressed in the the first group, but not in the second group. Such heterogeneties are unconstrained during deformation in the cylindrical deformation configurations, although the outer shape of the sample does not change. In the first case the experimentalist can answer the question: "what will happen if the specimen is forced into bulk simple shear deformation?". In the second case, the question must be: "what will happen if a specimen is subjected to a shear stress (or displacement) on two sides?". The two questions will give different answers if the sample is anisotropic. The difference is illustrated with figure 3.4.

A layered specimen consisting of a hard and soft layers is subjected to a bulk simple shear (constraints on all sides) in fig. 3.4.a. Both the hard and the soft material must deform an equal amount and the measured stress / strain rate will reflect mostly the flow properties of the hard material. In fig. 3.4.b the shear stress / displacement is only applied on the top and bottom side of the specimen. As the specimen is not constrained laterally, the hard and soft material will deform at different rates. The specimen as a whole will now be much softer than in case (a). The measured properties of the specimen will be relatively insensitive to the orientation of the soft layer in case (a), but highly sensitive to it in case (b). The deformational geometry in natural shear zones is most similar to case (b). To investigate simple shear deformation in anisotropic rocks, as occurs in shear zones, one would therefore choose experimental configuration (b).

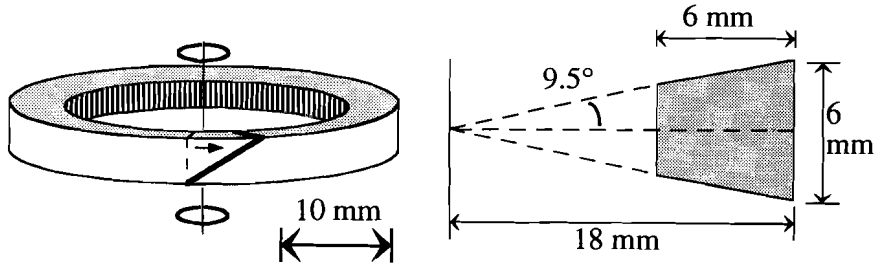

Fig. 3.5. (a) Deformation geometry of the new bulk ring shear apparatus. (b) cross-section through the specimen.

A new simple shear apparatus for rock analogues

A new deformation apparatus for simple shear deformation was designed and built in this study. The design was based on the existing hollow cylinder ring shear and cone-and-plate configurations. The apparatus was especially designed for the the deformation of rock-analogues such as OCP and camphor. The requirements for the design were the following:

1) the shear zone must be circular to enable very high shear strains;
2) a normal stress can be applied on the grips and the sample is confined on all sides to avoid dilatency and detachment of the specimen from the grips;
3) The seal works up to very high shear strains;
4) Confining pressure and shear stress of up to about 2 MPa are possible;
5) Temperature can be controlled accurately and set up to about 300°C;
6) Strain localisation is not forced, nor inhibited;
7) observation of the specimen is possible by using transparent (glass) parts. This is not yet implemented.

A "doughnut" shaped sample is held between two cylindrical grips at the top and bottom surface (fig. 3.5.a). Deformation is imposed on the sample by rotating the grips with respect to each other. The grips are inclined towards the centre (fig. 3.5.b). In this way the bulk shear strain is independent of the distance from the centre of rotation. Since a normal stress is required on the grips to transmit the shear stress on to the specimen, the sides are confined by rigid cylinders to avoid extrusion and/or dilatency of the specimen. A disadvantage is that this will cause friction at these sides, which distorts the stress and strain rate distributions inside the specimen. It is essential that this friction is kept as small as possible by lubrication (see Appendix B for an estimate of the magnitude of the friction).

The configuration has three main features:

1) Deformation does not change the outer shape of the sample. High shear strains can therefore be achieved.
2) A normal force is applied on the grips. This will produce counter forces by the rigid sides, since the specimen is fully constrained by the grips and the rigid cylinders. Thus a hydrostatic stress is achieved in the specimen. This does not affect the differential stress in the specimen, but it will have an effect on the friction along the sides.
3) Deformation is only constrained by a shear stress applied at the grips and zero displacement outwards and inwards, thus ensuring bulk plane strain simple shear, but no constraints on the vertical shear distribution.

The apparatus is described in the section below. Specifications on the apparatus are given in table 3.1. The method to determine the applied shear stress and the measured bulk shear strain and shear strain rate is described in appendix A.3.2&3. Calibrations are given in appendix B.2.

3.1.3 Bulk ring shear creep apparatus - description

A photograph of the apparatus is shown in figure 3.6 and a schematic drawing in figure 3.7. In the following description the parts are labelled as in this drawing.

A doughnut-shaped specimen (a) is held between two steel cylindrical grips (b&c) with radial corrugations to hold the specimen. The lower grip is fixed to the upper base plate (i). The upper grip is rotated to deform the specimen. Smooth confining cylinders (g&h) on the inside and outside constrain the sample laterally. The space between the confining cylinders and the grips is <0.02 mm, to avoid friction between the rotating grips and the cylinders. Some of the specimen material can be extruded through this narrow slot. In practice this is a negligible amount. The two confining

steel cylinders around the specimen are not fixed to the apparatus, but are held in place by the sample. The confining cylinders can rotate as the cylinders are not fixed to the apparatus. The rotation speed is about half that of the upper grip, when deformation in the sample is not localised in either top or bottom half of the specimen. The surfaces of the confining cylinders in contact with the specimen were lubricated to avoid friction caused by sticking of the specimen to the surface of the confining cylinders. In the first 7 experiments thin machine oil was used, as did Jessell (*pers comm*) in transparent deformation cell experiments. In subsequent experiments a lubricating grease (APIEZON AP-101) was used since thin oil may tend to migrate away from the cylinder surface into the specimen. No difference in lubrication was noticed. The magnitude of friction in at the confining cylinders is still poorly constrained. An estimate is given in appendix B.2.

specimen size:	inner radius	12.00 ±0.01 mm			
	outer radius	18.00 ±0.01 mm			
	height at r=15 mm	5 mm (ideally)			
inclination of grips: 9.5°					
radial corrugations 0.4 mm deep, 0.5 mm wide at top (at outside grip)					
springs (factory settings):					
number	length (mm)	spring constant (N/mm)	force at reference length		
1	60	74.04	1569.06 N	at	38.5 mm
2	72	38.42	1068.92 N	at	44.2 mm
3	74	15.69	576.63 N	at	37.1 mm
weight of driving wheels and shaft: 4.125 kg.					
Total pressure on sample at spring (nr. 1) length of 46 mm: 1.9±0.1 MPa					
radius of driving wheels:	small wheel 48.7 mm				
	large wheel 197 mm				
potentiometer: 0.00 - 10.00 ± 0.015 V single coil, continuous					
radius wheels:	nr. 1 5.91 mm				
	nr. 2 12.35 mm				
	nr. 3 24.05 mm				
steel wire 0.86 mm diameter					
Temperature controller type Omega 6100, Omega Engineering Inc., Stamford, Connecticut, USA.					
2 heater elements, 75 Watt each. Power setting at 40% of maximum.					
Material. All metal parts are made of stainless steel, except:					
central shaft (d):	hardened stainless steel				
driving wheel & base plates (i,j,k):	aluminium				
base block with heating (r):	brass				

table 3.2. *specifications of the bulk ring shear apparatus*

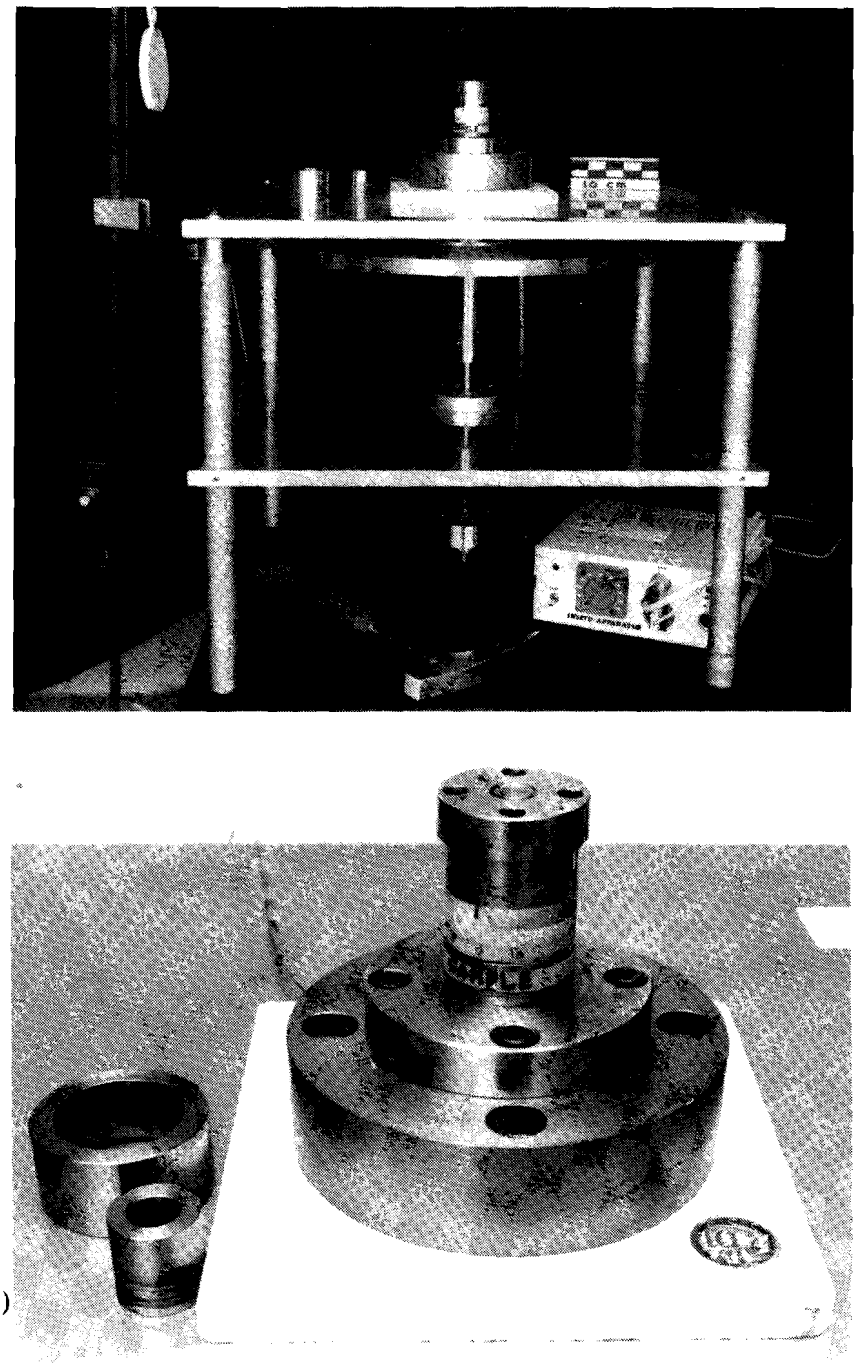

(a)

(b)

Fig. 3.5. (a) Photograph of the bulk ring shear apparatus. (b) Detail of the sample chamber. The confining cylinders (left) are not placed.

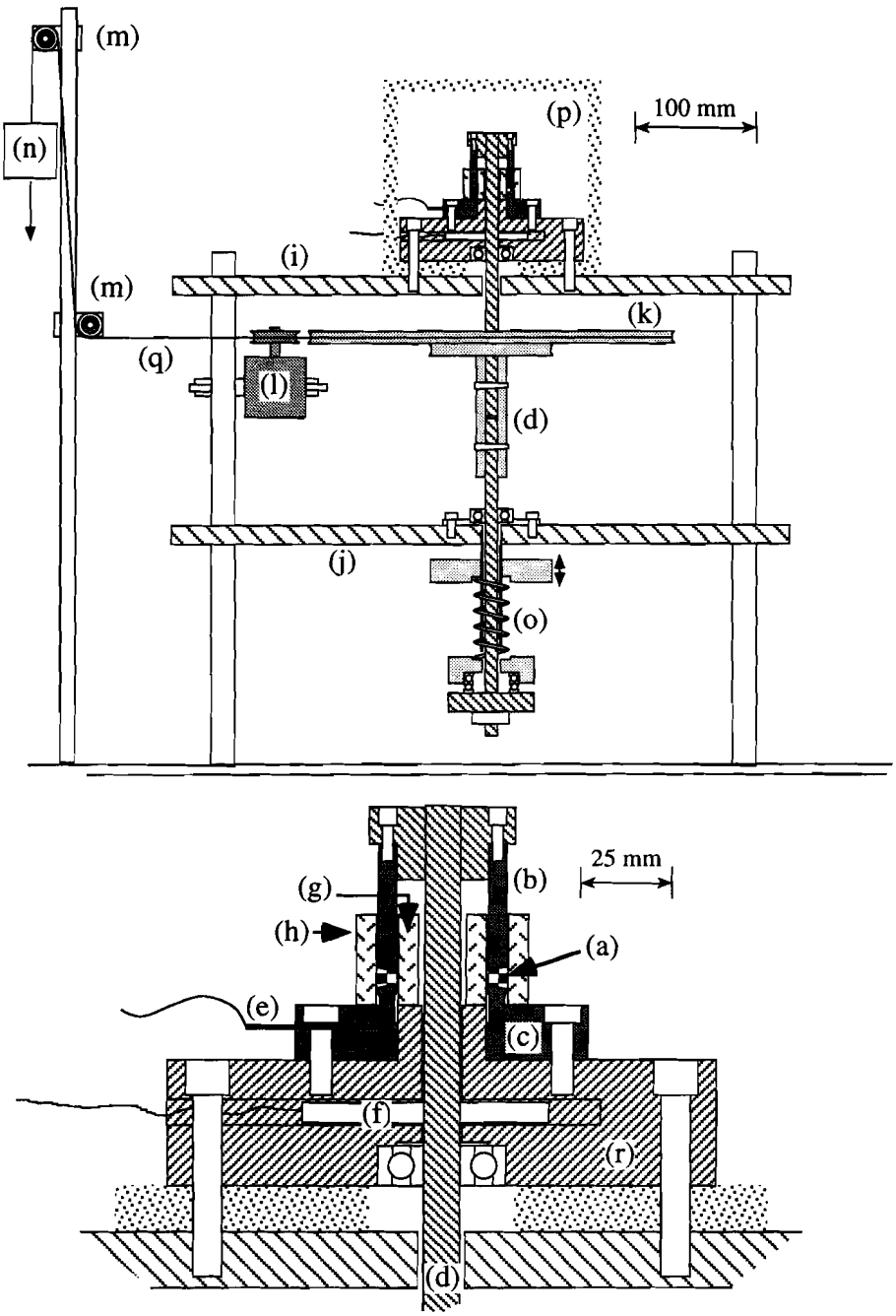

Fig. 3.7. Schematic drawing of whole bulk ring shear apparatus (top) and close-up of part with specimen and grips. (a) specimen, (b,c) upper and lower grip, (d) shaft, (e) thermocouple, (f) heater element, (g,h) inner and outer confining cylinder, (i,j) upper and lower base plate, (k) driving wheels, (l) potentiometer, (m) pulleys, (n) dead weight, (o) spring-construction, (p) insulation, (q) wire and (r) brass base block.

Shear stress

The upper grip is fixed to a central shaft (d) that extends downwards to below the lower base plate (j). This shaft is made of two parts that can be disconnected to open the specimen-chamber before and after an experiment. The shaft is kept in place by two ball-bearings at the two base-plates. These ball-bearings allow for vertical movement, but constrain the lateral movement to within 0.02 mm. A torque is applied on the shaft by a dead weight that hangs on a steel wire (q) which is wound around one of two driving wheels (k) on the shaft just below the upper base plate. The driving wheels are used to amplify the torque on the shaft. The wire is led over two pulleys (m) to allow the weight to descend over a distance of about 2 metres before it reaches the floor, to allow relatively high finite shear strain without interruptions. The shear stress applied on the specimen is determined by the mass of the dead weight and the radii of the driving wheel and the grips (Appendix A.3.2).

Measurement of bulk shear strain and shear strain rate

The wire is led along a wheel of a potentiometer. The unwinding of the wire causes a rotation of the potentiometer wheel. The potentiometer produces an output voltage (0-10 V) that is linearly dependent on the orientation of the wheel. The output voltage was recorded by a personal computer and a chart recorder. The bulk shear strain and bulk shear strain rate in the specimen can be derived from the output voltage, the radii of the potentiometer wheel, the driving wheel and the height of the sample at a reference radius (Appendix A.3.3). The potentiometer has three wheels attached to it with different radii. The choice of the radius of the potentiometer wheel depends on the desired accuracy of the shear strain (-rate) measurements.

Confining pressure

A confining pressure is applied by a normal force on the grips. This is needed to achieve a firm grip of the corrugated grips on the specimen and to prevent dilatancy. The normal force is applied by pulling the central rotating shaft, attached to the upper grip, downwards with a spring (o). A plate with ball-bearings is fixed to the shaft at its lower end, below the lower base plate. The non-rotating spring rests on the plate with ball-bearings. The spring can be shortened with a threaded ring, attached to the lower base plate. The confining pressure can be adjusted (0-2 MPa) by using different springs and adjusting the length of the spring.

Heating

Two 75 W heater elements (f) are located in a brass-block (r) below the lower grip. A K-type thermo-couple (e) is located between the heater-elements and the specimen. The brass block is separated from the base plate with a plate of insulating ceramic material. An insulating cover (p) can be placed over the upper part of the apparatus.

Sample preparation

A specimen is made by first placing the two confining cylinders in position and distributing a measured amount of the granular sample material evenly on the lower grip. The upper grip, attached to the upper half of the shaft, is then placed in position and fixed to the lower half of the shaft. Then the spring is tightened to pull down the upper grip and compress the granular sample material. The temperature is raised to about 70°C in most cases to speed up the compaction. Depending on the material used it then takes about 1 to 4 days to achieve a solid, translucent, fully compacted sample.

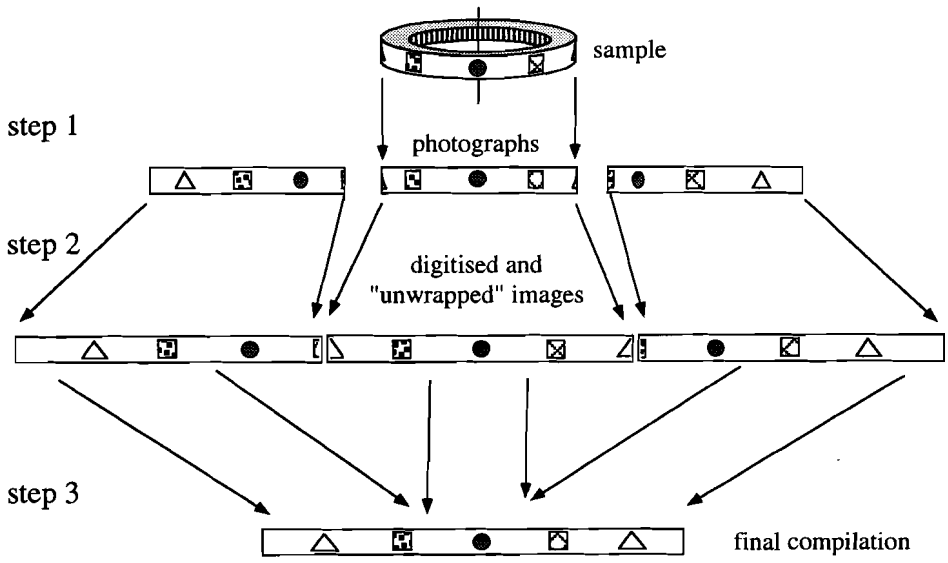

Fig. 3.8. Procedure of producing one single unwrapped image of the outer surface of a specimen. Step 1: the outer surface is photographed from different angles (3 in this example). Step 2: the photographs are digitised and "unwrapped". Step 3: the unwrapped images are fitted together to create one single image.

Observation & photography of sample

When the outer confining cylinder is removed, the outside surface of the specimen can be observed. This is done at the end of an experiment, but can also be done during an experiment, to study the development of microstructures. The following procedure was followed to produce an image of the whole outer surface of the specimen (Fig. 3.8).

The surface of the sample was photographed, from different angles, with a Mamiya 6x6 cm camera with macro lens and extension tubes to produce about life-size black and white negatives. 13x18 cm prints of these were digitised to 72 dpi 256 grey-scale PICT-files for a Macintosh computer. These images were then transformed to produce "unwrapped" images, correcting for the fact that the photographs were made of a cylindrical surface. The unwrapped images were then fitted together manually on the computer display to create one image of the whole outer surface of the specimen.

3.2 Transparent deformation cell

The rock-analogues described in chapter 2 are soft enough to be deformed in a transparent deformation cell. The sample is deformed between glass plates in a small rig that fits on an optical microscope stage. Thus one can observe the development of microstructures throughout the deformation experiment. Several designs have been developed by different workers in the field. Only the basic deformation configurations will be discussed here.

3.2.1 Basic deformation configurations

In all designs, the specimen is a thin sheet, sandwiched between two glass plates to allow observation of the specimen (fig. 3.9). The thickness of the sheet can vary from a few tens of microns (melt-grown para-dichlorobenzene, OCP (Ree 1990)) to about 1 mm (ice, Wilson 1986). Deformation is approximately plane strain as the specimen is confined between two glass-plates. A specimen can thicken or thin somewhat in most cases, when the glass plates are not completely fixed with respect to each other or because of bending of the glass plates.

Deformation is imposed by a thin piston (of the same thickness as the specimen) that is pushed between the two confining glass-plates in the design described by Urai *et al.* (1980) and Urai (1987). In most other designs the two glass-plates themselves are displaced with respect to each other (fig. 3.9.a). The specimen is then deformed by

pistons (cover-slips) that are glued on the glass-plates (e.g. Means 1983, and fig. 3.9.b) or by so-called *frosted grips* (e.g. Means & Xia 1981), fig. 3.9.b). In the latter case the surface of the glass is roughened with grinding powder to hold the sample.

The choice of the type of grips depends on the material to be deformed and on the desired flow-type. Some materials, such as camphor, have a tendency to detach from frosted grips and the use of pistons is then preferable or mandatory. If a specimen is made form a melt it is difficult to make it with a preset thickness, as is necessary when pistons are used. Then the use of frosted grips is preferred.

Pistons are best used for pure-shear deformation or moderately non-coaxial deformation. Non-coaxial deformation can be achieved by orienting the pistons at an angle to the displacement direction. High non-coaxiality (simple shear) cannot be achieved with pistons, as pistons allow for slip parallel to the piston-sample contact. Pure shear can also be achieved with frosted grips, but with the limitation that lateral slip at the grips is limited and strong barreling may occur. Frosted grips are best suited for simple-shear or strongly non-coaxial deformation.

Instead of straight frosted grips one can use circular frosted grips and rotate instead of translate the glass-plates with respect to each other (Jessell & Lister 1991, and fig. 3.9.c). This has the important advantage that very high shear strains can be achieved. Deformation is simple-shear with a circular flow plane (Couette-type). The shear-strain distribution is not homogeneous as the applied shear stress decreases linearly with the distance from the centre of rotation.

3.2.2 Equipment used

The experiments with a transparent deformation cell that are included in this thesis have been done using:

1) a press built by Urai and de Graaff. The apparatus consists of a metal base block and cover plate, holding the glass plates (50 x 25 x 1.5 mm, with thin-section cover slips, 0.1 mm thick). The glass plates with the sample sandwiched in between are pressed together by bolts with springs. The upper glass plate is translated at a constant speed by a motor driven ram. Lateral movement of the glass plates is inhibited by adjustable guides. A heater element and thermocouple are positioned in the base block for temperature control. The sample can be viewed in transmitted light with an optical microscope through apertures in the base block and the metal cover.

2) a press designed by Jessell (fig. 3.10), similar to the one described by Jessell & Lister (1991). The apparatus consists of a metal base plate and top plate. Glass plates

with circular frosted grips are fixed in apertures in these plates. Sample thickness is adjustable and can be controlled by bolted leaf springs. The thickness of the specimen is not fixed during an experiment, but decreases as the sample material flows outwards. If the sample thickness is fixed, the sample material slowly detaches from the frosted grips (ten Brink, *pers. comm.*). Rotation of the top plate is driven by a stepper motor, which allows a continuous range (two orders of magnitude) of rotation speeds for each gearbox, and thus a continuous range of applied bulk shear strain rates in the specimen. Rotation is transmitted via a cog-wheel, surrounding the base plate, with a cantilevered steel plate to a thrust pin fixed to the top plate. A heater element and thermocouple are positioned in the base plate for temperature control.

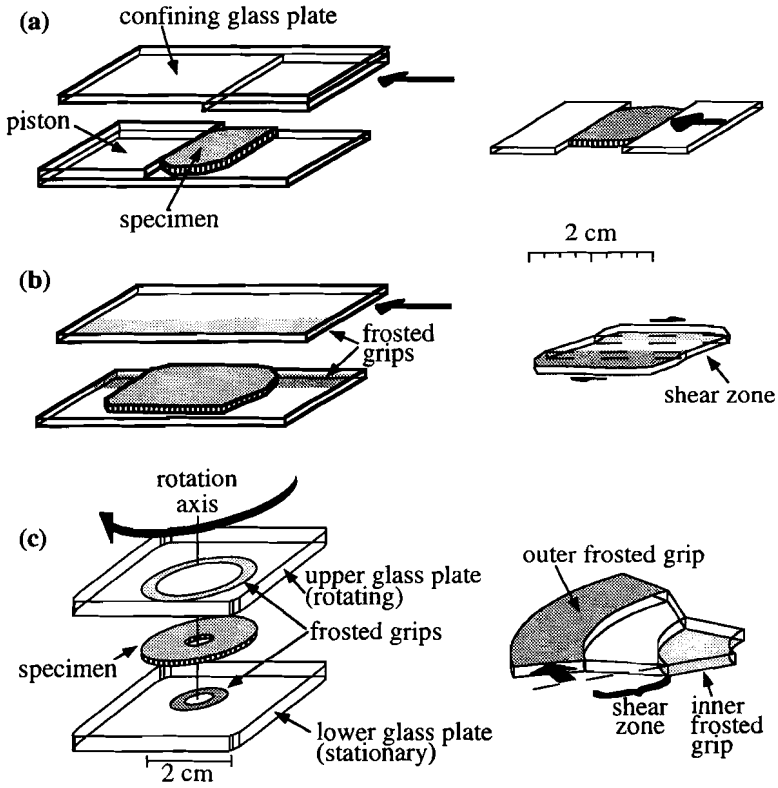

Fig. 3.9. *Basic deformation geometries in transparent deformation cell. (a) The sample is confined between two glass plates with thin pistons glued to them. The upper glass plate is translated by a ram to impose coaxial deformation. (b) The sample is confined between two glass plates with frosted grips grinded on them. The upper glass plate is translated by a ram to impose simple shear deformation. (c) The sample is confined between two glass plates with circular frosted grips grinded on them. The upper glass plate is rotated to impose torsional simple shear deformation. (fig. c, courtesy of ten Brink)*

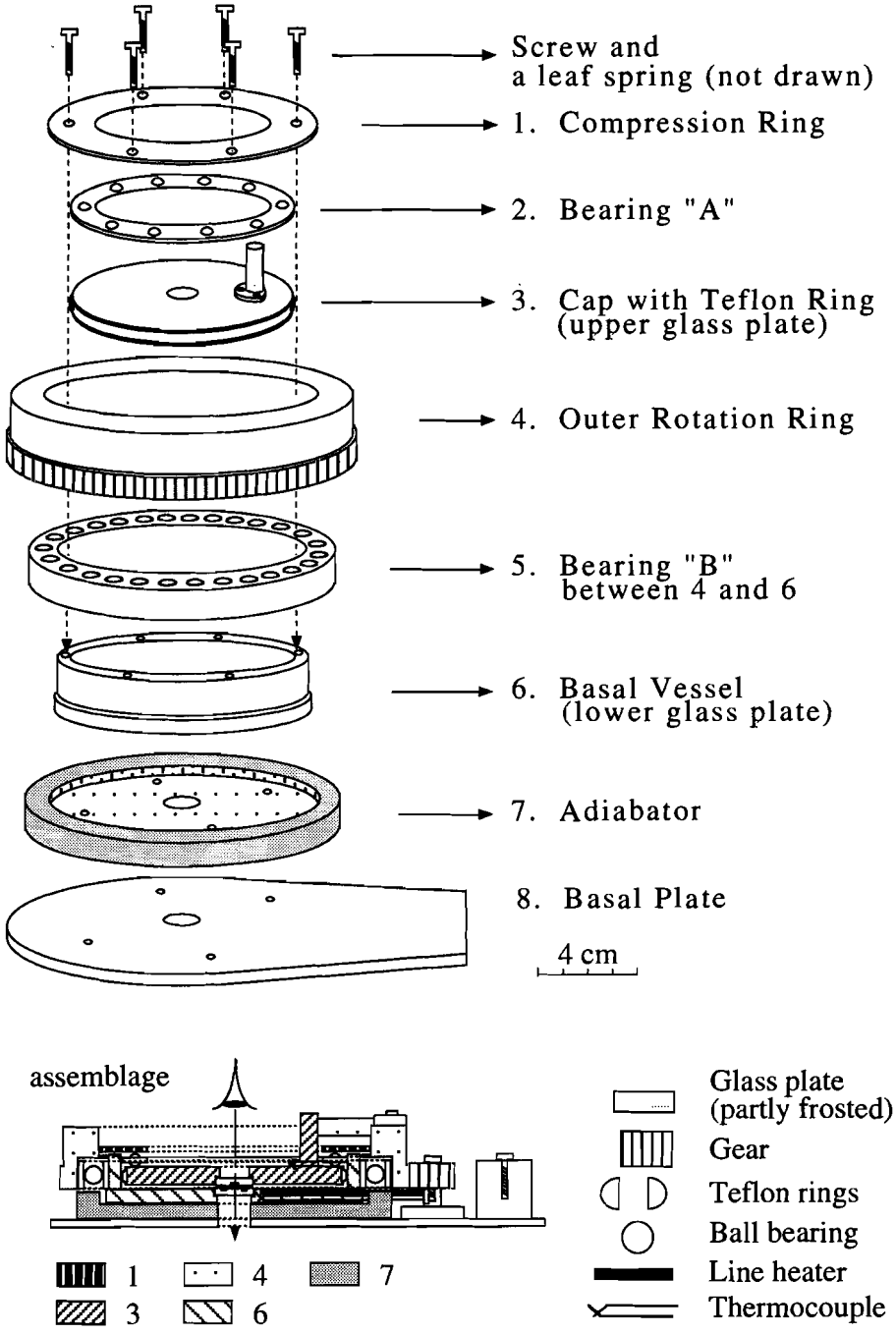

Fig 3.10. *Schematic drawing of the transparent deformation cell for simple shear deformation in a circular shear zone, designed by Jessell. Lowermost drawing shows the whole assemblage of the individual parts shown above. Drawing courtesy of Jessell and Otoh.*

Chapter 4

The analysis of progressive deformation in rock analogues §

4.1 Abstract

Two-dimensional deformation experiments using analogue materials such as octachloropropane and camphor have proven to be a powerful tool in the investigation of microstructural development, since they make it possible to observe the specimen throughout its deformation history. The addition of dispersed marker particles makes it possible to trace the movement of material points during deformation. From this information the flow and deformation can be interpolated for any point within the specimen at any time. The geometry of the flow and deformation can then be visualised in the form of grids, contour-plots, strain ellipses and other methods.

Despite this apparently ideal setting to study flow and deformation, the need to use marker particles to trace material points introduces unexpected problems in the analysis. We present a computer program to analyse the movement of marker particles. Digitization of marker particle positions is improved by the use of video input and semi-automatic digitization of marker particles. The use of polynomials to describe the complete path of marker particles and least-squares best fit solving improves the analysis of the data.

4.2 Introduction

The development of microstructures during ductile deformation in rocks can be modelled with crystalline rock-analogues such as octachloropropane and camphor that exhibit crystal-plastic behaviour at room temperature. These materials can be deformed between thin glass plates in a rig that can be mounted on a microscope stage (Means 1977, 1989 and references therein). In this way a deforming specimen can be observed throughout its deformation history. Analogue experiments are becoming increasingly popular for research and teaching purposes because they are

---

§ P.D. Bons, M.W. Jessell & C.W. Passchier, Journal of Structural Geology, Vol. 15, No. 3-5, pp 403-411, 1993

the only technique available to structural geologists where the processes and kinematics of deformation can be directly observed at the grain scale. They are useful tools for demonstrating the principles of recrystallization, twinning and shear zone development.

One of the main aims of analogue experiments is the determination of the kinematics of deformation, which can then be linked to the observed microstructural phenomena. Progressive deformation can be studied by tracking the relative displacements of material points. It is not practical to inscribe a grid on the thin specimens of e.g. camphor as is the practice with clay or wax-experiments (e.g. Mancktelow 1991) and grain boundaries cannot serve as marker particles since they migrate through the material (e.g. Urai *et al.* 1986). Therefore small opaque marker particles are dispersed through the material (grinding powder (SiC), $\approx$ 5 to 30 μm in size). These particles move passively along with the deforming material (Means 1980, Jessell 1986).

Micrographs or video-images can be taken at specific intervals during an experiment. This produces a series of images with dispersed dots (Fig. 4.1). Two steps have to be taken from this stage to produce, for instance, plots showing the distribution of finite strain for a deformation episode between two photographs:

1) Digitization of the positions of each marker at each recorded stage.
2) Actual analysis of the kinematics of deformation.

The first step can be rather difficult if performed manually. Marker particles have to be as small as possible in order not to influence the experiment and therefore recognition of individual marker particles is difficult. Pattern recognition is therefore used to identify individual marker particles from a recognizable group.

The second step is analogous to the analysis of deformation using an inscribed grid (e.g. Mancktelow 1991). A difference is that our marker particles are randomly distributed. An imaginary grid has to be superposed on the specimen. For each grid node the deformation is then analyzed using the displacements of the marker particles nearest to that node. A simple method is described by Jessell (1986). It is based on the principle that if the positions before and after deformation of three marker particles are known, the position gradient tensor can be exactly calculated if deformation was homogeneous in the triangle with the three marker particles at its corners. The minimum number of three marker particles is derived from the fact that a tensor can only be reconstructed if changes in position of at least two points with respect to a third point are known. The third point is the base of the reference frame in which the tensor description is calculated. This method, however, is very sensitive to inevitable errors in digitised marker-particle positions (Ten Brink, unpublished data).

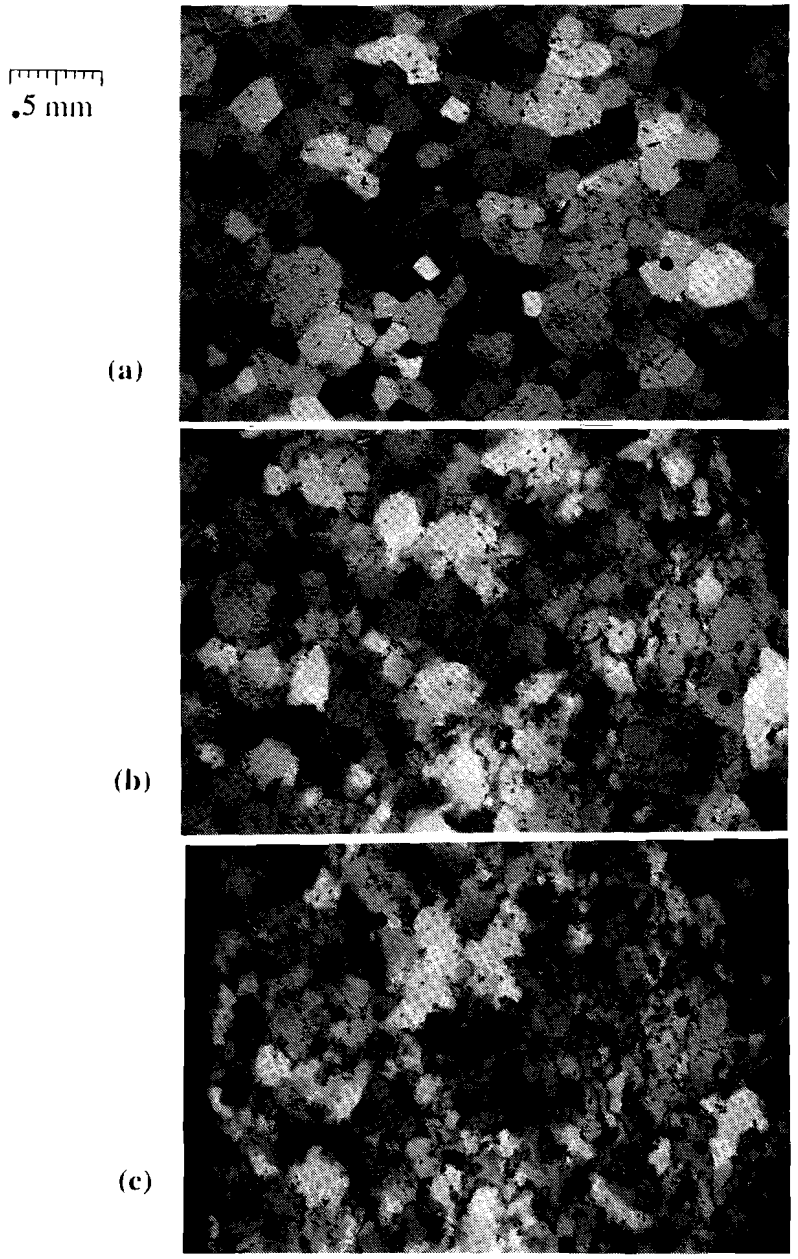

Fig. 4.1. *Micrographs of deforming norcamphor, taken at t=0 (a), 33 (b) and 66 min. (c). Shortening is in E-W direction. Scale bar is 0.5 mm. Small dots are SiC marker particles. Displacement of the marker particles can be used to determine deformation parameters. The five solid dots are marker particles that are also drawn on the plots in figures 4.6 and 4.7. Note dynamic recrystallization, especially at the right, where strain localization occurs.*

A more sophisticated approach is to use a least-squares approximation, which is less sensitive to these errors. It may also be desirable to know the material flow in the specimen rather than the finite deformation after a certain deformation increment. For this purpose velocities of marker particles have to be used instead of displacements.

In this paper we first discuss the basic principles of how to derive the position- or velocity gradient tensor and then present a number of ways to visualise the results. At the end we discuss one application of the method: investigation of grain boundary migration. Illustrations are derived from a typical experiment with polycrystalline norcamphor ($C_7H_{10}O$), deformed under pure shear conditions at 45°C (≈ 0.85 homologous temperature)(Fig. 4.1, 4, 6, 7).

We have developed a program that automates the major part of the marker-particle digitization and performs the deformation analysis (see § 4.4). It is specifically designed to analyse finite deformation and flow using randomly distributed marker particles. The latter is however not a requirement and it can be used to analyse inscribed grids as well.

4.3 The method

Basic principles

In any deforming body materials will be moving with respect to an external reference frame. We need to distinguish between deformation, which is the field describing the finite changes in position of material points, and flow, which is field describing the instantaneous velocities of these points. If the position of a material point after deformation ($\boldsymbol{x}'$) is assumed to be a function of its original position ($\boldsymbol{x}$) (e.g. McKenzie 1979, Spencer 1980, Passchier 1988a, Means 1990), then :

$$\boldsymbol{x}' = \mathbf{F}\boldsymbol{x} + \boldsymbol{d} \tag{4.1}$$

with $\mathbf{F}$ being the position gradient tensor and $\boldsymbol{d}$ the rigid body translation vector. The displacement vector $\Delta\boldsymbol{x}$ of a material point is a function of $\boldsymbol{x}$ as follows:

$$\Delta\boldsymbol{x} = \boldsymbol{x}' - \boldsymbol{x} = (\mathbf{F}-\mathbf{I})\boldsymbol{x} + \boldsymbol{d} \tag{4.2}$$

where $\mathbf{I}$ is the identity-tensor. Deformation is homogeneous if $\mathbf{F}$ does not vary as a function of $\boldsymbol{x}$. If $\boldsymbol{v}$ is the velocity of a material point with a position $\boldsymbol{x}$, the velocity gradient tensor ($\mathbf{L}$) and the rigid body velocity vector ($\boldsymbol{l}$) can be defined in a similar way (Spencer 1980, Passchier 1987):

$$\boldsymbol{v} = \mathbf{L}\boldsymbol{x} + \boldsymbol{l} \tag{4.3}$$

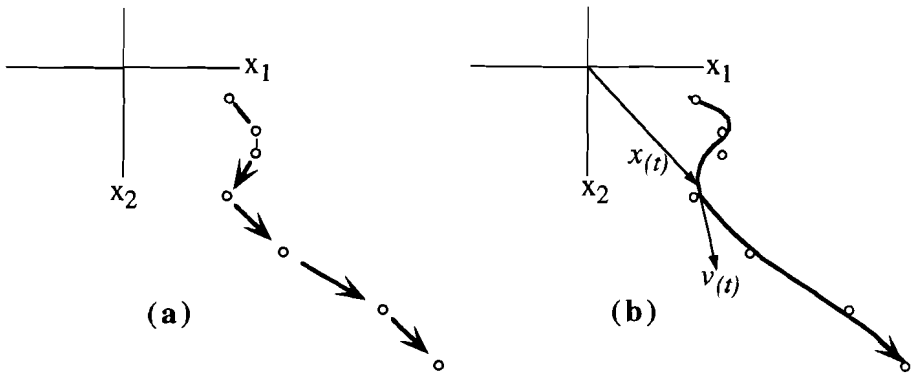

Fig. 4.2. The approximation of the path of a marker-particle from measured positions (dots) at discrete intervals. (a) Position of the particle at 7 times during the deformation. (b) Least-squares best fit with a fourth order polynomial in x_1 and x_2 direction separately, describing the position, $\boldsymbol{x}$, as a function of time, t. It is possible to assign a velocity vector v to the marker-particle at any time. This velocity vector lies at a tangent to the inferred movement path.

Again, if **L** does not vary as a function of $\boldsymbol{x}$, flow is homogeneous. In reality deformation or flow will rarely be homogeneous and the aim of the analysis is to find the distribution of **F**, $\boldsymbol{d}$, **L** and $\boldsymbol{l}$ in the deforming material by solving equations (4.1-3).

The marker particles represent a set of material points of which the positions $\boldsymbol{x}$ are known at specific moments during progressive deformation when their positions were recorded on micrographs or video (Fig. 4.2a). This is the basic set of data, which can be used to solve equations (4.1) or (4.2). The velocities of marker particles, needed to solve equation (4.3) are however not known, but can be approximated in the following way: Assuming that the actual paths of the marker particles were smooth, the positions of these marker particles at any time t can be interpolated, by describing the position of each marker as a function of time:

$$\boldsymbol{x} = \boldsymbol{x}(t) \tag{4.4}$$

We have chosen a polynomial function (Fig. 4.2b), treating position in each direction (i=1,2) separately:

$$x_i(t) = \sum_{n=0}^{N} (c_n)_i t^n \tag{4.5}$$

The order N of the polynomials can be adjusted to the complexity of the paths and the number of time-increments recorded. The N+1 coefficients $(c_n)_i$ in each polynomial can be calculated with a least-squares best fit method. The advantage of using polynomials is that a limited set of coefficients defines the whole path for each marker particle. These coefficients can be calculated once and stored in memory or on file for

later use. Another advantage of using a smoothed path to describe positions of marker particles is that errors in digitizing the positions of marker particles can be smoothed, if a suitable order of the polynomial is chosen. Now we have the position of each marker as a function of time, the velocity of each marker-particle at any time can be calculated by taking the derivative with respect to time at the desired time:

$$v_i(t)=\sum_{n=1}^{N} n(c_n)_i t^{n-1} \tag{4.6}$$

To solve equation (4.2) (describing deformation) one needs data on the position of marker particles at two times. These can be the times of digitization, or any chosen times if marker particle paths are calculated with equation (4.5). To solve equation (4.3) (describing flow), the positions of marker particles at a certain time and their velocities have to be known. These data have to be derived from equations (4.5) and (4.6).

Both in the case of deformation or flow, a set of vectors ($\Delta\boldsymbol{x}$ or $\boldsymbol{v}$) at a set of points ($\boldsymbol{x}$) are known. Using these data, equations (4.2) or (4.3) have to be solved for the whole area of interest. As these equations are essentially of the same form, the method is the same for both deformation and flow, and yields either **F**-**I** and $\boldsymbol{d}$, or **L** and $\boldsymbol{l}$. These are calculated for regularly distributed points in the field of interest, for instance the nodes of a rectangular grid.

To solve equations (4.2) and (4.3) for a node, deformation has to be treated as having been homogeneous in a small area around that node so that small scale inhomogeneities are neglected. These equations can then be solved exactly with three data-points (marker particles) that lie in the area near the node. Using more data-points over-determines the solution and a least-squares best fit method has to be used. The advantage of the latter is that the effect of digitizing errors is subdued. The program therefore uses at least 4 data-points, which have to be distributed around the node, to calculate **F** and $\boldsymbol{d}$ or **L** and $\boldsymbol{l}$, by solving equation (4.2) or (4.3). The maximum area for which deformation is treated as homogeneous, is defined interactively by the user. If one uses all data-points one gets the bulk **F** and $\boldsymbol{d}$, or **L** and $\boldsymbol{l}$ (Mancktelow 1991) (Fig. 4.3).

If the area is too small, not enough data-points will lie in the area and if the area is set too large, deformation cannot be treated as having been homogeneous and the method cannot be used. However, if these requirements are met, the program solves equation (4.2) or (4.3) and after all nodes have been dealt with, **F** and $\boldsymbol{d}$ or **L** and $\boldsymbol{l}$ are known for the nodes of the grid.

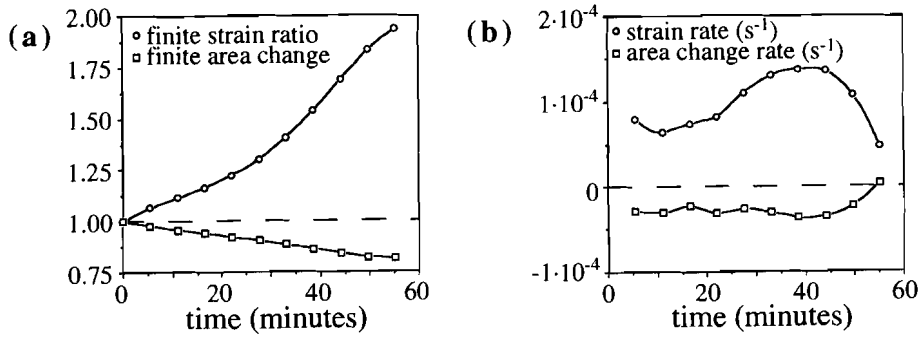

Fig. 4.3. Bulk flow and finite strain in the norcamphor experiment shown in Fig. 4.1, calculated by interpolating velocity and displacement vectors of all marker particles. The marker particles occupied a region of appr. 3.5x2.5 mm^2, which is about 10% of the whole area of the specimen. (a) Finite strain ratio and finite area change as a function of time. There is a significant loss in area (≈18%), probably caused by thickening of the specimen. (b) Strain rate and area change rate as a function of time. Note that the strain rate changes with time, because of strain localization either inside or outside the region occupied by marker particles.

Error reduction

The resulting tensor and vector have certain errors, caused by: 1) errors in the digitised positions of marker particles or measurement-errors, and 2) heterogeneity of deformation around the grid node. The treatment of deformation in the area occupied by four marker particles as having been homogeneous is only approximately valid if this area is small (and thus the density of marker particles high) relative to the deformation gradient. However when the marker particles density is high, the errors in determining the marker-positions become relatively more important. The density of marker particles should therefore be adjusted to the accuracy of measurement of their positions. In practice there will always be a certain error in the interpolated tensors and vectors. These errors will multiply when deformation-parameters are calculated from the tensors.

Data can be enhanced by using the fact that analogue experiments are carried out in thin samples between stiff glass plates and that the analogue materials are practically incompressible. This information is not used in the calculations described above. If the experiment is exactly plane-strain, the area change in the plane of measurement should always be zero. In most cases however the whole sample will flatten or thicken somewhat. Area change will vary gradually over the sample or even be constant. One can now iteratively adjust $\boldsymbol{d}$ or $\boldsymbol{v}$ of each grid node to fulfil the requirement of homogeneous area change for a small area around the grid node. Now

F or **L** can be recalculated using ***d*** or ***v*** of the surrounding grid nodes. An example of the effect of this improvement is given in Fig. 4.4. One should note that this enhancement may only be carried out if there is reason to believe that area changes vary only gradually. When for instance grain boundary diffusion or pressure solution are the deformation mechanisms, this is clearly not the case (Ree *pers. comm.*).

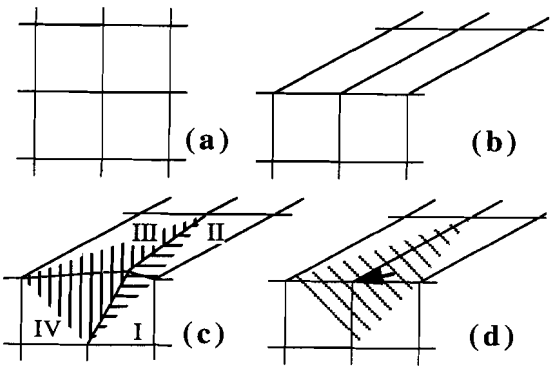

Fig. 4.4. The procedure to reposition grid nodes assuming incompressibility and using an initially square grid. (a) actual situation before strain increment. (b) actual situation after strain increment. (c) Interpolated grid with an obviously erroneous interpolation of the displacement of the middle grid node. four neighbouring triangles are dashed according to their apparent area change: triangles I and II are too small, triangles III and IV too large. (d) The interpolated grid after repositioning (arrow) the middle grid node, in such a way that all four triangles have the same size.

Vorticity and spin

A special problem in kinematic analysis is the distinction between vorticity (W) and spin (S) in progressive deformation (Fig. 4.5). Vorticity is defined as the summed angular velocity of orthogonal material lines with respect to the instantaneous stretching axes (ISA), while spin is the rotation of ISA in an external reference frame (Means *et al.* 1980, Lister & Williams 1983, Passchier 1986, 1987). From a position gradient tensor **F** representing a single deformation increment, it is possible to measure the rotation of two orthogonal material lines with respect to an external reference frame. A sum of mean vorticity and spin can be determined in this way if flow parameters do not change rapidly during the increment. To calculate mean spin, only the difference in orientation of ISA before and after the same deformation increment have to be measured. These can be derived from the velocity gradient tensors **L** at the beginning and at the end of the deformation increment. The method described in this paper allows for the calculation of both **F** and **L**, so in principle spin and vorticity can be distinguished.

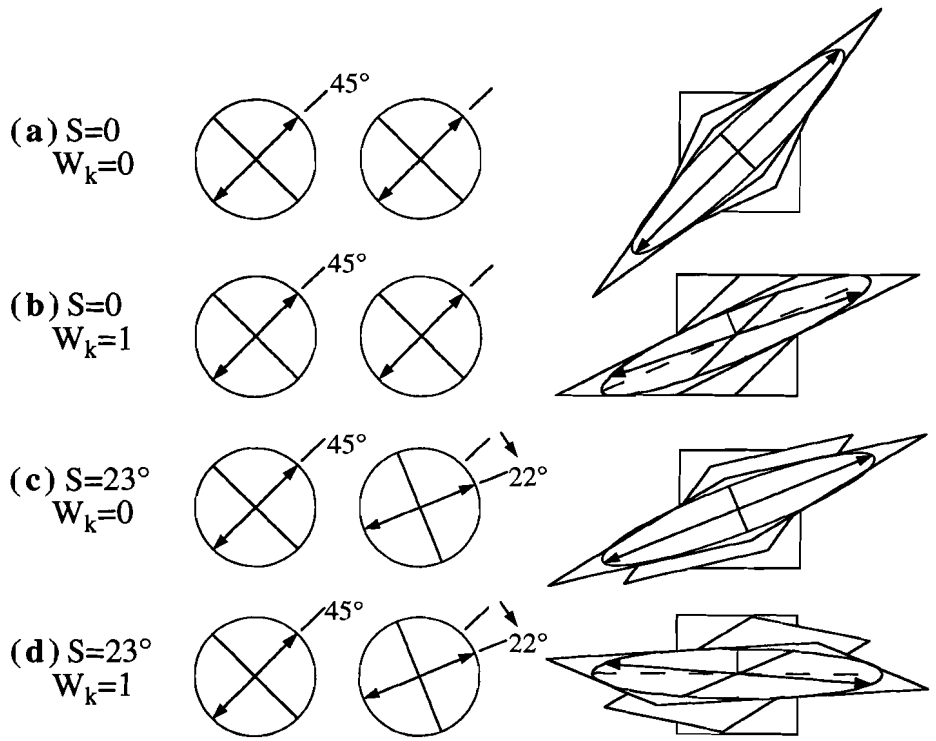

Fig. 4.5. The analysis of spin (S) and vorticity (given as kinematic vorticity number W_k) for four cases: (a) S=0 & W_k=0. (b) S=0 & W_k=1. (c) S=23° & W_k=0. (d) S=23° & W_k=1. Column (1) shows the orientation of the ISA before the strain increment (t=t1), column (2) the same at the end of the strain increment (t=t2). Column (3) shows the finite deformation and rotation of an original square. Finite strain ellipses are drawn in the deformed squares, with the principle stretching directions (PSD) as dashed lines and the material lines that coincided with the ISA of t=t1 as solid lines.

The procedure is as follows: For a deformation increment from t_1 to t_2 at a certain point x(a grid node) one can calculate

a) the local velocity gradient tensor, $\mathbf{L}_{(t1,x)}$ at that point from the velocity-vectors of the surrounding marker particles at t_1,
b) the local position gradient tensor $\mathbf{F}_{(t1\text{-}t2,x)}$ at that point for the whole deformation increment, using the displacement vectors of the surrounding marker particles, which gives the position x' of the material point x after the deformation increment,
c) and the local velocity gradient tensor, $\mathbf{L}_{(t2,x')}$ at point x' from the velocity-vectors of the surrounding marker particles at t_2.

The ISA orientations at t_1 and t_2 are now known, and the orientation of the deformed material lines which were originally the ISA at t_1, can be calculated and compared with the principal stretching directions (PSD), which are the long and short axes of the strain ellipsoid. Figure 4.5 shows the results for four cases with time-independent deformation. In case of zero vorticity the PSD and the material lines which coincided with the ISA at t_1 should be identical at t_2. When vorticity is non zero these two do not coincide.

Note that $\mathbf{L}_{(t1,x)}$ and $\mathbf{L}_{(t2,x')}$ can only be calculated if the positions of marker particles were recorded at at least three stages of the deformation, and preferably more. If the positions are only known at two stages, $\mathbf{L}_{(t1,x)}$ and $\mathbf{L}_{(t2,x')}$ will always be the same as both calculated velocity vectors and displacement vectors will lie parallel. An inherent problem of vorticity and spin analysis is that the deformation increment must be large to accurately determine $\mathbf{F}$, whereas it should be as small as possible to approximate time-independent flow parameters during the increment. This inevitably puts limitations on the accuracy of distinguishing between spin and vorticity.

Visualization

Once $\mathbf{F}$ and $\boldsymbol{d}$, or $\mathbf{L}$ and $\boldsymbol{l}$ are calculated for all grid nodes, several techniques for displaying the deformation field have been incorporated into the program and examples are given in Figures 4.6 and 4.7.

The first display mode is a "deformed grid", which is probably the best way to visualise finite deformation (Fig. 4.6a,b,c). This grid is constructed by adding the displacement $\boldsymbol{d}$ of each grid node to its original position and linking all nodes with straight lines. A number of kinematic parameters such as vorticity and stretching rate can be calculated from the tensors $\mathbf{F}$ and $\mathbf{L}$ (Passchier 1988a,b, Means 1990) which are best displayed in the form of contour-plots (Fig. 4.6d,e & 7a,b). Strain ellipses show the magnitude of finite strain and the direction of the principal stretching directions (Fig. 4.6f,g). Plots of velocity-vectors or displacement vectors demonstrate the flow pattern in the material (Fig. 4.7c). This can also be done by drawing the paths of all marker particles (Fig. 4.7e). It can also be useful to plot the orientations of ISA at a certain time (Fig. 4.7d). Plots of these orientations can be a tool to recognise inhomogeneities in vorticity and/or spin.

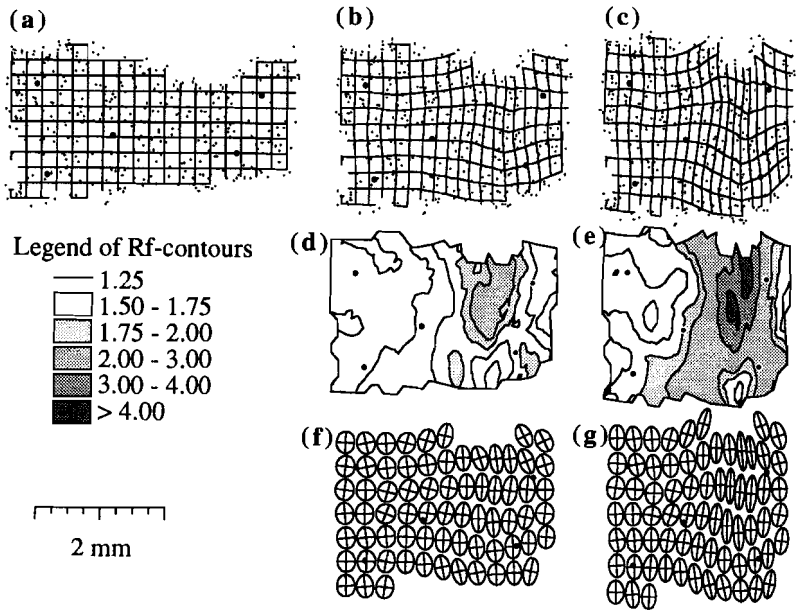

Fig. 4.6. Plots showing finite deformation parameters for the norcamphor experiment shown in Fig. 4.1. The five solid dots are the marker particles highlighted in Fig 4.1. (a,b,c) deformed grids at t=0, 33 and 55 min.. Small dots represent marker particles. (d,e) Finite strain ratio contours at t=33 and 55 min.. (f,g) Finite strain ellipses at t=33 and 55 min..

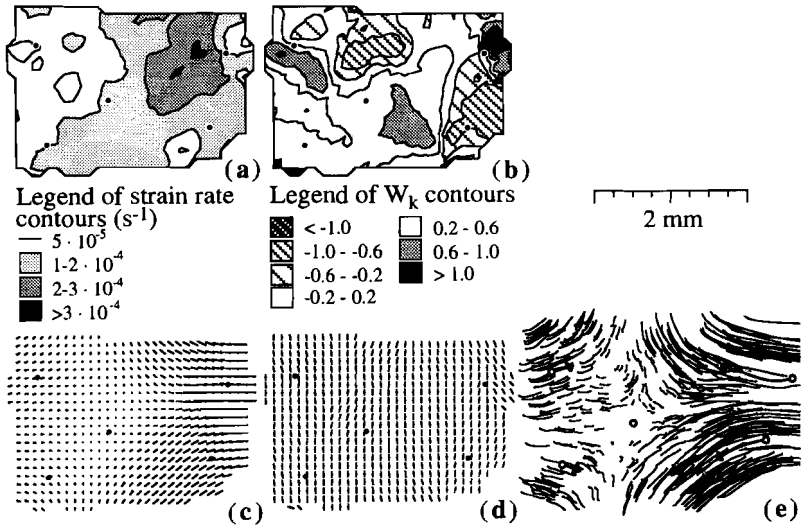

Fig. 4.7. Plots showing flow parameters for the norcamphor experiment shown in Fig. 4.1 at t=33 min.. The five solid dots are the marker particles highlighted in Fig 4.1. (a) contours of strain rate. (b) contours of kinematic vorticity number W_k, uncorrected for spin. (c) plot of velocity vectors. (d) plot of ISA orientation. (e) approximate paths of all markers from t=0 to t=55 min.. The paths are approximated with fourth order polynomials.

Grain boundary migration

Analogue experiments are well suited to study grain boundary migration (Jessell 1986, Means & Ree 1988, Urai 1987, Urai *et al.* 1986, Wilson 1986). During deformation grain boundaries will change their shape due to two different processes: a) because grain boundaries move passively *with* the deforming material (strain) and b) they migrate *through* the material (grain boundary migration). At first sight these two modes of shape change of grain boundaries are often indistinguishable. To determine actual amount of grain boundary migration the following method can be used (Fig. 4.8):

Grain boundaries before and after a deformation increment are digitised in the form of points (nodes) linked by straight lines (Fig. 4.8a,b). Just as **F** and ***d*** could be calculated for nodes on a grid, these can be calculated for the nodes on grain boundaries. "Deformed grain boundaries" can be constructed the same way as a "deformed grid". The "deformed grain boundaries" represent the grain-boundaries after the deformation increment if no grain boundary migration would have taken place. The difference between the actual position of grain boundaries after deformation and the calculated "deformed grain boundaries" represents the actual grain boundary migration (shaded areas in Fig. 4.8c).

4.4 Conclusions

Although analogue experiments seem to produce an "ideal" data set where "everything is known", it is still surprisingly difficult to calculate some deformation and flow parameters. This is due to the inherent problems in the determination of instantaneous movement of particles, in the recognition of a material point and in the errors in determining its position. The method described here allows us to analyse such a data set and to extract as much information as possible. The use of functions describing positions of marker particles as a function of time, makes it possible to determine the flow-field in the deforming material, instead of only the finite deformation.

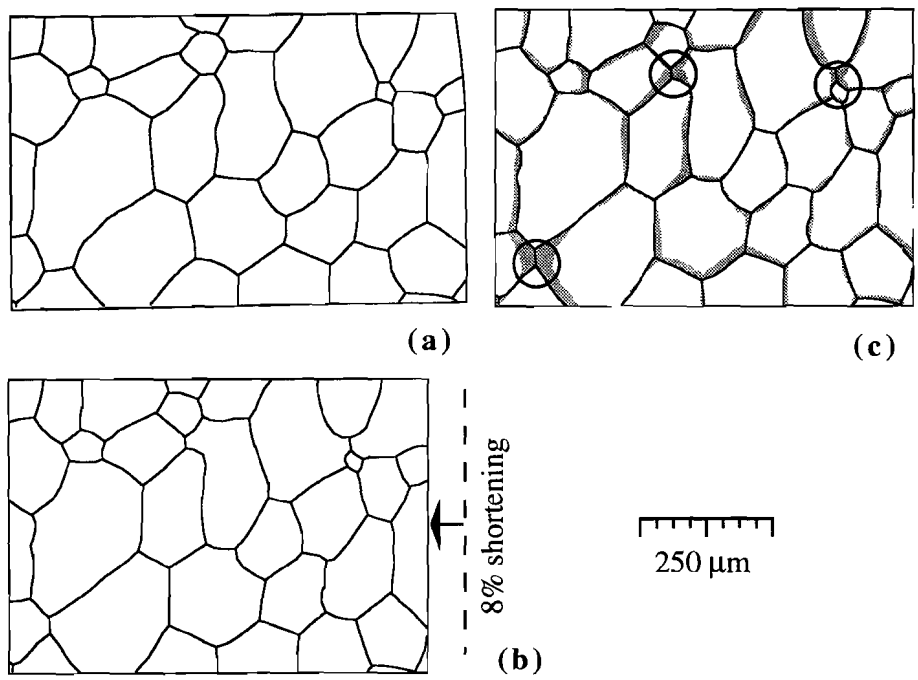

Fig. 4.8. Example of the analysis of grain boundary migration, taken from an experiment with octachloropropane (C_3Cl_8), deformed under pure shear at an applied strain rate of $2 \cdot 10^{-5}$ s^{-1} and a temperature of 75 °C. (a) Digitised grain boundaries at beginning of strain increment (t=0 min.). (b) Digitised grain boundaries at t=72 min. after strain increment of about 8% shortening in E-W direction. (c) Original grain boundaries (t=0 min.) are repositioned as passive markers, according to the deformation field calculated with marker particles, and superposed on the actual grain boundaries at t=72 min.. The areas through which grain boundaries have migrated are shaded. Note three neighbour-switching events (circles).

Acknowledgements - We wish to thank Boudewijn van Milligen and Majid Hassanisadeh for their suggestions and for reviewing the principles of the method. Furthermore we thank Coen ten Brink, Win Means, Jin Han Ree, Janos Urai and the reviewers Stefan Schmid, Renée Heilbronner and an anonymous reviewer and for criticism and suggestions. Paul Bons acknowledges the financial support by the Netherlands Organization for Scientific Research and the hospitality of the Department of Earth Sciences of Monash University, Melbourne, Australia.

Appendix Computer program

All routines described in this paper are combined into two compatible and fully menu driven programs, implemented for Apple Macintosh computers. The programs are written in C. Full colour screen and about 1 Mb of RAM are recommended. All output is in TEXT- or PICT-format which is compatible with most graphics-, spreadsheet- and word-processing applications available for Apple Macintosh computers. The program occupies 214 Kb and can be obtained free from the authors. Please include a 3.5" floppy disk. A manual is in preparation.

Chapter 5

Axisymmetric deformation experiments §

5.1 Abstract

Organic crystalline rock analogues have proven to be useful materials to study microstructural developments during deformation. We describe a series of constant load creep experiments with two phase mixtures of these analogues, where these are used as mechanical analogues of polymineralic rocks. The components are camphor and octachloropropane (OCP), which are both power-law creep materials. The strain rate difference is two to three orders of magnitude at the experimental stress values. Mixtures of OCP and camphor are also power-law creep materials within the experimental range of stresses (0.2-1.2 MPa). The soft phase OCP forms a matrix around the harder camphor inclusions and can accommodate most of the deformation. The OCP therefore dominates the flow behaviour of the mixtures, even at low volume fractions.

5.2 Introduction

Despite the amount of work done so far to determine the flow properties of monomineralic materials, our knowledge of the flow properties of polyphase rocks is still limited. Understanding the flow properties of polyphase materials is crucial for understanding of the flow properties and dynamics of the crust and mantle because most rocks in the earth's crust and mantle consist of more than one mineral.

A considerable amount of theoretical work has been published on the subject of the properties of polyphase materials. Starting with properties of isotropic composites of linear-elastic or Newtonian viscous components (see e.g. Wat *et al.* 1976), theory has been extended to cover non-linear properties of the constituent phases (e.g. Ponte Castañeda 1991; Willis 1991) and anisotropic composites (e.g. Benveniste *et al.* 1991; Lea & Mear 1991). These extensions are important since most rock forming minerals have a nonlinear rheology and rocks are mostly anisotropic. Relatively few

---

§ P.D. Bons & J.L. Urai, *Experimental deformation of 2-phase rock analogues*, Journal of Materials Science and Engineering, 1993, submitted

attempts have been made so far to apply these theories to the flow properties of polymineralic rocks in the Earth's crust and mantle, as for instance did Wenk *et al.* (1991). It is common practice to use the flow law of a dominant mineral to estimate the flow properties of polymineralic rocks: "wet quartz" for crustal rocks and "wet olivine" for mantle rocks.

Theoretical predictions of flow properties of rocks should be complemented and tested with experimental data. One can do so by experimentally determining the flow properties of natural polymineralic rocks, such as granite, aplite, websterite, diabase and quartz-feldspar rocks (see listing in Carter & Tsenn (1987) and Kirby & Kronenberg (1987)). Another approach is to experiment with artificial rock-like composites of two or more materials. Examples are the work on composites of halite and calcite (Jordan 1986, 1987, 1988), halite and anhydrite (Ross *et al.* 1987) and camphor and ice or napthalene (Burg & Wilson 1987). An advantage of the second approach is the possibility to systematically vary the parameters that determine the properties of a composite of two or more components, such as the volume fraction of each phase.

In this paper we present results of a series of such experiments, using two-phase composites of organic crystalline rock analogues. Our aim is to investigate the flow properties of such composites as a function of volume fraction of each of the components with known flow properties. First we briefly describe the microstructural behaviour of the components and the experimental apparatus. Then we present and discuss the experimental results.

5.3 Organic crystalline rock analogues

General

Some crystalline organic materials can be used as model systems for high T/Tm deformation of minerals because they deform by a combination of dislocation creep and diffusional creep, analoguous to naturally deforming rocks. The advantage is that they do so at room temperature and low stress. The softness of organic analogues permits creep tests at high strain rates in a simple apparatus together with transmitted light deformation experiments (Means 1980, 1989). Such experiments are more difficult or impossible to do with real rocks. Sample preparation is relatively easy. The materials can be cut with a razor blade and pressed in a hand press to obtain practically zero-porosity samples. A limiting factor is the small number of known crystal plastic organic rock analogues. Even a smaller number can be used to make 2-

phase aggregates as most of the known analogues form eutectic melts at room temperature. This has so far limited us to only use octachloropropane (OCP) and camphor so far. We also did experiments with mixtures of OCP and quartz-sand (SiO_2), which is rigid and inert at the given low stress and temperature.

Both OCP and camphor are power-law creep materials at room temperature as are rocks deforming by intracrystalline deformation mechanisms (e.g. Nicolas & Poirier 1976). The effective viscosity of camphor is about 2-3 orders of magnitude higher than OCP at room temperature and differential stresses ranging from 0.1 to 1.0 MPa.

OCP

OCP (C_3Cl_8) is hexagonal and melts at 434 K. Deformation usually leads to the formation of a crystallographic preferred orientation (Jessell 1986). From this it is inferred that at room temperature OCP deforms by dislocation creep with slip mainly on the basal plane. Deformation is accompanied by grain boundary migration and subgrain formation (Means & Ree 1988). Grain growth rates are relatively high and a coarse foam texture can be achieved from a fine grained starting material within hours or days, depending on temperature. At low strain rates and/or elevated temperature this foam texture can largely be preserved during deformation (Bons & Urai 1992; Ree 1991). At high strain rates and low temperature the grain size is reduced and mechanical twins or kinks are sometimes observed (Jessell 1986).

Camphor

Camphor ($C_{10}H_{16}O$) is rhombohedral below 365 K and cubic up to the melting temperature of 452 K. It mainly deforms by slip on the basal plane and by kinking or possibly twinning (Urai *et al.* 1980). Continuing lattice rotation within the kinkbands, subdivision of the kinkbands and accompanying dynamic recrystallisation can rapidly reduce the grain size during deformation. Camphor has a tendency to localise deformation in fine-grained shear zones with a strong crystallographic preferred orientation (Urai & Humphreys 1981). A foam texture is reestablished by static grain growth in hours or days after deformation.

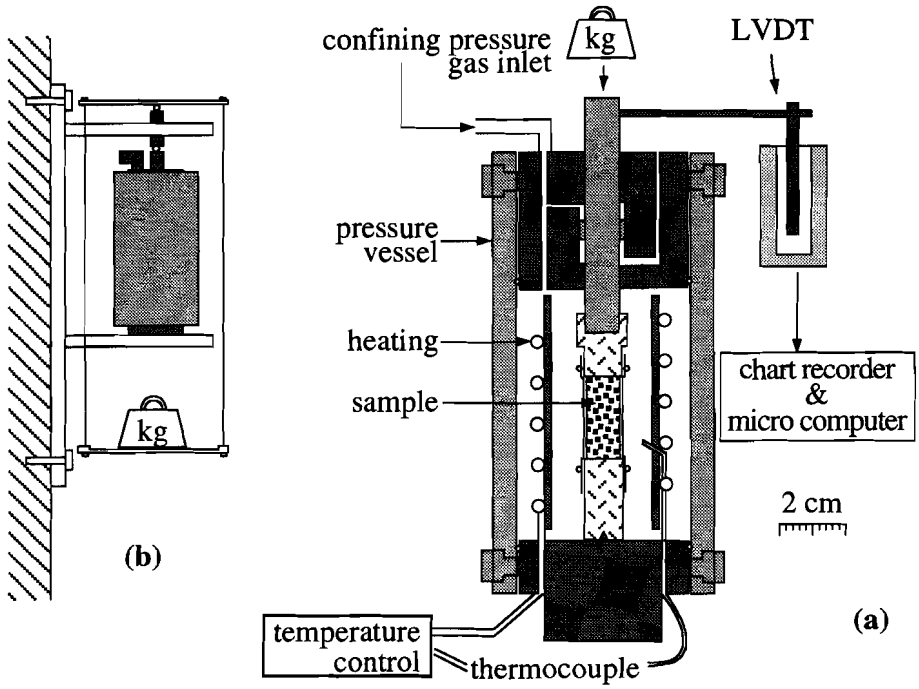

Fig. 5.1. (a) Schematic cross-section of the miniature gas apparatus. (b) The apparatus with its frame and the tray mounted to carry the dead weight to apply a constant load on the upper piston.

5.4 Experimental method

Creep tests were carried out in a miniature triaxial gas apparatus (Fig. 5.1.a). The apparatus consists of a vertical piston-sample assembly in a steel pressure vessel. A cylindrical sample (10 mm in diameter, 15-20 mm in length) is placed between the upper and lower piston and jacketed with rubber. A confining pressure is applied on the sample by pressurising the vessel with compressed air, typically 0.6 MPa. Seals are low friction - low clearance metal-to-metal ones that allow a small amount of air to leak during operation. The sample is loaded via a compensated piston assembly (see figure 18 in Tullis & Tullis 1986) with a dead weight (Fig. 5.1.b). All load applied on the upper piston by the dead weight, calibrated for the friction of the piston in its shaft, produces the vertical differential stress on the sample. We will refer to this as the "stress" or σ for the rest of this paper. The relative displacement of the upper piston is measured with an LVDT (Linear Variable Displacement Transducer) and logged on a personal computer. Strain (ε) is defined as the change in length relative to the undeformed sample length. Strain rate ($\dot{\varepsilon}$) is defined as the rate of change in length relative to the current sample length. A coiled heater element surrounds the

piston assembly within the vessel and temperature is measured with a thermocouple (K) near the sample. Temperature was 301 K for all experiments presented in this paper. Temperature was calibrated by inserting a second thermocouple through a hollow piston into a dummy sample of camphor. This showed that temperature variations over space and time were within ±1 K at a set temperature of 301 K.

The error in stress measurements is about ±0.01 MPa (≈1-5%) due to variation in friction along the upper piston. With increasing strain the error increases as the sample deforms into a barrel shape. Some experiments were done with a piston of 10 mm diameter, but most with 12 mm diameter. The slightly greater diameter of the piston than the sample avoids wrapping of the sample around the pistons. Stress is corrected by assuming a constant volume and a cylindrical shape of the sample during the experiment. The error of the LVDT is less than ±0.01 mm and the errors in measurement of the length of the sample before and after deformation about 0.1 mm. The error in strain and strain rate values is therefore less than about ±2%.

Samples were prepared by cutting pure OCP and camphor with a razor blade into 1-2 mm cubes. These cubes were mixed thoroughly and pressed together in a die with an arbor press at approximately 100 MPa for 10 seconds. The result is a translucent cylindrical specimen with virtually zero porosity. The shape of the original cubes is largely lost as the softer OCP flowed into all existing voids (Fig. 5.2.a). After deformation, slices were cut off the sample with a microtome or razor blade. The distribution of camphor and OCP could then be observed (Fig. 5.2.b) using reflected light microscopy or by making peels of etched surfaces. Ethanol was used for the etching and a 2-component dentist's putty§ to make the peels. Thin sections cannot be made as the material is too soft.

We carried out two series of two types of experiments (table 5.1): a) constant load tests, wherein the applied load was left constant during the entire experiment, and b) variable load or stepping tests, wherein the load was changed every few percent of strain (e.g. Schmid *et al.* 1980). Each step was continued until the strain rate settled to a constant value: the strain rate value for that step. To increase the initial grain size some of the samples were annealed at about 340 K for 2 hours, followed by cooling to 301 K in about one hour, prior to deformation. If samples were not to be annealed, they were placed in the apparatus immediately after manufacturing and the temperature controller was set at 301 K. The sample was then left for about half an hour for the temperature to settle after which the load was applied. Annealing caused

§ Coltène® President Putty Soft supplied by Coltène AG, feldwiesenstrasse 20, CH-9450 Altstaetten/Switzerland

the grain size to increase from an average of less than 10 μm to about 100 μm in both phases, as shown by experiments with a transparent deformation cell under the same conditions. All stepping tests were done with un-annealed samples.

test	% OCP	initial length (mm)	sample mass (g)	finite strain (%)	strain rate at 5% strain	strain rate at 10% strain	strain rate at 15% strain
Series 1, OCP + camphor, 0.6 MPa, annealed							
pdb 25	0	15.6	1.21	18	2.6×10^{-7}	3.6×10^{-7}	3.5×10^{-7}
pdb 24	25±1	15.1	1.45	34	2.9×10^{-6}	3.6×10^{-6}	3.7×10^{-6}
pdb 26	39	14.5	1.60	33	3.5×10^{-6}	4.3×10^{-6}	4.3×10^{-6}
pdb 21	49±3.5	15.1	1.64	42	1.1×10^{-5}	1.1×10^{-5}	1.1×10^{-5}
pdb 22	74±1	14.8	1.93	33	1.4×10^{-4}	6.1×10^{-5}	3.6×10^{-5}
pdb 23	100	14.9	2.21	32	1.3×10^{-3}	3.8×10^{-3}	1.9×10^{-4}
Series 2, OCP + camphor, 1.0 MPa, annealed							
pdb 28	0	15.3	1.19	35	2.1×10^{-6}	3.3×10^{-6}	3.5×10^{-6}
pdb 33	19±3	15.2	1.43	34	1.3×10^{-5}	1.5×10^{-5}	1.7×10^{-5}
pdb 31	39±1	14.7	1.59	33	7.5×10^{-5}	5.6×10^{-5}	5.3×10^{-5}
pdb 32	59±1	14.8	1.78	33	6.0×10^{-4}	3.3×10^{-4}	2.3×10^{-4}
pdb 57	59±0.5	15.2	1.85	32	8.8×10^{-4}	4.0×10^{-4}	2.3×10^{-4}
pdb 29	79±0.5	14.8	2.01	30		1.5×10^{-3}	7.5×10^{-4}
pdb 27	100	14.7	2.24	29		6.5×10^{-3}	2.8×10^{-3}
Series 3, OCP + camphor, 1.0 MPa, not annealed							
pdb 62	0	14.6	1.13	31	6.4×10^{-6}	6.2×10^{-6}	6.3×10^{-6}
pdb 58	20±1	15.2	1.42	29	3.1×10^{-5}	2.5×10^{-5}	2.3×10^{-5}
pdb 59	40±1	15.1	1.63	32	1.5×10^{-4}	1.1×10^{-4}	9.0×10^{-5}
pdb 54	59±3	15.1	1.79	30	1.2×10^{-3}	6.0×10^{-4}	5.1×10^{-4}
pdb 53	75±1	15.7	2.06	38		2.1×10^{-3}	1.1×10^{-3}
pdb 52	88±1.5	14.5	2.05	34		8.0×10^{-3}	2.7×10^{-3}
pdb 50	100	15.2	2.31	43			7.0×10^{-3}
Series 4, OCP + quartz, 0.35 MPa, not annealed							
pdb 75	100	15.0	2.23	16	6.0×10^{-5}	2.5×10^{-5}	1.0×10^{-5}
pdb 77	92.4	14.9	2.27	21	4.3×10^{-5}	2.0×10^{-5}	1.0×10^{-5}
pdb 78	87.1	15.6	2.41	19	3.0×10^{-5}	1.0×10^{-5}	7.0×10^{-5}

Table 5.1.a. *Experimental details of the constant load experiments .*

test	% OCP	initial length (mm)	mass (g)	Number of steps
pdb 10	0.00	19.90	1.54	11
pdb 11	0.00	13.90	1.08	7
pdb 2	20±2	15.05	1.39	8
pdb 1	39 ± 2	14.65	1.55	9
pdb 7	60±3	15.02	1.81	10
pdb 16	80±3	19.54	2.66	10
pdb 30	100.00	15.64	2.33	4
pdb 17	100.00	18.65	2.77	5

Table 5.1.b. *Experimental details of the stepping tests (b).*

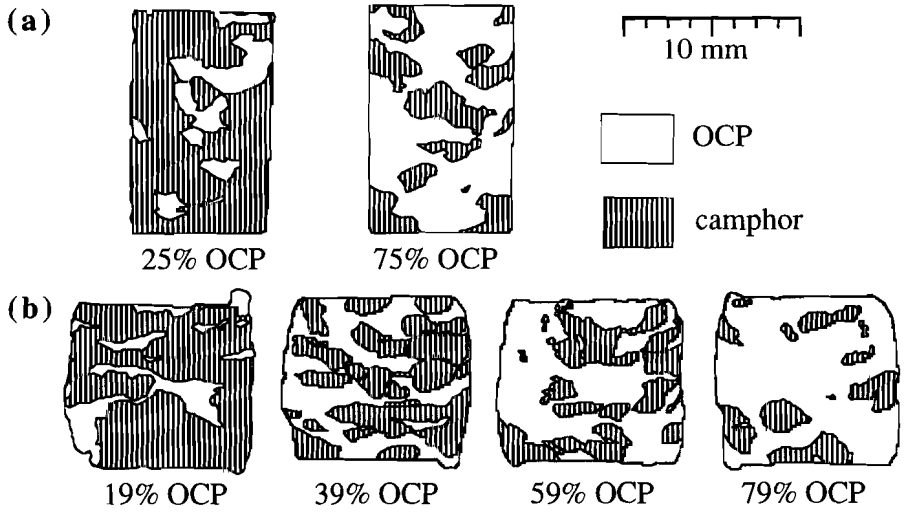

Fig. 5.2. *(a) Two examples of a section through an undeformed sample, showing the distribution of camphor and OCP. (b) Sections through deformed samples (samples pdb 33, 31, 32, 29)*

5.5 Experimental results

Pure components

First we present the data on the pure components. Two creep curves for OCP are shown in figure 5.3.a. One is for an annealed sample, the other for an un-annealed sample. These curves show that there is an effect of annealing on the strain rate. The results of two stepping tests with OCP are shown in figure 5.4.a. These data were used to determine a flow law for OCP. As all stepping test data correlate well in the log(σ)/log(ε̇) plot we chose a power-law of the form

$$\dot{\varepsilon} = A\sigma^n, \qquad (5.1)$$

The values of the pre-exponential factor, A, and the stress exponent, n, were determined with a linear regression through the log(σ)/log(ε̇) data, with log(ε̇) as the dependent variable (table 5.2). The actual temperature dependence was not determined as all experiments were performed at the same temperature.

Two creepcurves for camphor are shown in figure 5.3.b. Here we see a distinct difference in shape between the unannealed and the annealed sample. The un-annealed sample has a constant strain rate up to about 20% shortening, after which the strain rate decreases. The annealed sample initially shortens at a slower rate. The strain rate increases from about 5% shortening. The increase is strain rate in the annealed sample probably is the result of a reduction in grain size, accompanied by localisation of deformation as described by Urai & Humphreys (1981). Data of two stepping tests with camphor are shown in figure 5.4.b, together with a power-law best fit.

% OCP	log(A)	n	number of data points
0	-4.877 ± 0.003	3.3 ± 0.3	18
20 ± 2	-4.25 ± 0.04	4.3 ± 0.3	8
39 ± 2	-4.00 ± 0.09	4.5 ± 0.3	9
60 ± 3	-2.98 ± 0.06	5.1 ± 0.1	10
80 ± 3	-2.58 ± 0.07	4.7 ± 0.1	10
100	-2.21 ± 0.17	4.5 ± 0.3	9

Table 5.2. *Regression parameters through stepping test data for flow laws of the form* $log(\dot{\varepsilon})=log(A)+n \cdot lg(\sigma)$

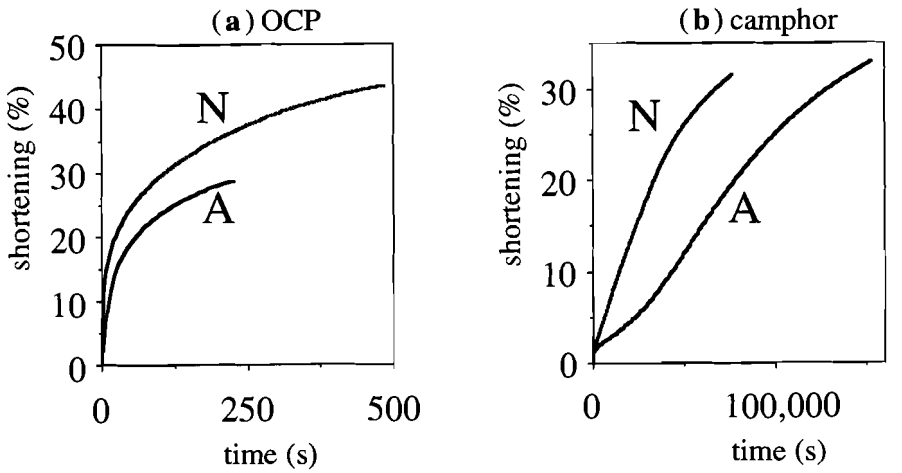

Fig. 5.3. (a) two creepcurves (shortening against time) of deformation experiments with pure OCP, one with an annealed sample (A, pdb 27) and one with an unannealed sample (N, pdb 50). (b) The same for camphor, one annealed sample (A, pdb 28) and the other unannealed (N, pdb 62). All experiments were done at an initial stress of 1.0 MPa.

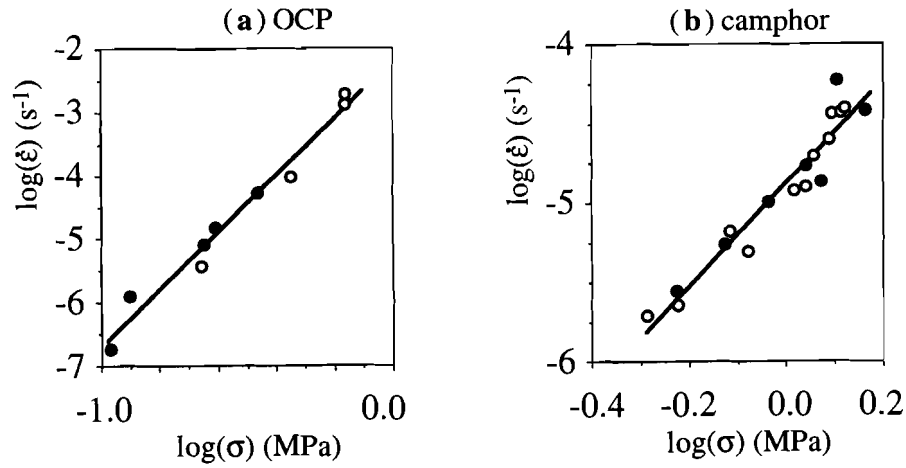

Fig. 5.4. Data from stepping tests as log(ε̇) against log(σ). Each graph shows data from two experiments. (a) OCP, pdb 17 (black circles) and pdb 30 (open circles). (b) camphor, pdb 10 (open circles) and pdb 11 (black circles).

Mixtures

Both constant load and stepping tests were carried out on mixtures of OCP and camphor. Figure 5.5 shows the results of the stepping tests with OCP-fractions of 0.2, 0.4, 0.6 and 0.8. It can be seen that the data of the mixtures also fall on roughly straight lines in a $\log(\sigma)/\log(\dot{\varepsilon})$ plot. Thus we also made regressions for power-law behaviour for the mixtures (table 5.2). A surprising result is that all stress exponents are about the same as for OCP, even at low fractions of OCP (Fig. 5.6). This causes the 20% OCP regression line to intersect the pure camphor line. There are few data in the low strain rate region, so we will not draw any conclusions from this cross-over.

Figure 5.7 shows the results of three series of single load tests with various fractions of OCP and camphor. The results are shown as strain rate - strain curves as these show the relative strain rates and the softening/hardening behaviour. Series 1 was done with an initial stress of 0.6 MPa, series 2 and 3 with an initial stress of 1.0 MPa. The samples of series 1 and 2 were annealed prior to deformation, whereas un-annealed samples were used for series 3 and 4. Two main observations can be made:

1) The shape of the curves changes gradually from pure OCP (decreasing strain rate) to pure camphor (constant or increasing strain rate up to 10% shortening).
2) The log of the strain rate of the mixtures is roughly proportional to the fraction of the components (Fig. 5.8).

The size of the OCP and camphor chunks in the samples is relatively large compared to the size of the samples. There will be some effect of the distribution and shape of the pieces of OCP and camphor on the overall strain rate. One experiment was repeated under exactly the same conditions (series 2, 60% OCP, pdb 58 and 59) and yielded results that were accurate within 10%.

OCP with rigid inclusions

The strain rate difference between camphor and OCP is about three orders of magnitude at the given conditions. One can therefore expect that camphor is virtually rigid when embedded in an OCP matrix. We therefore carried out some experiments in which the inclusions in the OCP were really rigid. We deformed samples of OCP with small fractions of well-rounded quartz sand (series 4). The grain size distribution was four equal fractions between 0.1 and 1.0 mm. Samples were not annealed and the initial stress was 0.35 MPa. Results are shown in figure 5.8. The addition of a small fraction of rigid quartz has the same effect as the addition of a small amount of camphor, so at low fractions of camphor, the camphor indeed

behaves as a rigid phase. One difference in behaviour that was observed was a tendency of OCP to develop cracks and flaws emanating from the quartz grains. Experiments where this was observed showed a wide scatter in strain rate values and were not included in table 5.1. This behaviour was never observed in mixtures of camphor and OCP. The stress concentrations needed to initiate brittle failure in OCP can probably not build up at camphor inclusions as camphor is not completely rigid.

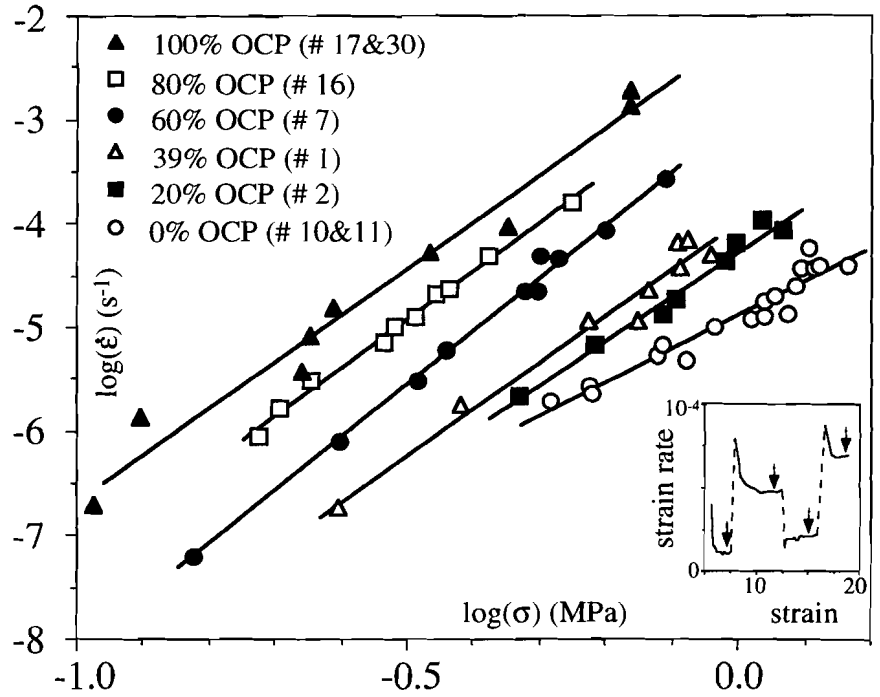

Fig. 5.5. All data from the stepping tests with mixtures of OCP and camphor, plotted as log(ε̇) against log(σ), together with best fits for power-law flow laws. The data represent the steady state shear strain rate achieved at the end of each "step" (inset). The strain rate values were averaged over the range where the strain rate remained constant.

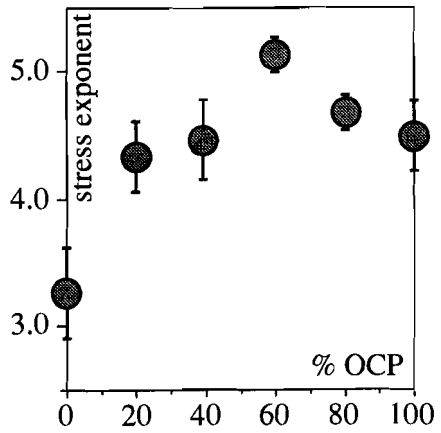

Fig. 5.6. Stress exponents (n) of mixtures of OCP and camphor as a function of composition.

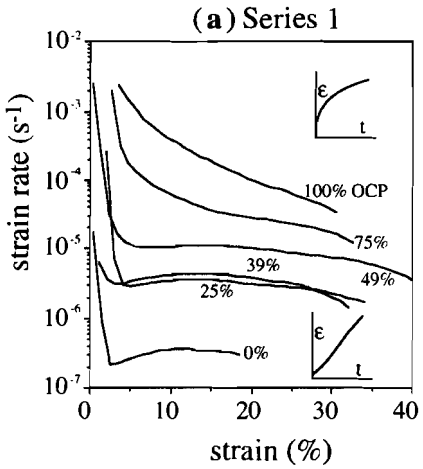

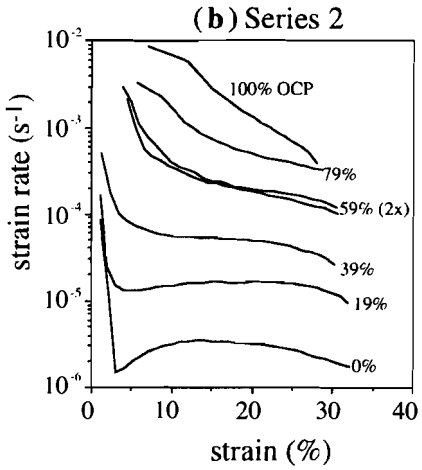

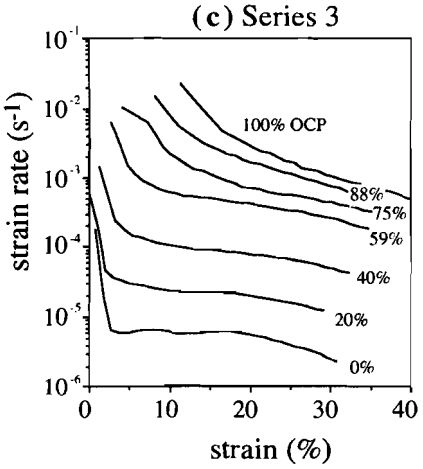

Fig. 5.7. Strain rate ($\dot{\varepsilon}$) as a function of strain (ε) for all single load experiments with mixtures. (a) Series 1, initial stress of 0.6 MPa, samples annealed. Small insets show the creep curves for pure OCP and pure camphor. (b) Series 2, initial stress of 1.0 MPa, samples annealed. (c) Series 3, initial stress of 1.0 MPa, samples not annealed. Strain rates higher than about 0.01 s^{-1} could not be measured. The strain rate data were derived from the strain - time data with a moving 3-point window scheme with $\dot{\varepsilon}_i=(\varepsilon_{i+1}-\varepsilon_{i-1})/(t_{i+1}-t_{i-1})$ and $t_i=(t_{i+1}-t_{i-1})/2$. Since data were recorded at small intervals, the strain rate time data were averaged over a range of $\Delta\varepsilon=2\%$.

5.6 Discussion

The data presented here are useful for testing theoretical models to estimate flow properties of polyphase materials. This has for instance been done by Tóth *et al.* (1993), who applied their Self Consistent model to these data and predicted the flow stress of the mixtures within 7% accuracy.

The stepping tests suggest that the camphor-OCP mixtures observe a power law stress/strain rate relation. However, this cannot be true towards lower stresses than the range of stress values used for the experiments. Tullis *et al.* (1991) suggested that the flow properties of a two-phase composite of power-law creep materials could be approximated with power-laws as well, with the stress exponent of the composite (n_c) given by:

$$n_c = 10^{\{F_1 \cdot \log(n_1) + F_2 \cdot \log(n_2)\}} \quad (5.2)$$

where F is the fraction of each component and the subscripts represent the two phases. When we apply this to our case we would get lower stress exponents than determined with the experiments. Equation (2) was derived from the assumption that a mixture of two power-law creep materials will also be a power-law creep material. For two power-law creep materials there will be one stress value at which the strain rates of the two materials are the same. Any mixture of these materials must have the same strain rate at this "equiviscous point". In the $\log(\sigma)/\log(\dot{\varepsilon})$ plot (Fig. 5.6) all regression lines of mixtures cross the pure-camphor line at different stresses. This indicates that the assumption of a power-law for mixtures is invalid over a range of stress/strain rate values extending towards the equiviscous point. Towards the equiviscous point, the stress exponents of the mixtures must decrease as the flow properties of the mixtures must remain within the bounds determined by the components. This implies that the $\log(\dot{\varepsilon})$-fraction curve (Fig. 5.8) will become concave upwards towards the equiviscous point.

The reason that the experimentally determined stress exponents for OCP and camphor mixtures are of the same order as the soft component OCP, may lie in the fact that the contrast in flow properties is high at the given conditions. The difference in strain rate is about two to three orders of magnitude at a stress of 1.0 MPa. At high contrasts in flow properties between the phases, the general equation for the properties of a composite (P_c) reduce to (Tharp 1983):

$$P_c = P_c(P_{matrix}, F_{inclusions}, G) \quad (5.3)$$

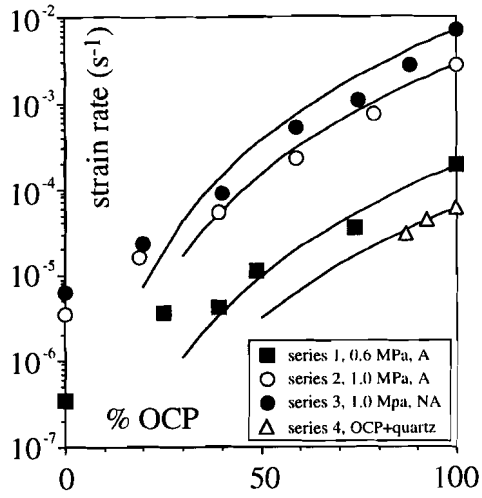

Fig. 5.8. Strain rate ($\dot{\varepsilon}$) as a function of composition for series 1, 2 and 3 at 15% shortening and at 5% shortening for series 4. The lines are the predictions of equation (5), assuming that the camphor and quartz are rigid compared to OCP. A = annealed, N = not annealed.

The properties of the composite (P_c, which may for instance be viscosity or elasticity) are a function of the properties of the matrix phase (P_{matrix}, e.g. suspending fluid in a suspension), the fraction of the inclusion phase ($F_{inclusions}$) and the internal geometry (G) of the composite. The properties of the inclusion phase play no role any more if the inclusion phase is effectively rigid or has no effective strength compared to the dominant/matrix phase (regime 1 and 2 in Handy 1989). If the hard phase is the matrix-phase, the mixture can be regarded as a porous aggregate of the hard phase with the pore-space filled with a material with no effective strength. If the soft phase is the matrix component, the mixture is analogous to a suspension of rigid particles in a fluid. Equations for the effective viscosity of a suspension (η_c) are of the same type as equation (5.3) (Einstein 1906; Barnes et al. 1989):

$$\eta_c = \eta_s \cdot f(F_{inclusions}, G) \tag{5.4}$$

η_s is the effective viscosity of the suspending fluid and f a function of the fraction of suspended particles and the internal geometry. This means that the flow law of the mixture (η_c) is a power-law if the matrix is a power-law material (at a given G) and both will have the same stress exponent. For a power law matrix with rigid equiaxed inclusions Yoon and Chen (1991) propose the following equation:

$$\dot{\varepsilon}_c = (1-F_{inclusions})^{2+n/2} \cdot A\sigma^n \tag{5.5}$$

Here $\dot{\varepsilon}_c$ is the strain rate of the composite. In figure 5.8 one can see that there is a reasonable good agreement between the strain rates predicted with equation (5.5) and our experimentally determined strain rates, for fractions of OCP larger than 0.25. We therefore conclude that camphor behaves as virtually rigid and the OCP as a matrix phase that dominates the flow properties of the mixtures, even at low OCP-fractions. Similar results were reported by Price (1982), who showed that the strength of aggregates of rocksalt (soft) - anhydrite (hard) mixtures only increased significantly at anhydrite fractions of more than 0.75.

At a certain relative volume fraction of the components there will be a transition from the dominance of one phase to the other on the flow properties of a mixture. The fraction at which this occurs depends on the internal geometry of the mixture. As the geometry of a mixture is strain dependent, so will the rheological behaviour of the mixture be strain dependent, especially near the transition fraction. As the soft phase deforms more than the hard phase, it will have a tendency to deform into flattened inclusions that can line up to effectively become the matrix phase (Dell'Angelo & Tullis 1982; Jordan 1987; Ross *et al.* 1987). The flow properties of mixtures with low to intermediate fractions of the soft phase will become increasingly dominated by the soft phase with increasing strain. This implies major strain softening at high contrasts in flow properties. That the soft phase OCP behaves as the matrix phase in our experiments, even at low fractions of OCP, is probably due to the method of sample preparation, that causes the OCP to fill up the space between the pieces of camphor. In that situation however, the composite properties should be nearer to the constant-stress (Reuss) bound than to the constant-strain rate (Voigt) boundary. This is not what is observed here: the mixtures are relatively hard. This may be due to the strain-sensitive behaviour of camphor. The flow properties of camphor were determined from experiments at up to 25% shortening. The camphor inclusions in the mixtures deform much less than this 25% and do not achieve steady state, because deformation is accommodated by the OCP. Camphor may then be effectiviely much harder in the mixtures than determined with the experiments with pure camphor. The properties will move towards the constant-stress bound if one corrects for this.

The experimental results described here can be applied to deforming polymineralic rocks, where the difference in effective viscosity between the different minerals is of the same order. An example is a quartz-feldspar rock such as a granite, which is composed of about 60% feldspars and 40% quartz. Most deformation in a quartz-feldspar rock is accommodated by the quartz (e.g. Handy 1989) during high temperature deformation. Allthough the feldspar usually forms a connected network in an undeformed granite, the quartz usually forms a matrix phase with feldspar inclusions after some deformation (Dell'Angelo & Tullis 1982). One would then expect the stress exponent of the quartz-feldspar rock to be the same as of the power law creep material quartz. The strain rate would then be about 15 to 40 times lower (using equation 5) than for pure quartz at a given stress, depending on the stress exponent of quartz, which may range from 1.9 to 4 depending on water content (Carter & Tsenn 1987; Kirby & Kronenberg 1987).

5.7 Conclusions

We have used soft crystalline ductile power-law creep materials, OCP and camphor, as mechanical analogues to rocks. With these materials we have obtained a data-set on the flow properties of 2-phase rock-like mixtures.

Under the given experimental conditions the mixtures obey a power-law relation between the strain rate and stress. The stress-exponent was about equal to that of the soft component OCP for all mixtures ranging from 20 to 90% OCP. It is argued that the flow properties of these mixtures is a function of only the flow properties of the soft phase and of the volume fraction and distribution of the hard phase. The hard phase camphor behaves as virtually rigid inclusions. This implies that a two-phase material can be modelled as a matrix with rigid inclusions, using models such as of Yoon and Chen (1991), if the contrast in effective viscosity of the components is more than two orders of magnitude. A quartz-feldspar rock is such a mixture.

The flow properties of both components determine the properties of a mixture at a lower competency contrast (towards the equiviscous point). The flow properties of a mixture of two power-law creep materials with different stress exponents can therefore not be described with a single power-law for a stress/strain rate range extending near the equiviscous point.

The flow properties of a mixture depend on the internal geometry of the hard phase, and therefore on strain at low to intermediate volume fractions of the soft phase.

Acknowledgements - The authors thank the two reviewers for their comments and useful suggestions. PDB acknowledges the financial support by the Netherlands Organisation of Scientific Research (NWO).

Chapter 6

Ring shear experiments

High shear strain deformation experiments in simple shear were performed with the bulk- and the transparent ring shear deformation apparatus.

Ten experiments were performed in the bulk ring shear apparatus with pure OCP or camphor and mixtures thereof (table 6.1). These experiments were performed to investigate the development of microgeometry and the changes in shear strain rate in mixtures deformed to high shear strain. First the experiments with pure OCP and pure camphor are discussed (ch 6.1) and then the experiments with mixtures, either OCP as the matrix phase (6.2), or camphor as the matrix phase (6.3).

The experiments were part of the development of the newly built apparatus and some problems were met. Suggestions for improvements are given in section 6.d. Several experiments with the transparent ring shear apparatus were performed. This work is still in progress and only one experiment is described in this chapter (Fig.6.15).

6.1 Experiments with pure OCP and camphor

6.1.1 RS1-3 & RS6 pure OCP

Four experiments were performed with pure OCP to:
- test the new apparatus,
- investigate the rheology of OCP at high shear strain ,
- study possible shear localisation / heterogeneities in OCP.

The experiments were performed at a constant applied shear stress of 0.23 MPa (RS1-3) or 0.28 MPa (RS6) and at a temperature of 29°C. The bulk shear strain - time and bulk shear strain rate - bulk shear strain graphs are shown in figure 6.1. The shear strain rate versus shear strain graphs for experiments RS1-3 and RS6 are shown together in figure 6.2. In the this chapter shear stress (τ), shear strain (γ) and shear strain rate ($\dot{\gamma}$) denote the overall or bulk values, since that is what is measured in this type of experiments (see also Appendix B).

In experiments RS1-3 one can observe an increase in bulk shear strain rate from about $1 \cdot 10^{-4}$ to $3\text{-}3.5 \cdot 10^{-4}$ s^{-1} at a bulk shear strain of 3-5. Experiment RS1 was

continued to a bulk shear strain of over 40. The shear strain rate fluctuated between 2.5 and $3.5 \cdot 10^{-4}$ s^{-1}. In experiment RS1 and RS2 the shear strain rate first decreases to a shear strain rate of $1 \cdot 10^{-4}$ s^{-1} at a bulk shear strain of about 0.5. These low strain data are however not very reliable, since these can be influenced by the tightening of the wire used to apply the load. This may cause a shift of the measured shear strain values. The data are not corrected for the possible tightening of the wire and no conclusions are therefore drawn from this initial shear strain rate decrease. The shape of the shear strain rate - shear strain curved for experiments RS1-3 is the same up to a shear strain of 3, but experiment RS2 is shifted $\gamma \approx 0.25$ towards higher shear strain values. Experiment RS6 also showed an initial increase in shear strain rate up to a shear strain of 5, followed by a minor decrease after which the shear strain rate varied between 4 - $5 \cdot 10^{-4}$ s^{-1}.

Coarse thin sections, about 1 mm thick, were cut with a razor blade from the sample of experiment RS1, directly after deformation. These sections showed that :

1) an oblique grain shape preferred orientation had developed at approximately 10-15° to the flow plane. The axial ratio of the grains was in the order of 5-10. Equidimensional grains with smooth grain boundaries were also observed.
2) a crystallographic preferred orientation had developed, with extinction (basal plane) parallel to the flow plane.

A likely explanation for the increase in shear strain rate observed in all four experiments is the establishment of this microstructure. The equidimensional grains observed in the deformed sample could be the result of post-dynamic grain growth. Experiment RS2 was stopped at a shear strain of 3.5 and then left for one night. After this period the shear strain rate commenced at a lower rate then before. This lower shear strain rate could be caused by recovery / grain growth that partly destroyed the existing fabric.

The relation between differential stress and shortening rate for OCP was experimentally determined, as described in chapter 5. This relation can be converted for simple shear (Appendix A), giving: $\dot{\gamma} = 8.4 \cdot 10^{-2} \cdot \tau^{4.49}$ (table 6.2). The predicted shear strain rates are $1.0 \cdot 10^{-4}$ s^{-1} for experiments RS1-3 at a shear stress of 0.23 MPa and $2.8 \cdot 10^{-4}$ s^{-1} at 0.28 MPa for experiment RS6. These values are in good agreement with the observed initial shear strain rates (at $\gamma < 1$). At low shear strain there seems to be no difference in flow properties in pure shear and simple shear as has been observed by, for example, Franssen & Spiers (1990). However, at higher shear strain such a difference may develop. This cannot be tested, since no data are available at equivalent strains in pure shear.

The distribution of shear strain (rate) was investigated in experiment RS3 and RS6. This was done by cutting the compacted specimen in two, applying some fine black powder on the cuts and putting the halves together again. In this way vertical black planes were made normal to the flow direction. After deformation, these black planes have deformed into an S-shape (figure 6.3). At a bulk finite shear strain of 8.7 (RS3) the finite shear strain in the middle of the sample is about 2.8 and most shear has taken place near the two grips. At a bulk finite shear strain of 29 (RS6) the finite shear strain in the middle of the sample is found to be only about 16. How and when the differentiation develops and whether it stabilises remains unknown, since the sample cannot be observed continuously during deformation.

experi-ment	composition (OCP:camphor)	shear stress (MPa)	Finite shear strain	duration (s)	Interruptions
RS1	100 : 0	0.23	0-44.3	$1.7 \cdot 10^5$	-
RS2	100 : 0	0.23	0-5.9	$9 \cdot 10^4$	no load for one night (γ=3.2)
RS3	100 : 0	0.23	8.7	$3 \cdot 10^4$	-
RS4	100 : 0				not included, because insuffi-cient data measured
RS5	68 : 32	0.23	<32	$1.3 \cdot 10^6$	γ=1.02, 2.75, 10.3, 16.2 & 30.9
		0.28	32 - 122	$1.3 - 2.6 \cdot 10^6$	γ=46, 74, 78, 111, 116 & 122
RS6	100:0	0.23	30	$7 \cdot 10^4$	-
RS7	67 : 33	0.28	76	$8 \cdot 10^5$	γ=8.0, 23.6, 59.6 & 68.4
RS8	62 : 38	0.28	195	$4 \cdot 10^6$	-
RS9	0 : 100	0.28	<0.05	$1.1 \cdot 10^6$	-
		0.39	0.05-0.28	$1.1 - 2.1 \cdot 10^6$	-
		0.79	0.28-17.27	$2.1 - 2.33 \cdot 10^6$	-
		0.23	17.27-17.33	$2.33 - 2.48 \cdot 10^6$	-
RS10	24 : 76	0.28	1.5	$3.4 \cdot 10^6$	-

Table 6.1. *Conditions of experiments discussed in this chapter.*

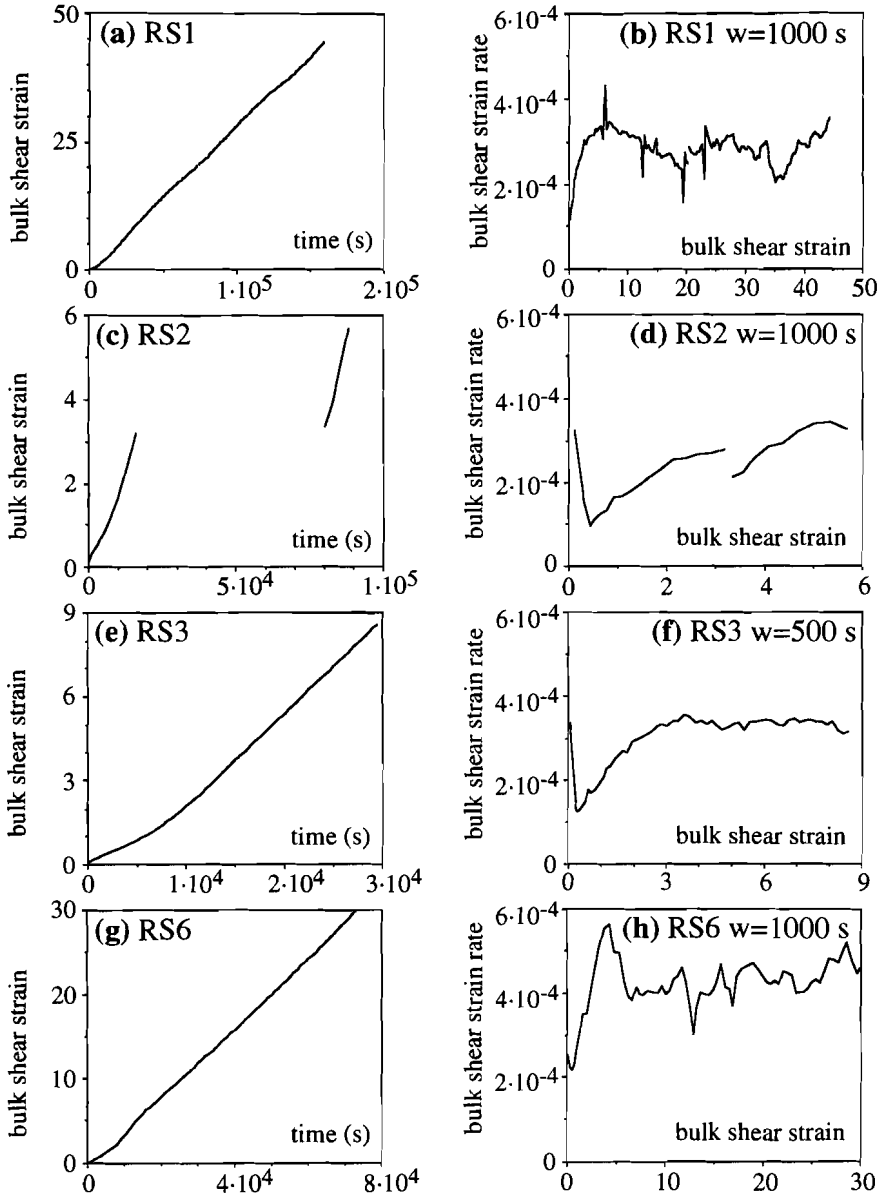

Fig. 6.1. Bulk shear strain versus time graphs and bulk shear strain rate versus bulk shear strain graphs for experiments RS1 (a,b), RS2 (c,d), RS3 (e,f) and RS6 (g,h). Time in s and shear strain rate in s^{-1}. The width (w) of the window for interpolation of the determination of the shear strain rate is 1000 s for RS1, RS2 and RS6 and 500 s for RS3.

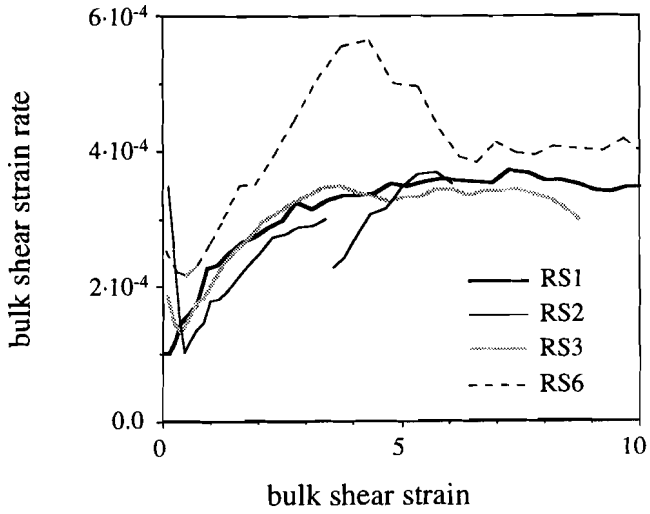

Fig. 6.2. Combined bulk shear strain rate versus bulk shear strain graphs of RS1-3 and RS6.

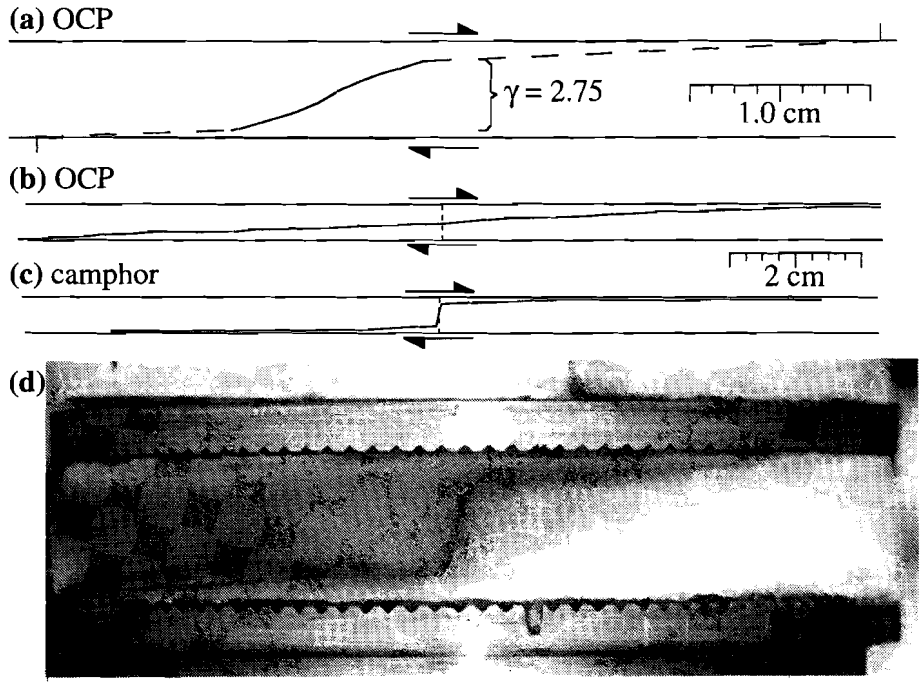

Fig. 6.3. Drawings of the shape of a deformed originally vertical plane. (a) RS3, OCP at a shear strain of 8.5, (b) RS6, OCP at a shear strain of 29 and (c) RS9, camphor at a shear strain of 17.3. (d) photograph of RS9, after deformation. Only weak shear strain localisation occurs in OCP, whereas very strong localisation occurs in camphor.

6.1.2 RS 9 pure camphor

One experiment was performed with a sample of pure camphor. The sample was deformed to a shear strain of 17.3, using four different applied shear stresses (figure 6.4). Almost all deformation took place during the third stage at a shear stress of 0.79 MPa. The shear distribution at the end of deformation is shown in fig 6.3.c. One can see that there is very strong strain partitioning. The middle 65% of the sample is hardly deformed. Two zones of about equal width at the grips have accommodated all deformation. The finite shear strain in these zones is almost 50. These zones are clear (very fine grained), whereas the undeformed zone has a granular appearance. This shear localisation is in accordance with the known behaviour of camphor (Urai & Humphreys 1981). The boundary constraints are such that the shear localisation is not inhibited at all. This makes it difficult to interpret the shear strain rate data, since the measured shear strain rate is the average over the whole shear zone. For homogeneous deformation one can predict a shear strain rate for a given stress with the flow law determined in chapter 5, converted for simple shear ($\dot{\gamma} = 9.1 \cdot 10^{-5} \cdot \tau^{3.26}$, table 6.2). The predicted shear strain rates are given in table 6.3, together with the observed bulk shear strain rate and the shear strain rate in the localised shear zones, assuming that these had a constant width of 0.35 of the total width.

The shear strain rate in the first two stages was much lower than predicted with the axisymmetric experiments. However during the third stage the shear strain rate rapidly increases to a value that is higher than predicted. Within the localised shear zones the shear strain rate is about 7 times higher that predicted. Grain size reduction and the development of a LPO probably caused a significant change in flow properties and maybe in deformation mechanism. In the last stage, where the stress is of the same order as in the first two stages, one can observe a decrease in shear strain rate and the shear strain rate towards a value that is of the same order as predicted from the pure-shear flow law.

% OCP	A	n
0	$9.1 \cdot 10^{-5}$	3.26
20	$3.9 \cdot 10^{-4}$	4.33
39	$7.4 \cdot 10^{-4}$	4.47
60	$9.9 \cdot 10^{-3}$	5.14
80	$4.0 \cdot 10^{-2}$	4.67
100	$8.4 \cdot 10^{-2}$	4.49

Table 6.2. *Parameters for the power law relation between the shear strain rate ($\dot{\gamma}$) and the shear stress (τ) of the form $(\dot{\gamma}) = A \cdot \tau^n$. The values of A and n are derived from the experiments in pure shear presented in chapter 5.*

	shear stress (MPa)	bulk shear strain range	predicted shear strain rate (s^{-1})	bulk shear strain rate (s^{-1})	shear strain rate in localised zones (s^{-1})
a	0.28	0.045	$1.4 \cdot 10^{-6}$	$4 \cdot 10^{-8}$	$1.1 \cdot 10^{-7}$
b	0.39	0.2	$4.3 \cdot 10^{-6}$	$3 \cdot 10^{-7}$	$7.4 \cdot 10^{-7}$
c	0.79	16.7	$4.2 \cdot 10^{-5}$	$1 \cdot 10^{-4}$	$2.8 \cdot 10^{-4}$
d	0.23	0.06	$7.2 \cdot 10^{-7}$	$3 \cdot 10^{-7}$	$8.6 \cdot 10^{-7}$

Table 6.3. *Predicted shear strain rate, measured bulk shear strain rate and shear strain rate in the localised shear zones at the upper and lower grip for experiment RS9.*

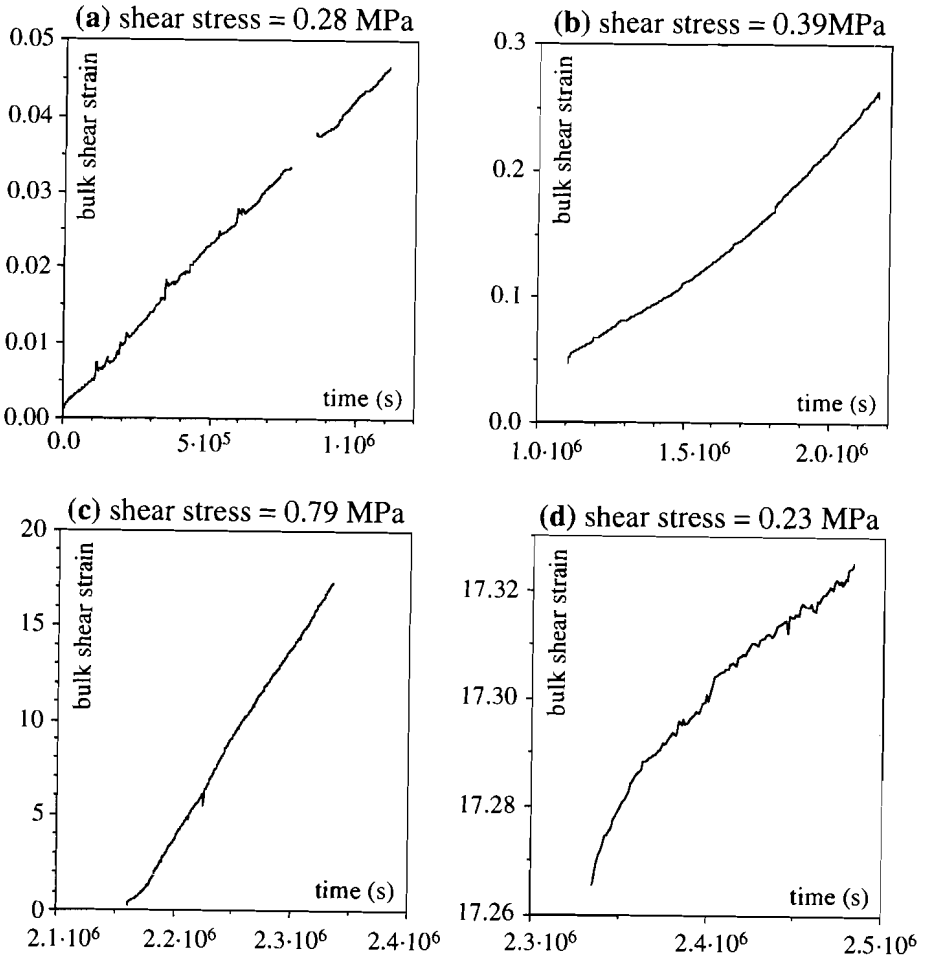

Fig. 6.4. *Bulk shear strain versus time for the four steps (see table 6.2) of experiment RS9 with pure camphor.*

6.1.3 Discussion

The experiments with OCP have shown that experiments are reproduceable and that observed bulk shear strain rates are in accordance with those predicted with the flow laws derived from the pure-shear experiments at low finite strain. This suggests that friction in the apparatus and at the confining cylinders probably only plays a minor role and does not vary much over time.

Localisation of shear strain is observed both in camphor and in OCP. In OCP this is relatively minor, with the finite shear strain in the middle of the sample about half the bulk finite shear strain and increasing smoothly towards the grips. Localisation is however very important in camphor, where hardly any deformation takes place in the middle of the specimen and all shear takes place in two sharply bounded zones at the grips. The localisation behaviour is therefore material dependent and one has to take this material behaviour into account when interpreting the bulk shear strain (rate) data from these experiments.

6.2 Experiments with mixtures of OCP and camphor

6.2.1 RS5

Experiment RS5 was performed with a mixture of 68% OCP and 32% camphor. The camphor was pressed and then chopped to small pieces (about 1-4 mm), that were mixed with fine-grained OCP and compressed to a solid sample at about 63° in 24 hours. The OCP was mixed with very fine black powder to be able to distinguish the camphor and OCP in the mixture. The specimen was then deformed at a shear stress of 0.22 MPa at 29°C. The shear stress was raised to 0.28 MPa at a bulk shear strain of 32. The γ/t and $\dot{\gamma}/\gamma$ graphs are given in figure 6.5. Deformation was stopped at a bulk shear strain of 122. Photographs of the outer surface of the specimen were taken at intervals (fig 6.6). These photographs were used to make the line drawings (Fig. 6.7, see Chapter 3.1.3 for method). The experiment had to be stopped and the outer confining mantle had to be removed in order to make these photographs. The outer surface was slightly etched with methylated spirit to enhance the colour difference between OCP and camphor. This disturbance caused a temporary increase in shear strain rate in most cases.

The harder camphor inclusions deform into flattened lenses at the beginning of deformation. Shear localisation occurs near the grips. Corners of the camphor inclusions tend to deform more than the inclusions themselves, which leads to the formation of short "tails", especially near the grips. The camphor inclusions that initially touched the grips have a tendency to move away from the grips, causing a weak differential layering to develop. With progressive deformation the inclusions develop into strongly flattened lenses or layers lying parallel or oblique to the flow plane. No observations were made between a shear strain of 46 and 111. By then, all inclusions have stretched into layers parallel or at a small angle to the flow plane. Some of these camphor layers are folded. The experiment was then interrupted again at a shear strain of 116 and stopped at a shear strain of 122. The development of the fold trains is illustrated at three stages (Fig. 6.16).

6 series of photographs were made after deformation of sample (figure 6.8). The outer 0.5-1.0 mm thick layer of the specimen was scraped off for each series. Figure 6.9 shows drawings based on these photographs. These photographs and drawings show more detail then the photographs made during the experiment, because the specimen could now be etched more strongly and then left for about one day to enhance the difference in appearance of OCP and camphor.

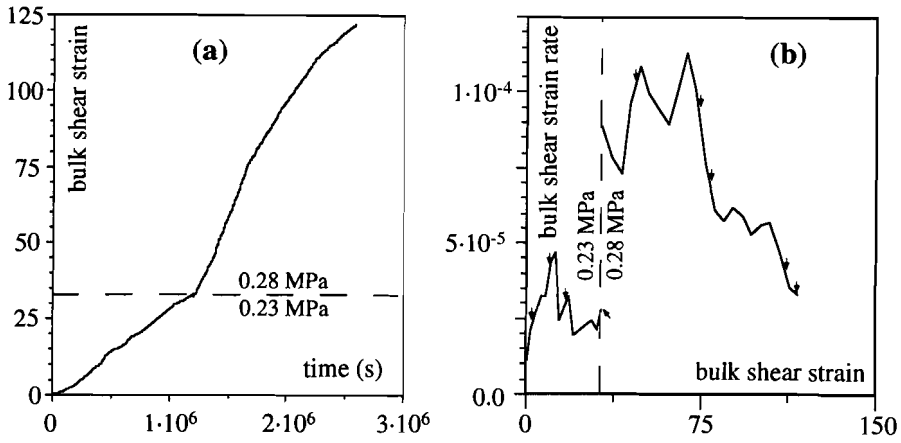

Fig. 6.5. Bulk shear strain versus time (a) and bulk shear strain rate against shear strain (b) for experiment RS5. The shear stress was increased from 0.23 to 0.28 MPa at a bulk shear strain of 32. Arrows indicate interruptions for photography.

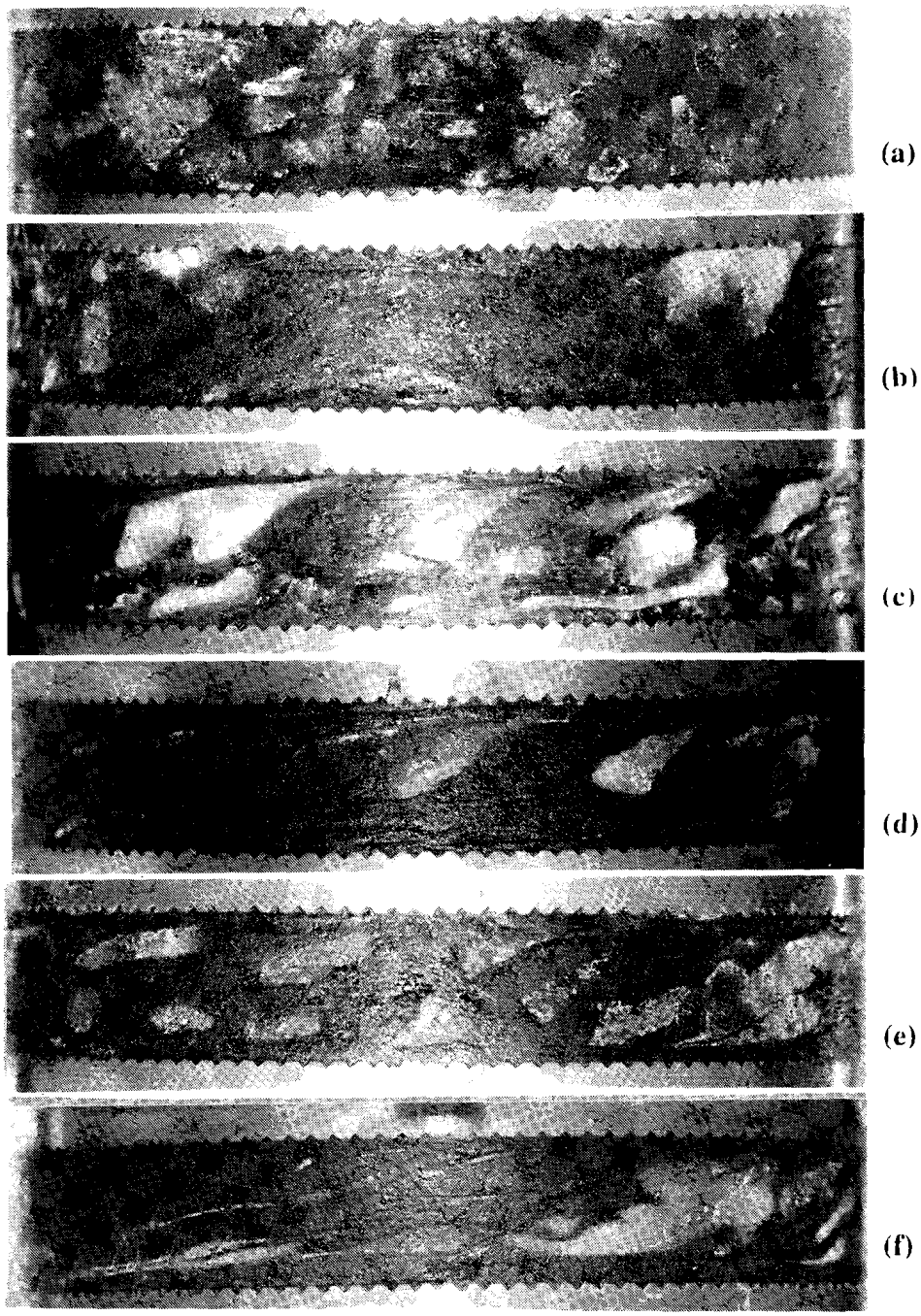

Fig. 6.6. *Photographs of the outer surface of specimen RS5 taken at intervals during deformation. (a) starting material, (b) at γ=2.8, (c) at γ=10.3, (d) at γ=16.2, (e) at γ=31, (f) at γ=46, (g) at γ=111, (h) at γ=116 and (i) at γ=122. OCP is dark, camphor lighter. Difference in appearance between the photographs is due to varying success with etching.*

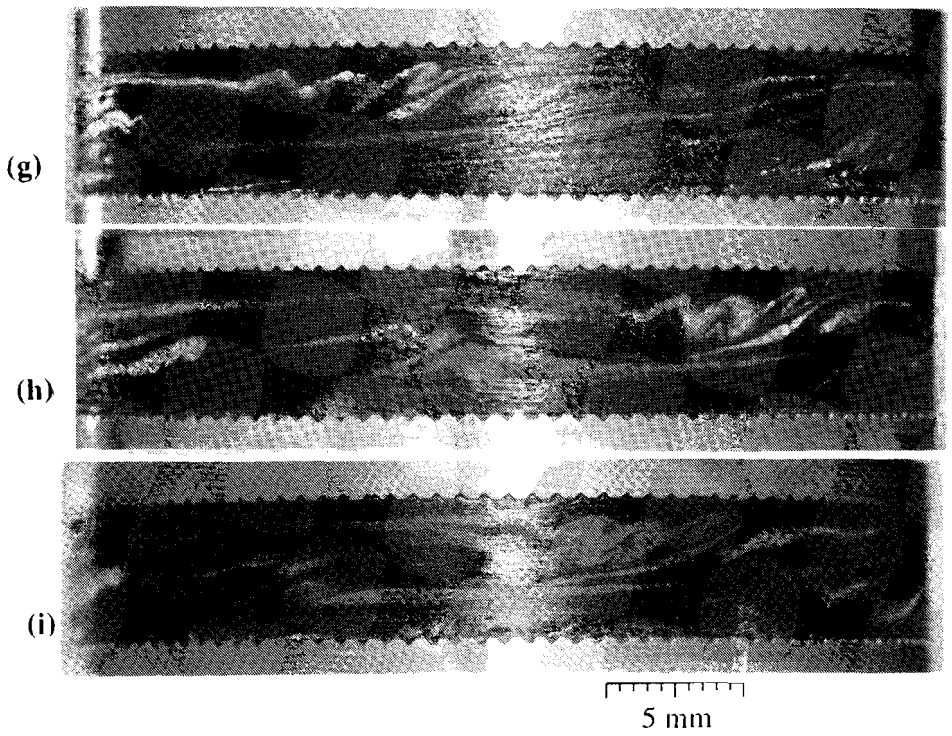

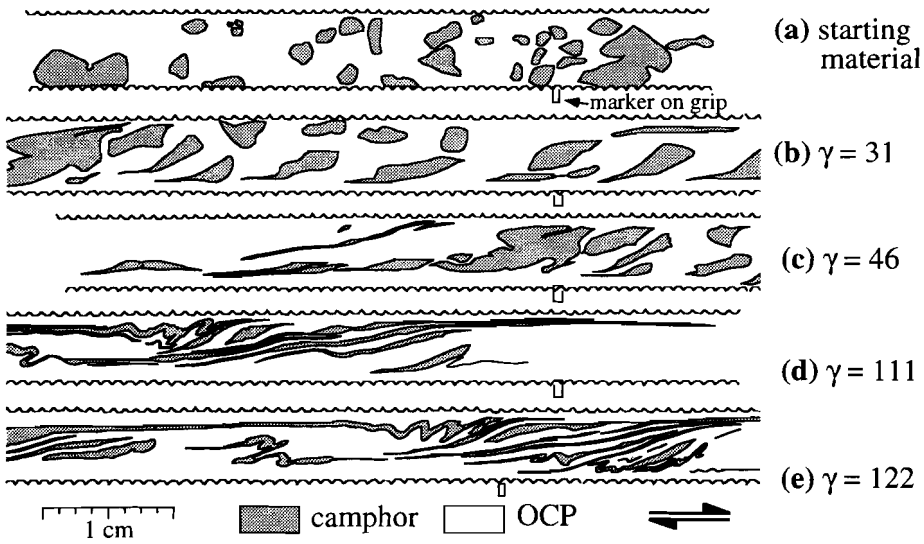

Fig. 6.7. Drawings of the outer surface of specimen RS5, showing the microstructure at several stages during deformation. (a) starting material, (b) at γ=31, (c) at γ=46, (d) at γ=111 and (e) at γ=122. Camphor is shown in grey, OCP in white. Dextral shear.

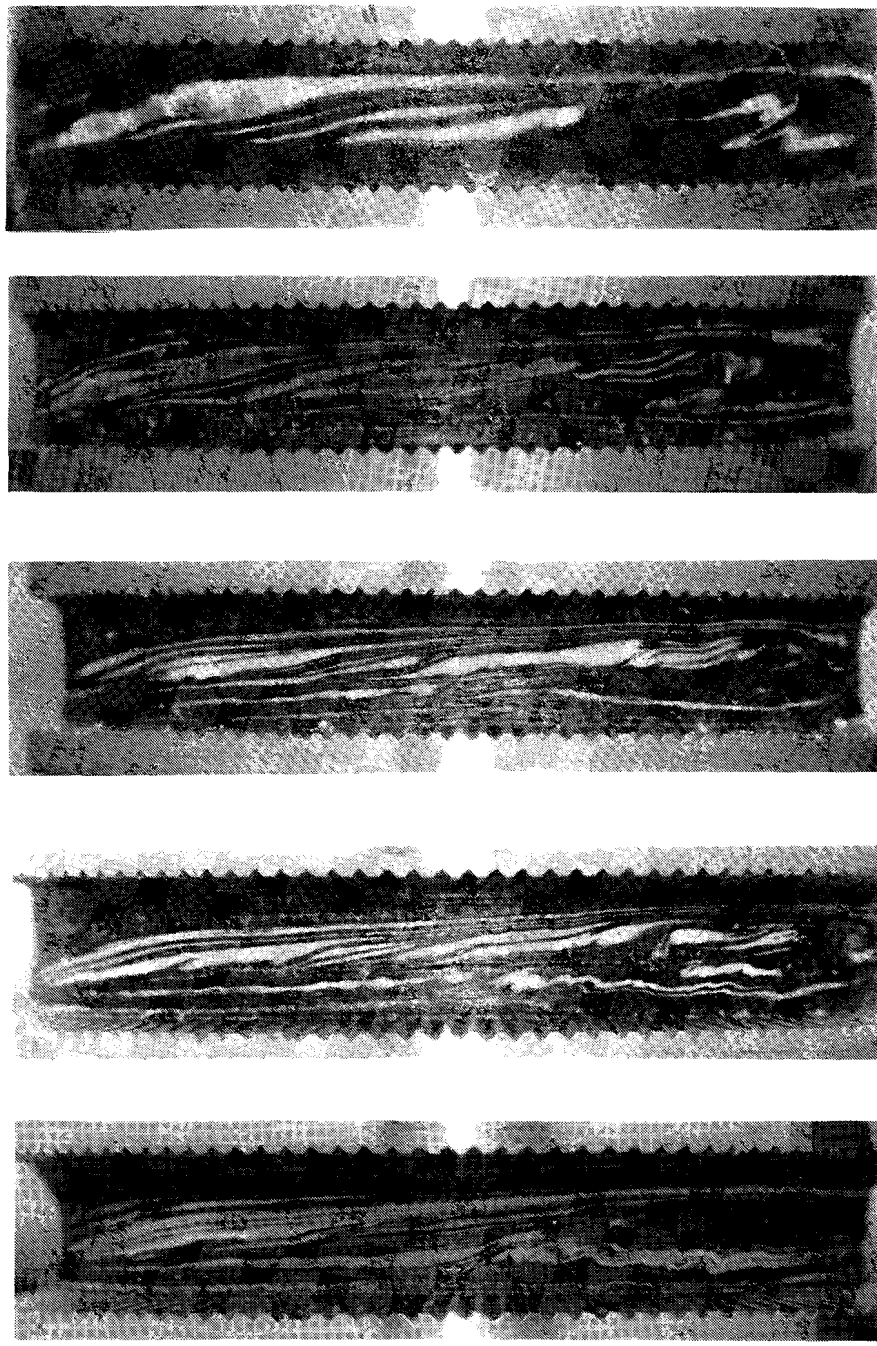

Fig. 6.8. *Photographs of sample RS5 after deformation at two sites on the specimen at difference radii (r) (a-e and f-j). (a,f) Outer surface, r=18 mm, (b&g) r=17 mm, (c&h) r=16.6 mm, (d&i) r=16.1 mm and (e&j) and r=14.6 mm.*

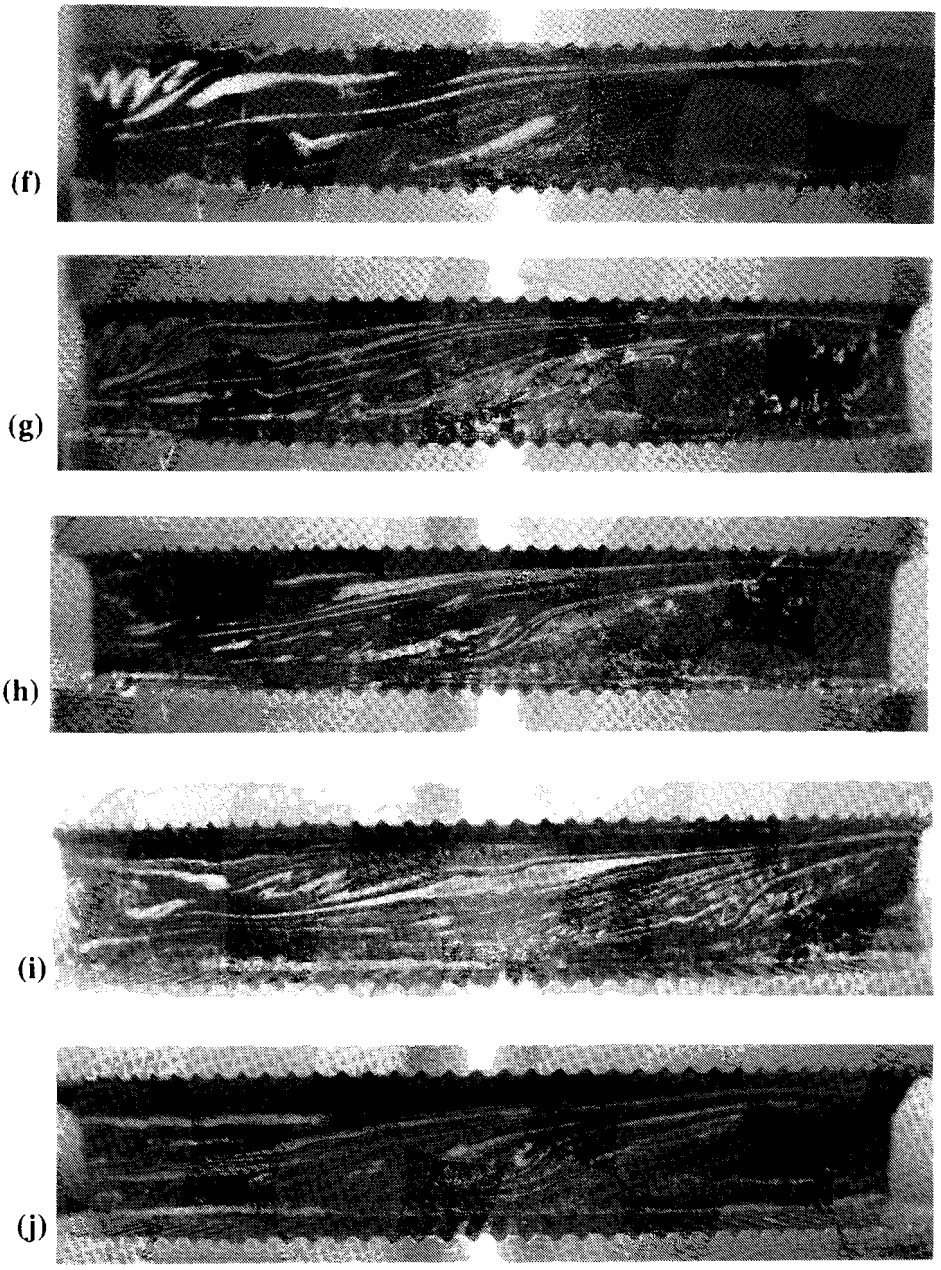
(f)
(g)
(h)
(i)
(j)
5 mm

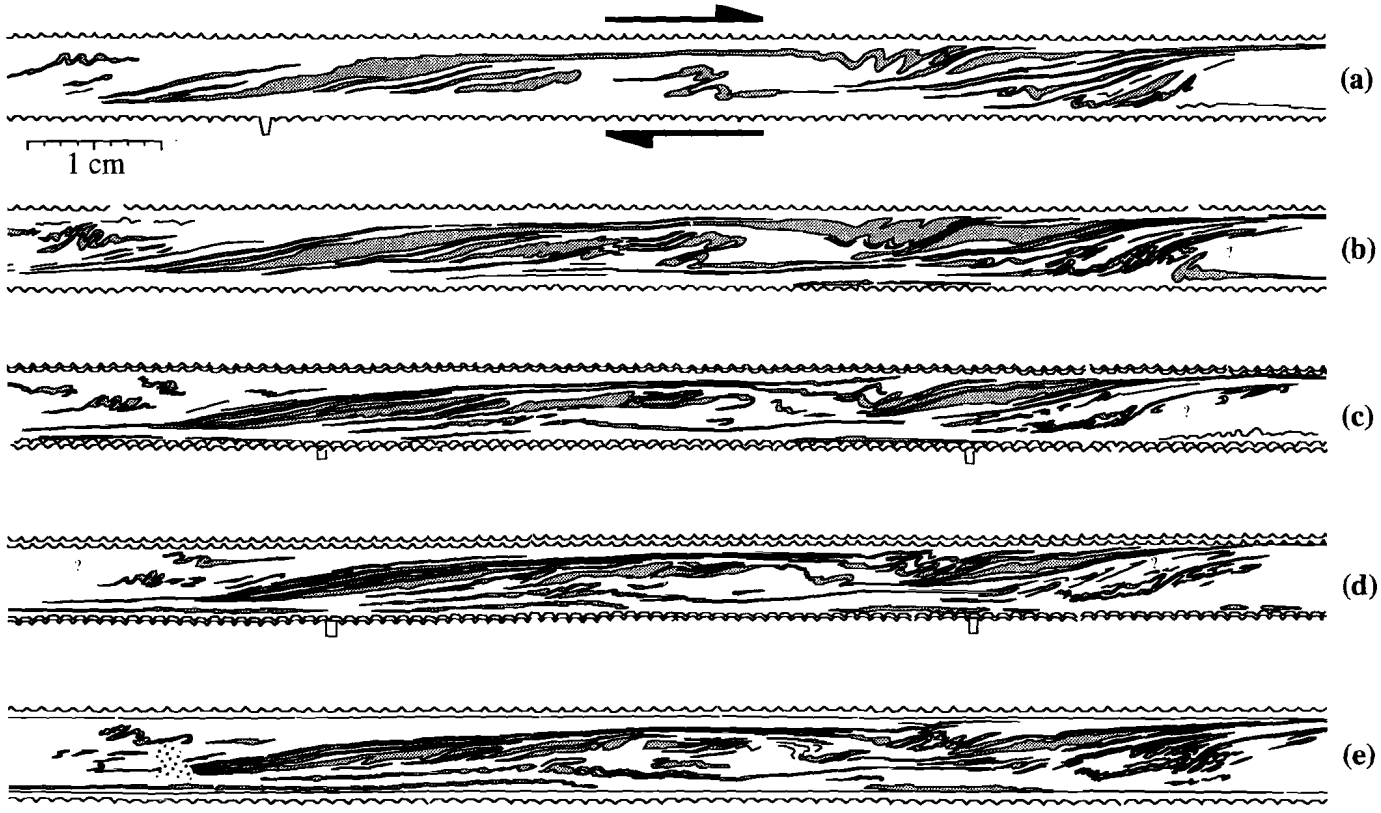

Fig. 6.9. *Drawings of sample RS5 after deformation at different levels in the sample: (a) outer surface, r=18 mm, (b) r=17 mm, (c) r=16.6 mm , (d) r=16.1 mm and (e) r=15.5 mm. Camphor is shown in grey, OCP in white*

6.2.2 RS7

Experiment RS5 was repeated under the same conditions as RS5, with the exception that 1) the shear stress was set at 0.28 MPa from the beginning of the experiment and 2) the camphor (33%) was mixed with black powder instead of the OCP. Since etching makes the camphor white and does not change much of the appearance of the OCP, this did not help to enhance the difference in appearance of OCP and camphor. The experiment was interrupted several times to observe the microstructure (fig 6.10) The experiment was stopped at a shear strain of 76, because the specimen broke when the outer mantle was removed. Figure 6.11 shows the γ/t graph and the $\dot{\gamma}/\gamma$ graph.

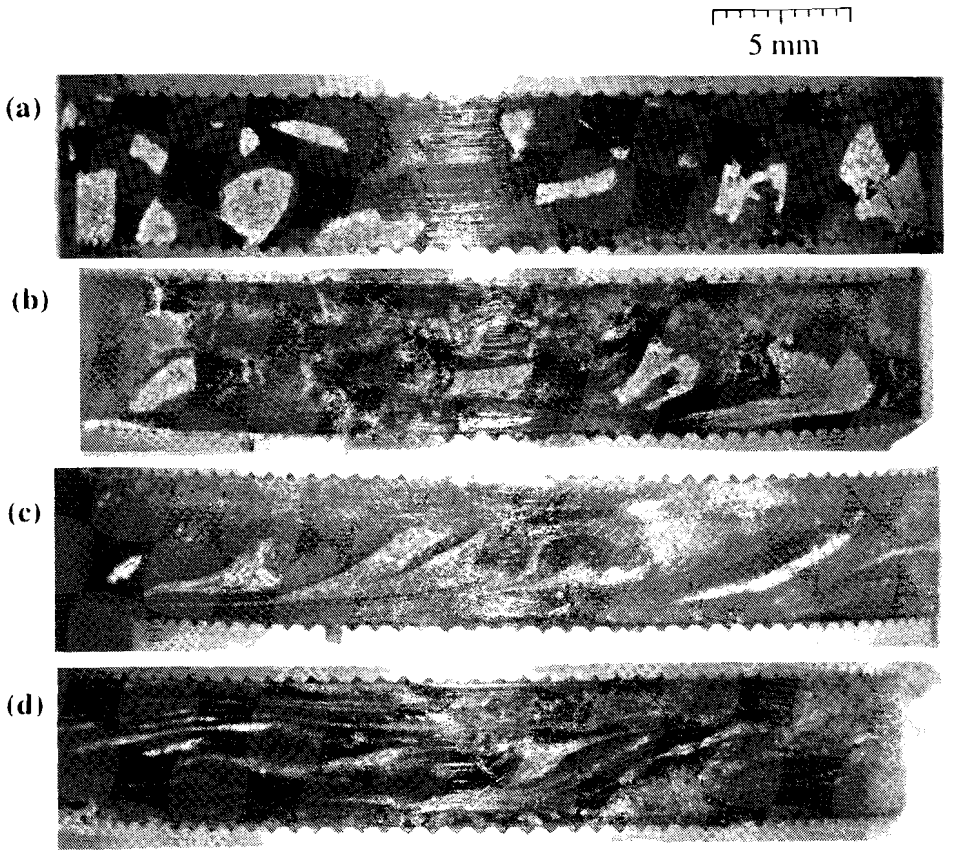

Fig. 6.10. *photographs of microstructure in experiment RS7 at four stages during deformation. (a) starting material, (b) at γ=8, (c) at γ=23.6 and (d) at γ=68.4. Camphor is the light material, OCP is dark.*

The microstructural development is similar to that in experiment RS5. Localisation occurs near the grips, where parts of the camphor inclusions can be seen to have sheared into the zones of localised deformation. Eventually all camphor inclusions become stretched to elongate lenses and layers, folded in open folds at a shear strain of 68. The shear strain rate rapidly increases after each time the experiment was interrupted. The highest rate is achieved at a shear strain of about 30, after which there is a general decline in shear strain rate.

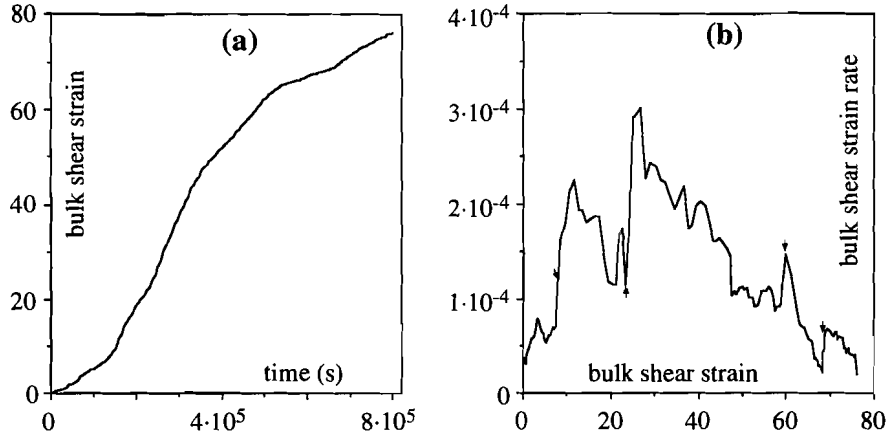

Fig. 6.11. Shear strain versus time (a) and shear strain rate versus shear strain (b) for experiment RS7. Arrows indicate interruptions for photography.

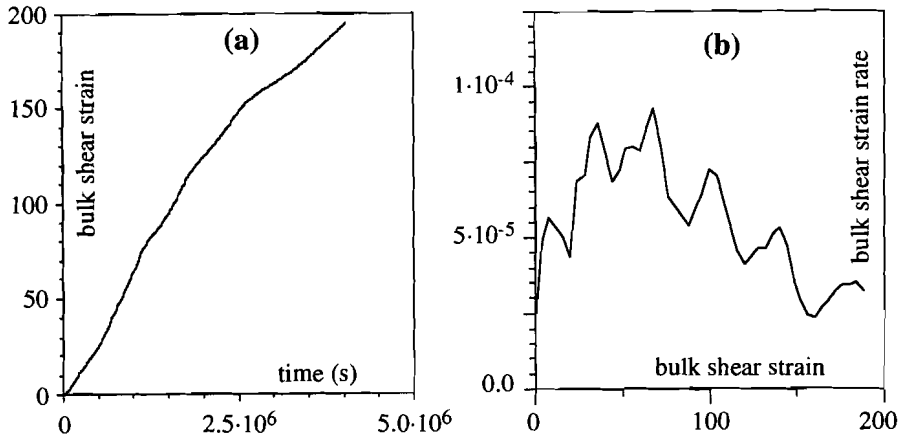

Fig. 6.12. Shear strain versus time (a) and shear strain rate versus shear strain (b) for experiment RS8.

6.2.3 RS8

Since experiments RS5 and RS7 showed that interruptions of the experiment to observe the specimen may significantly influence the rate of deformation, experiment RS8 was performed without any interruption. The sample was composed of about 38% camphor as inclusions in OCP, which was mixed with blackening powder. The specimen was compressed at 29°C for 2 days prior to deformation to a finite shear strain of 195 at a shear stress of 0.28 MPa at 29°C. Figure 6.12 shows the γ/t graph, the $\dot{\gamma}/\gamma$ graph and photographs of the starting and deformed material are shown in figure 6.13. Two differences in the microstructural development can be observed, compared with experiments RS5 and RS7:

1) The differential layering is strongly developed with almost all camphor having migrated away from the grips.
2) The camphor inclusions are not stretched as much (axial ratio of inclusions is smaller than in experiments RS5 and RS7) as in the other experiments. Some folding has occurred. Some inclusions have long narrow tails.

The shear strain rate rapidly increased at the onset of deformation, from an initial value of about $2.5 \cdot 10^{-5}$ s^{-1} to about $5.0 \cdot 10^{-5}$ s^{-1} at a shear strain of 4. Up to a shear strain of about 75 there is a general, but slower increase in the shear strain rate. Then the shear strain rate decreases again to approximately the starting value.

6.2.4 Discussion

Deformation of camphor inclusions

Camphor inclusions deform significantly. Stretching is initiated at the corners of the inclusions where tails are developed, especially near the grips. This heterogeneity in deformation rate can be explained by stress concentrations that occur at extruding parts (corners) of the camphor inclusions accompanied by softening in the camphor caused by recrystallisation. The formation of very long long tails from isolated camphor clasts deforming in simple shear in an OCP matrix has has been reported by Ten Brink & Passchier (1992, 1993) and Passchier *et al.* (1993). In those experiments the amount of recrystallised material is only minor and the clasts develop into δ-clasts. In the experiments described here there is much less differentiation between the recrystallised, stretched material and the relatively undeformed cores, except in some inclusions in experiment RS8. The whole inclusions deform and eventually get stretched to elongate lenses and layers.

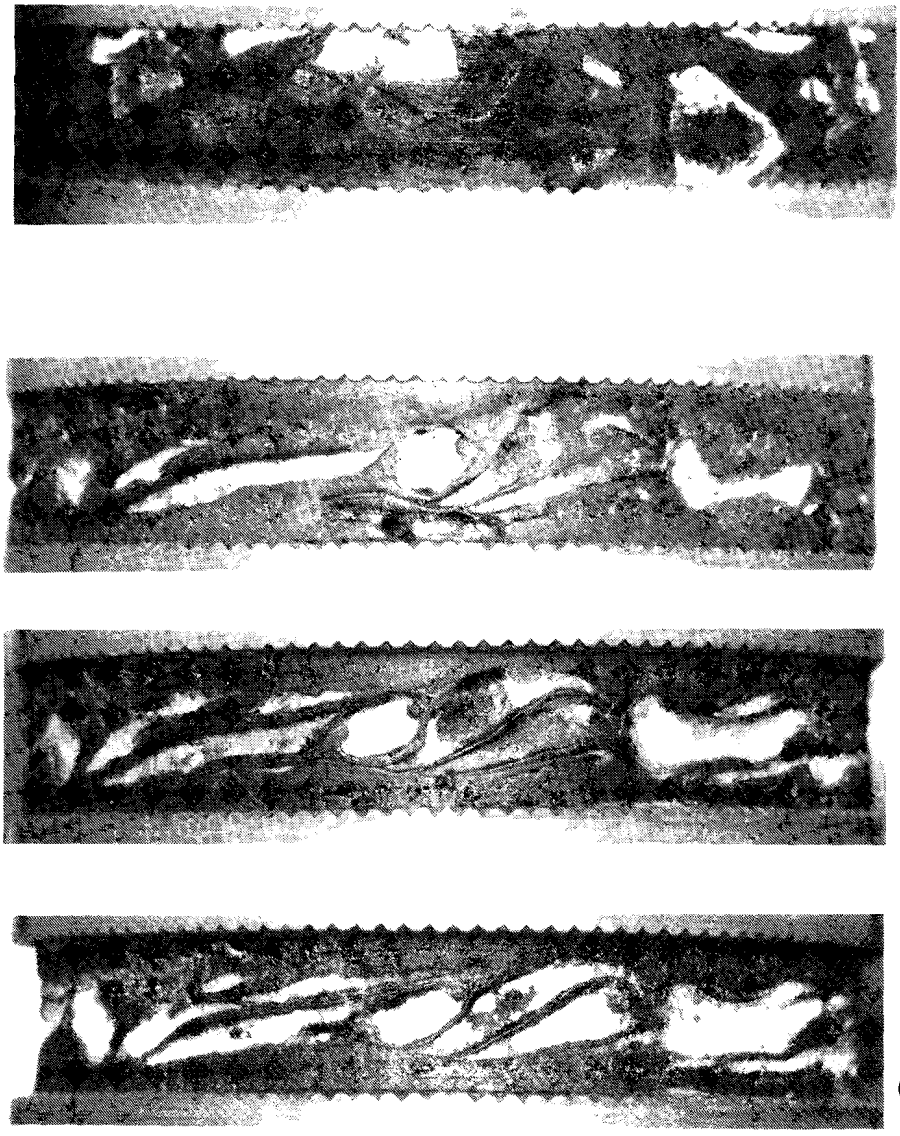

Fig. 6.13. *Photographs of the microstructure in experiment RS8. (a) starting material and at a finite bulk shear strain of 195 at two sites on the sample (c-e) and (f-h) at different depths in the sample: (b&e) outer surface, r=18 mm, (c&f) 17.3 mm and (d&g) 16.8 mm. OCP is dark, camphor light.*

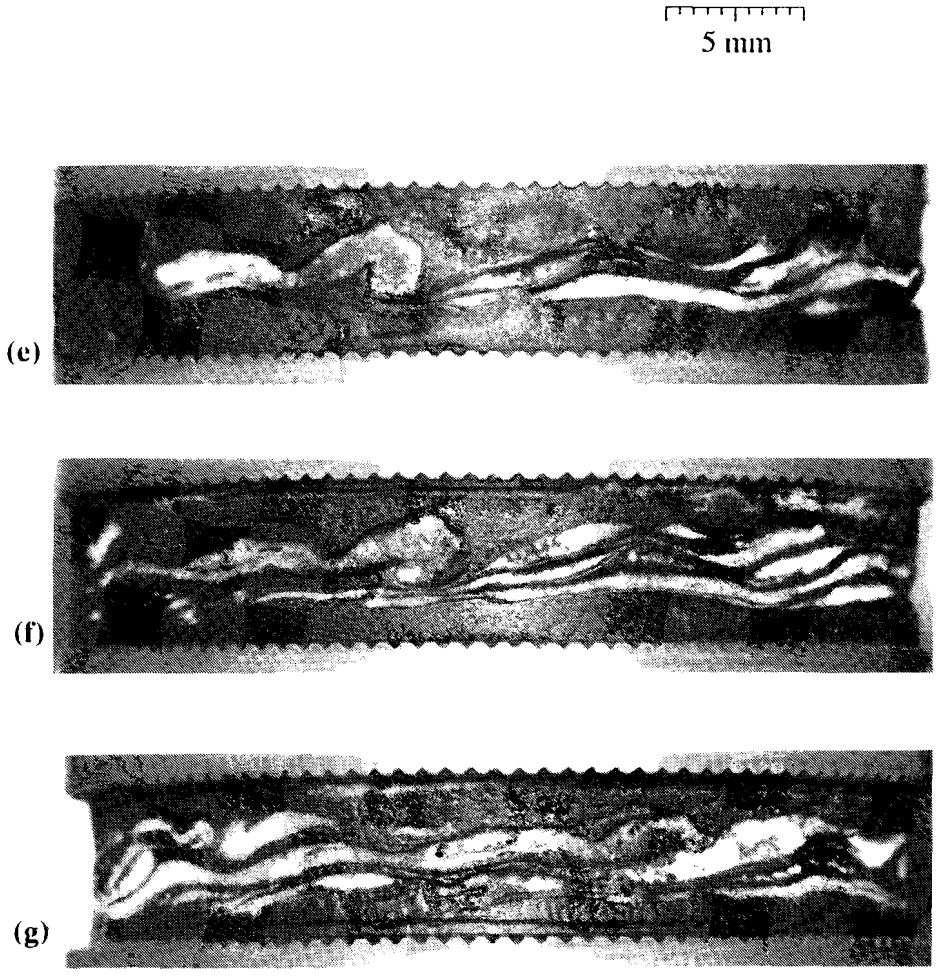
5 mm
(e)
(f)
(g)

In chapter 5 it was shown that the influence of camphor on the flow properties of the mixture was about the same as that of rigid inclusions. This apparently does not mean that the inclusions do not deform. The rate of deformation of the inclusions is, however, much lower than the bulk rate.

Shear localisation

A localisation of shear in the zones adjacent to the grips is observed in all three experiments. This zone becomes depleted of camphor by a movement component of the camphor inclusions perpendicular to the grip plane. This phenomenon is most obvious in experiment RS8. The structure in the experiments, especially RS8, where high shear strain rate zones exist that are depleted of the hard phase, is reminiscent of shear bands (e.g. fig 10 in Gapais & White 1982). The mechanism of segregations seems to be purely mechanical. The difference in flow properties do not only cause a partitioning of deformation rate, but also of the the vorticity of deformation, with the weakest phase in general deforming at a higher kinematic vorticity number than the strongest phase (Ishii 1992; Lister & Williams 1983; Treagus 1988). The harder camphor inclusions will therefore tend to stretch and rotate within the OCP matrix. Near the grips this cannot occur in a symmetric way and the camphor inclusions will move away from the grips (fig 6.14). It cannot be determined whether the segregation is only caused by the grips. Planar zones with a higher than average concentration of camphor inclusions may have the same effect as the rigid grips. Such a zone would then cause increasing segregation. The relative width of the sample with respect to the size of the inclusions was too small to observe such an effect, but in wider (natural) shear zones it is possible that this mechanism plays a role in the formation of shear bands, where the distance between the shear bands is determined by previously existing variations in the distribution of the phases and the size of the harder phase inclusions.

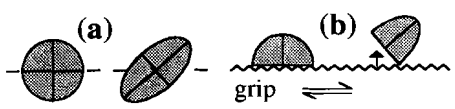

Fig. 6.14. *Simplified sketch showing that a hard object (shaded) in a soft matrix deforming in simple shear does deform and rotate, but remains in the flow plane (a), whereas an object that initially lies on the grip (rigid boundary) will have a component of movement normal to the flow plane.*

Folding

In all three experiments folding occurs. This folding can only occur after the camphor inclusions have stretched a certain amount. Only a gentle open folding has developed in experiment RS7, but in RS5 several open to isoclinal folds have developed. Only few folds have developed in RS8, where the camphor inclusions have not deformed much. Folding is by layer parallel shortening, causing buckling, as can be observed in the developing fold trains shown in figure 6.16. Interaction of layers and lenses probably causes local perturbations of the simple shear flow field, which caused (parts of) these layers and lenses to shorten and fold.

The axial planes of the buckle folds start off at high angle to the flow plane. Once the folds have developed they start to be sheared, causing a tightening of the folds and a rotation of the axial plane towards the flow plane. Such folds are often observed in natural shear zones, see for example figure 1.c in Hudleston & Lan (1993). Isoclinal folds with axial planes parallel to the flow plane are observed and these may undergo another folding phase (see fig 6.8.c). The simple shear deformation therefore leads to continuous folding and refolding of individual layers and lenses, as is also observed by Mawer & Williams (1991). The shearing of the folds is not passive, because of the relative strength of the camphor. The set of limbs in lying in the shortening direction, called *forelimbs* here after Ray (1991), may buckle again (probably in antiform 2 in figure 6.16.a) and/or rotate. Interaction between the layers, lenses and fold trains can lead to continuous folding, refolding and transposition of the folds (Hobbs *et al.* 1976).

When the folds tighten, the foldtrain can start to behave as one single unit that rotates due to the vorticity of flow, thus becoming a forelimb of a larger scale fold. The two backlimbs on either side are pushed away from their original plane (Fig 6.16.c). This process of backlimb separation was also observed in one experiment with a transparent deformation apparatus (fig 6.15). Similar structures have been described by Rykkelid & Fossen (1992) in naturally deformed rocks. Rykkelid & Fossen interpret these structures as passive, being caused by either local areas of compression or local dipping of the layers behind "tectonic lenses". The observations here suggest that these widening folds are caused by the contrast in flow properties between the phases.

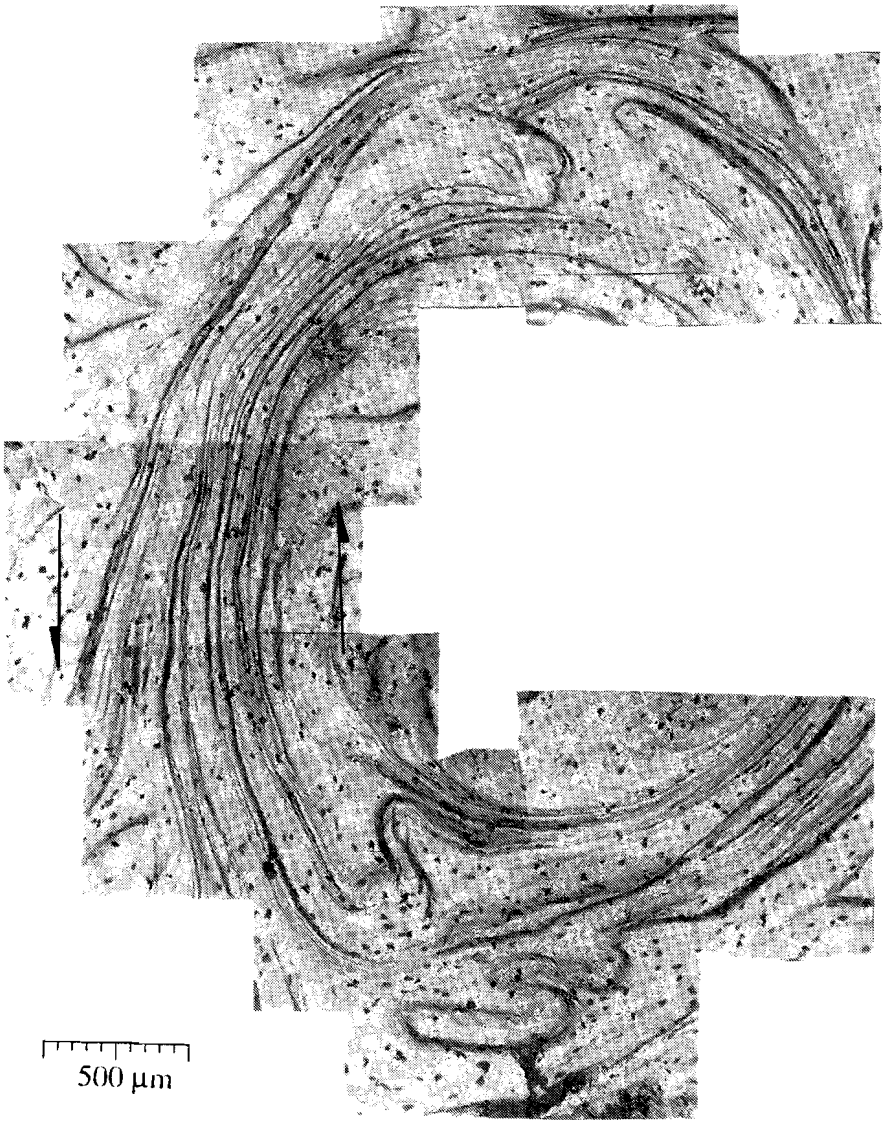

Fig. 6.15. *Folding in experiment with transparent deformation apparatus. Bulk sinistral shear strain rate is* $4 \cdot 10^{-4}$ s^{-1}*, temperature is 30°C. The figures (from video-images) show the development of two fold systems. (a) overview of the circular shear zone at the end of the experiment (after 17 hours and 15 mins.). (b) Development of a pair of intrafolial folds. Numbers indicate time (in hours and minutes) elapsed since start of experiment. (c) The development of a fold in a layer that has flowed past a large camphor inclusion.*

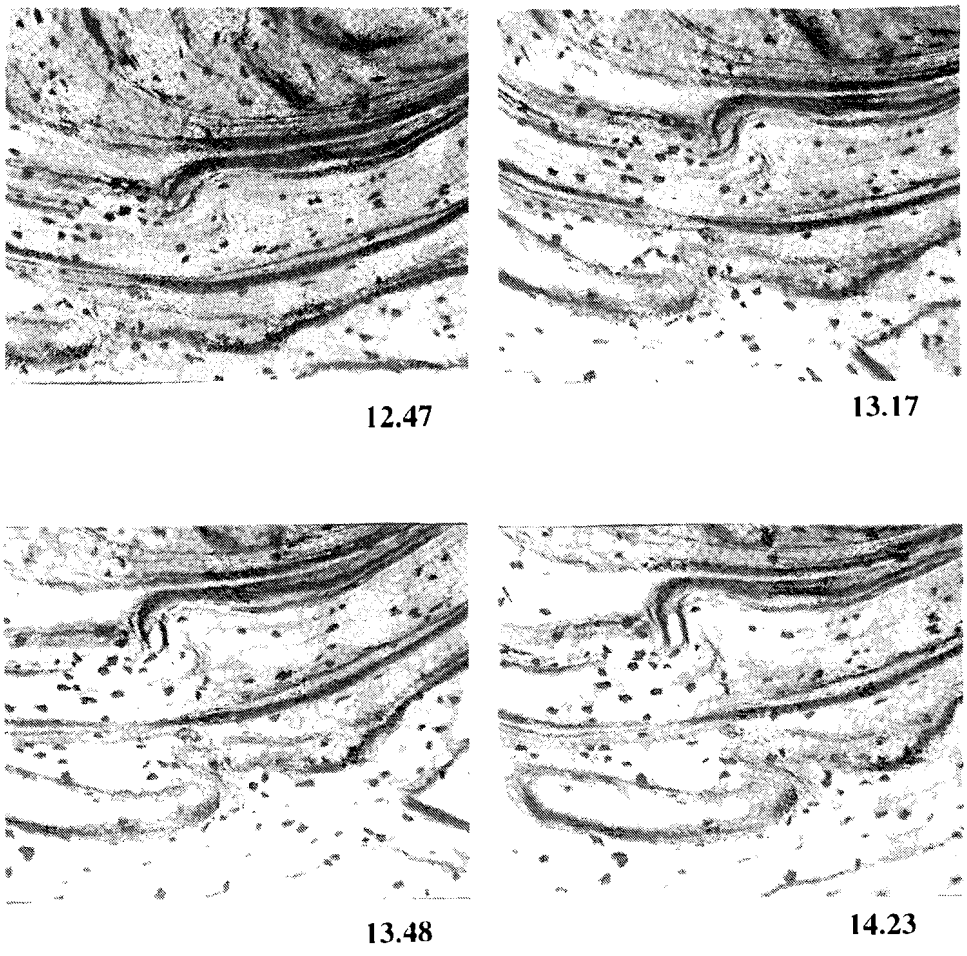

Fig 6.15.b

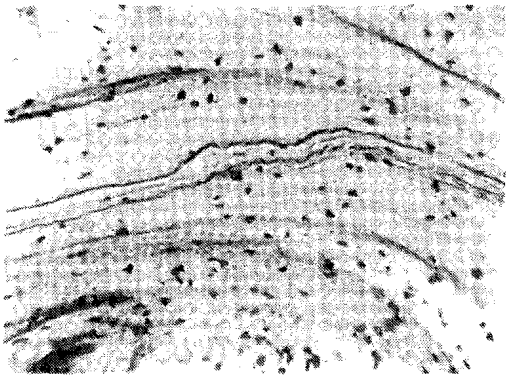

11.21

11.50

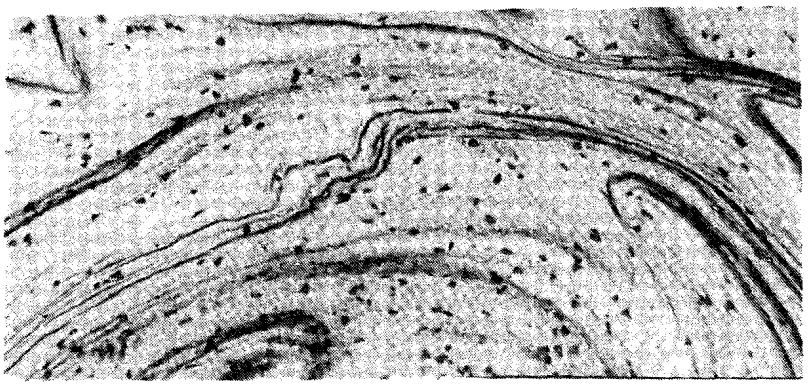

12.20

Fig 6.15.c

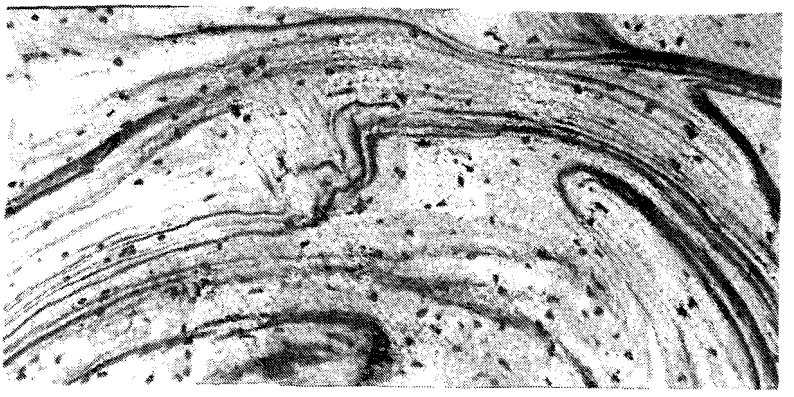

13.20

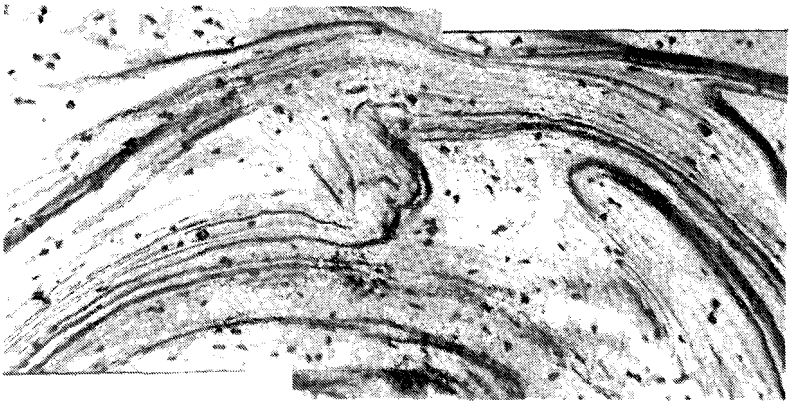

14.30

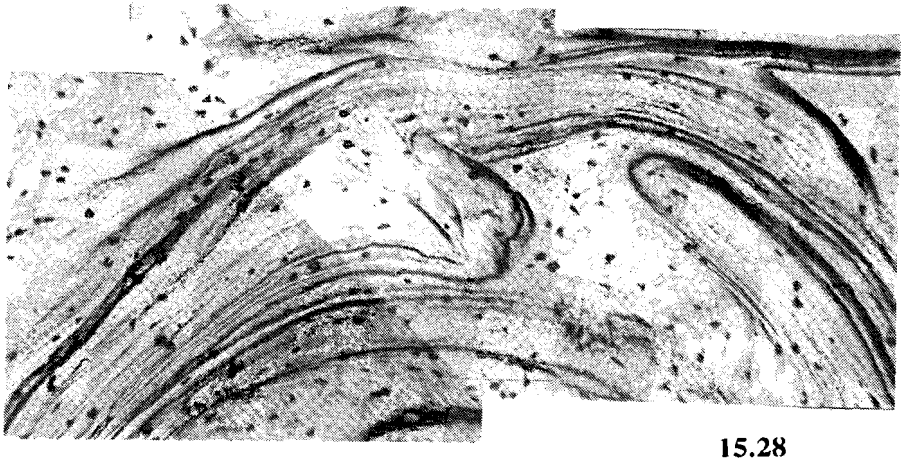

15.28

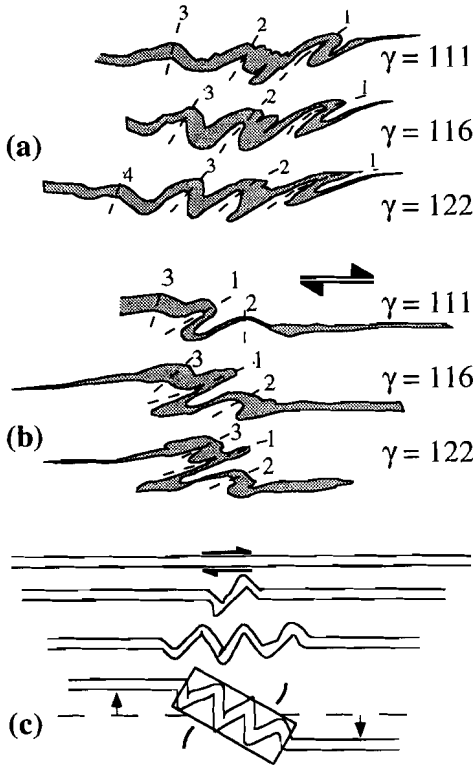

Fig. 6.16. Fold development in two stretched camphor inclusions (shaded). The axial planes of the antiforms are drawn with numbers indicating their age relation ship (nr 1 is oldest). (c) Schematic drawing of the development of a fold train and subsequent backlimb separation as the foldtrain rotates.

Shear strain rate history

The shear strain rate predicted with the tests described in chapter 5 would be between $2.9 \cdot 10^{-5}$ s^{-1} (40% camphor) and $1.0 \cdot 10^{-4}$ s^{-1} (20% camphor). The shear strain rates are in general low compared to the pure shear experiments, except in experiment RS7.

Localisation (partitioning) of deformation into the OCP is enhanced by the formation of a compositional layering and the flattening of the camphor layers, in other words foliation development. An increase in shear strain rate at a constant shear stress is therfore expected. A general increase in shear strain rate is indeed observed in experiments RS5 (up to $\gamma \approx 50$), RS7 (up to $\gamma \approx 25$) and RS5 (up to $\gamma \approx 70$). The first rapid increase in shear strain rate (up to $\gamma \approx 3$-5) can be explained with the development of a crystallographic and grain shape preferred orientation within the OCP and maybe camphor, as is observed in experiments RS1-3 and RS6. From these experiments it is inferred that a steady state fabric is reached in OCP at about $\gamma \approx 3$-5. Further increase in shear strain rate may then be due to the foliation

development. In terms of connectivity (chapter 7), this foliation development means a decrease in connectivity in the direction perpendicular to the flow plane and an increase in connectivity parallel to it. This will be discussed further in chapter 8. Another possible cause for softening is softening of the camphor inclusions that undergo significant deformation, contrary to the camphor inclusions in the axisymmetric experiments.

Experiments RS5, RS7 and RS8 all three show a general decrease in shear strain rate at high finite shear strain. There are two possible explanations for this decrease:
1) increasing friction in the apparatus, only becoming significant at very high shear strain. This possibility cannot be ruled out, because the amount of friction at the mantles is presently unknown (see Appendix B). From the experiments with pure OCP it was inferred that friction cannot play more than a minor role, but these experiments were not carried out to high shear strains. The fact that the sample RS7 broke when the mantle was removed indicates that adhesion to the mantle was strong at that moment.
2) Folding causes the camphor layers to carry more of the stress, then when the camphor forms layers parallel to the flow plane. This will cause a decrease in shear strain rate. The folding or the general destabilisation of the foliation may therefore explain the decrease in shear strain rate at high shear strain. The decrease in shear strain rate and the onset of folding coincide in experiment RS5. Only few folds are found in sample RS8, but the folds are in thicker inclusions and may have had relatively more effect than the folds in the thin layers and lenses of experiment RS5. Only open folding is found in experiment RS7, which must have developed between a shear strain of about 25 and 60.

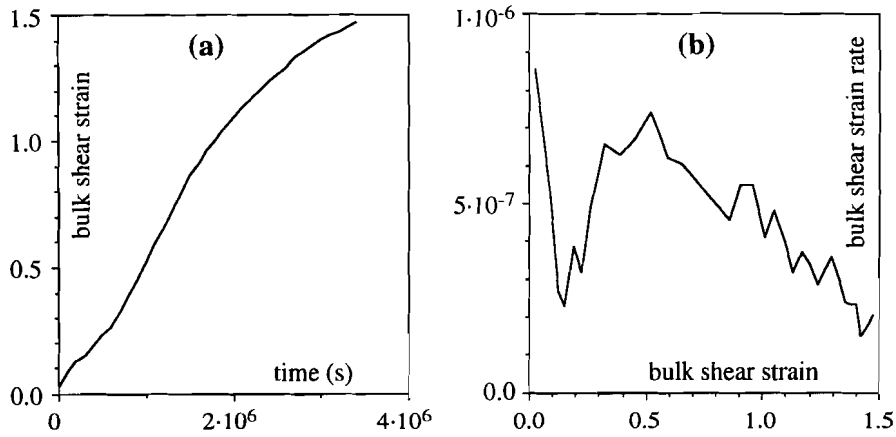

Fig. 6.17. Bulk shear strain versus time and shear strain rate versus shear strain graphs for experiment RS10 with OCP inclusions in a camphor matrix.

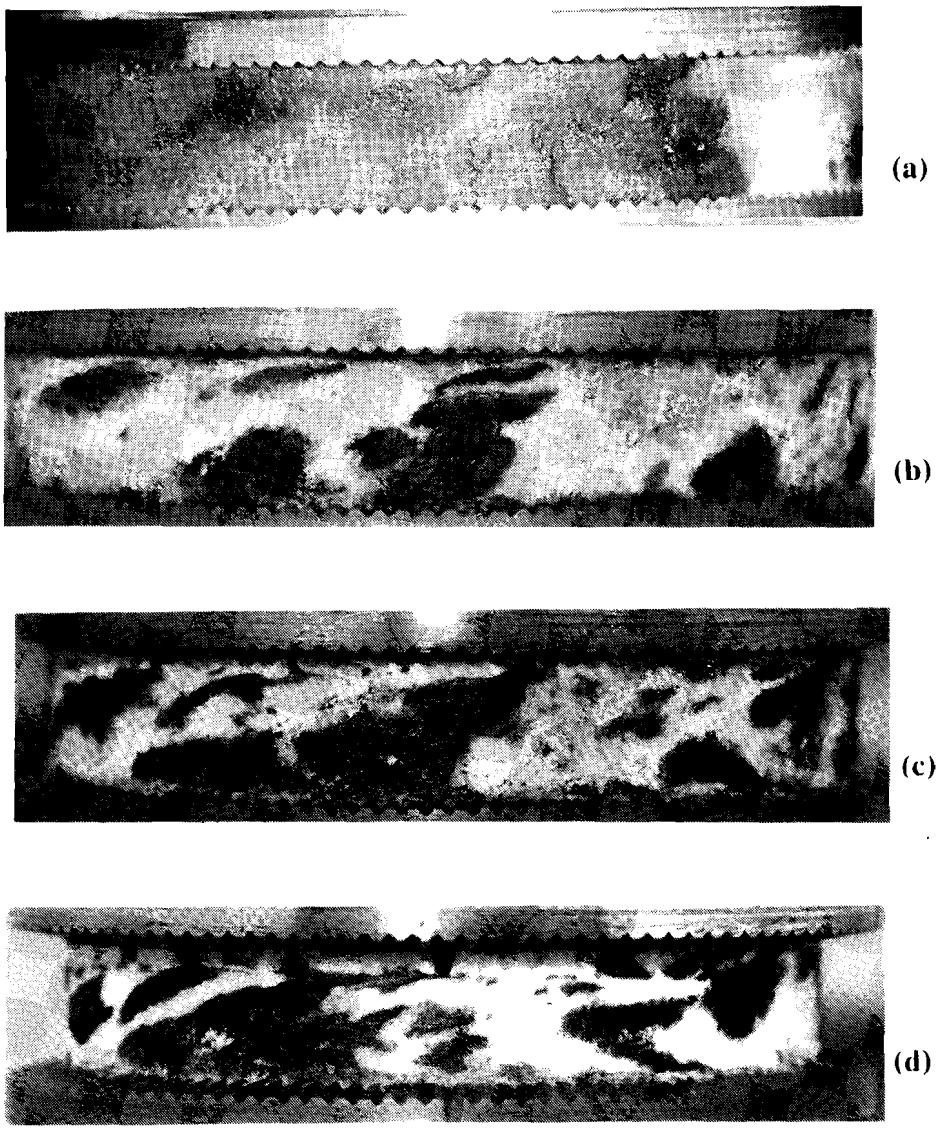

Fig. 6.18. *Photographs of the microstructure in experiment RS10 at two sites in the specimen (a-d and e-h). (a&e) The outer surface (r=18 mm) before deformation (b-d and f-h) After deformation to a finite shear strain of 1.5 at different levels in the specimen: (b&f) outer surface, r=18 mm, (c&g) r=16.7 mm and (d&h) r=15.5 mm. OCP is dark.*

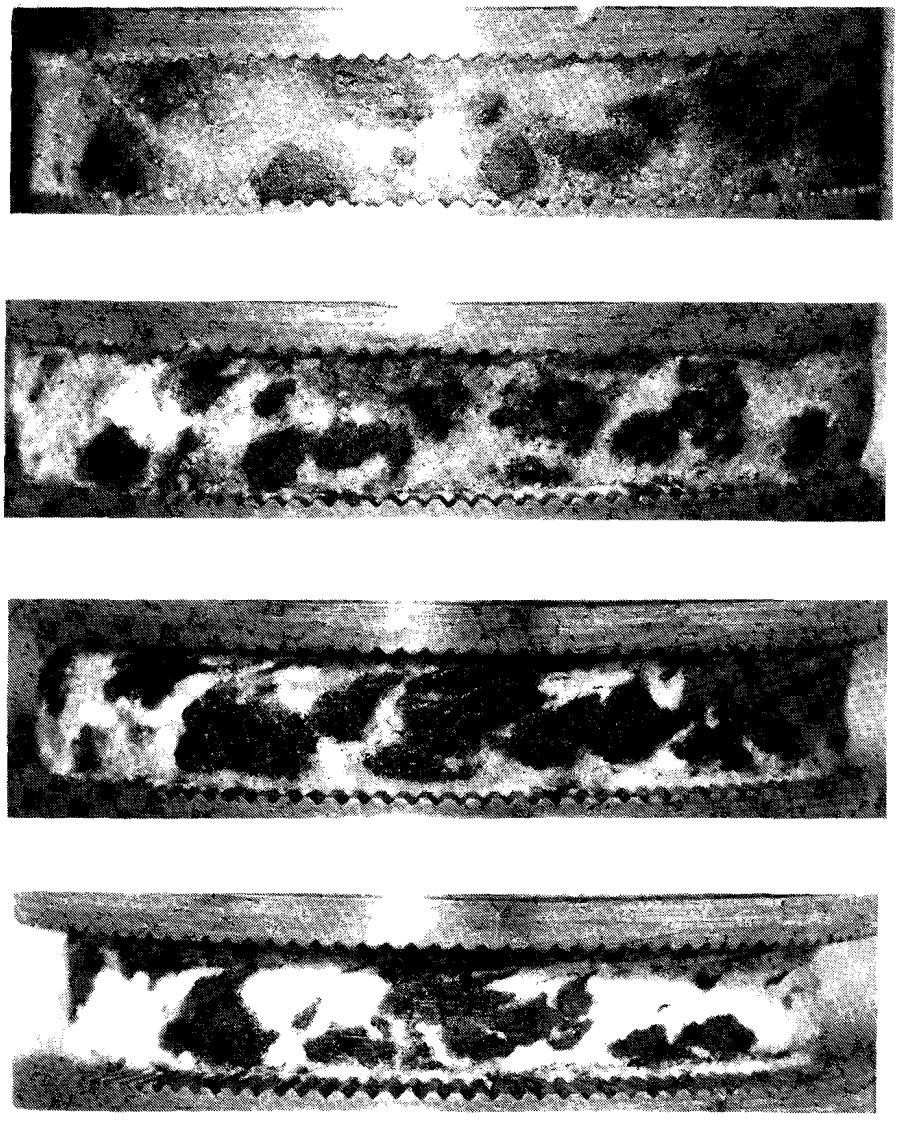
5 mm

6.3 OCP inclusions in a camphor matrix

One experiment, RS10, was performed with a mixture of camphor (76%) and OCP (24%) where the OCP (blackened with powder) formed inclusions in a matrix of camphor. This experiment was performed under the same conditions as experiment RS7 and RS8: a shear stress of 0.28 MPa and a temperature of 29°C. The experiment was not interrupted to photograph the specimen. The γ/t and $\dot{\gamma}/\gamma$ curves are shown in figure 6.17 and photographs and drawings of the microstructure in figure 6.18 and 6.19.

On the photographs one can see that most deformation took place in the upper half of the specimen, where the OCP inclusions are sheared into elongate inclusions. A through-going thin localised shear zone connects the OCP-inclusions. This localised shear zone lies at the upper grip in parts of the specimen, and away from the grip towards the centre of the specimen (fig 6.18.d,h and 6.19.c).

The shear strain rate decreased from about $8 \cdot 10^{-7}$ s^{-1} to $2.5 \cdot 10^{-7}$ s^{-1} in the first $\gamma=0.1$ of deformation. As mentioned before, this apparent decrease in shear strain rate could be caused by a tightening of the wire to apply the load. From a shear strain of 0.1 to 0.5 there is an increase in shear strain rate to $7 \cdot 10^{-7}$ s^{-1}, followed by a decrease in shear strain rate to $2 \cdot 10^{-7}$ s^{-1}. An increase in shear strain rate would be expected by the formation of a through-going localised shear zone. The predicted shear strain rate (chapter 5) for a 20% OCP mixture is $2.8 \cdot 10^{-6}$ s^{-1}. This rate is about 10 times higher than that measured in experiment RS10. The microstructure here is not the same as in the pure shear experiments, however. There the mixture was made by compressing blocky pieces of both camphor and OCP together, whereas in experiment RS10, the sample was made by mixing fine grained camphor powder with cubes (1-3 mm) of OCP, to make a mixture where the OCP occurs as inclusions. The fact that the camphor forms a matrix, as can be seen in figure 6.18, makes the composite stronger than in the pure shear experiments. The final decrease in shear strain rate is difficult to interpret. Again it could be due to friction at the mantle or elsewhere in the apparatus, or it could be caused by "locking-up" of the localised shear zone, which is not straight.

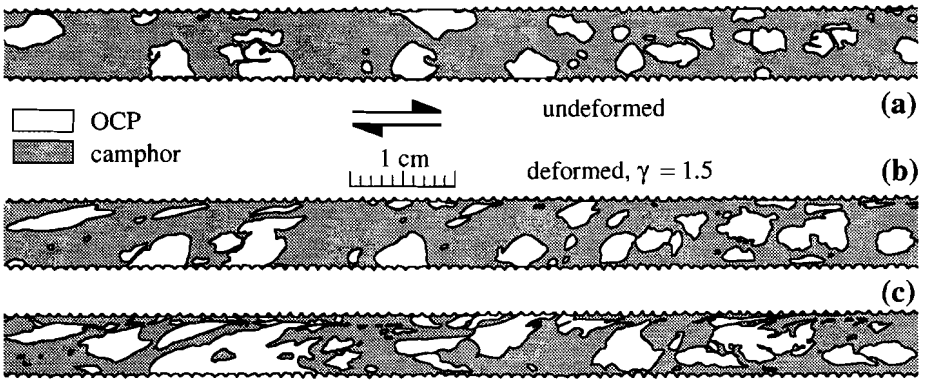

Fig. 6.19. Drawings of the microstructure of RS10, starting material (a) and deformed specimen, at the outer surface (b) and at r=16.75 mm (c). OCP is white, camphor grey.

6.4 Problems and suggested improvements for the ring shear apparatus

The experiments described in this chapter show that the new ring shear apparatus is a useful tool to investigate the microstructural development and its relation to changes in bulk rheological properties. However, some problems were encountered during the experiments with the prototype of the apparatus.

The amount of friction in the system (at ball bearings) and sticking of the specimen to the confining mantles remains unknown. The friction at the ball bearings that transmit the normal stress to the grips can be reduced to a negligible amount, but friction caused by sticking of the sample to the mantles maybe not, although a suitable lubricant and the use of low friction materials (for instance teflon) may reduce the friction. It is advisable to try to measure how much of the applied torque is actually transmitted to the opposite grip.

Shear strain rate measurements are sensitive to noise and errors in the measurement of the finite shear strain and time, since it is a derivative of the shear strain-time data (see Appendix B). Measurements can be improved by using a more sensitive potentiometer or maybe another device and by using a small potentiometer wheel in combination with a large driving wheel in the present set-up. It is however advisable to measure the shear strain directly at the rotating column, and not at the unwinding wire. This way one can also accurately measure the shear strain (rate) at the onset of deformation.

The confining cylinders, presently made of steel, may be replaced by glass cylinders to allow observation of the deforming sample during deformation. It would also be desirable to add a constant shear strain rate option. This can be done by rotating the upper grip with a motor and measuring the applied load to do so with strain gauges, possible in a way similar to that for the transparent ring shear apparatus (Fig. 3.9.b).

Chapter 7

Numerical Modelling

7.1 Introduction

The experimental approach to the problem of the mechanical properties of twophase materials (as discussed in the previous chapter) has two main limitations:

1) The range of combinations of flow-properties (type of flow and competence contrast) is limited by the availability of suitable materials and the experimental equipment.
2) It is difficult to systematically vary the internal geometry of the composite.

Finite element modelling (e.g. Zienkiewicz 1977) is a valuable complementary approach to the problems studied in this work. Various types of constitutive laws can be assigned to the elements in the model and the parameters can be varied by the user. Any desired distribution of elements with certain properties can be made for a given mesh type. Finite element modelling has its limitations as well: material properties are restricted to limited, often simple constitutive laws and the number and shape of elements is limited by the program, computer capacity and calculation time. Still, finite element modelling can be a valuable complementary approach to problems such as the one subject of this study.

Two software packages were used:

1) HEL, provided by S.J.D. Cox, a finite element program to model linear elastic materials (chapter 7.2),
2) BASIL, written and provided by G.A. Houseman and T.D. Barr, a finite element program to model power-law creep materials (chapter 7.3).

7.2 Modelling with HEL

7.2.1 The program HEL

HEL (Hexagonal or Honeycomb ELements) was used to model two-phase composites of isotropic linear elastic materials. This implementation models linear elastic behaviour, but the results are useful in addressing our problem as they may be considered a "snapshot" of progressive deformation, with quantitative interpretation

by converting "strain" to "strain rate". The model is a modification by Cox & Paterson (1990, 1993) of the program described by Desai & Abel (1972). It is written in the programming language C and was implemented on a SUN workstation. The 2-dimensional model uses a honeycomb mesh of 30x30 elements, each composed of six constant strain triangles, with nodes at their three vertices (Fig. 7.1.a&b). Material properties can be assigned to each element in the form of a Young's modulus and a Poisson's ratio. Vertical displacements (leaving horizontal displacement unconstrained) to achieve an extension of 0.1% are assigned to all nodes lying on two opposite sides of the mesh. The stiffness of the composite (E_c), defined here as the average normal stress in the direction of extension, was calculated. The stiffness is normalised to the stiffness of the strong phase, which is set to unity. Although the properties of the components are isotropic, the composite is not. The calculated stiffness is therefore dependent on the direction of extension. Poisson's ratio was set to 0.2 in all cases and the ratio of Young's moduli (R^E) between the phases was 10^1, 10^2, 10^3 and 10^6.

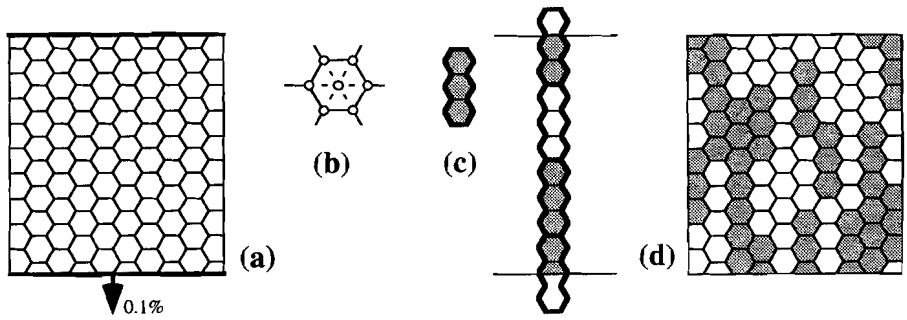

Fig. 7.1. The honeycomb mesh used for the HEL finite element program. (a) A 10x10 elements mesh. The arrow shows the displacement direction of the nodes on the bottom boundary with respect to the top boundary. (b) One element consists of six constant-strain triangles (dashed lines) with nodes (small circles) at the vertices. (c) One inclusion of vertical elongation 3 and an example of a column composed of a sequence of inclusions of elongation 3 (heavy outlines). The sequence of inclusions has a random starting point, parts of inclusions outside the mesh boundaries are "discarded". (d) Example of a 10x10 mesh with $E^{(ver)}$=3. The two different shadings represent the two phases.

7.2.2 Experimental program

The two objectives of the HEL-modelling work were:

1) To investigate the effect of R^E and the fraction of the weak phase (F_w) on the stiffness of the composite.
2) To investigate the effect of an anisotropic distribution of the phases over the elements, at different Young's modulus ratios and fractions of the two phases.

Over 2000 realisations were made, with 3 parameters systematically varied:

1) The Young's modulus ratio ($R^E = 10, 10^2, 10^3$ or 10^6)
2) The relative fraction of the two phases ($0 \leq F_w \leq 1$)
3) The distribution of elements.

Model generation

The geometry of the mesh is defined in terms of the relative occurrence of the two phases. A two stage procedure is used to create this, in order to ensure that the distribution of phases is stochastic, but subject to the constraint that, for a single run, the mesh is constructed from grains or *inclusions* of a consistent aspect shape. First, the mesh is divided into inclusions of a particular length. *Elongation* (El) is defined as the number of elements in an inclusion (note that the term *elongation* is used here in a different sense than in strain nomenclature). This is done for one column of elements at a time, simply by fixing a starting point for the sequence randomly (Fig. 7.1.c). In this way it is ensured that there is no correlation between the locations of inclusions in adjacent columns. Secondly, the material properties of the inclusions are assigned randomly, with the required fractions of each phase (Fig. 7.1.d). The applied extension of the whole mesh can be parallel to the elongation, in which case we will call the elongation *vertical* ($El^{(ver)}$). The other case studied here is where the elongation is perpendicular to the extension, which we call *horizontal* ($El^{(hor)}$).

This model generation routine produces a *statistically homogeneous, anistropic* (if $El \neq 1$) and *symmetric* distribution of the phases over the elements. The material is statistically homogeneous, because the chance that an element is of a given phase is independent of its spatial position. If $El \neq 1$, the distribution of the phases is anisotropic, because the chance that two elements are of the same phase depends on the orientation of the tie-line between these two elements. The distribution of the phases is symmetric because the shape of the inclusions of both phases is the same. A symmetric distribution is rare in rocks where the different minerals in a rock

usually have distinctly different shapes (see also Corson 1974a&b and Watt *et al.* 1976 for the statistical definitions of phase distributions).

Before proceeding to investigate the effects of R^E and distribution on the properties of the models, we must check whether other factors do not play a role. The data presented below will show what the effects of changing the mesh size, the direction of extension or the Poisson's ratio are.

Effect of mesh size

Fig. 7.2 shows E_C/F_W data, for $El^{(ver)}=1$, calculated with mesh sizes of 10x10, 30x30 and 40x40. One can see that difference between the results is that the spread of data decreases with increasing size of the mesh. A small mesh size is favoured for practical reasons (calculation time, use of disk space and computer memory). However, a large mesh size is preferred to avoid too much statistical variation (especially at high elongation, when the number of inclusions becomes considerably smaller). A mesh size of 30x30 elements was chosen as a compromise, limiting the calculation time to about 2-3 minutes per test.

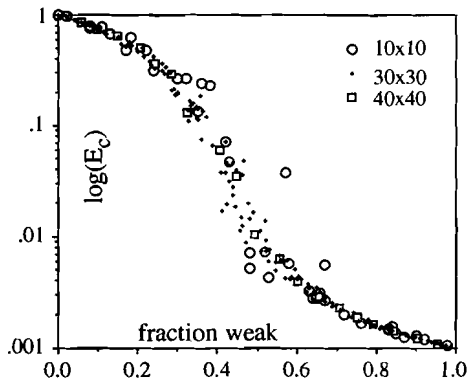

Fig. 7.2. Effect of mesh size. Log(E_C) is plotted against F_W, for three different mesh sizes: 10x10, 30x30 and 40x40 elements. R^E=1000. The data overlap, but the spread in the data is highest for the smallest mesh size.

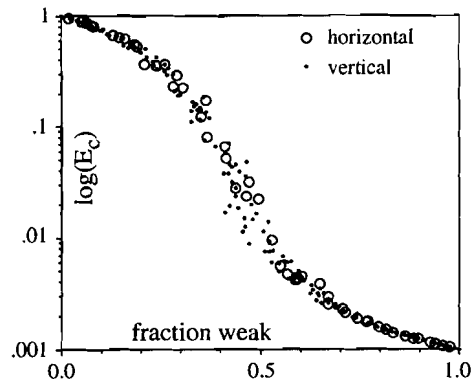

Fig. 7.3. The effect of direction of extension. Circles are for horizontal extension, and solid dots for vertical extension. The data are plotted as log(E_C) against F_W. $El^{(ver)}=El^{(hor)}=1$, $R^E=1000$ and L=30.

Effect of direction of extension

The honeycomb mesh has a hexagonal symmetry. Two directions of extension were used for the modelling: horizontal and vertical. This means that the elements are differently oriented with respect to the applied strain in the two cases and it is of importance to see whether this makes a significant difference for the relative stiffness. Figure 7.3 shows a combined plot of E_c/F_w data for $El^{(ver)}=1$ and $El^{(hor)}=1$. Again, no significant difference is observed.

Effect of Poisson's ratio

A Poisson's ratio of $\nu=0.2$ was chosen for the modelling with HEL. However, it is important to investigate the effect of different values. Figure 7.4 shows the relative effect of two Poisson's ratio's, $\nu=0.05$ and 0.4, compared with $\nu=0.2$. The E_c values were calculated using exactly the same phase distributions for the three cases. $\nu=0.4$ changes the results by less than 1% and $\nu=0.05$ by less than 3%. The effect of different ν for each phase was not investigated.

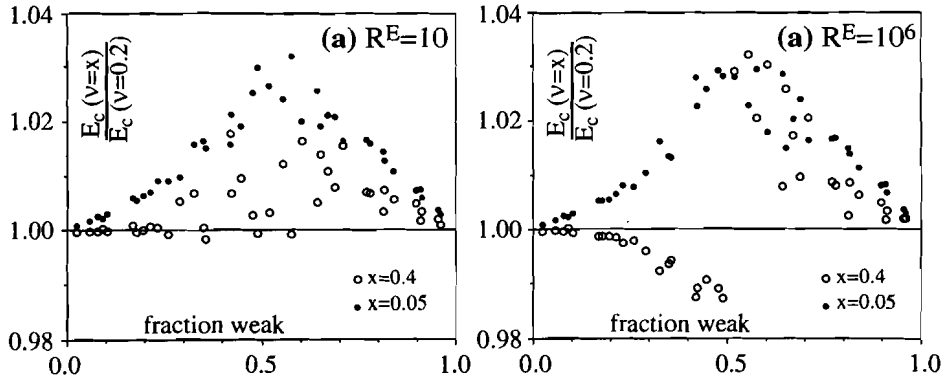

Fig. 7.4. The effect of different Poisson's ratios. Comparison of data for different Poisson's ratio's (ν). E_C data for $\nu=0.05$ and $\nu=0.4$ for both phases are given relative to the data for $\nu=0.2$ (as used for all other tests). $El^{(ver)}=1$ and $L=30$. (a) $R^E=10$. (b) $R^E=1\cdot10^6$.

7.2.3 Results

Isotropic distributions

The relative stiffness as a function of F_w and R^E, for an isotropic distribution ($EI^{(ver)}=1$), is discussed in this section. All data are shown in figure 7.5 in four different graphs. The first is E_c against F_w (Fig. 7.5.a), which serves well to show the data at low F_w. If R^E is higher than one order of magnitude, all data at high F_w become approximately zero and therefore graphs of $1/E_c$, normalised to 1 for $F_w=1$, are shown as well (Fig. 7.5.c). The $\log(E_c)$ or $\log(1/E_c)$ against F_w graphs (Fig. 7.5.b&d) are best suited to observe the data at intermediate fractions, especially at high R^E.

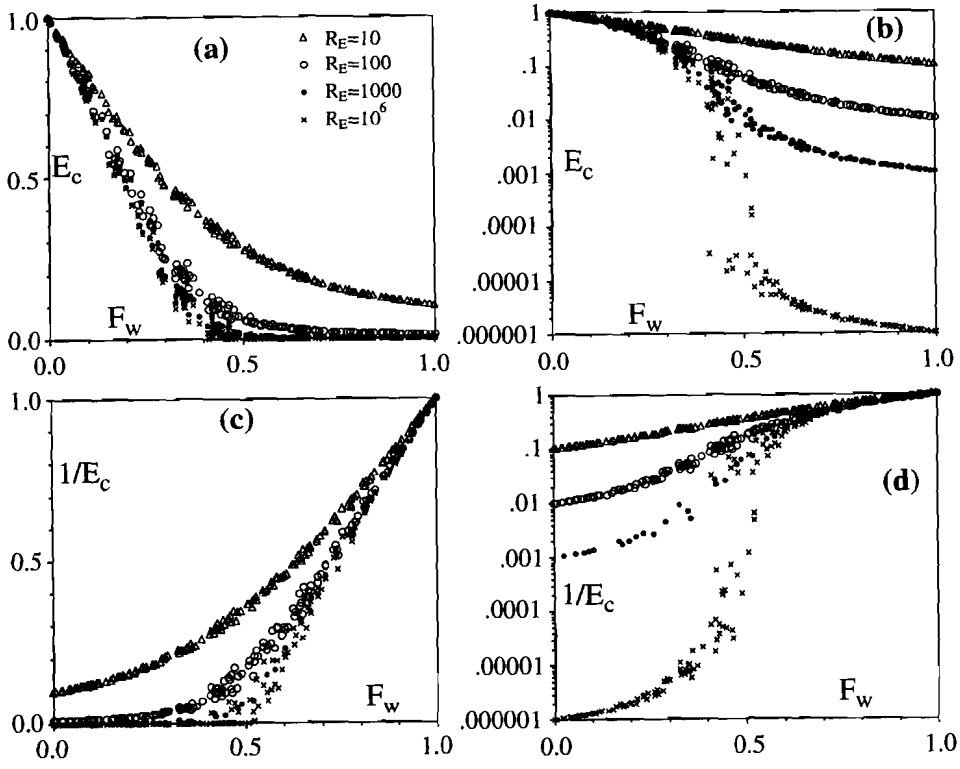

Fig. 7.5. All data for $EI^{(ver)}=1$, $L=30$ and $R^E=10$, 100, 1000 and $1\cdot10^6$. (a) E_C against F_W. (b) $\log(E_C)$ against F_W. (c) $1/E_{C(normalised)}$ against F_W. (d) $\log(1/E_{C(normalised)})$ against F_W.

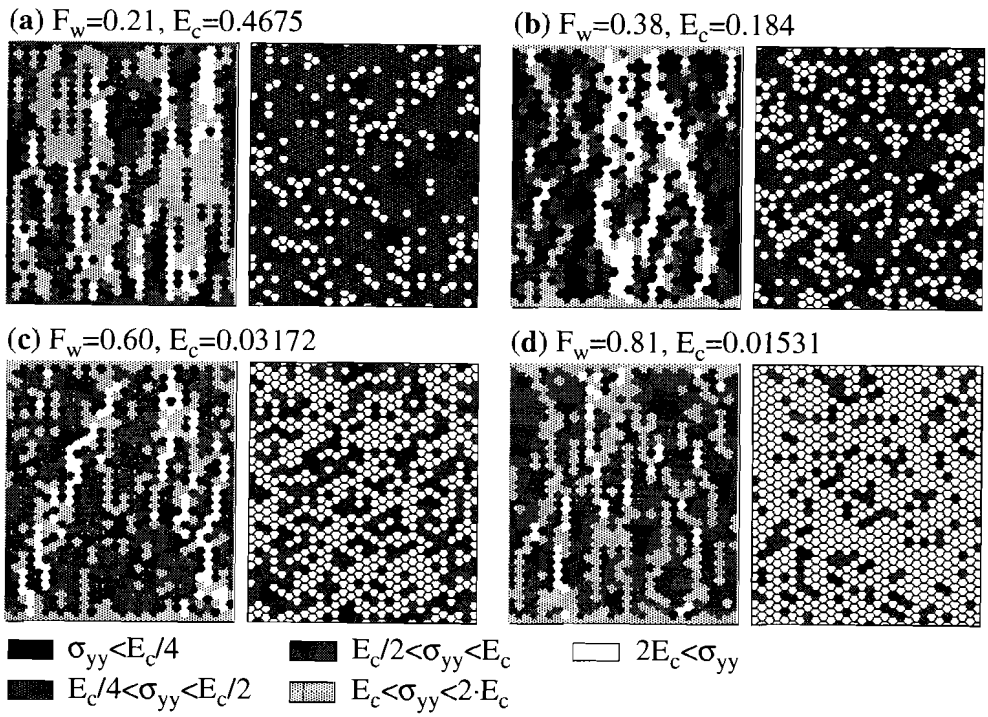

Fig. 7.6. Grey-scale contour plots of vertical stress (left) and distribution of phases over the elements (right) for $El^{(ver)}$=1, L=30, R^E=100 and F_w = 0.21 (a), 0.38 (b), 0.60 (c) and 0.81 (d). Grey scale contour interval boundaries are $E_c/4$, $E_c/2$, E_c and $2E_c$, from black to white. The average (over 6 triangles) stress values of each element is used for the grey-scale plots. (The apparent homogeneous stress at the top and bottom row of elements is an artefact. Stresses vary from element to element, but their values are averaged before contouring. This artefact is a left-over from previous applications of the program HEL) In the phase-distribution plots, the weak phase elements are shown in white, and the strong phase in balck and grey: strong phase elements that form part of clusters that span the mesh from top to bottom are shown in black, and other strong-phase elements in grey.

At $R^E \geq 100$ and at low F_w, the composite stiffness decreases approximately linearly with F_w. E_c becomes negligible at F_w of ≈0.5. At high F_w, $1/E_c$ decreases linearly with increasing F_h (= decreasing F_w). E_c decreases most rapidly at F_w=0.5, at high RE, as can be seen in the $\log(E_c)/F_w$ plot.

Figure 7.6 shows the distribution of the phases over the elements and the distribution of vertical stresses (σ_{yy}) for four selected realisations with different F_w, at R^E=100. At F_w<0.5, the strong phase elements form continuous clusters that span the entire mesh. The weak phase elements occur as isolated inclusions or small clusters. At F_w>0.5 the situation is reversed. Now the strong phase elements occur as inclusions and the weak phase forms clusters that span the entire mesh. The

fraction at which the transition occurs between the two situations will be called the *transition fraction*, F^t. At low F_w (Fig. 7.6.a), stresses are variable in the strong phase elements, varying around the average stress. Stresses are concentrated in the elements of the strong phase that form the shortest "paths" through strong phase elements from top to bottom in the mesh, as F_w approaches F^t (Fig. 7.6.b). Stresses outside these regions are relatively low in both strong and weak phase elements. The average stress in the mesh drop significantly as F_w becomes larger than F^t (Fig. 7.6.c&d). Stresses in the weak phase elements now vary around the average stress, and highest stress values occur in the strong phase elements that form part of clusters with the largest length in the vertical direction.

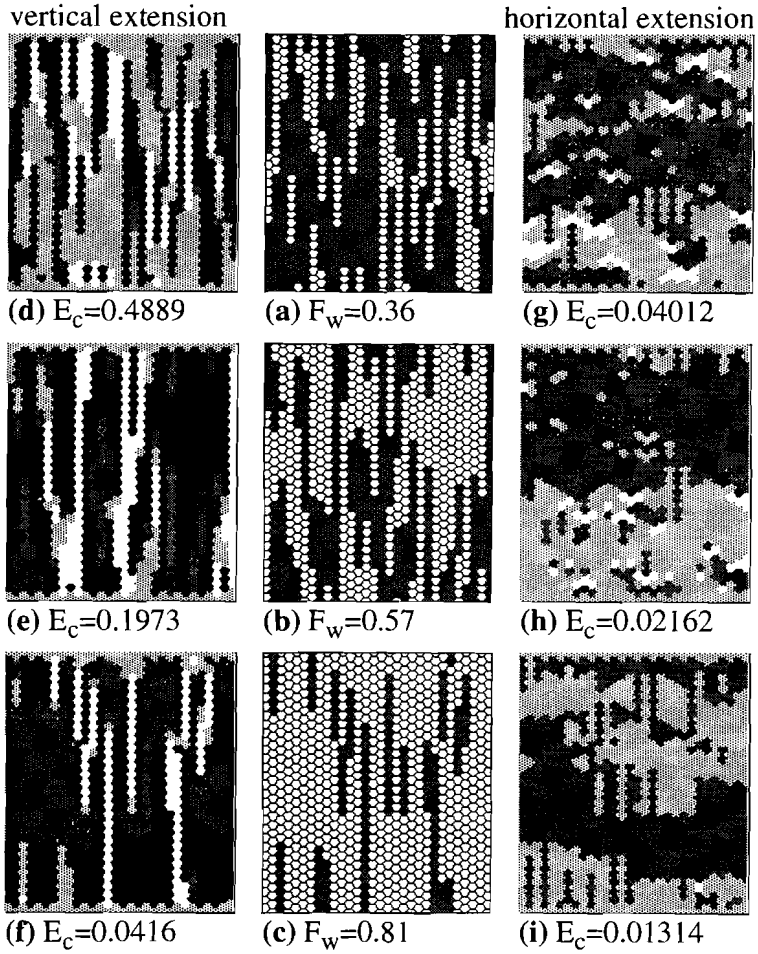

Fig. 7.7. *(a-c) Distribution of phases over the elements for an elongation of 8. (d-f) grey-scale plots of vertical stresses under vertical extension, (g-h) grey-scale plots of horizontal stresses under horizontal extension (see Fig. 7.6 for explanation of grey-scales).*

Elongations greater than one

The phase distribution for three realisations with an elongation of 8 is shown in figure 7.7. The distribution of vertical stresses under vertical extension (that is σ_{yy} for $El^{(ver)}=8$) and the horizontal stresses under horizontal extension (that is σ_{xx} for $El^{(hor)}=8$) are shown. The spread in stress values is much higher when the elongation is parallel to extension than when it is perpendicular to extension.

The distribution in (a) is such that narrow straight links of the strong phase elements exist from top to bottom. Stress is concentrated in the narrowest parts of these links in case of vertical extension. Strong phase elements are linked from the left to the right boundary of the mesh as well. Extension in the horizontal direction can be achieved by bending, rather than stretching, of the strong phase links. The stiffness for extension in a vertical direction is more than an order of magnitude higher than for horizontal extension.

In case (b) we see that continuous clusters of strong-phase elements span the mesh from top to bottom, but not from left to right. Again the stiffness for vertical extension is much higher than for horizontal extension.

Strong-phase elements do not form clusters that span the entire mesh in any direction (case c). Still there is a significant difference in stress patters between horizontal extension and vertical extension. Stress is concentrated in the strong-phase elements, but under horizontal extension there is relatively little stress partitioning (and thus high strain partitioning).

Figure 7.8 shows results for different elongation values at $R^E=10$ and 10^3. One can see that the shape of the curves is essentially the same for all elongation values, but the transition fraction is shifted towards lower F_w for horizontal elongation and towards higher F_w for vertical elongations. The range of possible stiffnesses are given by the Voigt, Taylor or constant strain bound and the Reuss, static or constant stress bound (Hill 1963; Reuss 1929; Voigt 1928). The data lie about halfway between these bounds, in a *horizontal* direction, for an isotropic distribution of the elements. For vertical elongations the data move towards the Voigt bound and for horizontal elongations the data lie more towards the Reuss bound. The data for each elongation all lie at approximately the same relative horizontal distance between the Reuss and the Voigt bounds. This relative horizontal distance at a certain normalised stiffness can be defined in terms of the fractions of the composite ($F_{w(E_c)}$) and the fractions on the bounds ($F_{Reuss(E_c)}$, $F_{Voigt(E_c)}$) at the given stiffness (Fig. 7.8.d):

$$H = \frac{F_{w(E_c)} - F_{Reuss(E_c)}}{F_{Voigt(E_c)} - F_{Reuss(E_c)}} \qquad (7.1)$$

The graphs in figure 7.8 show that H is mainly dependent on the microgeometry (elongation) and relatively independent of F_w and R^E. This implies that the composite stiffness can be estimated if one knows the relation between H and the microgeometry.

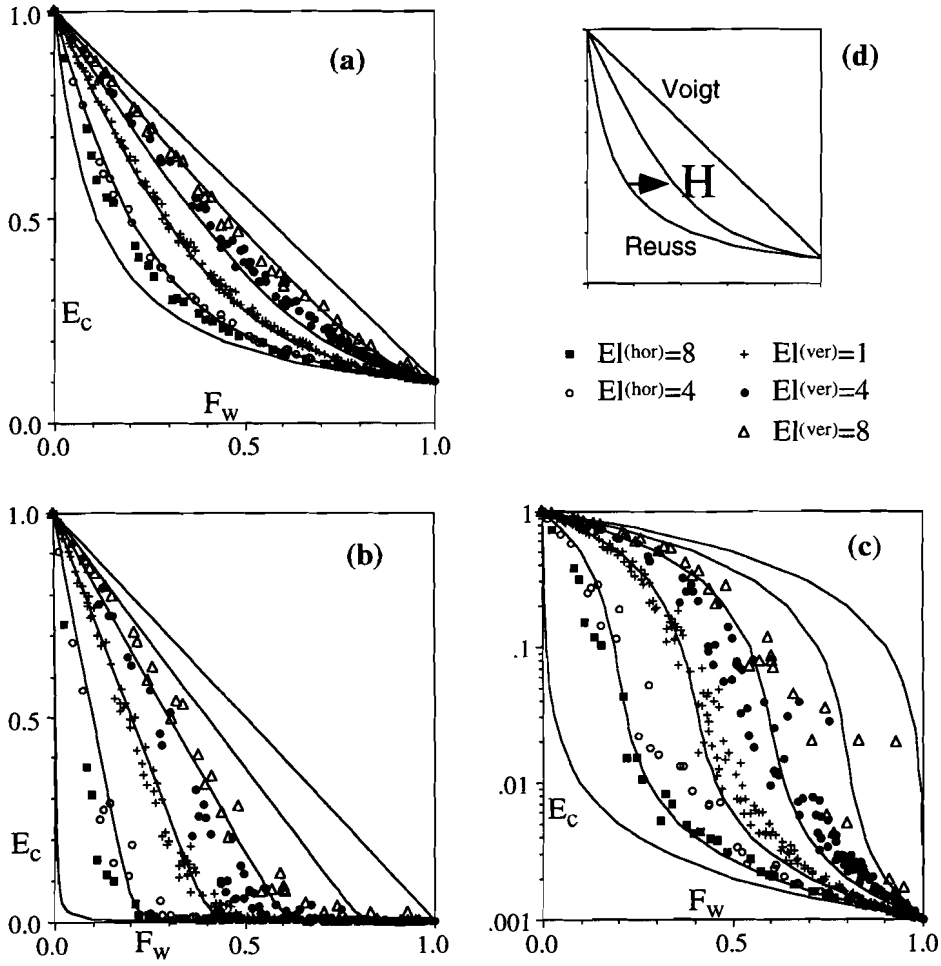

Fig. 7.8. *E_C against F_W for different elongation values. L=30. (a) E_C against F_W, $R^E=10$. (b) E_C against F_W, $R^E=10^3$. (c) log(E_C) against F_W, $R^E=10^3$. The Voigt and Reuss bounds are drawn as well as lines at constant horizontal distance H=0.2, 0.4, 0.6 and 0.8 (see inset (d)) between these bounds.*

7.2.4 Relation between Ft, H and the microgeometry

The relation between the factor H and the microgeometry will now be discussed in terms of *percolation theory*. It was shown in the previous section that the composite stiffness is strongly related to the structure of the clusters of the strong-phase elements. This structure depends on the elongation of the inclusions. With increasing F_w a fraction is reached, the transition fraction, where the strong-phase elements do not form continuous clusters in the direction of extension any more. The determination of the transition fraction is one of the subjects of percolation theory.

Percolation theory

Percolation theory basically deals with the problem of connectivity. The reader is referred to Kesten (1982) and Stauffer (1985) for general introductions to the theory and mathematical foundations. The original and mathematically simplest treatment of percolation theory was restricted to connectivity in a two dimensional lattice or mesh. Two types of connectivity or percolation are distinguished in a lattice: site- and bond percolation. The principles of percolation theory will be illustrated using site percolation in a honeycomb mesh, since that is directly applicable to the HEL-model.

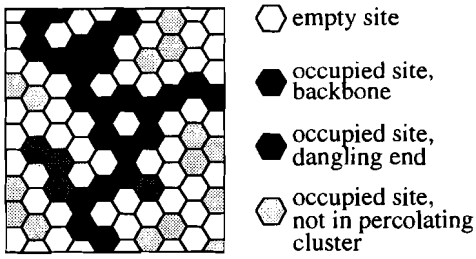

Fig. 7.9. Example of a honeycomb mesh where the fraction of occupied sites is above the percolation threshold.

Let us consider an infinite honeycomb mesh in which each element is called a "site". A site can either be "occupied" or "empty". Two neighbouring sites are connected if they are both occupied, and a group of connected sites is called a "cluster". Within a cluster one can go from any site to any other site via connected occupied sites. The smallest cluster is one occupied site. Let us now define P as the chance that a site is occupied and therefore (1-P) is the chance that a site is empty. P is equal for each site. If P is small, the occupied sites are scattered and isolated and the clusters are small. If we increase P, more sites will become occupied and thus the clusters grow and start to coalesce. At a critical fraction one cluster becomes infinite in size. This chance P at which this occurs is called the percolation threshold, P^c, and

the system is said to "percolate" if an infinite cluster exists. If $P<P^c$, the chance for the occurrence of an infinite cluster is zero, if $P>P^c$ it is one. Not all sites will be part of the percolating cluster at P just above P^c. The fraction of occupied sites that are part of the percolating cluster rapidly increases just above the percolation threshold and obviously becomes one at P=1. Figure 7.9 shows a mesh where the fraction of occupied sites is above the percolation threshold. Two other terms are illustrated in that figure: the *back-bone* of the cluster and *dangling ends*. Dangling ends are dead-end parts of the cluster. If the cluster would represent the path of a fluid through a porous medium, flow would occur through the back bone and no flow would occur in the dangling ends.

For site percolation in a honeycomb mesh $P^c=0.5$. The transition fraction in the HEL-mesh with El=1 is equivalent to P^c, and F_w or F_h are equivalent to P and (1-P) respectively.

Directed and correlated percolation

In the previous section the chance P of a site being occupied is equal for all sites and independent of the occupancy of a neighbouring. P is therefore not equivalent to Fw in the case that the elongation is greater than one. The chance that an element is of the weak phase is the same for all elements, but the chance that two neighbouring elements are of the same phase is dependent on direction. If a certain element is of one phase then the chance that the elements adjacent to it parallel to the inclusion is greater than the chance that other neighbouring elements are of the same phase, which is the same as the fraction of that phase. The distribution of the phases over the elements is correlated. Percolation of uncorrelated distributions of sites over various types of meshes has been studied extensively, but the author was unable to find anything on the subject of *correlated percolation* except the paper by Kinzel (1983), where a related problem, that of *directed percolation* is treated. Following Kinzel it will now be shown that for a distribution with elongate inclusions, the percolation threshold is dependent on direction.

Consider the mesh in figure 7.10.a. Site A at the origin is occupied and sites B and C are sites on the y and x-axis respectively. In the drawing A is connected to B and C by a continuous path along occupied sites, allowing "steps" parallel to the x and y-axis only. If B and C lie at infinity, the chance that such a path exists in only non-zero if $P>P^c$. Let us consider the same mesh, but now only steps to the left and right and upwards are allowed. In the example (Fig. 7.10.b) only B, not C, can now be reached from A. If C lies at infinity from A, then C can only be reached if P=1. This

is the case of directed percolation. It is for instance applicable to the spreading of a bush fire. The fire can spread if the trees are near enough to each other ($P>P^c$). On a windless day the fire will spread in all directions, but if there is a strong wind in one direction, the fire will spread in one direction: a tree at B will get burned eventually, but not a tree at C.

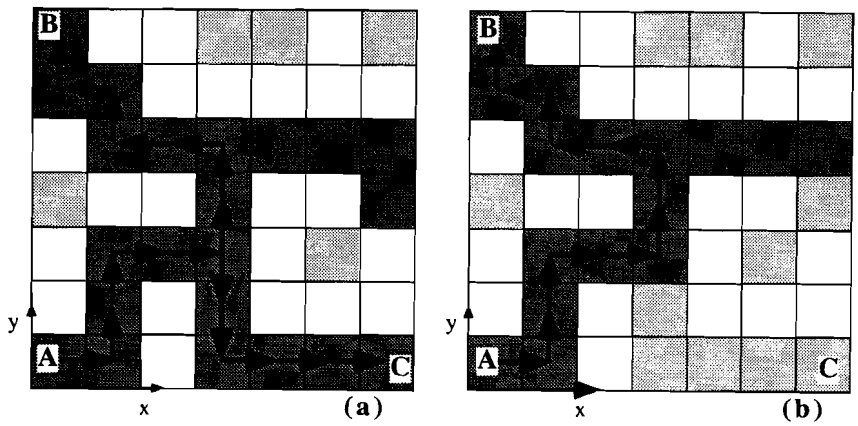

Fig. 7.10. (a) Normal percolation in a mesh of square elements. Paths via occupied sites exist from site A at the origin to sites B and C. Steps in ±x and ±y direction are permitted, no diagonal steps. (b) Same situation as (a), but now only steps in ±x and +y direction are permitted. Site C is not connected to A in this situation. The occupied sites that are connected to A are shown in dark-grey, other occupied sites as light-grey.

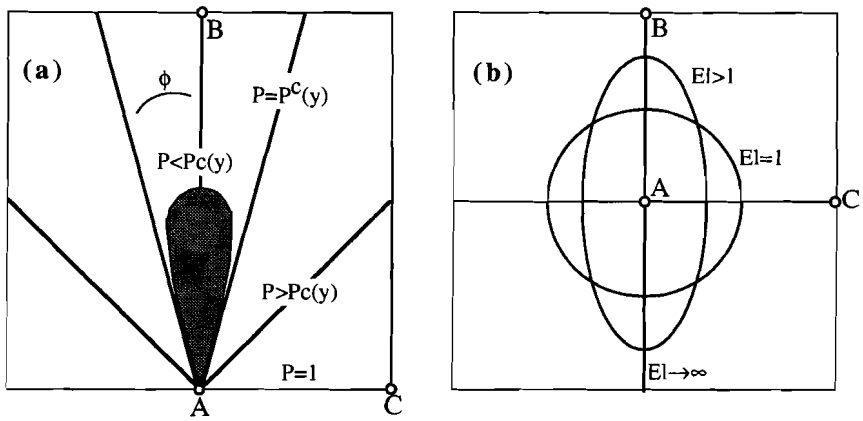

Fig. 7.11. (a) The average shape of a cluster of sites connected to the origin for different fractions (P) of occupied sites in the case of directed percolation. Below the vertical percolation threshold ($P^c(y)$), the cluster is finite in length, above it is cone shaped (after Kinzel 1983). (b) The average shape of a cluster, for $P<P^c(y)$ of sites connected to the origin for different elongations (El) of inclusions of occupied sites. The cluster shape is a circle for El=1 and a line for El→∞.

The critical fraction of occupied sites to reach site B from A is defined as the vertical percolation fraction, $P^c(y)$. The shape of the average cluster in the case of directed percolation, of which the origin A is part, at $P<P^c(y)$ is shown in figure 7.11. When $P \geq P^c(y)$, the cluster is wedge-shaped (cone-shaped in 3-D) and infinite in the vertical direction. The cone can be defined by the opening angle ϕ. Any site within the cone defined by ϕ has a non-zero chance of being connected to the origin. ϕ is related to P, as the cone widens with increasing P, until $\phi=90°$ at P=1. The position of a site can be defined in spherical coordinates as (r,ϕ). Kinzel showed that the critical fraction $P^c(\phi)$ at which the chance that a site at $(r\rightarrow\infty,\phi)$ is connected to the origin is related to ϕ as shown in figure 7.12.a.

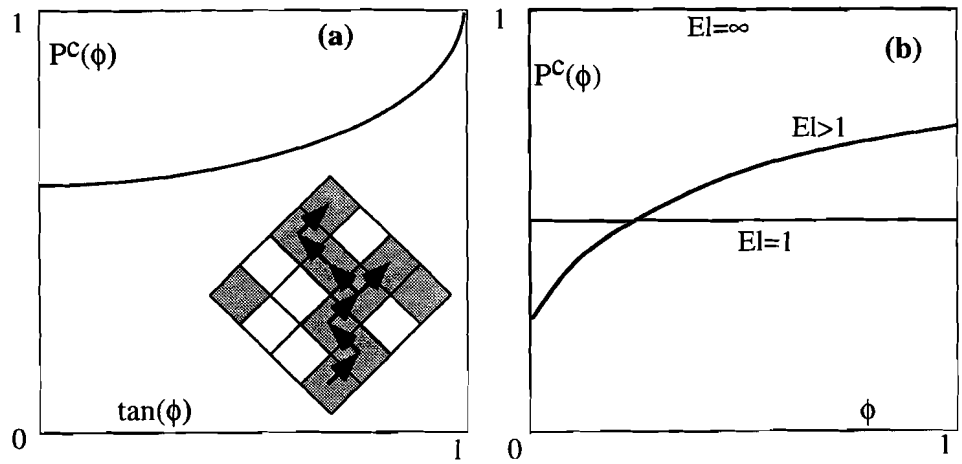

Fig. 7.12. (a) Percolation fraction, $P^c(\phi)$, as a function of direction, tan(ϕ), for directed percolation. The maximum angle of percolation is 45°, for the given type of directed percolation as drawn in inset (after Kinzel 1983). (b) Percolation fraction, $P^c(\phi)$, as a function of direction ϕ, for El=1, El>1 and El→∞ (dashed line) in the HEL-mesh with elongate inclusions. (a) and (b) only show the approximate shape of the curves.

It is now proposed, without mathematic proof, that the case of percolation in the HEL-mesh with elongate inclusions is comparable. Here the average cluster is anisotropic (elongate in the direction parallel to the inclusion elongation, taken vertical here, Fig. 7.11.b) because the chance of stepping parallel to an inclusion is greater than that of of stepping perpendicular to an inclusion. One difference with directed percolation is that, unless El=∞, $P^c(\phi=90°)<1$. The relation between $P^c(\phi)$ and ϕ then resembles the graph shown in figure 7.12.b.

The aim of the preceding section was to show that the connectivity of an anisotropic material is anisotropic as well: the percolation threshold depends on direction. This holds for the case of the HEL-mesh with aligned elongate inclusions, but also for a rock with a shape preferred orientation of the minerals. The exact relation between $P^c(\phi)$ and ϕ for the 30x30 elements HEL-mesh remains to be determined. The percolation fraction as a function of elongation was estimated with a Monte Carlo procedure, described below.

Percolation thresholds in the 30x30 HEL-mesh

For a given elongation, the mesh was filled with occupied and open sites for a set fraction of occupied sites. Then it was checked whether there existed a continuous cluster of occupied sites (elements) from top to bottom of the mesh. If no such cluster existed, the set fraction was incremented (typically 1%) and the routine was repeated, until percolation was reached. For each elongation value, the $P^{c(ver)}$ was determined one hundred times. The median and quartiles of the 100 realisations were calculated and plotted in figure 7.13. One can see that $P^{c(ver)}$ decreases with increasing $El^{(ver)}$. Since the onset of percolation of occupied sites in the vertical direction stops the percolation of empty sites in the horizontal direction, the relation between $P^{c(hor)}$ and $P^{c(ver)}$ is:

$$P^{c(hor)} = 1 - P^{c(ver)} \tag{7.2}$$

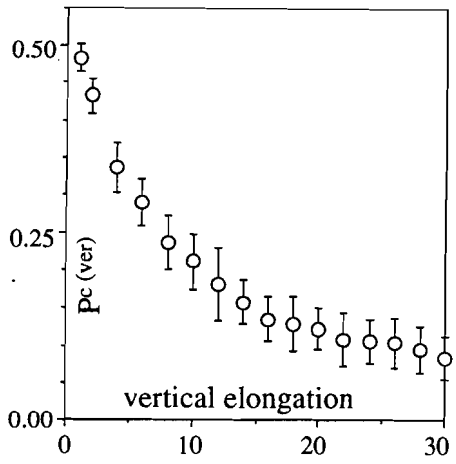

Fig. 7.13. Fraction ($P^{c(ver)}$) at which continuous clusters are achieved, in the direction parallel to elongation of inclusions, as a function of elongation, for the 30x30 HEL-mesh, determined with a Monte Carlo procedure. Dots represent the median and error bars the quartiles

Note that the distribution of the phases over the elements is symmetric, i.e. the shape of the inclusions of each phase are the same (see chapter 8). Therefore:

$$P_{c(ver)_{(weak)}} = 1 - P_{c(ver)_{(hard)}} = P_{c(hor)_{(hard)}} \quad \text{and v.v.} \qquad (7.3)$$

This means that hard phase clusters of inclusions with a vertical elongation of 8 form through-going clusters from top to bottom of the mesh when Fw<0.75. For 0.25<Fw<0.75 both phases form continuous clusters in the vertical direction and therefore none in the horizontal direction. For a horizontal elongation of 8, this is only the case for Fw<0.25. The percolation fraction in the following text is the fraction of the weak phase at which the hard phase loses its through-going clusters.

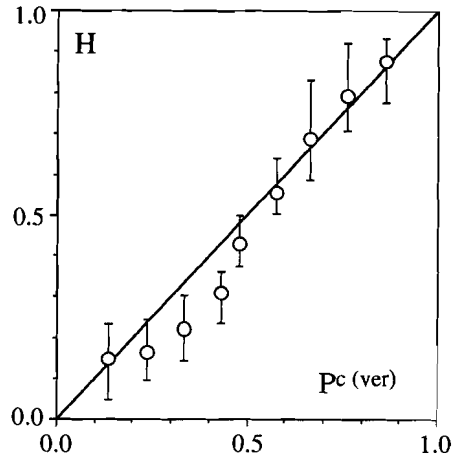

Fig. 7.14. Horizontal relative distance between the Voigt and Reuss bounds (H) versus the percolation fraction of the hard phase in the direction of extension for different elongations: ($El^{(hor)}$=2,4,8,16 and $El^{(ver)}$=1,2,4,8,16) plotted against $pc^{(ver)}$ for these elongations.

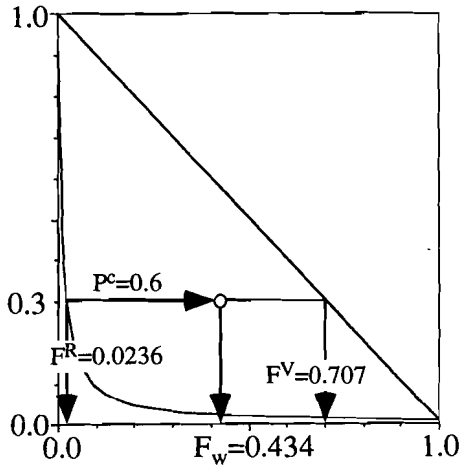

Fig. 7.15. Example of the application of equation 7.5. $R^E = 100$ and $pc^{(ver)}$=0.6. At Ec=0.3, the fraction at the Voigt boundary (FV) is 0.707 and at the Reuss boundary (FR) it is 0.0236. The fraction of weak material that has an E_C of 0.3 is 0.434.

7.2.5 The relation between microgeometry and stiffness

A plot of H against Pc(ver), both dependent on the elongation, is shown in figure 7.14. One can see that H and Pc(ver) are closely related: $H \approx P^{c(ver)}$ at $P^{c(ver)}>0.5$. For $0.2<P^{c(ver)}<0.5$ H is smaller than $P^{c(ver)}$. Neglecting this difference, we can rewrite equation 7.1 to:

$$P^{c(ver)} \approx H = \frac{F_{w(E_c)} - F_{Reuss(E_c)}}{F_{Voigt(E_c)} - F_{Reuss(E_c)}} \tag{7.4}$$

$$\Leftrightarrow \quad F_{w(E_c)} = P^{c(ver)} \cdot (F_{Voigt(E_c)} - F_{Reuss(E_c)}) + F_{Reuss(E_c)} \tag{7.5}$$

The stiffness of the composite can now be *estimated* with this simple equation for any geometry, once its connectivity properties are known, since Voigt and Reuss bounds can be determined for any set of properties of the constituent phases of a composite. For example, what is F_w at which $E_c=0.3$, for $R^E=100$ and a distribution where $P^{c(ver)}=0.6$? The fractions at the bounds are (see chapter 8 and Fig. 7.15)

$$F_{Voigt(0.3)} = \frac{0.3 - 1}{0.01 - 1} = 0.707$$

$$F_{Reuss(0.3)} = \frac{1/0.3 - 1}{100 - 1} = 0.0236$$

The resulting fractions at the bounds can be inserted in equation (7.5), giving:

$F_{w(0.3)} = 0.6 \cdot (0.707-0.0236) + 0.0236 = 0.434$.

To determine E_c for a particular composition, the above method must be inverted. When $P^{c(ver)}<0.5$ this method will overestimate E_c, since $H<P^{c(ver)}$. The reason for the difference in behaviour on either side of $P^{c(ver)}=0.5$, probably lies in the different structure of the through-going clusters (see figure 7.7). Even when the hard phase forms through-going clusters perpendicular to the elongation direction, these clusters are relatively weak, since deformation can take place by bending and rotation of the clusters instead of stretching of clusters. The method produces an estimate, not an accurate determination of E_c for a particular geometry. The advantage is that it is a simple method which seemins applicable to any geometry for which a transition fraction can be determined. At the moment this relation between microgeometry and composite properties has only been established for the particular case of the HEL-model with elongate inclusions. Because the parameter H is the relative horizontal distance between the bounds, the method will be referred to as *Horizontal Distance Method*, abbreviated to HDE. The HDE will be further discussed and compared with other models in chapter 8. The application to composites with other constitutive laws will also be discussed there.

7.3 Modelling with BASIL

BASIL is a finite element program, similar to HEL, to model power-law creep materials. Because of the non-linear properties that can be assigned to the elements, each test takes considerably more time to run and only a limited series of tests was done to:

1) Compare results for linear elasticity with linear viscosity (= power-law creep with a stress exponent of 1)
2) Explore the effects of different stress exponents

7.3.1 The program

BASIL is an implementation originally used to model deformation around a fault embedded in a non-linear ductile medium (Barr & Houseman 1992a&b). It was modified by T.D. Barr to simulate the deformation of a twophase composite of power-law creep materials with equal stress exponents. The mesh is composed of 16x16 or 32x32 squares, each composed of 2 elements (Fig. 7.16). Each triangular elements has six nodes (3 vertex nodes and 3 mid-point nodes). The phases are distributed as inclusions of 2x2 squares (16x16 squares mesh) or 4x4 squares (32x32 mesh). The material is assumed to be incompressible with a constitutive law defined by equations (A.8&9) (Appendix A). A plane-strain deformation was applied, with a constant normal velocity and zero shear stress on the top and bottom boundary, and zero stress on the side boundaries.

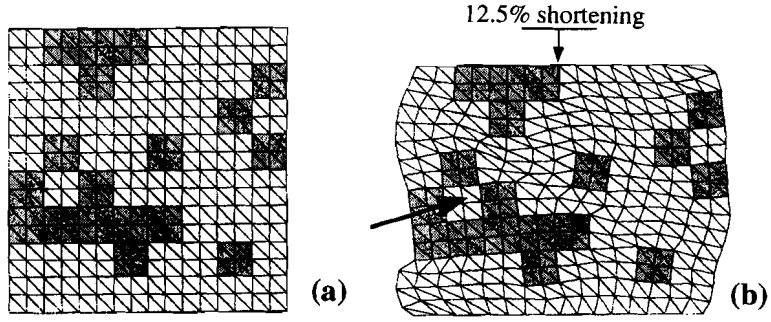

Fig. 7.16. (a) Example of the BASIL-mesh, showing the distribution of elements (lines) and phases (white=soft, grey=hard). The applied deformation is vertical shortening, as shown in (b), where the actual displacements of the nodes are exaggerated to a shortening of 12.5%. Note that the soft inclusion (arrow) surrounded by hard inclusions is little deformed, although the hard inclusions only touch at the corners.

The stress needed for one deformation increment (2.5% shortening) was then calculated and normalised to the stress needed to deform the hard phase by the same amount. Arbitrary viscosities are chosen to begin with and the velocity and pressure at each node are calculated, by setting up and solving the matrix of force balance equations. The viscosities are then adjusted and the calculation repeated in an iterative routine, until the stress - strain rate relation in each element is according to the constitutive law assigned to that element.

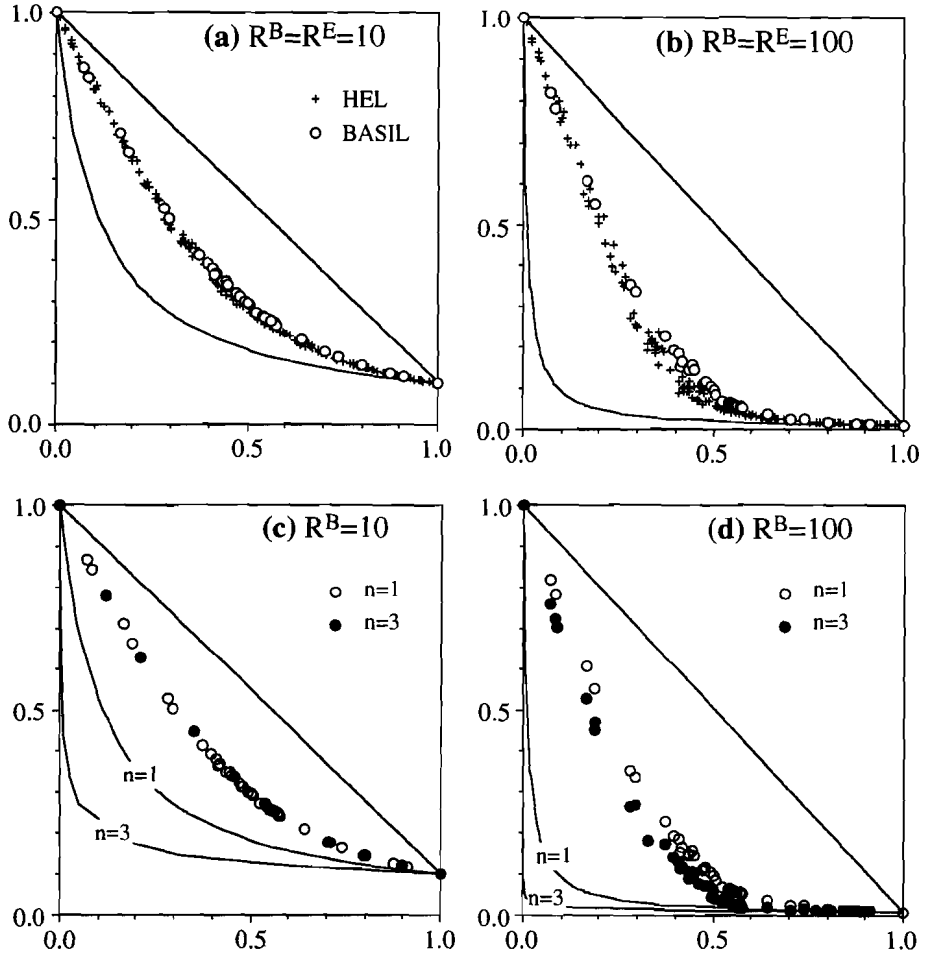

Fig. 7.17. (a) Normalised strengths for $R^B=10$ & n=1 (BASIL), compared with the normalised stiffnesses for $R^E=10$ (HEL), plotted against fraction of the soft phase. (b) The same as (a) for $R^B=R^E=100$. Normalised strength at RB=10 (c) and RB=100 (d) plotted against the fraction of the soft phase. Voigt and Reuss boundaries are added in all plots.

7.3.2 Results

Linear viscosity

Three series of tests were done with linear viscous material properties assigned to each element. Instead of setting the Young's modulus ratio (R^E), now a ratio of the pre-exponential coefficient (B in equation A.8, appendix A) had to be set, which was normalised to 1 for the hard phase. The ratio of these coefficients, R^B, or the ratio of viscosities, was set to 10 and 100 (Fig. 7.17.a&b). One can see that the results for $R^B=R^E$ are approximately similar. At intermediate fraction BASIL produces slightly higher values of relative strength.

Power law creep

Two series were done with $R^B=10$ and 100 and stress exponents of 3 for both components instead of 1 (Fig. 7.17c&d). At RB=10, there is no noticeable difference, but at $R^B=100$, the increase of n from 1 to 3 causes a decrease in strength of the composite. The effect on strength is minor compared to the effect on the Reuss boundary (The Voigt boundary is independent of n, and only depends on R^B). This means that the values of the relative horizontal distance, H, between the boundaries is dependent on the stress exponent. In figure 7.18 the values of H are plotted for n=1 and n=3. H shows a linear dependency on Fw, up to Fw≈0.7.

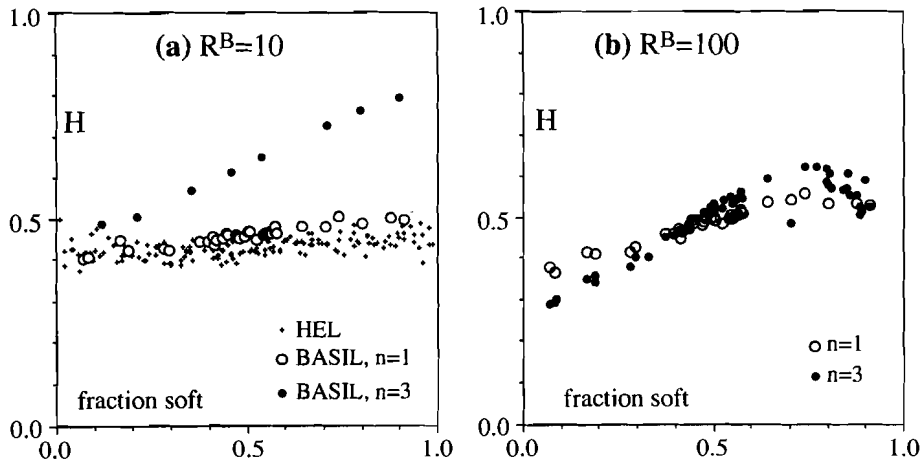

Fig. 7.18. H plotted against fraction of the soft phase for (a) $R^B=R^E=10$ and (b) $R^B=100$.

Resolution and the square mesh

The phases are distributed as squares that join at their corners. The contact area at these corners is infinitely small, but the strength is not. This situation is unrealistic and it is better to use a mesh where the inclusions only join along lines, as in the HEL-mesh (Cox *et al.* 1993). The possible error that is introduced by the use of square inclusions was not determined, as no other routine to create meshes was available. It is likely that the effect depends on the fractions of the phases, since only at intermediate fractions will there be relatively many of these corner-to-corner contacts.

Problems with resolution were also encountered when modelling with BASIL, especially for R^B=100 and n=3. At Fw>0.7 the calculated strengths were relatively low, sometimes even lower than the Reuss bound. The calculated strength fell in between the Voigt and Reuss bounds when the same distribution of the elements was used with on a 32x32 squares mesh (instead of 16x16). This clearly indicates that lack of resolution is the cause of the deviating strengths. The problem of resolution may be related/aggravated by the use of square elements.

7.3.3 Discussion

The modelling work with BASIL was a first attempt to determine the strength-fraction relation for composites of power-law creep materials. It was observed that the horizontal distance between the Voigt and Reuss bounds (H in equation 7.5) was not constant but linearly dependent on the composition, especially when the stress exponent was set to 3 and at R^B=100. At these conditions the data are however the least reliable, due to insufficient resolution and the fact that the inclusions were squares. It is therefore still uncertain whether the dependence of H on Fw is (i) caused by the fact that the components are power-law creep materials instead of linear elastic materials or (ii) an artefact caused by insufficient resolution and the use of square inclusions. At low R^B and n=1, where these artefacts can be expected to have the least influence, the results of HEL and BASIL are practically the same. This is an indication that the results from the modelling work with HEL are applicable to linear viscous behaviour as well. Whether the results are also applicable to power-law creep materials remains uncertain as yet.

Now the problems with the model are defined, these can be solved and then BASIL may provide a valuable tool to investigate the properties of composites of power-law creep materials. It is the intention of the author and T.D. Barr to do so in the future.

Chapter 8

Discussion and conclusions

One of the main conclusions to be drawn from the results of the experiments and modelling described in the previous chapters is that the connectivity of the phases in a composite is important for the properties of a composite. In chapter 7 a method was proposed to estimate the composite stiffness of a composite with linear elastic components when the stiffnesses of these components and the transition fraction (F^t) for the microgeometry are known. The transition fraction is the fraction at which the phases change their role as matrix phase and inclusion phase. The transition fraction is a function of the percolation fractions of the phases, that depend on the microgeometry of the composite, i.e. on the geometry and distribution of the phase regions. The method is referred to as the *Horizontal Distance Estimate*, abbreviated to HDE. In the follow section the HDE will be further discussed and compared with existing models (§ 1.2). The experimental results will then be compared with the existing models and the HDE.

8.1 Horizontal distance estimate

Equation (7.4) was derived for the case of a composite of linear elastic materials. It will now be investigated whether this equation has a more general validity and can be used for other types of constitutive behaviour, such as linear or power-law creep. For this purpose equation (7.4) can be rewritten to:

$$F^t \approx H = \frac{F_w - F^R}{F^V - F^R} \tag{8.1}$$

At a given strain or strain rate, F^V and F^R are the fractions at the Voigt and Reuss bounds that would give a given stress. F^V and F^R in can be found with equations (1.2&6)for a given constitutive equation of the components. For instance for a linear viscous material ($\sigma=\eta\cdot\dot{\varepsilon}$) :

$$F^V = \frac{\sigma/\dot{\varepsilon} - \eta_w}{\eta_w - \eta_h} \tag{8.2}$$

$$F^R = \frac{\dot{\varepsilon}/\sigma - 1/\eta_h}{1/\eta_w - 1/\eta_h} \tag{8.3}$$

(subscripts h and w for hard and soft phase respectively)

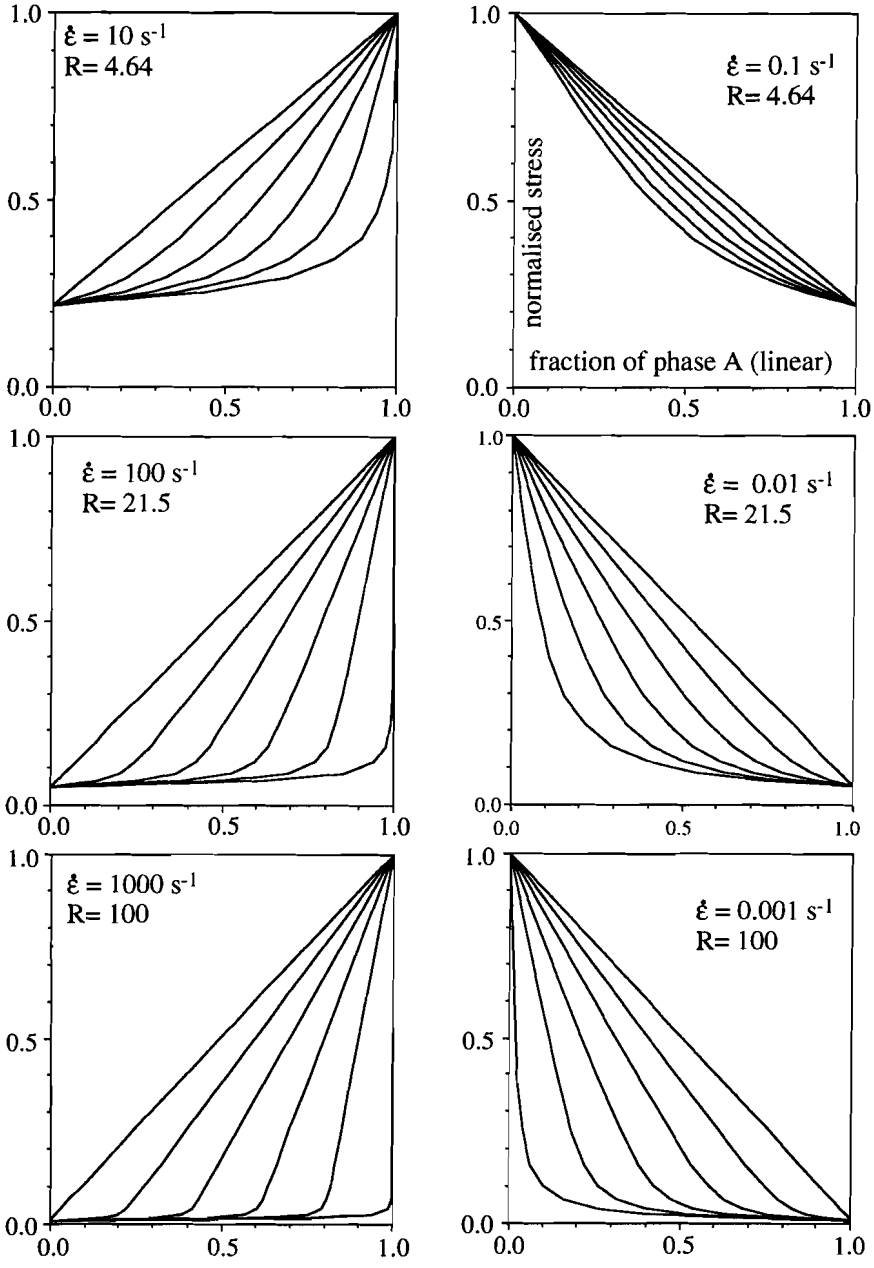

Fig. 8.1. Constant-H lines (H=0.0, 0.2, 0.4, 0.6, 0.8 and 1.0) in normalised flow stress against fraction graphs, for mixtures of a linear viscous material (phase A) and a power-law creep material with stress exponent of 3 (phase B). The equiviscous point is at a shear strain rate of one. The graphs are drawn for 6 different strain rates and the flow stress ratios (R) at these strain rates is given.

If the relation between stress and strain rate is a power-law relation one has to solve equations (1.2) and (1.3) iteratively (e.g. Tullis *et al.* 1991).The iteration routine is however simple and converges rapidly. Figure 8.1 gives an example of HDE estimate of the normalised stresses as a function of fraction for power law creep materials for a two phase composite. The flow laws are defined as $\dot{\varepsilon}=\sigma$ for phase A and $\dot{\varepsilon}=\sigma^3$ for phase B. Note the difference in shape of the curves at low stress contrasts for phase A as hard phase ($\dot{\varepsilon}>1$) or phase B as hard phase ($\dot{\varepsilon}<1$), because the Reuss bound is most strongly determined by the stress exponent of the soft phase.

One stiffness or strength parameter does not suffice in case of an anisotropic microstructure. Deformation in such a composite will then depend on the deformation geometry (axisymmetric deformation, simple shear, etc.) and its orientation with respect to the orientation of the anisotropy. The HDE is only intended as a first estimate and it has not been developed here to the extent that a stiffness or strength tensor can be determined. How anisotropy may be incorporated will be shown in the examples discussed later in this chapter.

One reason why equation 8.1 may be valid in general can be seen if we consider a composite of materials with a high contrast in strength between the phases (zero strength of soft phase). The hard phase forms a connected network at low fractions of the soft phase. The strength of the composite decreases with increasing fraction of the soft phase until it reaches zero at the transition fraction F^t. F^t must be equal to H at this transition fraction, as will be shown below. At other fractions however F^t may be different than H. If however the strength of the composite decreases linearly with the fraction of the weak phase, then $H=F^t$. A linear decrease in stiffness was observed with the HEL-simulations, and also in the SCT calculations on elastic moduli of composites with high contrasts between the phases (Wu 1966). If the HDE is applicable to high contrast cases, then it should be in line with observations and theory on suspensions with rigid particles.

2 and 3 dimensions

In 2 dimensions, the percolation of one phase in one direction excludes the percolation of the other phase in the perpendicular direction. If percolation is anisotropic, more phases can percolate in one direction. The situation is different in 3 dimensions. Both phases in a 2-phase composite can percolate in all directions at the same time (for instance a porous sandstone, through which water can flow in all directions). The important percolation fraction now is the percolation fraction of the hard phase in the direction under consideration. For instance in simple shear, this will

be the direction perpendicular to the flow plane. The soft phase can only accommodate most deformation and dominate the behaviour of the composite if the soft phase is continuous in a plane (not necessarily a flat plane) parallel to the flow plane.

HDE and suspensions with rigid inclusions

The transition fraction is exactly the limit of the validity of equations of type of equation (1.17). The advantage of equation (8.1) is that it is applicable on either side of this fraction. Let us now see how well equation (8.1) for materials with high viscosity ratio compares with these equations, especially the K-D equation (1.13). For a suspension of rigid particles in a Newtonian viscous fluid, the Voigt and Reuss bounds can be defined as follows:

Voigt: $F^V=0$ (8.4.a)

Reuss: $F^R=1-\eta_0/\eta$ (8.4.b)

Equation (8.1) can be rewritten to $F_h=HF^R+(1-H)F^V$ (8.5)

Combining (8.4) and (8.5) then gives

$F_h=H(1-\eta_0/\eta) \Leftrightarrow \eta=\eta_0(1-F_h/H)^{-1}$ (8.6),

which is quite similar to the K-D equation if $H=F^m$ and $[\eta]/F^m=1$. In chapter 7 it was already observed that $H\approx F^t$ and one can see that F^t is in fact similar to the maximum packing fraction. Note that the composition is here expressed in the fraction of the hard phase, not of the soft phase as in chapter 7. To explain why the power exponent in the K-D equation is -1 and a value of usually 1-3 in the K-D equation, we have to take a closer look at the intrinsic viscosity $[\eta]$. Both F^m and $[\eta]$ are empirical factors that are found to be mainly dependent on the shape of particles, but also on shape preferred orientation and spatial distribution. For a dilute suspension of spheres the maximum packing fraction is about 0.4 and the intrinsic viscosity about 2.5, and hence $[\eta]/F^m=1$. For a larger range of fractions, $[\eta]=3.28$ and $F^m=0.61$ are found to give a best fit of the K-D equation to experimental data (listed in Barnes *et al.* 1989). It is assumed that F^m does not change with fraction. However, at small fractions of suspended particles, the particles have a Poisson random distribution, for which the maximum packing fraction is about 0.4 for spheres. At higher fractions, the particles are forced into an equidistant distribution, for which F^m is higher.

One can take F^m as a function of fraction and use equation 8.6 to determine F^m. Figure 8.2 shows the values of F^m as a function of F_h to fit the K-D equation estimate for different cases listed in Barnes *et al.* (1989). For spheres, one then finds that F^m increases from about 0.31 at $F_h=0$ to 0.61 at $F_h=0.61$. Equation 8.6 seems to

be physically more realistic than the K-D equation, since it allows for a maximum packing fraction that varies with fraction, whereas the K-D equation does not, but compensates for this by adding an empirical coefficient - the intrinsic viscosity - to the exponent.

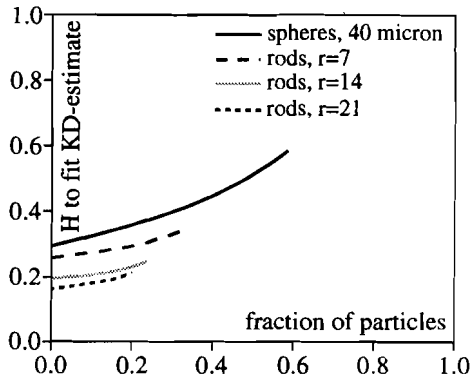

Fig. 8.2. H as a function of fraction of rigid particles in a suspension, to fit equation (8.6) to the K-D equation. 4 cases are given: 40 μm spheres ($[\eta]$=3.28, F^m=0.61), glass fibres with axial ratio (r) of 7 ($[\eta]$=3.8, F^m=0.374), 14 ($[\eta]$=5.03, F^m=0.26) and 21 ($[\eta]$=6.0, F^m=0.233) (Giesekus 1983, listed in Barnes et al. (1989, page 125).

Yoon & Chen (1990) proposed a model, similar to the K-D equation, for composites of rigid inclusions in a power-law creep matrix. To compare the HDE with the model of Yoon & Chen, equations (8.1) and (1.21&23) are now rewritten to give σ_c/σ_0, i.e. the composite stress at a given strain rate, divided by the stress for the pure power-law (with stress exponent n) matrix at that strain rate:

HDE: $\sigma_c/\sigma_0 = (1-F_h/H)^{-1/n}$ (8.7)

Yoon & Chen: $\sigma_c/\sigma_0 = (1-F_h)^{-(2/n+1/2)}$ (8.8)

Equation (8.8) is proposed by Yoon & Chen for spherical inclusions. Both equations are of the same form, but the exponents differ and the HDE has the factor H, comparable to the maximum packing fraction, which causes σ_c/σ_0 to become infinite when the fraction of rigid inclusions reaches the transition fraction. Both models (HDE with H=0.4 and 0.6) are compared in figure 8.3. The Yoon & Chen model and the HDE with H=0.4 give approximately the same results at very low fractions of rigid inclusions. The HDE with H=0.6 gives a better match with the Yoon & Chen model at higher F_h. σ_c/σ_0 reaches infinity at F_h=1 according to the Yoon & Chen model. This is physically not realistic, since the rigid spheres will form a load bearing framework at a lower F_h, about 0.6-0.7, which is taken into account in the HDE. For a dilute suspension H should be lower than for a more concentrated suspension, as discussed earlier. The HDE therefore matches the Yoon & Chen model at low to intermediate fractions of rigid inclusions. An improvement is that the effect of a maximum packing fraction of the inclusions is incorporated.

Equation (8.6) and (8.7) are only valid if the hard phase is effectively rigid compared to the soft phase. If both phases contribute significantly to deformation one has to insert the properties of both phases into equation (8.1). Another difference is that for suspensions a single value, the maximum packing fraction suffices to take into account the effect of internal geometry. Viscosities of suspensions are determined at high finite shear strains and over a large range of finite shear strain (in e.g. a viscometer). For geological purposes one is also concerned with the zero to low strain properties of composites and then one has to use the directionally dependent F^t with respect to the stress orientation.

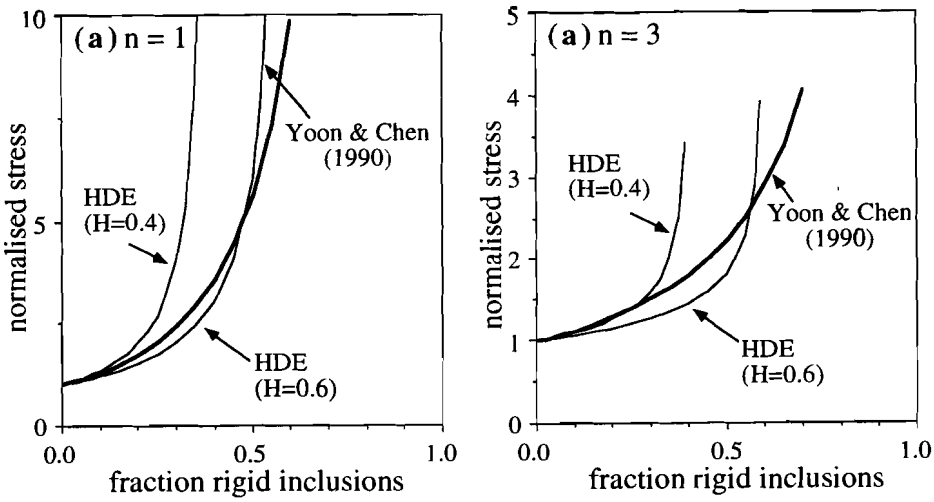

Fig 8.3. Comparison of the HDE and the model proposed by Yoon & Chen (1990) for rigid spheres in a power-law creep matrix. The HDE estimates were made using H=0.4 and H=0.6. The stress exponent of the matrix is 1 (a) and 3 (b).

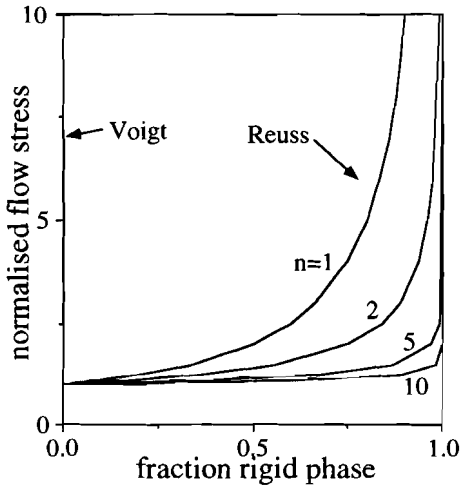

Fig. 8.4. The Reuss bound for a composite of a rigid and a power-law creep phase, shown in the plot for the normalised composite stress verus the fraction of the rigid phase.

Implications for the relation between geometry and properties

The transition fraction, and thus the parameter H, depends on microgeometry. It chapter 7 it was also observed that F^t depends on direction if the microgeometry is not isotropic. Wu (1966) and Lee & Mear (1991b) calculated the stiffnesses of composites (metals) with randomly oriented rigid spheroidal inclusions. In general the HDE will predict a higher stiffness for non-spherical inclusions, as do Wu and Lee & Mear. This is because one can fit less randomly oriented non-spherical spheroidal inclusions in a certain volume than spherical ones. The transition fraction of such inclusions will therefore shift to lower fractions of the inclusions. The exact transition fraction will depend on the axial ratio, shape (prolate - oblate) and distribution. Lee & Mear also predict that the stiffness increase is stronger in power-law creep materials than in linear creep materials. This is also predicted by the HDE, because the non-linearity causes a shift in the Reuss bound only and not in the Voigt bound (Fig. 8.4).

Lee & Mear (1991a) also treated the case of transverse isotropic distribution of the rigid spheroidal inclusions. All symmetry axes (long for prolate or short for oblate inclusions) of the inclusions are aligned parallel to each other in this particular type of anisotropy (as in chapter 7). Composites with non-spherical inclusions are predicted to be stronger than those with equivalent fractions of spherical inclusions in the case of axisymmetric loading, parallel to the symmetry axes of the inclusions. The results of the HEL-modelling are different. There it was observed that for axisymmetric extension perpendicular to the inclusions the stiffness is relatively low, whereas when the extension was parallel to the inclusions the stiffness is relatively high, in accordance with Lee & Mear.

The difference in boundary constraints between the model of Lee & Mear and HEL may be the reason for the difference between the results. Displacement constraints are applied on two opposite boundaries of the HEL-mesh, and the other two boundaries are free. The model of Lee & Mear uses a homogeneous macroscopic stress and strain (rate) field as a constraint (Fig. 8.5). HEL gives the same resulting stiffnesses for both horizontal and vertical elongations if displacements are prescribed to all four boundaries of the mesh.

In case of simple shear deformation with the vorticity vector parallel to the symmetry axes (in-plane shear) there is a major difference between the effect of prolate and oblate objects. Prolate objects give a slight decrease in strength compared with spherical objects, but oblate objects have a large strengthening effect. Both oblate and prolate inclusions make the composite weaker than do spherical inclusions

in case of simple shear deformation with the symmetry axes of the inclusions perpendicular to the flow plane (out -of-plane shear). The effect is most pronounced in the case of oblate inclusions.

This can also be explained in terms of the HDE. For instance for oblate inclusions (disks) lying parallel to the flow plane, the fraction of the hard phase at which it looses its connectivity in the shortening direction is high. For the soft phase this means that at relatively low fractions it already forms continuous layers that can accommodate most of the deformation and the composite behaviour will be near the Reuss bound.

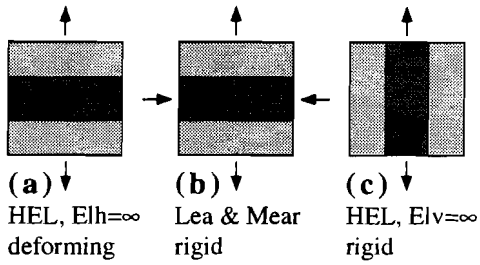

Fig. 8.5. Schematic drawing showing the effect of different types of boundary constraints in the HEL model and the Lee & Mear model for a layered composite. Dark layer is rigid, grey layer is plastic. Arrows indicate the applied extension on the boundaries.

Examples of applications to geology

The HDE only treats the effect of microgeometry on the composite properties and is applicable when the properties of the constituent phases are known. No attempt is made in this study to apply the model to real rocks. For each case this would require a careful examination of the available (experimental) data on microstructure, deformation mechanisms, temperature, pressure effects, influence of fluids, etc., which was beyond the scope of this study. However, a few examples are given below to illustrate how the HDE could be applied.

Figure 8.6 gives three examples of how the HDE could be applied to deforming rocks. The examples are given for a linear composite with a viscosity ratio of 100. The microstructure in figure 8.6.a and 8.6.b is such that the hard phase is connected in the vertical direction if $F_w<0.45$. After a deformation increment, the hard phase spheres may have deformed to ellipsoids with a different distribution. The hard phase will only form load-bearing clusters if $F_w<0.25$ in the example, since connectivity in the vertical direction is reduced. In the stress-F_w plot (Fig. 8.6.d) this means that the composite will soften from a value $F^t=H=0.45$ above the lower (Reuss) bound to a value $F^t=H=0.25$ of the distance between the lower and upper (Voigt) bounds. As F_w remains constant, this implies a decrease in composite flow stress at a constant strain rate. For $F_w=0.4$ (Fig. 8.6.a) this change in microgeometry causes an

estimated 2.5 times decrease in flow stress. For F_w=0.7 (Fig. 8.6.b) the estimated decrease is only by a factor 1.2. In the first case there is a loss of connectivity of the hard phase, in the second case the hard phase was not connected from the beginning of deformation, and the softening effect of deformation is minor compared with the first case. With the proposed method one can outline in which cases (composition, microgeometry) one can expect significant changes in strength of a composite due to changes in microstructure.

Changes in composition may also cause a significant drop in strength of a material in certain cases. Such a change in composition is sometimes observed in for instance retrograde shear zones in feldspar-quartz-mica host rocks where the dissolution or decomposition of the relatively hard feldspar has occurred (Dipple & Ferry 1992; O'Hara 1990). In the two cases discussed by O'Hara, the host rocks had an original feldspar fraction of 0.4-0.5, whereas the shear zones had fractions of about 0.15-0.25. An equivalent situation is shown in figure 8.6.c for an increase in F_w from 0.4 to 0.6 and the estimate decrease in viscosity is of a factor four in that case. At other starting compositions of the host rock the effect of the change of composition may be different. The fact that metasomatism and deformation are both localised may indicate that the metasomatism played a role in the localisation.

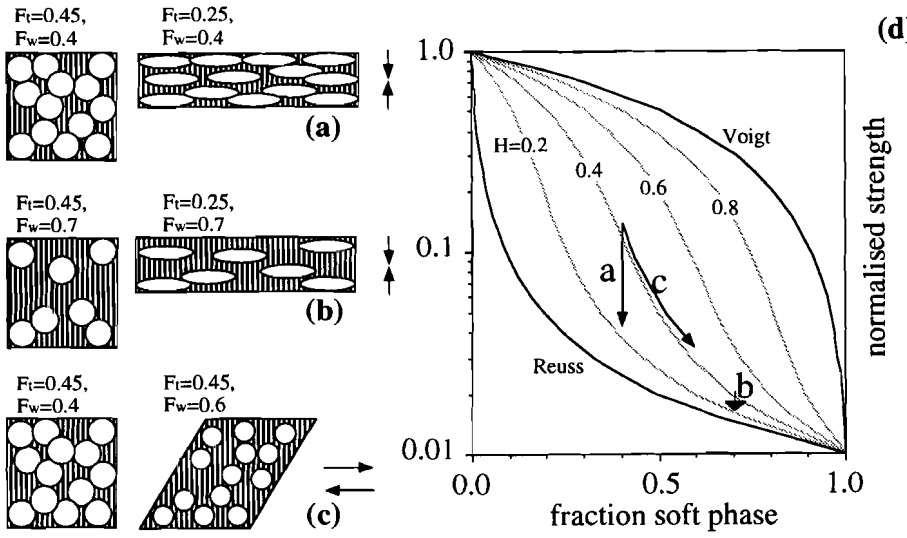

Fig. 8.6. (a-c) Three examples of a possible change in microgeometry before (left) and after deformation (right). Hard phase is shown in white, soft phase is grey. (d) the estimated change in flow properties if both phases are linear viscous materials and the viscosity contrast is 100. (a) F^t changes from 0.45 to 0.25, F^w=0.4, (b) the same, with F^w=0.7 and (c) constant F^t=0.45, but change in composition due to dissolution or decomposition of the hard phase.

8.2 The experiments with OCP and camphor

In chapter 5 it was argued that OCP dominated the behaviour of the OCP+camphor aggregates, because OCP formed a connected matrix even at fractions of OCP as low as 0.2. In the HDE model this would mean that H is small, 0.2 at the most. Figure 8.7 shows the HDE predictions for H=0.2. One notes that the HDE then predicts that the composites follow a power-law relation with a stress exponent equal to that of pure OCP. In fact the stress exponent is not constant, but in the stress-strain rate window shown in figure 8.7, the lines for the composites appear as virtually straight. However the stresses are lower than determined experimentally. As discussed in chapter 5 this may be due to the strain softening behaviour of camphor. The experiments with camphor and OCP show that even a simple model as the HDE becomes difficult to apply on materials with properties that involve work-softening/hardening, tendency of shear localisation, etc..

Simple shear deformation of camphor inclusions in OCP (chapter 6) leads to the development of a foliation. In terms of connectivity this foliation causes an increase in connectivity of both phases in the direction parallel to flow, and a decrease in connectivity perpendicular to the flow plane. The starting material resembled the materials for the axisymmetric tests and we can therefore assume that, in the undeformed state, camphor would form a load bearing framework at fractions above 0.6-0.8 ($=F_{OCP}<0.2$-0.4). The composite flow properties of the mixture will then be near the Reuss bound ($H\approx$0.2-0.4). The foliation development will reduce the value of H even more and thus the shear strain rate increases. Since H is already low, a further reduction of H will not cause a very high increase in shear strain rate.

A more pronounced strain softening effect is expected for OCP inclusions in camphor. The fraction of OCP is smaller than H in that case. Deformation will reduce H and at a certain stage the fraction of OCP is becomes equal and then higher than H. The beginning of this process was observed in experiment RS10. The experiment was however not continued to a very high strain to see whether the expected softening would occur.

Within the experimental range of stresses, the difference in strain rate at a constant stress between pure camphor and OCP was 2 to 3 orders of magnitude. Camphor was found to be effectively rigid in the shortening experiments with camphor and OCP. This suggests that the threshold for the use of matrix-rigid inclusion models (Yoon & Chen, HDE) is at the most a difference in strain rate (at a given stress) of about 2 orders of magnitude. This is of course only valid when the soft phase forms the matrix. One then only needs to know the properties of the soft phase, its fraction and the microgeometry to make an estimate of the composite properties.

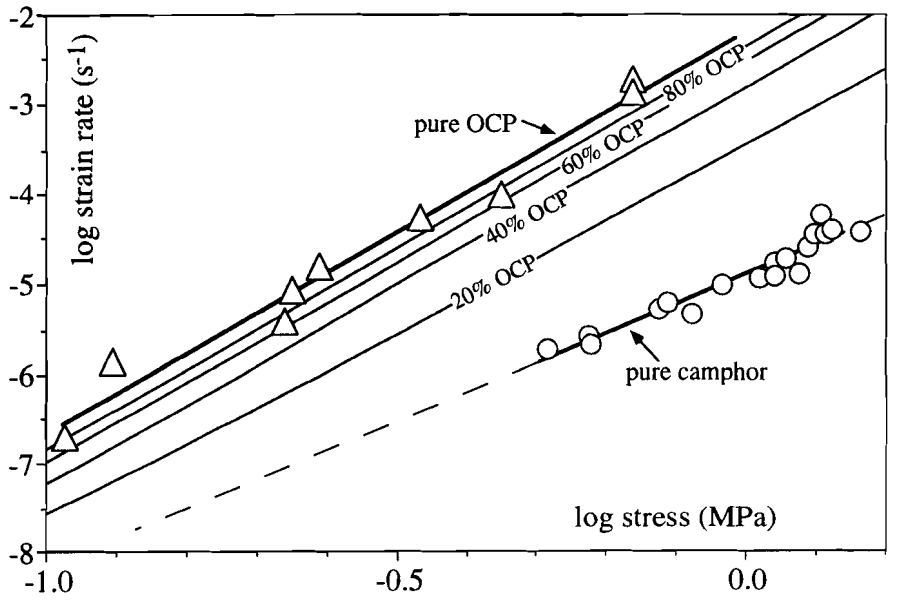

Fig. 8.7. HDE estimates of the relation between log stress and log strain rate for mixtures of OCP and camphor (fractions of OCP 0.2, 0.4, 0.6 and 0.8) together with the data from stepping tests and the pure phase flow laws determined form these data (heavy lines). The HDE estimate was made with H=0.2.

8.3 Conclusions

Rock analogues have proven to be suitable materials to model geologically relevant systems, with relatively simple equipment. The new ring shear apparatus presented in chapter 6 is a valuable addition to the available methods to study deformation with rock analogues.

Deformation experiments with the two-phase system OCP+camphor and numerical modelling showed that the connectivity of the phases is an important parameter for the flow properties of a composite. Mixtures of OCP and camphor were power-law creep materials with stress exponents approximately the same as of the soft phase OCP, because OCP formed the matrix phase even at small fraction of OCP. Camphor was effectively rigid in the shortening experiments. Composites with a similar contrast in flow properties between the components can be described as matrix-rigid inclusion systems.

A method is proposed to estimate the rheological properties of a composite. The method uses the fraction at which the phases change their role as connected phase and inclusion phase to determine the relative position of the composite properties between the constant stress and constant strain rate bounds.

The proposed method can be used to estimate the strength of polyphase materials with any microgeometry. It can therefore also be used to estimate the changes in strength that may occur due to strain induced changes in microstructure (foliation development) or for instance metamorphic/metasomatic changes in composition. This way one may predict which rocks are sensitive to such changes in strength, which may lead to localisation of deformation in shear zones.

The method does not predict how microstructures will change during deformation and at which rate. Experimental deformation of organic rock analogues is a useful method to study this. Especially high shear strain experiments in a ring shear apparatus enables us to study both the microstructural development and the rheological properties of a composite simultaneously.

Chapter 9

Grain growth

9.1 Syndeformational grain growth: microstructures & kinetics §

9.1.1 Abstract

Grain growth can be an important high-temperature process in fine grained polycrystalline materials. We studied its effect on texture during deformation using a two-dimensional computer model and a see-through experiment with octachloropropane.

Syndeformational grain growth in geological materials can slow down the development of a grain shape preferred orientation or even obliterate it. Important processes are preferentially oriented deformation induced neighbour switches. The presence of a grain shape preferred orientation slows down the increase in grain size due to grain growth.

9.1.2 Introduction

Grain growth is usually defined as the recrystallisation process in a polycrystalline aggregate which results in a reduction of free energy through reduction of the total grain boundary area (Smith, 1964). In the absence of other processes this leads to a foam texture and to an increase in grain size. In other words growth of grains is a result of Grain Boundary Energy driven Grain Boundary Migration (GBEGBM). Post-tectonic GBEGBM can cause partial or complete destruction of a microstructure, such as grain shape preferred orientation, if the tectonite was subjected to a high enough temperature for a long enough time after deformation. However, significant GBEGBM may well take place during deformation, for example during decreasing strain rates at the end of a deformation episode which overlaps with high temperature metamorphism (Rutter & Brodie, 1985).

---

§ P.D. Bons & J.L. Urai, Journal of Structural Geology, Vol. 14, No 8/9, pp 1101-1109

The effects of GBEGBM during deformation have not yet received much attention, although several workers have mentioned it for playing a (minor) role during strain induced recrystallisation (Urai *et al.* 1986, Knipe & Law 1987, Ree 1991). Deformation experiments on fine grained wet quartz by Karato & Masuda (1989) have shown that grain size can increase considerably *during* deformation without the development of a grain shape preferred orientation (SPO). In metals the process has also been described to occur during high temperature creep of superplastic alloys (Suery & Baudelet 1978).

In this study we investigated the effect of GBEGBM on SPO development during deformation, and the effects of deformation on GBEGBM. We developed a computer model to single out GBEGBM from other processes that modify the grain shape.

9.1.3 Grain boundary energy driven grain boundary migration: GBEGBM

Several workers used soap froth and oil emulsions as analogues for GBEGBM in polycrystalline solids e.g. (Smith 1964, Ashby & Verrall 1973). The thin fluid-films between the gas or liquid filled cells are interfaces with an associated interfacial tension. The cell walls move when material inside the bubbles diffuses through the walls. A minimum grain boundary energy is achieved (independently of the grain size) when all cell walls are straight and meet at 120°. Such an ideal arrangement however does not exist in nature and natural foams or crystalline aggregates are therefore inherently unstable (Smith 1964).

The kinetics of GBEGBM can be described by:

$$(R-R_0) = k \cdot t^{(nd)} \qquad (9.1)$$

Where R is the grain size, R_0 is initial grain size, t is time, k is a constant and n = 0.4-0.5 (Olgaard & Evans 1986, Anderson 1988, Olgaard & Evans 1988). The parameter d is dependent on grain size R and is 1 if R is grain radius, 2 if R is grain area and 3 if R is grain volume (Anderson *et al.* 1984, 1985). The process is also dependent on initial geometry or topology. If for example the starting material is ordered, e.g. contains many regularly shaped six sided cells in 2D, growth will initially be slower (Glazier *et al.* 1987).

The growth process can be subdivided into two sub-processes: equilibration of cell-walls to achieve the lowest energy configuration and growth of cells. In a soap froth the first sub-process takes place instantaneously, because the walls and the contents of the cells (bubbles) have negligible strength and the second sub-process takes place by material transfer through the walls. In a crystalline aggregate the cells (grains) are

solid and both sub-processes have to take place by the time dependent transfer of material across the grain boundaries (Weaire & Kermode 1984, Wejchert *et al.* 1986).

In real polycrystals GBEGBM during deformation is always accompanied by the operation of deformation mechanisms (dislocation and diffusion) and usually also by other (dislocation driven) grain boundary migration processes. Although GBEGBM may be a significant microstructural process, its effects are difficult to study separately in experimental systems. For this reason we developed a computer model. Like many other workers we used a two-dimensional model, because the computer algorithms are simpler and Anderson *et al.* (1985) have shown that conclusions drawn from 2D are applicable to 3D (Weaire & Kermode 1983, Anderson *et al.* 1984, Srolovitz *et al.* 1984a, Srolovitz *et al.* 1984b, Grest *et al.* 1985, Soares *et al.* 1985, Srolovitz *et al.* 1986, Wejchert *et al.* 1986, Glazier *et al.* 1987, Anderson 1988, Stavans & Glazier 1989).

9.1.4 The model

Description

The model used in this study is a modification of the model of Soares *et al.* (1985). A 2D polycrystalline aggregate is modelled as a network of straight grain boundaries that meet at triple junctions. Grain growth takes place by moving the triple junctions in small steps. Because grain boundary energy is the driving force, each triple junction has to move in a direction that reduces the summed length of the three joining triple junctions and thus reduces the grain boundary energy. In our model the movement vector (v_o) of a triple junction is taken as the sum of the three vectors (v_a, v_b, v_c) which are parallel to the three grain boundaries (Fig. 9.1a):

$$v_o = v_a + v_b + v_c \tag{9.2}$$

The length of the three vectors is normalized to c, which is a user defined constant typically a few percent of the average grain diameter.

$$|v_a| = |v_b| = |v_c| = c \tag{9.3}$$

This has the effect that a triple junction will move towards a position where the three grain boundaries meet at angles of 120°.

To determine the movement distance of a triple junction in one time unit one has to take into account the grain boundary mobility. The displacement v_o would cause the grain boundaries to sweep a certain area A, shown grey in figure 9.1(a). In our model the effect of grain boundary mobility is simulated by setting the maximum

amount of material through which a grain boundary can migrate, i.e. the maximum swept area, in one time unit to a constant A_o. If A is larger than A_o, the length of v_o is adjusted according to:

$$v_o' = \frac{A_o}{A} v_o \tag{9.4}$$

This means that when A is small, either because the triple junction is almost in a stable position or the joining grain boundaries are short, the incremental triple junction movement is independent of the grain boundary mobility. When A is larger, the triple junction displacement is adjusted to take into account the limited rate at which grain boundaries can migrate through the material. The model is rather simple here, but the overall simplifications in the model do not justify a very elaborate modelling at this point. This adjustment of the displacement distance per time unit of a triple junction is the main difference with the model of Soares *et al.*

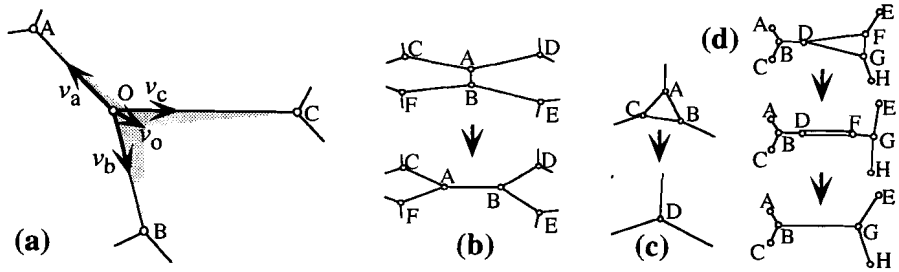

Fig. 9.1. Basic procedures of the model. (a) Movement of a triple junction, simulating GBEGBM. (b) Neighbour switching, or the T1-event. (c) Disappearence of an equidimensional three-sided grain, or T2-event. (d) disappearance of a strongly elongated three-sided grain via a T1-event followed by the disappearence of a two-sided grain.

As the grains grow, the arrangement of grains changes: grains will change their number of sides and small grains will disappear. The basic topological changes to achieve this are called T1 and T2 events (e.g. Weaire & Rivier 1984).

T1-event: When one of the grain boundaries of a given triple junction becomes shorter than a user defined minimum l_{min}, a neighbour-switch will occur (Fig. 9.1b). The grain boundary is replaced by a new grain boundary perpendicular to the old one and the triple junctions on either side will be rearranged. The length of the new grain boundary is set to a constant value (1.5) times the old length, to avoid reversal of the process during the next move of this triple junction.

T2 event: When a three sided grain becomes smaller than a user defined minimum, it disappears (Fig. 9.1c). The three triple junctions at its corners are merged to one new triple junction. The criterion for a T2 event to happen is that two of the grain boundaries merging at the selected triple junction are shorter than $2l_{min}$ and that these

two GBs are boundaries of a 3-sided grain. An elongated 3-sided grain disappears in two steps (Fig. 9.1d): First it sheds its short side in a T1 event, after which a 2-sided grain remains. Its two triple junctions rapidly move towards each other until they have reached the threshold distance for a T2 event, when the 2-sided grain disappears. These two sided grains are not visible in the graphic output of the model, because of the straight (and overlapping) grain boundaries.

During the simulation triple junctions are each randomly selected and moved according to equations (9.2) to (9.4), or altered by a T1 or T2 event. One selection and movement of a triple junction is defined to last one unit time. As the network is not periodic, some minor modifications are made for triple junctions at or adjacent to the network boundaries. Triple junctions can be displaced in small increments according to a user defined position gradient tensor, to model GBEGBM *during* deformation.

Test	Number of moves (x 1000)	strain rate ($move^{-1}$)	shear rate ($move^{-1}$)	Mean grain area at start	Mean grain area at end	Number of grains at start	Number of grains at end	c	l_{min}	R_a at start
0	100	-	-	799	2201	151	52	5	1	1.0
1	125	-	$1.6 \cdot 10^{-5}$	404	731	315	168	1	1	1.0
2	500	-	$4.0 \cdot 10^{-6}$	404	1741	315	68	1	1	1.0
3	125	$8.0 \cdot 10^{-6}$	-	404	685	315	177	1	1	1.0
4	500	$2.0 \cdot 10^{-6}$	-	404	1758	315	68	1	1	1.0
5	500	-	-	404	1718	315	72	1	1	1.0
6	350	-	-	404	894	315	131	1	1	4.0

Table 1. *Conditions of the model simulations*

Validity of the model

In the first of seven simulations (see Table 1) we studied GBEGBM without deformation (Test-0, Fig. 9.2). The starting material was copied from a picture of a two dimensional soapfroth (Fig. 2(b) in Glazier *et al.* 1987). During this run there was a threefold increase in mean grain area and the total unrecrystallized area at the end of the run was 49%. This simulation was used to test the validity of the model, by comparing it with theoretical and empirical work presented by other workers, e.g. (Anderson *et al.* 1984, Srolovitz *et al.* 1984b, Weaire & Kermode 1984, Glazier & Stavans 1987).

Figure 9.3a is a plot of grain area versus elapsed time. A growth-exponent (n in equation (9.1), with d=2) of 0.5 can be fitted to the data.

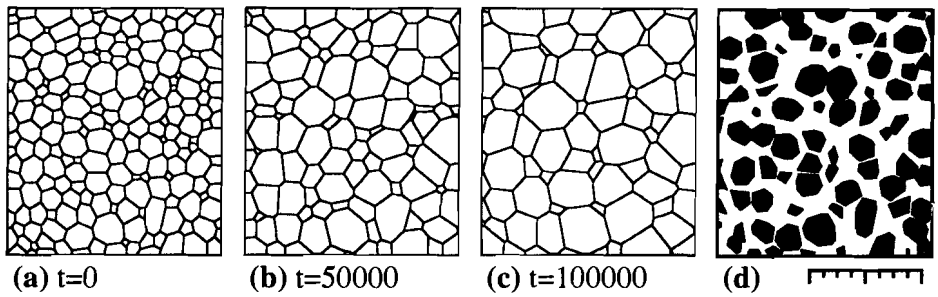

Fig. 9.2. Test-0. (a) Starting material, (b) and (c) at time 50000 and 100000 respectively. (d) unrecrystallized area (black) at t=100000. Scalebar 200 unit lengths.

According to Lewis's hypothesis, the normalized area of grains (grain area divided by average grain area) should remain a linear function of the number of sides of grains (Weaire & Rivier, 1984). Glazier *et al.* (1987) however found that Lewis's hypothesis does not hold for few sided cells in soap froth and the same result was produced by the computer model of Weaire and Kermode (1984). Fig. 9.4(a) shows that Lewis's hypothesis is met for 4 and more sided grains at t=0 and t=40000 (151 and 89 grains respectively, Fig. 9.4c).

According to Von Neumann's law (Von Neumann, 1952), the growth rate of individual grains should be linearly dependent on the number of sides and independent of time. Grains with more than six sides tend to grow and grains with less than 6 sides tend to shed sides and shrink. Again this is shown for t=0 and t=40000 (Fig. 9.4b). Here we see a deviation from theory: four sided grains shrink slower than expected and there are no measurements on 3 sided grains. This is partly due to the measurement method but also due to the fact that grain boundaries are assumed to be straight in the model. For few and very many sided grains the error by this simplification becomes noticeable. In real crystalline aggregates and soap froths 3 and 4 sided grains have boundaries with pronounced curvature, causing them to shrink faster than predicted by the model.

Except for the last point, the model appears to simulate GBEGBM well. Its accuracy is sufficient to demonstrate and illustrate the effects of GBEGBM during deformation. The model is indeed not designed to accurately investigate the details of GBEGBM itself.

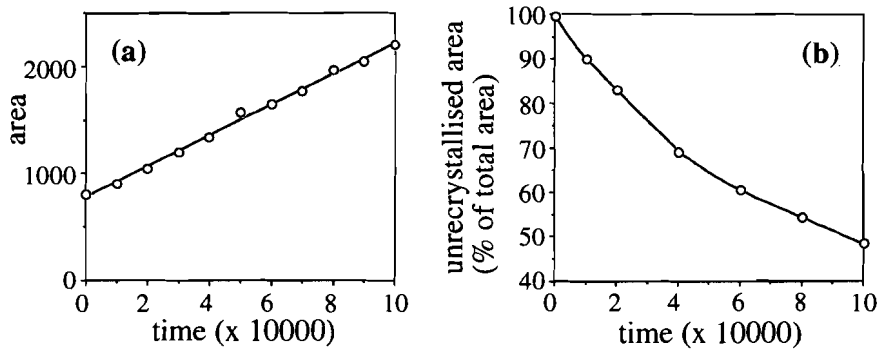

Fig. 9.3. Test-0: (a) Average grain area as a function of time. The straight line is a linear fit through the data. (b) Percentage unrecrystallized area as function of time.

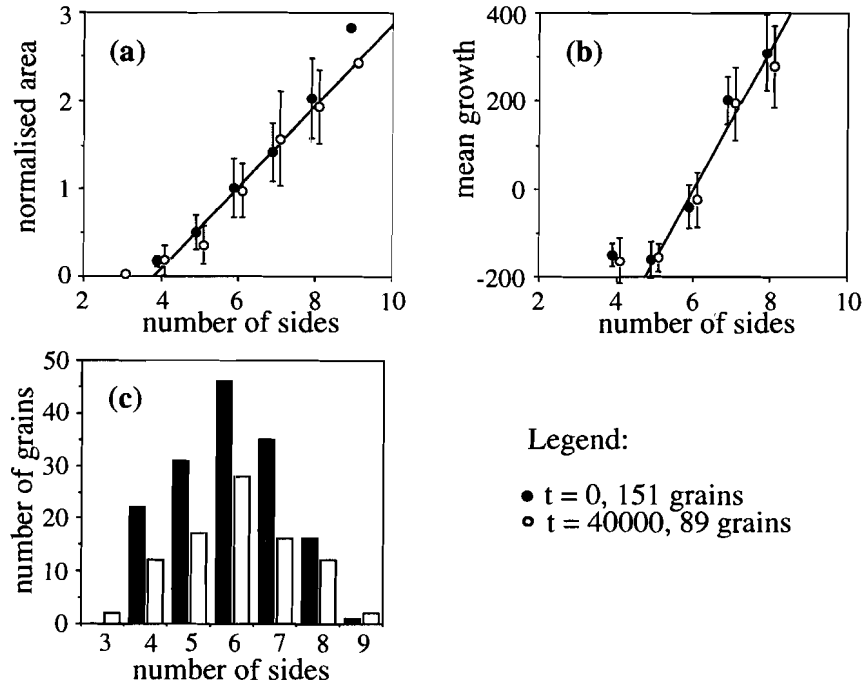

Fig. 9.4. Test-0: (a) Normalised area of grains as a function of number of sides of grains. Straight lines are fitted through the data of 4 to 8 sided grains. (b) Average increase in area as a function of number of sides. Straight lines are fitted through the data of 5 to 8 sided grains. (c) frequency of n-sided grains at t=0 and t=40000. (Error bars are one standard variation in length)

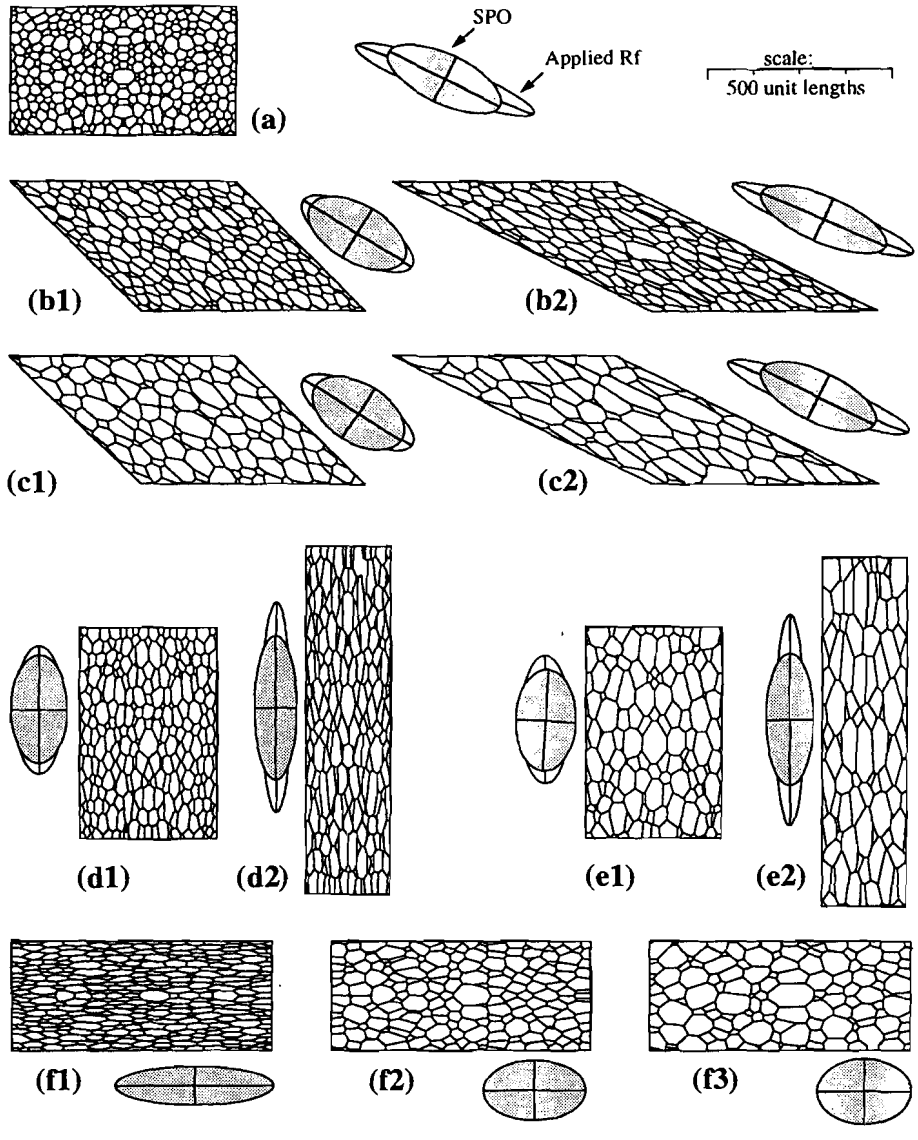

Fig. 9.5. Test-1 to 4 and 6: GBEGBM during deformation. (a) starting material. (b) Test-1: $\dot{\gamma}=1.6\cdot10^{-5}$ at t=62500, $\gamma=1.0$ (b1) and t=125000, $\gamma=2.0$. (b2). (c) Test-2: $\dot{\gamma}=4.0\cdot10^{-6}$ at t=250000, $\gamma=1.0$ (c1) and t=500000, $\gamma=2.0$. (c2). (d) Test-3: $\dot{\varepsilon}=8.0\cdot10^{-6}$ at t=62500, $\varepsilon=0.39$ (d1) and t=125000, $\varepsilon=0.63$. (d2). (e) Test-4: $\dot{\varepsilon}=2.0\cdot10^{-6}$ at t=250000, $\varepsilon=0.39$ (e1) and t=500000, $\varepsilon=0.63$. (e2). (f) Test-6: t=0 (f1), t=250000 (f2) and t=500000 (f3). Open ellipses show finite strain ellipse and dotted ellipse the average axial ratio and orientation of grains.

GBEGBM during deformation

To simulate the effect of GBEGBM during deformation, the grain aggregate in the model was deformed in small increments during the simulation. We present the results of six simulations, Test-1 to Test-4: area conservative pure shear and simple shear, both at two strain rates (Fig. 9.5b-e). A fifth simulation (Test-5) is of GBEGBM without deformation, using the same starting material as for Test 1 to 4. Test-6 shows the effect of GBEGBM in an aggregate with a pre-existing grain shape preferred orientation. The starting material was the same as for the other tests (Fig. 9.5a), but deformed in plane strain up to a strain ratio of 4 (Fig. 9.5f).

Using the method described by Panozzo (1983, 1984), the average grain shape preferred orientation (SPO) can be described by an ellipse with an aspect ratio (R_a) and an orientation of the long axis of the the ellipse (α). This ellipse was calculated at regular time intervals from the grain boundaries. Only grain boundaries that did not touch the network boundaries were used for the calculation. For comparison, the SPO development of the deforming starting material is calculated in the same way and plotted together with the results of the deformation simulations. The starting material had virtually no SPO (R_a=1.02, α=22°)

It can be seen that there is a distinct lag in R_a development, the strongest at the lowest strain rates (Fig. 9.6). In the pure shear simulations α rapidly becomes perpendicular to the shortening direction, independent of strain rate. With simple shear α starts at 45° to the flow plane (-line in 2D) and then rotates towards the flow plane. Only in Test-2 there seems to be a lag in rotation of α with respect to the maximum rotation speed. Up to $\gamma = 2.0$ the difference is hardly significant however.

The main reason that the simulations were not done to a higher finite shear was the fact that the model does not acurately describe the behaviour of small few sided grains. During deformation these will elongate disproportionally and introduce an error in the SPO measurements. Measured R_a values will therefore be too high and the rotation of α too fast. We are currently working on a modification of the model to correct for this effect.

The GBEGBM curve of Test-6 (Fig. 9.7a) shows an interesting effect. The rate of GBEGBM decreases with increase of SPO. The important factor is probably not the preferred orientation of all grains, but the fact that the individual grains are elongated, as in a Voronoi network (Soares *et al.* 1985, Wejchert *et al.* 1986). This effect was also observed, but less distinct, in an experiment with a two dimensional soapfroth. The SPO decreased rapidly in Test-6 (Fig. 9.7b).

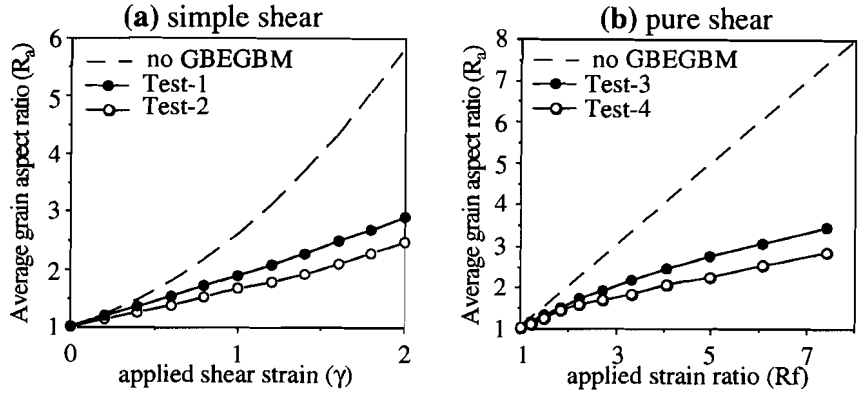

Fig. 9.6. Average grain aspect ratio (R_a) as function of applied strain ratio (Rf). (a) simple shear tests, Test-1&2. (b) pure shear tests, Test-3&4.

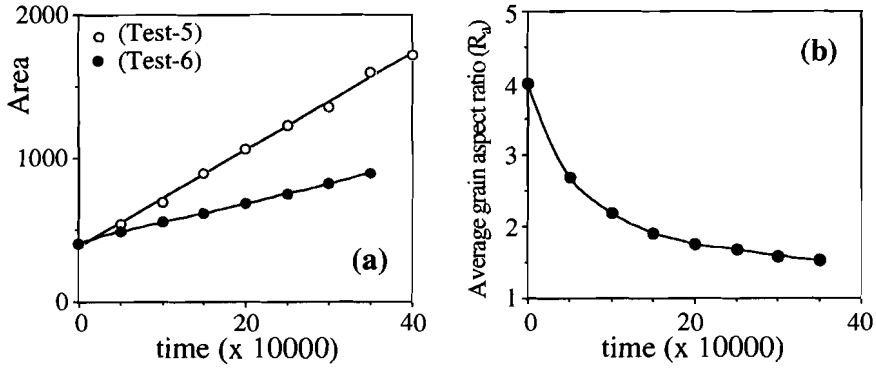

Fig. 9.7. Test-5&6: Average grain area (a) and average grain aspect ratio (R_a) (b) as a function of time.

9.1.5 OCP experiment

An annealed specimen of pure octachloropropane (OCP), mixed with marker-particles (26 μm), was deformed in pure shear to 23% shortening in a transmitted light deformation apparatus (see Urai *et al.* 1980, Means & Xia 1981, Means 1989 for description of experimental technique). Figure 9.8 shows the microstructure in a selected area at 3 stages, together with a grid to display the finite deformation at those stages (see Jessell (1986) for method of strain analysis). Deformation was heterogeneous because of the use of frosted grips.

A foam texture was largely preserved, indicating that GBEGBM was significant. Undulose extinction and the formation of large subgrains can be observed in several of the larger grains (see Ree (1991) for description of similar observations).

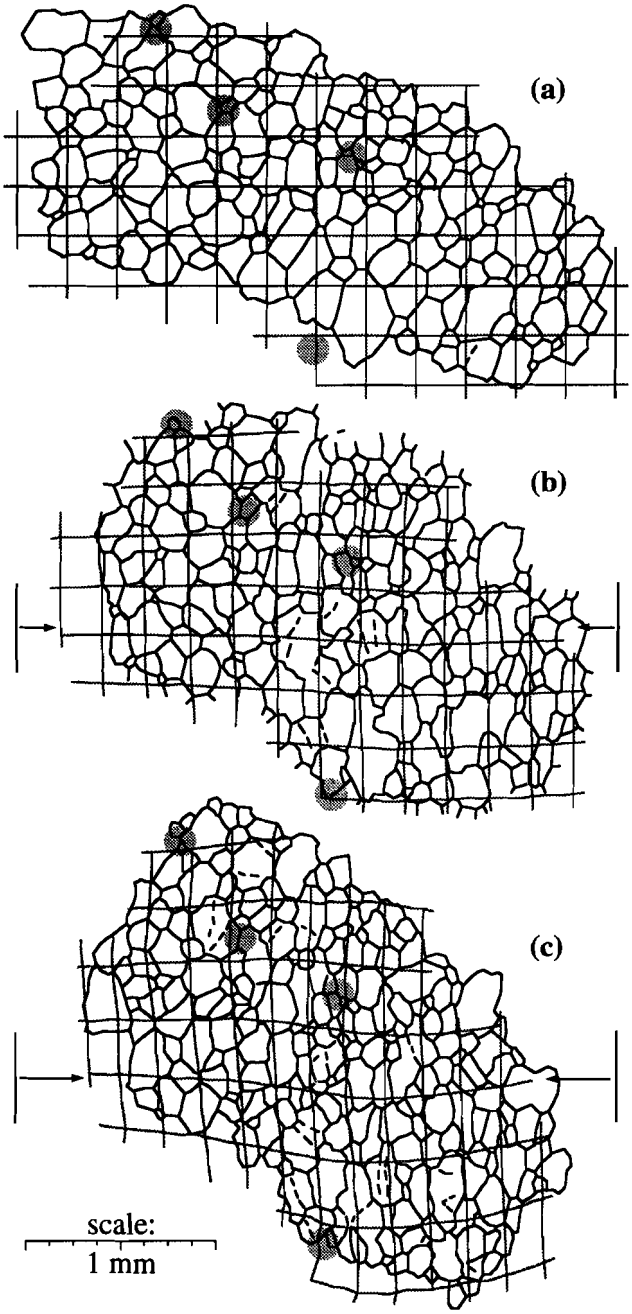

Fig. 9.8. *Deforming polycrystalline OCP. The grid is drawn to depict the finite strain at each stage. (a) Starting material. (b) 11% bulk shortening. (c) 23% bulk shortening, in E-W direction. Shaded areas show positions of detailed drawings of Fig. 9.9.*

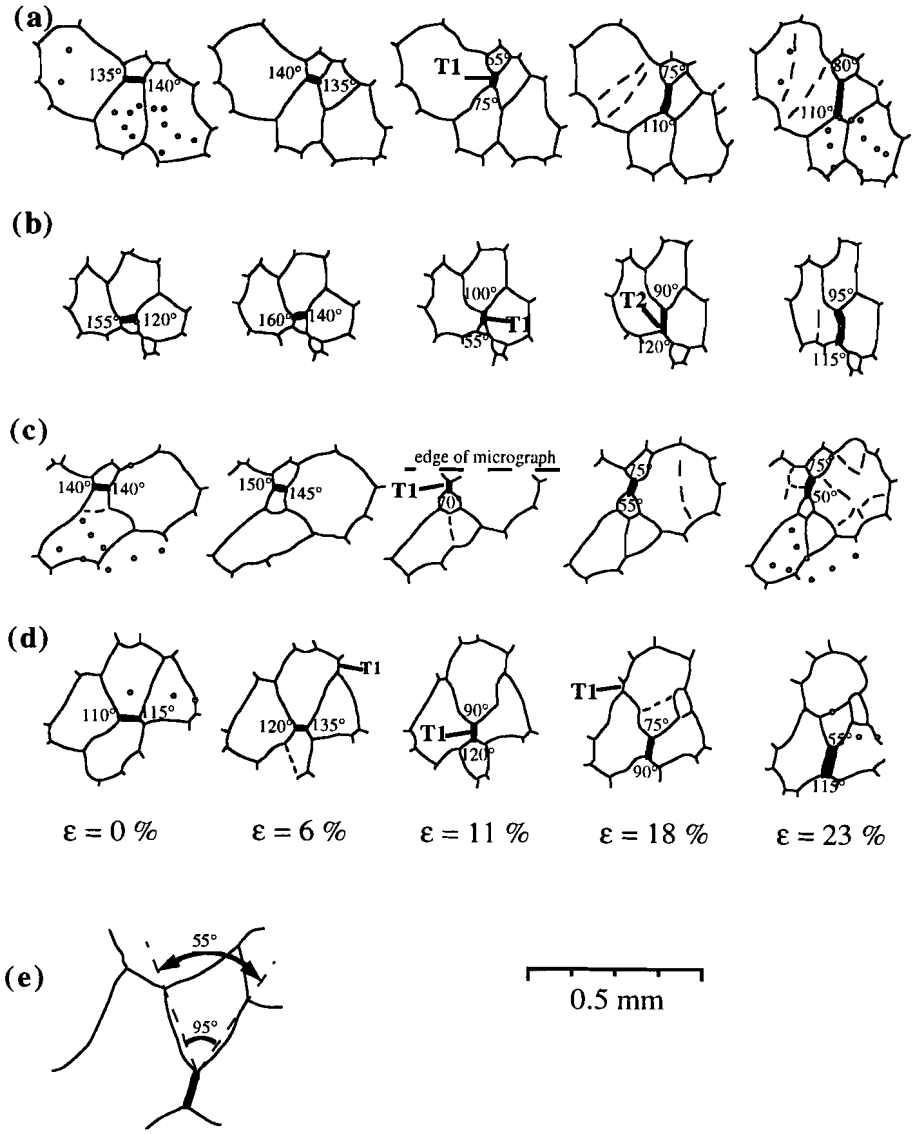

Fig. 9.9. *(a) to (d) Selected neighbour switches or T1-events in the OCP-experiment, taking place between 6 and 11% bulk shortening. The local grain boundary configuration is drawn for a bulk shortening of 0, 6, 11, 18 and 23%. Marker particles (if present) are drawn as small circles at 0 and 23% shortening. The numbers denote the opening angles (β) at the triple junctions. Note that these are on average larger than 120° before the switch and smaller after the switch. (e) shows how the angle α is measured, taking into account that grain boundaries are usually curved. In the given case β is 55°.*

27 T1 and several T2 events were observed. Some of these events are related because small four sided grains disappear by a T1, followed by a T2 event. Four T1 events are drawn in detail in Fig. 9.9. The T1 events have a strong preferred orientation with the newly formed grain boundaries preferentially perpendicular to the shortening direction. An R_a of 1.14, with the long axes of grains perpendicular to the shortening direction, was present at the start and increased to 1.33 at the end of the experiment when the applied strain ratio was 1.7. This means that the R_a-increase lags significantly behind the applied strain ratio. These observations are very similar to those by Ree (1991).

9.1.6 Discussion

GBEGBM has two main effects that both influence the texture in a tectonite: increase of grain size and the decrease of R_a. Test-6 shows that there is also an effect of texture on GBEGBM: its rate will decrease when grains flatten. The net effectiveness of GBEGBM depends on the extent to which it can 'keep up' with deformation, and on the importance of other competing microstructural processes (e.g. Urai *et al.* 1986).

Comparison with natural rocks and geological strain rates

In order to make predictions about the importance of GBEGBM during deformation for rocks under geological conditions we need to know GBEGBM rates in natural rocks. These will vary widely for different minerals, temperatures, pressure, fluid pressure, impurity content etc. We will restrict ourselves to one example: GBEGBM in a pure quartz aggregate at 600 °C and Pt = Pf = 3 kbar, for which Tullis and Yund (1981) provide GBEGBM rates extrapolated from their experiments on very fine grained quartz aggregates. They predict a grain diameter of 0.6 mm after 10^5 and 2.3 mm after 10^6 years, starting with a grain size less than 100 μm. To compare these values with our simulations we will express these in the form of equation (9.1) for area, assuming that the growth exponent n is 0.5 (which is roughly in accordance with the experimental data presented by Tullis and Yund and is equal to the growth exponent in our simulations).

$$R = -0.15 + 1.4 \cdot 10^{-13} t \quad (t=\text{time in seconds and R the area in mm}^2) \tag{9.5a}$$

In our simulations the growth function was:

$$R = 377.61 + 3.4 \cdot 10^{-3} t \tag{9.5b}$$

In order to calculate what strain or shear rates would be comparable to those used for the simulations we have to define the relative growth rate $\dot{R}$ at a given grain size:

$$\dot{R} = \frac{1}{R} \cdot \frac{\partial R}{\partial t} = \frac{k}{R} \quad \text{if } n=0.5 \tag{9.6}$$

and the relative strain or shear rate $\dot{\varepsilon}/\dot{R}$ or $\dot{\gamma}/\dot{R}$ (eq 9.7). As the grain size increases, the relative strain rate will decrease, so we will only look at relative growth rate and relative strain rate at the grain size of the starting material, which is $9.0 \cdot 10^{-6}$ in our simulations Test-1 to Test-4. The strain rates ranged from $2.0 \cdot 10^{-6}$ (Test-4) to $1.6 \cdot 10^{-5}$ (Test-1), giving relative strain rates of 0.22 to 1.8.

The following values give an impression of the strain rates for a quartz aggregate that are equivalent to these relative strain rates. For a grain diameter of 0.1 mm the shear rate of Test-1 would be $1.7 \cdot 10^{-11}$ s^{-1} and Test-4 $3.7 \cdot 10^{-12}$ s^{-1}. For a grain diameter of 5 mm these values would be $1.2 \cdot 10^{-14}$ s^{-1} and $1.5 \cdot 10^{-15}$ s^{-1} respectively. These values suggest that GBEGBM and its effects on the development of microstructures can be significant in fine grained rocks at low strain rates under geological conditions. It should be stressed that it will then only be one of the operating processes.

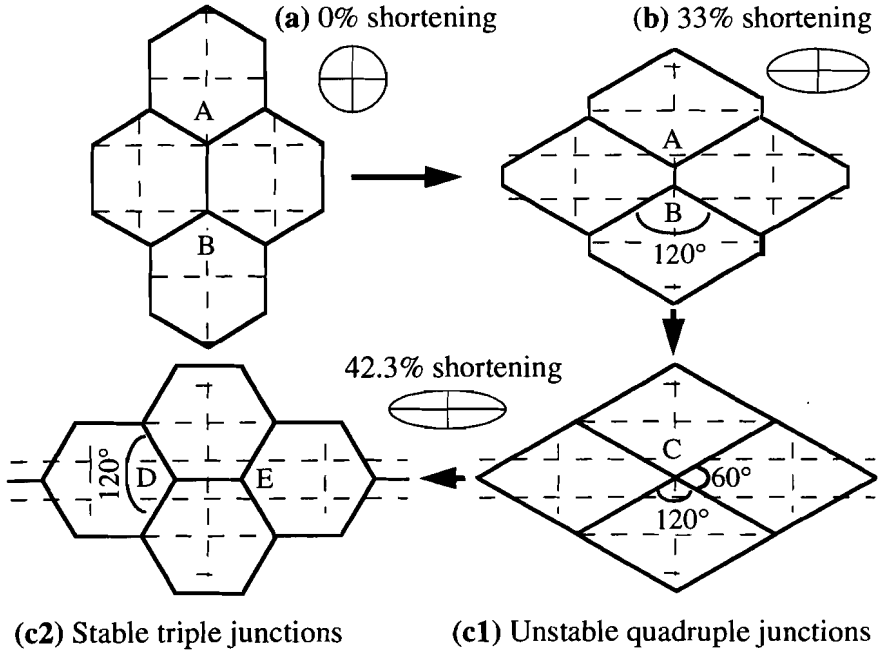

Fig. 9.10. Schematic drawing of strain-induced neighbour-switching in 2 dimensions. The rectangular grid represents material lines.

Neighbour switching

Neighbour switching, or the T1-event, is a well known result of GBEGBM. Soares *et al.* (1985) pointed out that only those switches occur, whereby relatively few sided grains of the four involved loose one side and become detached. This rule fails for GBEGBM during deformation. This was observed by Ree (1991). This process is best illustrated with the ideal hexagonal geometry (Fig. 9.10), where all grain boundaries are stable and therefore do not migrate. The stable triple junctions A and B become distorted when the material is flattened. A and B will therefore move towards each other in order to regain a stable geometry. At a strain of 42.3% ($1 - \frac{1}{3}\sqrt{3}$) A and B merge into one quadruple junction, C. Because this quadruple junction has two 60° and two 120° angles it is highly unstable and will rapidly fall apart into two new triple junctions: D and E. D and E now move apart in directions perpendicular to the original movement direction of A and B. It is important to note that the grain boundary migration here is entirely due to distortions of the grain boundaries by deformation. Grain size remains constant and at 42.3 % shortening all grains are equidimensional hexagons again.

A process giving similar textural developments, with an important contribution by neighbour switches, is (diffusion accommodated) grain boundary sliding (Ashby & Verall 1973). Although the actual flow of the material on the grain scale is completely different, these two mechanisms can (probably) not be distinguished using information on the resulting texture only. In 2D see-through experiments they can be distinguished if enough markers are present in each of the grains involved in the neighbour-switch. In the OCP-experiment presented here there are only few signs of grain boundary sliding (Fig. 9.9d), but not enough markers are present to rule it out unambiguously.

Looking at the displacements of centres of grains, as is done by Ashby & Verall, is not a valid method to prove grain boundary sliding. Grain centres are determined from the grain boundaries, which are not material entities. The grain centres themselves are therefore not material entities and one needs to know the flow pattern of material points to prove grain boundary sliding (e.g. Fig. 4 in Urai *et al.* (1986)).

One difference between the two mechanisms are the angles (ß) of grain boundaries joining at the ends of the grain boundary that is to be replaced during a neighbour-switch (Fig. 9.9e). Taking the ideal geometry of equidimensional hexagons, ß will remain 120° or increase if the neighbour switch is the result of GBEGBM and decrease to 90° if the switch is the result of sliding, using Ashby & Verall's (1973) model. In the OCP-experiment ß was in most cases well over 120° before the switch (Fig. 9.9).

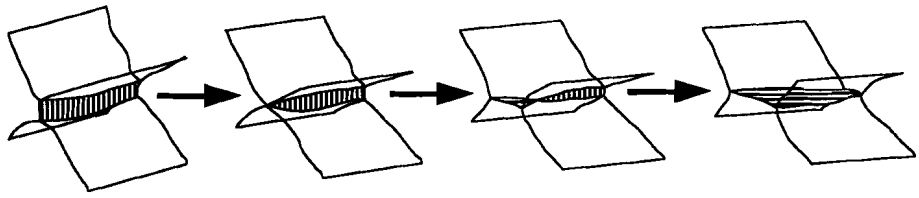

Fig. 9.11. Schematic drawing of strain-induced neighbour-switching in 3 dimensions.

Going from 2 to 3 dimensions

So far we have considered a 2-dimensional model. We will now briefly discuss the differences between the two and three dimensional case. The rate of increase of R_a will usually be lower in 3D than in 2D, and the observations in 2D have to be corrected for this. This is a simple geometrical correction, depending on the deformation (geometry) under consideration. Minimising the grain boundary area in grain growth is achieved by forming equidimensional grains and by increasing the grain size. When a SPO exists the first process will be faster in 3D than in 2D, because the grain boundaries can move in one extra dimension to create equidimensional grains and thus lower the SPO. The dynamics of a neighbour switch will be similarly affected. In 3D a neighbour switch involves the disappearance of a 2-D interface between two impinging grains and the formation of a new interface perpendicular to the old interface (Fig. 9.11). The two impinging grains will first meet at one side of the disappearing interface, where that interface will loose one side and the new interface will form with initially 3 sides. If the old plane was (almost) stable with respect to the angles at which grain boundaries intersect at its sides, the new intersection angles will be unstable at the sides of the new plane (compare with Fig. 9.10) and this plane will grow rapidly at the expense of the old one. The effect is that a neighbour switch may happen relatively faster in 3D than in 2D.

From this we can draw some qualitative conclusions on the difference between 3D and 2D. The increase of R_a will usually be slower and the rate at which grain growth can lower an SPO is higher, so the development of an SPO will be even more slowed down by GBEGBM in 3D compared with 2D.

9.1.7 Conclusions

(1) Grain boundary driven grain boundary migration (GBEGBM) is a mechanism that can slow down the development of a grain shape preferred orientation (SPO) during deformation or even obliterate it.
(2) Deformation can induce extra neighbour switching, which decreases the development of an SPO.
(3) The increase in grain size because of GBEGBM is slowed down by the presence of a SPO.
(4) GBEGBM can be significant under conditions of low strain rate, small grain size and high temperature.
(5) The lack of a GSPO at a small grain size is not sufficient to prove grain boundary sliding, but can be partly or completely the result of GBEGBM during deformation.
(6) These effects of GBEGBM during deformation can be observed in polycrystalline OCP, deformed at high homologous temperature and low strain rate.

Acknowledgements - The authors are grateful to W.D. Means, A. Vauchez and B.Ph. van Milligen for their comments on the manuscript. Financial support to P.D. Bons by the Netherlands Organization for Scientific Research (NWO) is gratefully acknowledged.

9.2 An improved model for static grain growth

The two dimensional computer model to simulate grain growth in 2 dimensions, presented and used in § 9.1, was further improved. The main improvement is to incorporate curvature of grain boundaries and the effect of pinning by second phase particles. The model is more realistic than the earlier model, but it does not alter the conclusions drawn in the previous section. The model has not yet been applied to study particular problems, but its potential is outlined below.

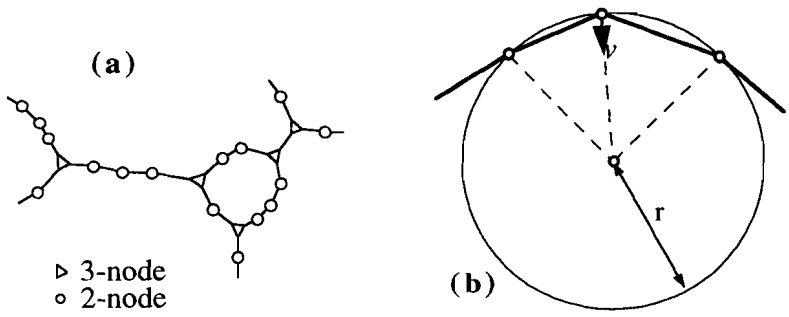

Fig. 9.12. (a) definition of the grain boundaries by 2-nodes (circles) and 3-nodes (triangles), linked by straight lines. (b) Definition of local curvature radius (r) at a 2-node and its velocity vector (v).

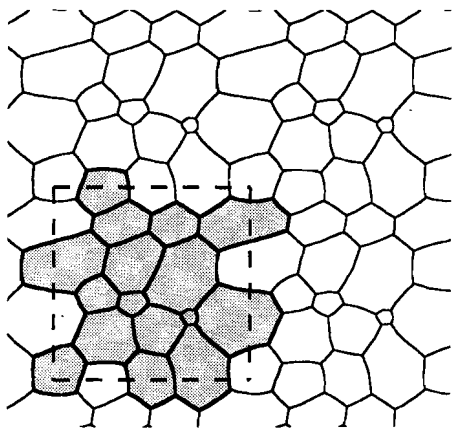

Fig. 9.13. The rectangular area (dashed square) in which the grain aggregate (shaded grains) is defined can be considered as a unit cell in an infinite aggregate. The same set of grains (shaded grains) are repeated on all sides of the unit cell

9.2.1 The computer model

Definition of the aggregate

Grain boundaries are modelled as points or *nodes*, that connect straight sections of the grain boundary (fig. 9.12.a). Each node has a position in space (x,y) and two or three neighbours. There are two types of nodes: *2-nodes* and *3-nodes*. 2-nodes lie on grain boundaries and have two neighbours on either side. A 3-node is a triple junction and has three neighbouring nodes. The whole grain aggregate is defined by the list of nodes, with their position and neighbours. The whole aggregate can be drawn by linking neighbouring nodes with straight lines. The more nodes, the better a smoothly curved grain boundary can be modelled. Memory space and calculation time however restrict the number of nodes.

The area modelled by the program can be considered a unit cell of an infinite aggregate. This unit cell is repeated on each side of the rectangular area (fig 9.13). When a node moves out of this rectangle, it reappears at the opposite side. This way there are no disturbing boundary effects. The average grain size of the aggregate can increase, until the grain size is more than half the unit cell size.

There are two ways of making an initial grain aggregate:

1) digitising a picture of an aggregate by hand, by clicking on triple junctions and defining 2-nodes with a mouse on a digitising board. This is extremely cumbersome and it is difficult to make the aggregate repeating on all sides (the top-most grains must match the lower most grains, as must the left most and right most grains). With such an aggregate one can simulate experimentally observed "real" grain growth histories.
2) creating an artificial grain aggregate. This is done by first creating a regular honeycomb mesh with only 3-nodes. The next step is to perform a number of random neighbour switches, which creates a grain aggregate of 4- to 8-sided grains. Then the 2-nodes are inserted and a period of normal growth is applied to achieve a "steady state" grain topology.

Grain growth is simulated by moving each node in turn and performing the necessary topological events (T1 and T2). The nodes are numbered randomly and the program works through the list of nodes forward and backward in one time increment, to avoid any artefacts that can arise when nodes on a grain boundary are moved in a regular sequence. Ech node is therefore moved twice in each time increment. A flow diagram of the program is given in figure 9.14. It contains the elementary steps in the model, which are described below.

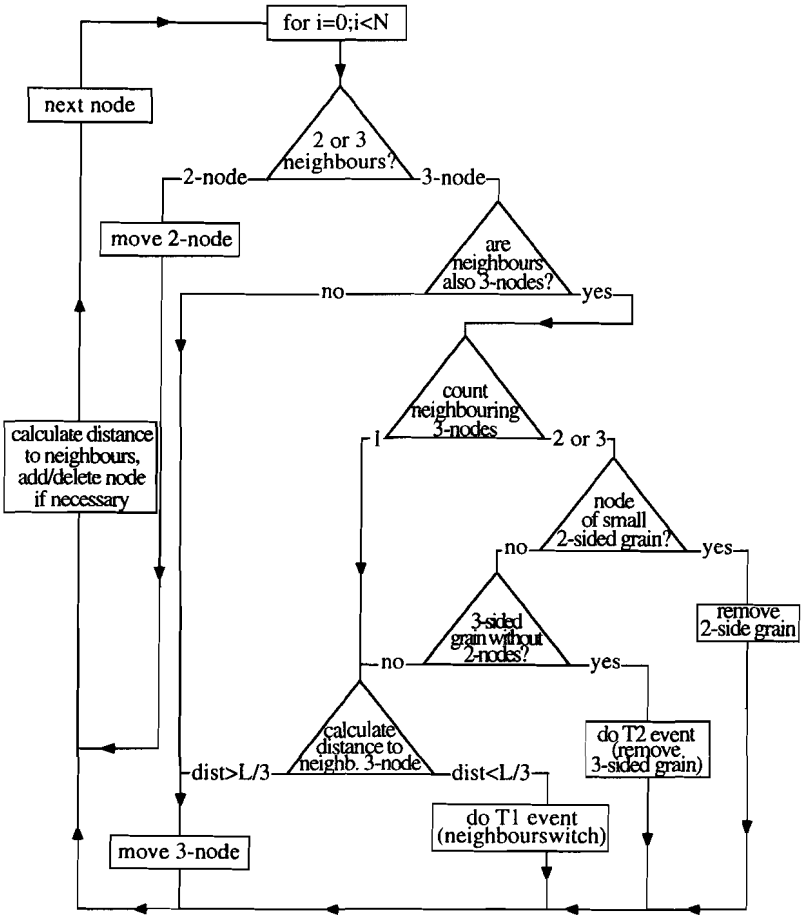

Fig. 9.14. Flow diagram of the computer model for the evolution of one node.

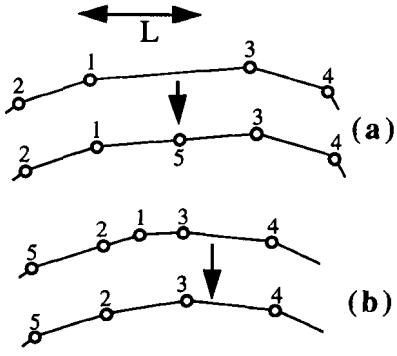

Fig. 9.15. (a) A new 2-node (nr. 5) is inserted when the distance between two nodes (nrs. 1&2) becomes more than L. (b) A 2-node (nr. 1) is removed when the distance between its 2 neighbours (nrs. 2&3) becomes less than L.

Displacement of one node to reduce curvature

The migration rate of the boundary is related to r, the radius of local curvature of the grain boundary. The migration direction of a point on a boundary is towards the centre of local curvature (fig 9.12.b). The migration velocity, v, can then be expressed as (Stüwe 1978):

$$v=\frac{\partial r}{\partial t} = MP = \frac{-2Mg}{r} \tag{9.7}$$

where M is the mobility of the grain boundary, P the driving force on the grain boundary and g grain boundary surface energy (Ceppi & Nasello 1984; Fradkov *et al.* 1985). Equation 9.7 can be numerically approximated by changing ∂r and ∂t to Δr and Δt respectively, giving:

$$\Delta r = \frac{-2Mg\Delta t}{r} \tag{9.8}$$

This is only valid if Δt is small enough such that Δr is small compared to r. Each 2-node is displaced in turn over Δr. The local curvature of the boundary at the node is determined by calculating the radius of a circle through the node and its two neighbours (fig 9.12.b).

The displacement of a 3-node is chosen as the sum of the 3 displacements calculated from the local curvatures of its three pairs of neighbours.

Distance between nodes

The distance between the nodes is determined with a user defined constant, L. When a grain boundary becomes longer, the nodes move apart. When the distance between two nodes exceeds L, a new node is inserted between the two nodes (fig 9.15.a). When a grain boundary shortens, the nodes converge. A node is removed when the distance between its two neighbouring nodes nodes becomes less than L (fig 9.15.b).

First test

The model was first tested by simulating simple situations. The simplest situation is a circular grain embedded in an infinite grain. Such a grain should remain circular (Anderson *et al.* 1984, 1985). Integration of equation (9.7) shows that the area of the grain should decrease linearly with time. A shrinking circular grain is shown at regular time-intervals in fig. 9.16.a, and this area as a function of time in figure 9.16.b. One can see that the requirements are fulfilled.

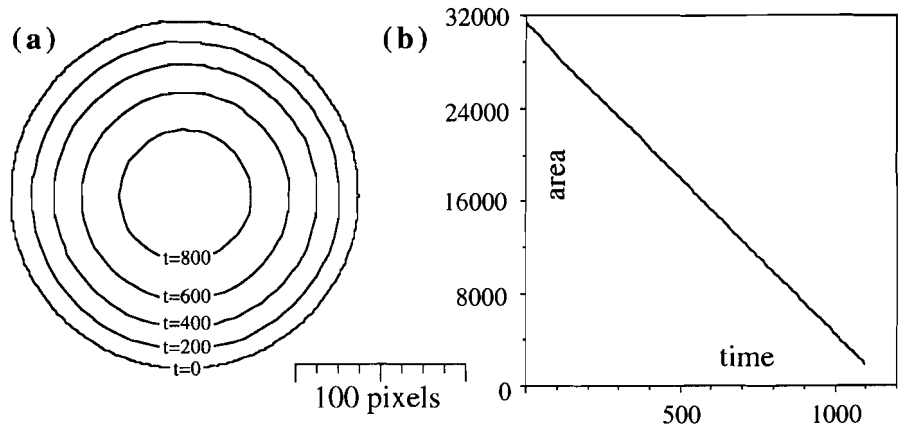

Fig. 9.16. (a) shrinking of a circular grain embedded in an infinite grain. The grain boundary is shown at regular time intervals (t=0, 200, 400, 600 and 800). (b) Linear decrease with time of the area of the circular grain.

Topological events

As described in §9.1 there are two basic events whereby the grains are rearranged with respect to each other. These events are shown in fig 9.17 in statically recrystallising norcamphor.

A T1-event, a neighbour switch, is initiated by the program when two converging 3-nodes become neighbours, i.e. when the last 2-node between them is removed, and their distance is less than L/3 (fig. 9.18.a). A new section of grain boundary, between the two nodes involved, is constructed perpendicular to the old one that is removed. The links between the neighbours are rearranged. To avoid possible reversal of the switch in the next time increment, a 2-node is inserted halfway the new grain boundary.

A T2-event, the disappearance of a 2- or 3-sided grain, is initiated when a grain has only 2 or 3 3-nodes and no 2-nodes (fig 9.18.b). A 3-sided grain is then replaced by one 3-node in its middle. A 2-sided grain is replaced by one 2-node, halfway its 2 3-nodes.

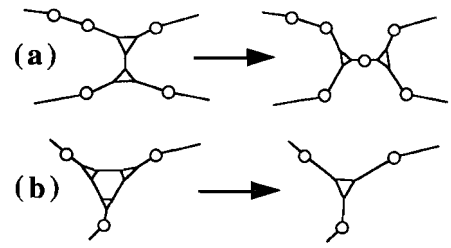

Fig. 9.18. T1-event (a) and T2-event (b) as performed by the model.

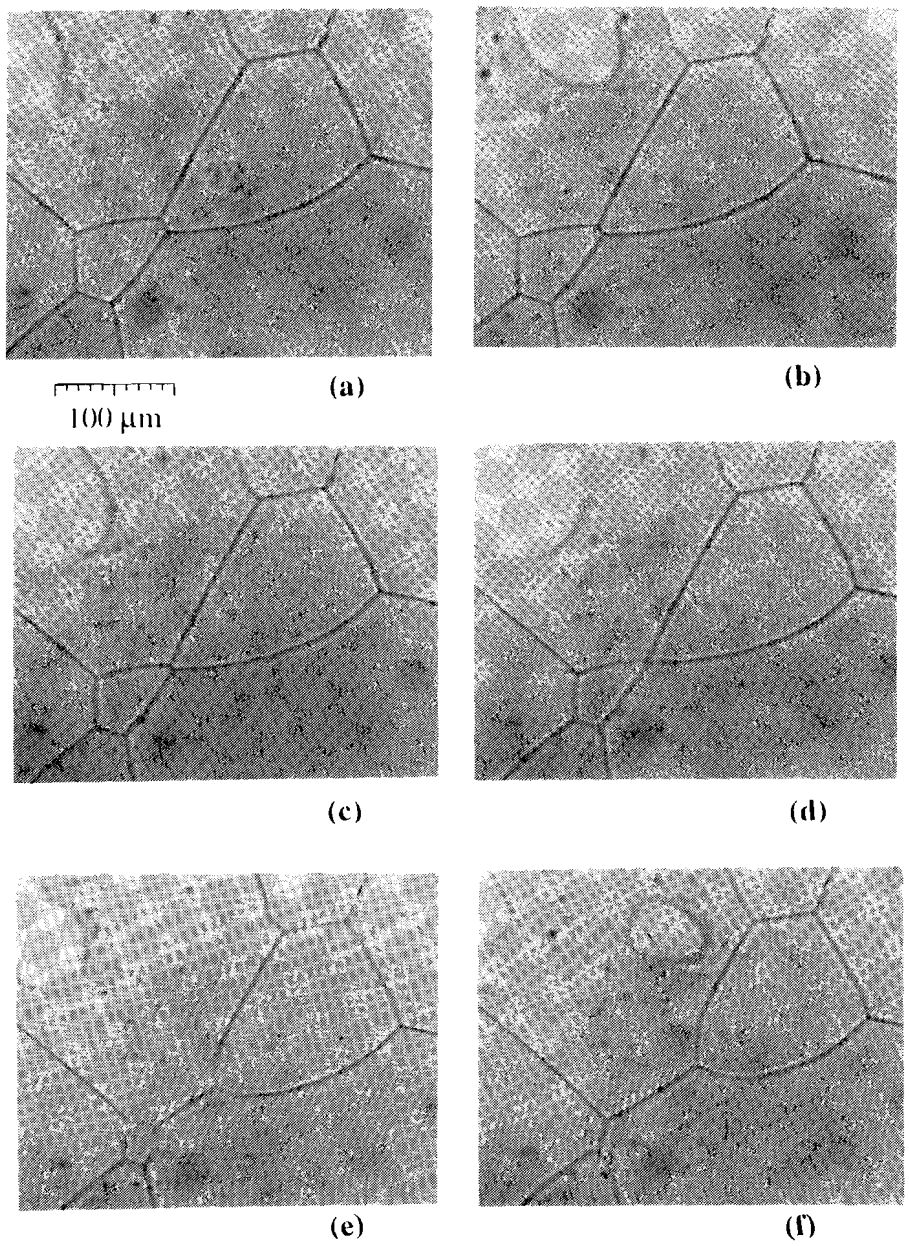

Fig. 9.17. *Topological events in a thin sheet of statically recrystallising norcamphor at 60 °C. (a-f) History involving a neighbour-switch (T1) and the disappearence of a small 4-sided grain (T2). The grain boundary between the two 5-sided grains shortens until its two triple junctions merge to become a short-lived quadruple junction (d) that falls apart into a new grain boundary, leaving the two 5-sided grains as 4-sided grains. The smallest 4-sided grains shrinks rapidly and has disappeared by stage (f). (a) t = +0 s, (b) t= +30 s, (c) t = +60 s, (d) t = +80 s, (e) t = +95 s and (f) t = +120 s.*

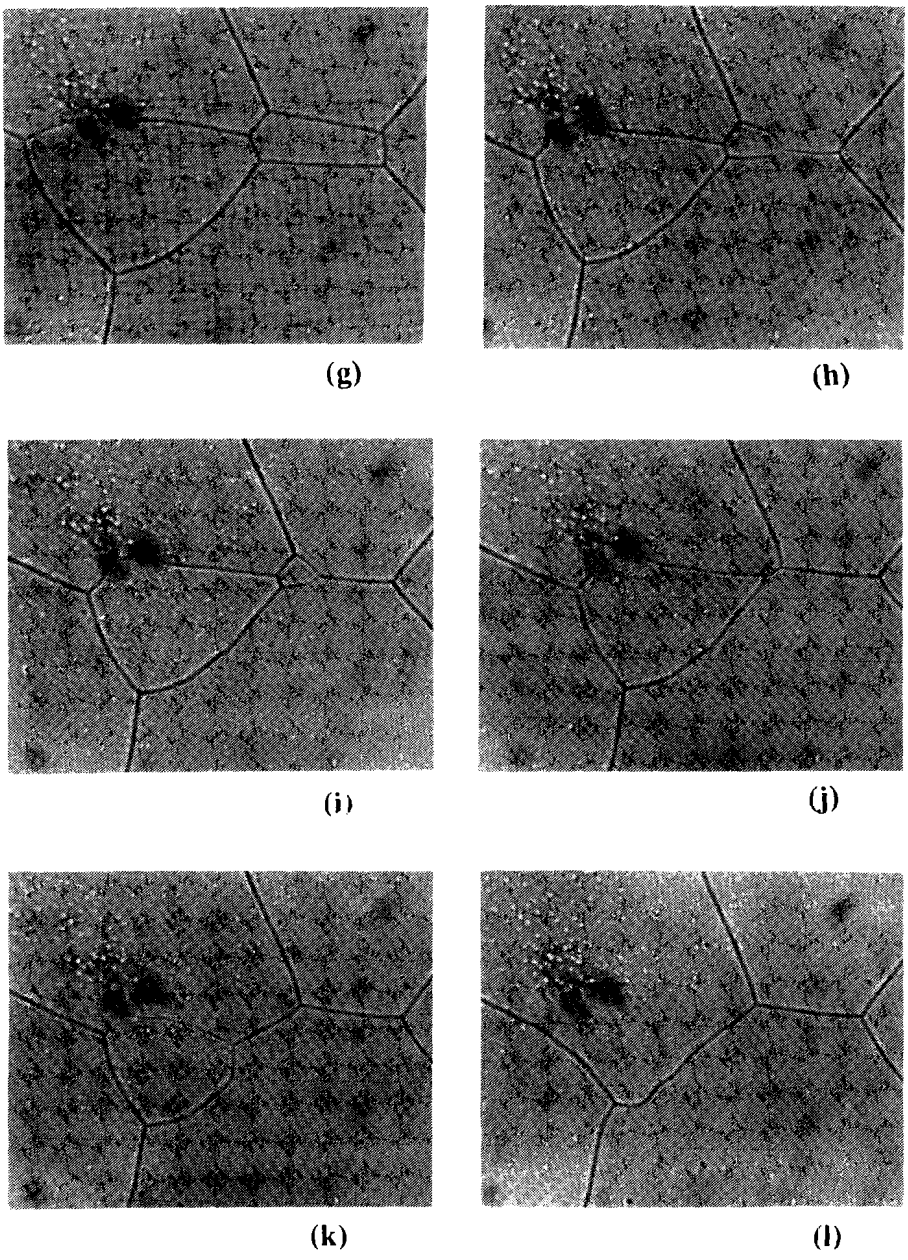

Fig. 9.17 continued. *(g-l) History involving two T1-events (g to h, i to j) and two T2-events (i to j, k to l). Note that grain boundaries are pinned by second phase particles and small bubbles and/or inclusions. (g) t = +0 s, (h) t = +270 s, (i) t = +285 s, (j) t = +300 s, (k) t = + 345 s and (l) t = +450 s. Width of view 0.4 mm.*

Results for normal grain growth

The grain aggregate seems to reach a topological steady state after a period of normal growth, (fig. 9.19). That is, it is impossible to tell how much the aggregate has grown, or what the scale is, by only looking at the texture. The growth rate (dA/dt, where A is the average grain size (fig. 9.20.a) is independent of time and average area of the grains:

$$\frac{dA}{dt} = \text{constant} \tag{9.9}$$

The constant depends on the grain boundary energy per unit grain boundary area.

One measure of the topological state is the so called *second moment*, $\mu 2$, which is a measure of the frequency distribution of n-sided grains. $\mu 2$ is defined as:

$$\mu 2 = \frac{1}{N_t} \sum_{n=1}^{n(max)} (n-6)^2 \cdot N_n \tag{9.10}$$

where n is the number of sides, N_n the number of n-sided grains and N_t the total number of grains (e.g. Stavans & Glazier 1989). A honeycomb-shaped grain aggregate has a $\mu 2$ of 0, and the $\mu 2$ increases if more grains have a number of sides other than 6. Since many sided grains are on average larger than few sided grains, the second moment is also a measure of the size frequency distribution of grains. Different results are presented in literature on the time dependence of $\mu 2$. $\mu 2$ may be time dependent (Anderson 1988; Soares *et al.* 1985; Weaire & Kermode 1983) or remain constant once a steady state topology has been reached (Stavans & Glazier 1989; Wejchert *et al.* 1986). With the model presented here it is observed that $\mu 2$ varies between 1.2 and 2.2 (fig 9.20.b). The growth history is too short to unambiguously see whether $\mu 2$ remains settles down to a constant value.

In a 3D aggregate the second moment must be defined differently, since the average number of sides per grain is not 6, but 12. However, one can assume that the same principle, that of a stable $\mu 2$, should apply to 3D. If one knows this stable $\mu 2$ for 3D, and how to calculate $\mu 2$ from a 2D section through a grain aggregate, one should be able to get an impression of the maturity of a recrystallised grain aggregate. The translation to 3D has not been done (yet), so at this stage only the possibility to use the second moment as a tool to determine maturity of an aggregate can be indicated. This also applies to the rest of this chapter.

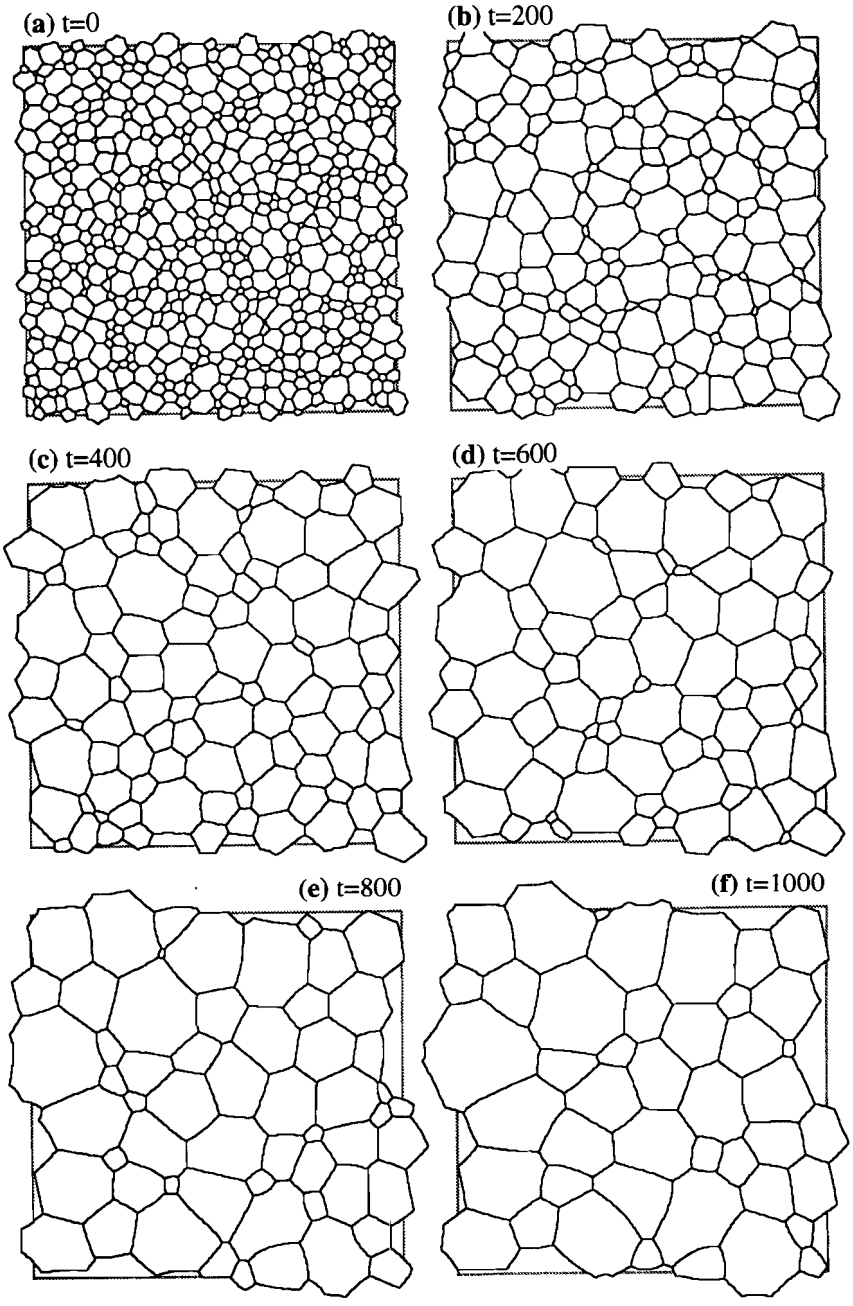

Fig. 9.19. *A grain aggregate growing from 602 to 44 grains in 1000 time increments (every node moved 2000 times). Settings: L=5 pixels, unit cell 400x400 pixels. $2Mg\Delta t=1$. The slight wiggle in the grain boundaries is an artefact of the drawing routine of the program: the true positions of the nodes (in floating points) is rounded of to screen coordinates in pixels (integers)*

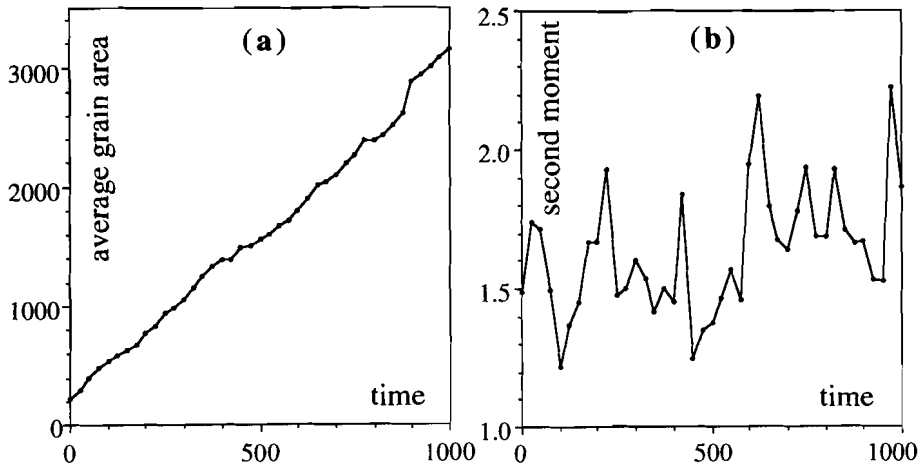

Fig. 9.20. (a) average grain area and (b) second moment as a function of time for the grain growth test shown in figure 9.19.

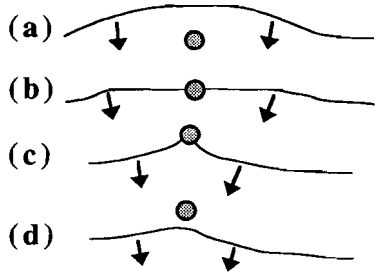

Fig. 9.21. Pinning and subsequent release of a migrating grain boundary by a small second phase particle.

9.2.2 Pinning by second phase particles

Grain boundary movement can be stopped or slowed down by second phase particles (Detert 1978; Gladman 1966; Stüwe 1978). This process is called *pinning*. The *pinning force* or *-strength* of a particle is proportional to its size. When a migrating grain boundary reaches a particle, it is stopped by the particle (fig. 9.21). The boundary adjacent to the particle may continue to migrate and than wraps around the particle (fig. 9.21.c). At a certain stage it may "break loose" again from the particle (fig. 9.21.d).

Modelling pinning

One problem to incorporate pinning in the computer model is the fact that the boundaries are defined by the nodes and if particles are small, two nodes may move past a particle without "noticing" the pinning particle. To incorporate pinning, the particles are made of size LxL. As soon as a node enters the region occupied by a particle, it gets pinned. The node is moved to the centre of the particle region and the program adds a "label" or "flag" to the node, indicating that it is pinned. In subsequent steps the desired displacement of the node is calculated each time, as if the node was not pinned. However, it will only be moved according to that displacement vector, if the calculated displacement is larger than a certain pre-defined minimum distance. This minimum distance represents the *pinning force* of particles. Dragging of the pinning particle by the grain boundary (Ashby & Centamore 1968) can be incorporated as well, by moving the particle according to the drag force exerted on the particle by the pinned grain boundary. The rather complicated algorithms involved in modelling this are however not yet finished.

Results

An example of growth influenced by pinning particles is shown in figure 9.22.a. Pinning stops the migration of grain boundaries at certain points and this of course slows down grain growth (fig. 9.22.b). A grain boundary that is pinned at two points will become straight and remains unchanged until it breaks loose from the pinning particles. Eventually all grain boundaries will become pinned and no growth will take place any more - the aggregate is effectively "locked" or "frozen" by the pinning particles. The grain size at which this will happen depends on the number of pinning particles and the pinning force - the more particles, the smaller the final grain size.

Most particles are inside grains at the onset of growth. The grain boundaries of shrinking grains eventually meet these particles and become pinned. Grains therefore often do not vanish completely, but remain as small completely pinned grains. This implies that the average grain size of the aggregate does not increase much. These small, pinned, grains often have few sides: 2, 3 or 4. Having many few sided grains implies having relatively many many-sided grains, since the average number of sides per grain must remain exactly six. Therefore the second moment will increase to values higher than 1.5-2 in case of pinning, which is indeed the case (fig. 9.22.c).

During unpinned growth, grains tend to be equidimensional, since their shape is only determined by the drive to achieve a minimum surface area. When pinning plays a role, the minimum surface area is not the only factor, and small grains are often strongly non-equidimensional, as their shape is determined by the distribution of the pinning particles.

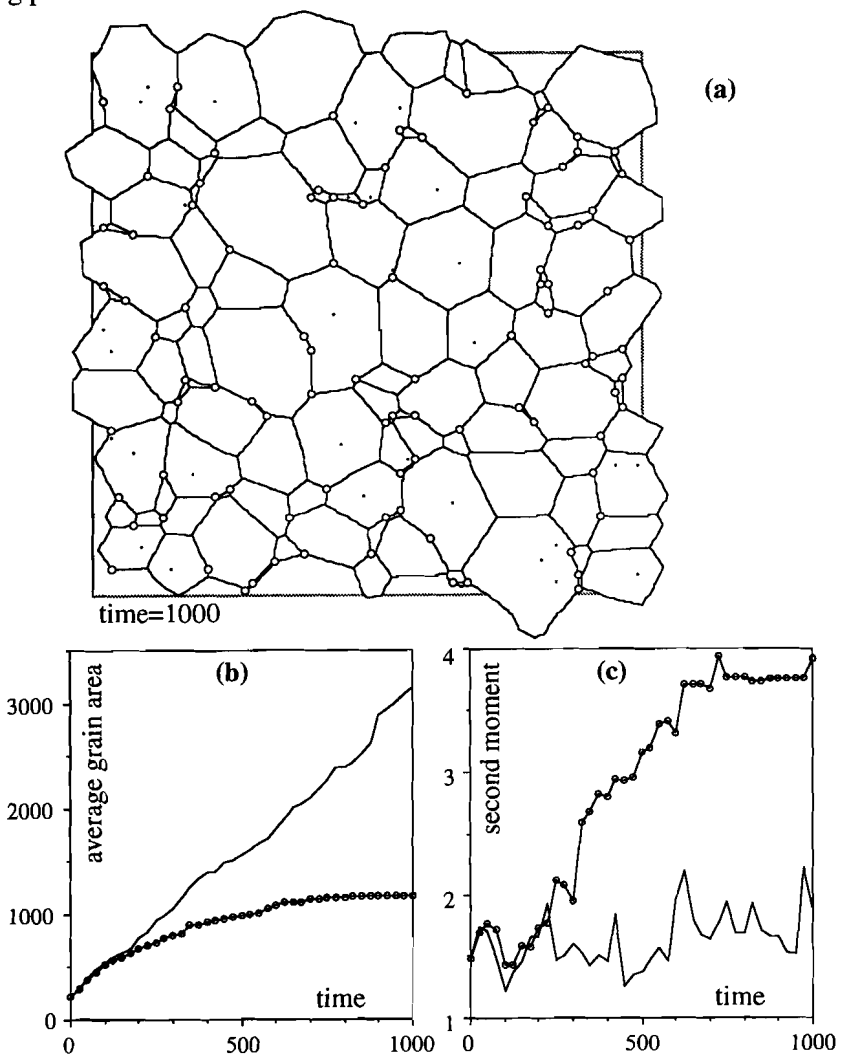

Fig. 9.22. Examples of growth with pinning by approximately 121 second phase particles. Starting materials is the same as shown in Fig. 9.19.a. (a) The grain aggregate after 1000 time increments. Particles inside grains are shown as small dots and particles that pin grain boundaries are shown as larger circles. Average grain area (b) and second moment (c) as a function of time for the run shown in (a) (dots), shown together with the data shown in Fig. 9.19, a run with the same growth settings, but no pinning.

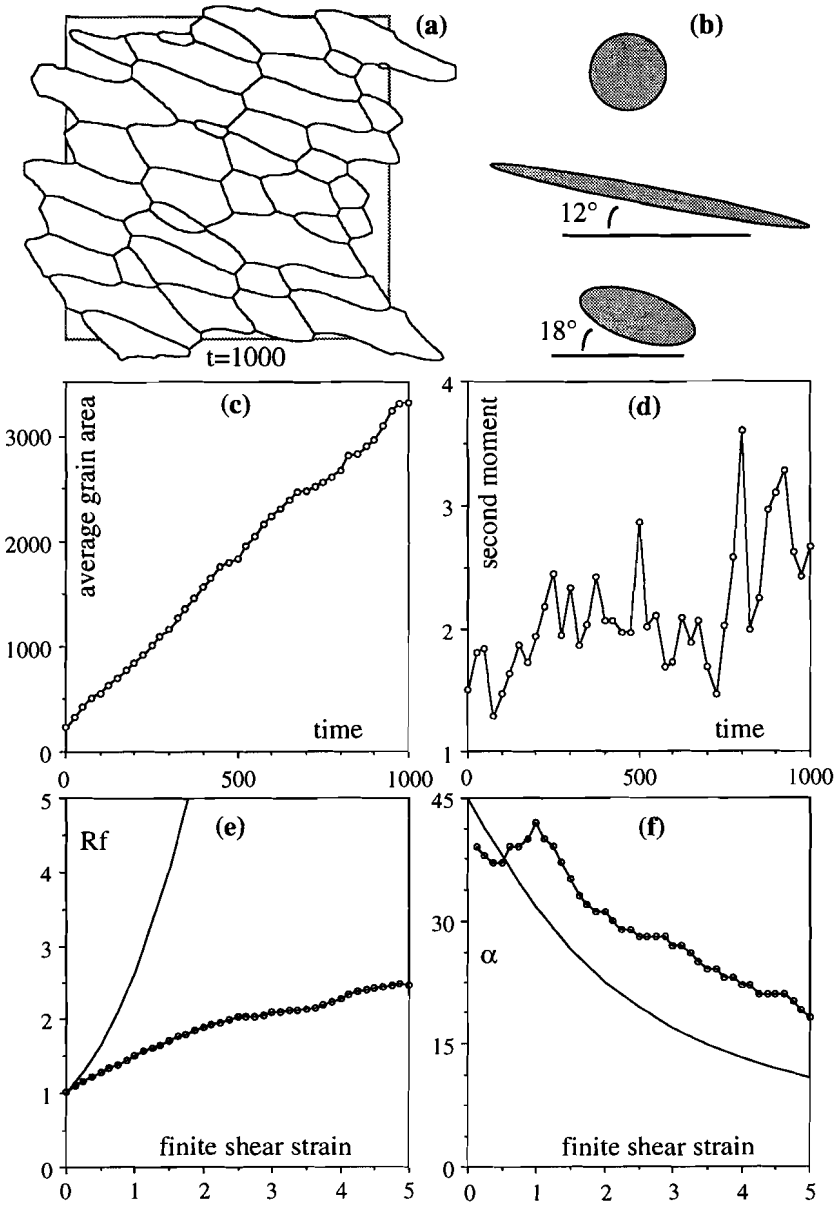

Fig. 9.23. *Example of growth during deformation. (a) the grain aggregate after 1000 time increments at a finite shear strain of 5 (top to left). (b) A passively deforming circle (top) would be sheared to an ellipse with an axial ratio of 26, making an angle of 12° with the flow plane (middle). The average grain shape after growth is an ellipse with an axial ratio of 2.4, making an angle of 18° with the flow plane (bottom). Average grain area (c) and second moment (d) as a function of time for the run shown in (a). Average grain ellipse axial ratio, Rf, (e) and orientation, α, (f) as a function of finite shear strain. Lines with small circles (datapoints) represent data from the run shown in (a) and the plain line represents a passively deforming circle.*

9.2.3 Deformation during growth

The effect of deformation during growth at conditions such that grain boundary energy is the dominant driving energy for migration of grain boundaries was discussed in §9.1. This process can be simulated with the improved model as well.

Modelling deformation during growth

Deformation during grain growth is simulated by deforming the grain aggregate (defined by node-positions) in small increments, between increments of growth. Deformation is defined by an incremental position gradient tensor **F**. The first and simplest way to simulate deformation is to take the position $\boldsymbol{x}$ of each node and multiply this by **F** to get the new position $\boldsymbol{x}'$. This routine corresponds to homogeneous intracrystalline deformation.

A different routine is aimed to simulate diffusion accommodated grain boundary sliding (Ashby & Verrall 1973). In this case the centre of each grain ($\boldsymbol{g}$) is calculated by taking the average of all positions of nodes on its boundaries. The position of the grain centre after a deformation increment ($\boldsymbol{g}'$) is then calculated by multiplying $\boldsymbol{g}$ with **F**. In case of grain boundary sliding, the whole grain moves with the same displacement vector $\Delta\boldsymbol{g}=\boldsymbol{g}'-\mathbf{g}$ (neglecting rotation). All nodes on the grain boundary get the same displacement vector. However, each grain boundary node is shared by 2 or 3 grains, resulting in 2 or 3 different displacements for each node. Moving grains as a whole leads to voids and overlapping grains. Diffusional mass-transfer transfers material from the overlapping sites to the developing voids during diffusion accommodated grain boundary sliding. This is simulated by taking the average of the 2 or 3 displacements for each node, and displacing the node according to that average. This way no voids or overlaps can develop.

Results

Figure 9.23 shows results for one run with the same starting grain aggregate as before. A simple shear deformation (top to left) using the grain boundary sliding routine was applied with a shear strain increment of 0.005 per time increment. The following observations are made:

(1) Growth rate is not significantly affected by deformation (fig. 9.23.c),
(2) The second moment is high and variable (fig. 9.23.d),
(3) The average grain shape axial ratio and the orientation of the average long axis of the grains lag behind the values for a passively deforming circle (fig. 9.23.b,e,f). Note that this is not only due to grain growth (§9.1), but also to the grain boundary sliding.

9.2.4 Discussion & conclusions

The model presented here enables a realistic simulation of grain growth. The basic structure of the model, the simulation of grain boundaries by series of nodes, is flexible and enables the modelling of several processes, such as pinning by second phase particles and contemporaneous deformation. Anisotropic grain boundary energies (Gleiter 1969a&b), i.e. grain boundary energies that are dependent on the orientation of the grain boundary with respect to the lattice orientations of the grains on either side of the grain boundary, are not (yet) incorporated in the model. Only few grain growth models incorporate this effect (Grest *et al.* 1985). The structure of the model presented here is such that anisotropic grain boundary energies can be modelled with little difficulty.

The first results presented in this section suggest that measurements of grain shape, second moment, shape preferred orientation, etcetera can give information on the maturity of the aggregate, the occurrence and significance of pinning by second phase particles and deformation during grain boundary energy induced grain boundary migration. A grain aggregate that has undergone a long period of grain growth without any disturbance by for instance pinning will have equidimensional grains with smoothly curved grain boundaries and a low second moment. Straight grain boundaries, a high second moment and non-equidimensional grains are signs of pinning by second phase particles. A foam texture with a shape preferred orientation and a moderately high second moment may be indicative of simultaneous deformation and grain growth. Strain analysis based on the grain shape is a very unreliable in that case.

An important step that still has to be taken is the translation of the findings from the two-dimensional model to 3 dimensions. The same principles do apply in three dimensions, but the values of topological parameters such as the second moment remain to be determined. An additional problem is the determination of these parameters from 2-dimensional (thin) sections.

This research is still in progress. The potential applications will be further investigated and tested in the future. The intention is to add routines to model the effect of anisotropic grain boundary energies, the dragging of pinning particles by grain boundaries and the effect of the spatial distribution of pinning particles. The model may also be used in the field of paleopiezometry (Drury, *pers comm.*). One would ideally also want to incorporate intracrystalline deformation mechanisms and their effect on the grain boundary migration. The basic set-up of the model, based on a network of grain boundary nodes, is however not very suitable for this and it is therefore qustionable whether this model can be extended for this purpose.

Appendix A

Definition of stress and strain rate tensors and 3-D power-law creep

A.1 General

Stress and strain rate tensors as used in this thesis are defined in this appendix. A 3 dimensional power-law relating differential stress and strain rate tensors is then given, with the equations to apply it to the two experimental deformational configurations: axisymmetric shortening and simple shear deformation. The principles and derivations can be found in standard text books on continuum mechanics.

Standard indicial notation is used in this thesis. When indices are not used, tensors are given in bold face capitals, vectors in bold face lower case italics and scalars in plain text.

A.1.1 Stress and strain rate tensors

The stress tensor (σ_{ij}, or Σ) defines the state of stress at a given point in a continuum. If $\boldsymbol{t}^{(n)}$ is the stress- or traction-vector acting on a surface element with $\boldsymbol{n}$ as the normal vector, then: $t_i^{(n)} = \sigma_{ij} n_j$ (A.1)

Compression is taken as positive (except in chapter 7.2, where extensional strain is modelled), as is common practice in geology. The hydrostatic pressure (P) is defined as the mean normal stress, which is one third of the trace of the stress tensor:

$$P = \sigma_{ii}/3 \quad (A.2)$$

In most cases it is useful to split the stress tensor in a hydrostatic stress tensor (Σ_H) and a deviatoric stress tensor (Σ_D or τ_{ij}): $\Sigma = \Sigma_D + \Sigma_H$ (A.3)

with:

$$\Sigma_H = \begin{pmatrix} P & 0 & 0 \\ 0 & P & 0 \\ 0 & 0 & P \end{pmatrix} \text{ and } \Sigma_D = \tau_{ij} = \begin{pmatrix} \sigma_{11}-P & \sigma_{12} & \sigma_{13} \\ \sigma_{21} & \sigma_{22}-P & \sigma_{23} \\ \sigma_{31} & \sigma_{32} & \sigma_{33}-P \end{pmatrix} \quad (A.4a,b)$$

In a deforming continuum, where each material point at position $\boldsymbol{x}$ has a velocity of $\boldsymbol{v}$, the velocity gradient ($\mathbf{L}$) tensor is defined as:

$$\mathbf{L} = \partial v_i/\partial x_j \quad (A.5)$$

The strain rate tensor ($\dot{\varepsilon}_{ij}$) is defined as:

$$\dot{\varepsilon}_{ij} = 1/2(\partial v_i/\partial j + \partial v_j/\partial i) \quad (A.6)$$

A.1.2 Power-law creep

A power-law relation between stress and strain rate is often found for minerals and rocks deforming in the ductile regime. This flow law is usually only used in one dimension:

$$\dot{\varepsilon}_{11} = A \cdot e^{-Q/RT} \cdot (\sigma_{11}-\sigma_{33})^n \qquad \text{(A.7.a)}$$

Here, stress and strain rate are scalars, with the stress usually defined as the difference between the maximum and minimum principle stresses. The pre-exponential factor A, the stress-exponent n and the activation enthalpy Q are material dependent. R is the gas-constant and T the absolute temperature. In this research the temperature was kept constant and equation (7a) can be simplified with a pre-exponential factor (B), which incorporates temperature:

$$\dot{\varepsilon}_{11} = B \cdot (\sigma_{11}-\sigma_{33})^n \qquad \text{(A.7.b)}$$

In three dimensions the equivalent of this equation is (e.g. Cobbold 1983; Schmid *et al.* 1987):

$$\dot{\varepsilon}_{ij} = B \cdot T_{II}^{n-1} \cdot \sigma \qquad \text{(A.8)}$$

Here B is again a material dependent pre-exponential factor and T_{II} is the second invariant of the deviatoric stress tensor:

$$T_{II} = \sqrt{(\tau_{ij}\tau_{ij})} \qquad \text{(A.9)}$$

It is assumed here that the same flow law applies for different deformation geometries, although this may not necessarily be the case (Franssen & Spiers 1990). However, not enough experiments were performed to determine flow laws for pure shear and simple shear independently and in fact the shear strain values predicted from the 3-D flow laws derived from axisymmetric shortening experiments (chapter 5) were in good agreement with the measured shear strain rates at low shear strain (chapter 6).

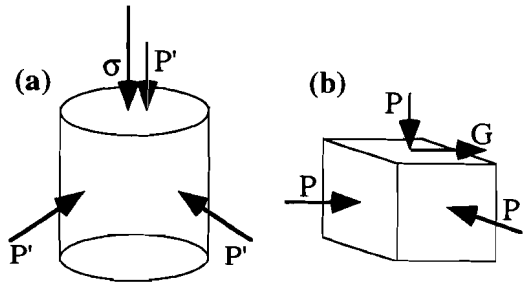

Fig A.1. Stress-vectors in the axisymmetric (a) and ring-shear configuration (b).

A.2 Axisymmetric deformation configuration

In the axisymmetric configuration a cylindrical specimen is subjected to an applied hydrostatic pressure P' and a stress σ in one direction (taken here as i=1, fig. A.1.a). The resulting stress tensor then is:

$$\sigma_{ij} = \begin{pmatrix} \sigma+P' & 0 & 0 \\ 0 & P' & 0 \\ 0 & 0 & P' \end{pmatrix} \quad \text{and} \quad \tau_{ij} = \begin{pmatrix} \frac{2}{3}\sigma & 0 & 0 \\ 0 & -\frac{1}{3}\sigma & 0 \\ 0 & 0 & -\frac{1}{3}\sigma \end{pmatrix} \qquad \text{(A.10a,b)}$$

and $T_{II} = \sigma\cdot\sqrt{2/3}$ (A.10.c)

Note that the actual hydrostatic pressure is not P, but P'+σ/3. The length (h) of the sample is monitored during an experiment. From this the shortening rate ($\dot{\varepsilon}$) in direction i=1 is derived with:

$$\dot{\varepsilon} = \dot{\varepsilon}_{11} = \frac{1}{h}\frac{\partial h}{\partial t} \qquad \text{(A.11a)}$$

If the material is incompressible - as is assumed - then:

$$\dot{\varepsilon}_{22} = \dot{\varepsilon}_{33} = -\frac{1}{2}\dot{\varepsilon}_{11} = -\frac{1}{2}\dot{\varepsilon} \qquad \text{(A.11.b)}$$

Combining equations 9, 10 and 11 gives:

$$\dot{\varepsilon} = B\left(\sigma\sqrt{2/3}\right)^{n-1}\sigma \;\Leftrightarrow\; \dot{\varepsilon} = B\left(\sqrt{2/3}\right)^{n-1}\sigma^{n} \qquad \text{(A.12)}$$

We now have an equation that relates the applied stress (σ) and the measured shortening rate ($\dot{\varepsilon}$). From this equation the stress-exponent and the pre-exponential factor can be calculated if several s-e measurements are available. This is done by making a linear regression through the log(σ)-log($\dot{\varepsilon}$) data.

A.3 Ring shear configuration

A.3.1 Applying 3-D flow law to simple shear

In the simple-shear configuration (fig A.1.b) a hydrostatic confining pressure (P) is applied on the specimen and a shear stress G on the grips. The stress and differential stress tensors now are:

$$\sigma_{ij} = \begin{pmatrix} P & G & 0 \\ G & P & 0 \\ 0 & 0 & P \end{pmatrix} \text{ and } \tau_{ij} = \begin{pmatrix} 0 & G & 0 \\ G & 0 & 0 \\ 0 & 0 & 0 \end{pmatrix} \qquad \text{(A.13.a\&b)}$$

and $T_{II} = G\cdot\sqrt{2}$ (A.13.c)

Note that Cartesian coordinates are used for a cylindrical geometry. This is necessary for compatibility with the treatment of the axisymmetric configuration. The circular shear zone is treated here as if being "unwrapped". The relative displacement rate (v)

of the upper grip with respect to the lower grip is measured during an experiment. The shear strain rate ($\dot{\gamma}$) for a specimen thickness of h is derived from this with:

$$\dot{\gamma} = \frac{v}{h} = 2\dot{\varepsilon}_{12} = 2\dot{\varepsilon}_{21} \qquad (A.14)$$

Combining equations A.9, A.13 and A.14 then gives:

$$\dot{\gamma}2 = B\left(G\sqrt{2}\right)^{n-1}G \Leftrightarrow \dot{\gamma} = 2B\left(\sqrt{2}\right)^{n-1}G^{n} \qquad (A.15)$$

Now we have an equation that relates the applied shear stress to the measured shear rate, according to the same flow law as used for the axisymmetric configuration.

A.3.2 Determining the shear stress

The shear stress is applied on the specimen through the torque that is applied on the upper grip (fig. A.2). Neglecting friction, this torque (T) is:

$$T = g \cdot M \cdot r_w \qquad (A.16)$$

(g= gravitational acceleration, r_w=radius of wheel (k), M=mass of weight)

The shear stress (G) on the specimen, in the flow plane, is related to the applied shear force (F) and the area (S) on which this force is applied by:

$$dF = GdS \qquad (A.17)$$

If the applied shear stress is independent of the radius (r) this equation can be rewritten as:

$$dF = 2G\pi r dr \qquad (A.18)$$

The torque at radius r is: $rdF = 2G\pi r^2 dr$ (A.19)

The total torque at the grip, from the inside at r_0 to the outside r_1, is equal to the applied torque:

$$T = \int_{r_0}^{r_1} rdF \qquad (A.20)$$

From which follows:

$$G = \frac{3T}{2\pi(r_1^3 - r_0^3)} = \frac{3gMr_w}{2\pi(r_1^3 - r_0^3)} \qquad (A.21)$$

A.3.3 Determining shear strain and shear strain rate

The applied shear stress on the sample causes the sample to deform in simple shear and therefore a rotation of the upper grip (fig A.2). The wire unwinds from the rotating wheel as the sample deforms. The rotation angle ($\Delta\omega$) of the upper grip is directly related to the bulk finite shear strain ($\Delta\gamma$) in the specimen:

$$\Delta\gamma = \frac{\Delta\omega \cdot r_s}{h} \tag{A.22}$$

where h is the height of the specimen at radius r_s. Ideally $h=r_s/3$ (A.23)

The displacement (Δu), or the unwinding length of the wire is given by:

$$\Delta u = \Delta\omega \cdot r_w \tag{A.24}$$

So the bulk shear strain is related to u as:

$$\Delta\gamma = \frac{\Delta u \cdot r_s}{r_w \cdot h} \tag{A.25}$$

The unwinding of the wire is monitored with a potentiometer. The wire is lead along a wheel on the potentiometer. The potentiometer produces a voltage which is linearly dependent on the orientation of the wheel on the potentiometer. Over 341° this voltage ranges from 0-10 V. The voltage (ΔV_p) is a linear function of the finite rotation of the wheel on the pot-meter ($\Delta\omega_p$):

$$\Delta V_p \propto c \cdot \Delta\omega_p \quad (c = 2.9343 \cdot 10^{-2}\ V/°) \tag{A.26}$$

As the orientation of the wheel with radius (r_p) on the potentio-meter is determined by the unwinding of the wire that is led along it equations A.22-26 can be combined to give the finite shear strain as a function of the voltage produced by the pot-meter:

$$\Delta\gamma = \frac{\frac{(\Delta V_p + k V_t)}{c} \cdot r_p \cdot r_s}{r_w \cdot h} \tag{A.27}$$

After one cycle of the potentio-meter the voltage returns to zero again. Therefore the voltage for one full cycle (V_t) has to be added to the voltage for the k previous full cycles of the potentio-meter. The voltage from the potentio-meter was recorded by a computer typically every 5-100 minutes, depending on the shear rate. The voltage - time data were then converted to finite shear strain - time data with a spread sheet program.

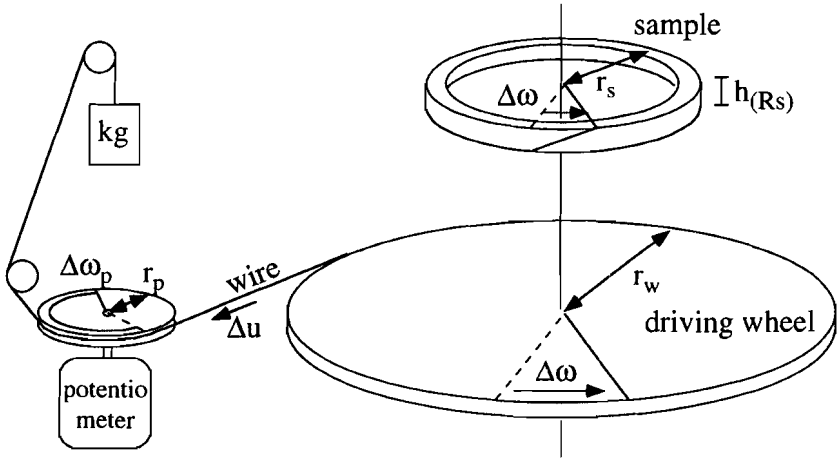

Fig A.2. *Schematic drawing of the ring shear set-up, where a wire is wound around a "driving wheel" that is fixed to the grips that hold the specimen. A dead weight hangs on the wire, which is lead along a potentio-meter to measure the unwinding of the wire as the sample deforms.*

Appendix B

Calibration of equipment

B.1 Calibration of the axisymmetric gas apparatus

The temperature control in the axisymmetric gas apparatus was checked with a thermocouple that could be inserted in a sample through a hollow piston (fig B.1.a). At a set point temperature of 30.0°C, the temperature in the sample was found to be 28°C. Temperature fluctuations over space and time were within ±0.5°C.

Displacement of the upper piston was measured with an LVDT. Its calibration is shown in figure B.2.a. Within the linear range the voltage changes 0.498 ± 0.005 V per mm.

The piston-sample column shortens elastically under an applied load. The amount of shortening was determined by measuring the displacement when a load was applied on the column, with the specimen replaced by a steel cylinder of 15 mm length and 10 mm diameter (fig. B.2.b). The displacement was found to be 0.04 mm at 1.0 MPa. This displacement is equivalent to 0.3% strain for a sample length of 15 mm. The displacement data were not corrected for this displacement, which occured at each load step.

Heating causes an increase in the total length of the sample-piston column. This was tested with a dummy-sample piston assembly, with the aforementioned steel cylinder as sample (fig B.2.c). Starting at a room temperature of 20°C the total column was found to increase 0.006 mm in length per degree centigrade. The amount of correction needed for each experiment depends on the ambient temperature at the start of the experiment. The initial increase in length was always recorded and the data corrected for this.

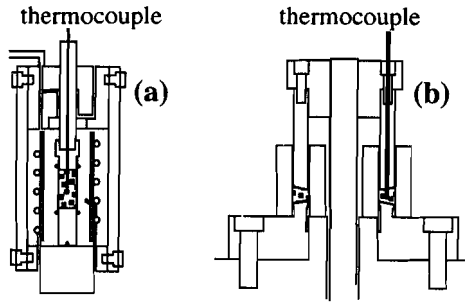

Fig B.1. *Thermocouples can be inserted in a specimen for calibration, through the the upper piston of the axisymmetric gas apparatus (a) and through the upper grip in the ring shear apparatus (b).*

B.2 Calibration of ring shear apparatus

The temperature inside the sample in the ringshear apparatus was calibrated with a thermocouple inserted inside a specimen through the upper piston (fig. B.1.b). A specimen of camphor, 3 mm thick in the middle was used and the temperature at a certain set point was measured at 4 different levels in the sample: at the upper grip, 1 mm deep, 2 mm deep and 3 mm deep, which is at the lower grip. The results for 3 different temperature settings are given in table B.1. There is a maximum temperature difference of 0.3°C within the sample, with the highest temperature at the lower grip (nearest to heaters). The difference in temperature reading between the fixed thermocouple and the actual temperature in the specimen is 0.25°C at the temperature at which all experiments were done. Recordings of the temperature reading during experiments showed that temperature fluctuated within ±0.5°C with time.

$T_{set\ point}$	$T_{reading}$	$T_{0\ mm}$ (at upper grip)	$T_{1\ mm}$	$T_{2\ mm}$	$T_{3\ mm}$ (at lower grip)
90 F	29.0	28.6	28.7	28.7	28.8
120 F	41.4	40.9	41.0	41.0	41.2
150 F	50.9	50.1	50.1	50.3	50.4

Table B.1. *Relation between set point temperature (in Farenheit), measured temperature at fixed thermocouple and temperatures measured at four levels inside a camphor specimen (all in °C).*

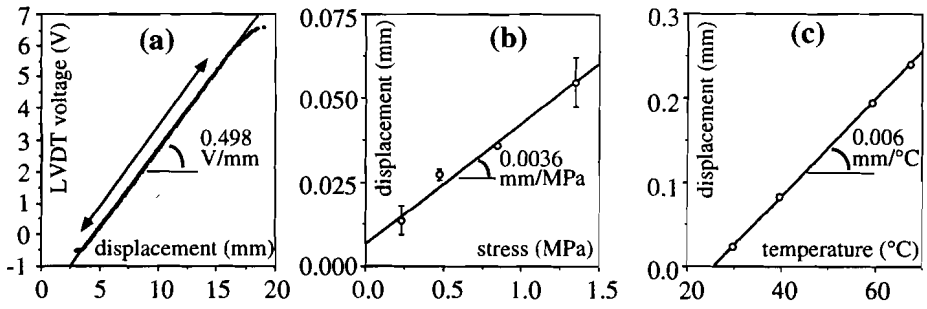

Fig B.2. *(a) Calibration of LVDT (Urai & Jessell, unpublished data). Output-voltage (in V) of the LVDT as a function of displacement (in mm). (b) Elastic deformation of pistons+sample column (vertical displacement in mm) as a function of applied stress (in MPa), determined with a steel dummy sample. (c) Expansion (in mm) of the pistons+sample column because of heating (in °C), relative to the length of the column at 20°C.*

The unwinding of the wire that transmits the force from the dead weight to a torque on the sample (fig A.2) is measured with a potentiometer. This device produces an output voltage that changes linearly with the angular rotation of its axis. The calibration of the angular orientation (ω_p) versus output voltage is shown in figure B.3. The output voltage returns to the original value after one full rotation of 360°. There is however a "window" of 19.2° in which no output is given.

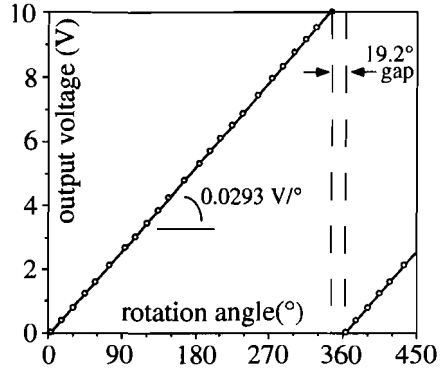

Fig. B.3. Calibration of the potentiometer: output voltage (V) as a function of rotation angle. The output voltage of the potentiometer is a linear function of the rotation angle of its central axis. The potentiometer does not produce a signal in a window of 19.2°.

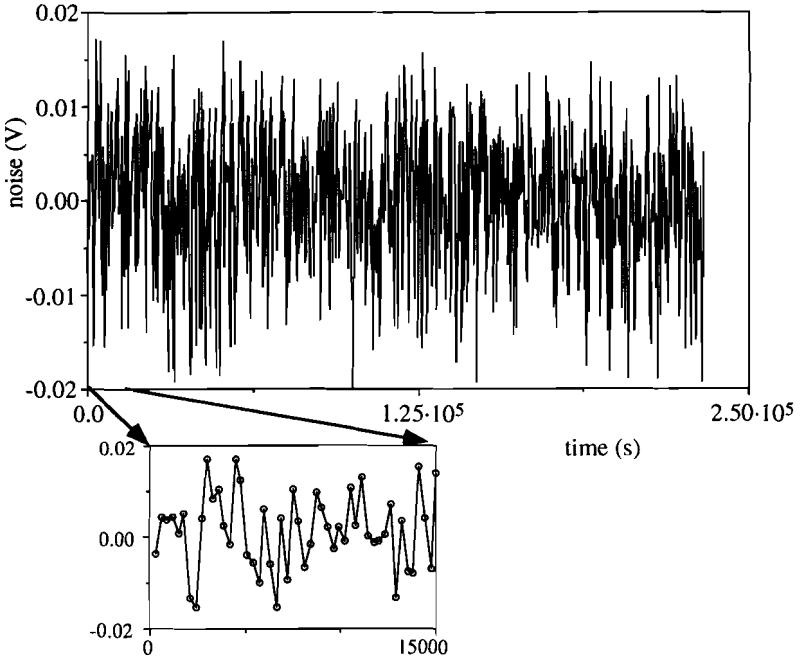

Fig B.4. Output signal of potentiometer, with constant rotation angle, recorded every 300 seconds (averaged over 30 s interval). The ideal signal would be zero Volt (average over all ≈750 data points), the deviations are noise. Blow-out shows the record over the first 1500 s, showing that (a major part of) the noise has a wave length less than 300 s.

Data analysis

To reduce noise at an early stage in the data recording the data were recorded over a period of time, typically 10% of the logging interval, and averaged. To test the remaining noise/errors in the output, the voltage was recorded every 300 seconds over a period of $2.3 \cdot 10^5$ s ($\approx$ 3 days), while the angular orientation of the potentiometer was not changed (fig B.4). It was found that the variation is in the order of ± 0.015 V ($\pm 0.15\%$ of signal range of 10 V, which is according to factory specifications). This means that the noise in the calculated bulk shear strain is about $\pm 10^{-4}$ (potentiometer small wheel, largest driving wheel) to $\pm 10^{-2}$ (potentiometer largest wheel, small driving wheel). This error is not visible in the bulk shear strain - time curves, but it can cause a problem for the calculation of the shear strain rate. This is illustrated in figure B.5.a. Here it is supposed that the signal shown in fig B.4 was the measured signal, which is converted to shear strain for the case where the largest wheel was used for the potentiometer in combination with the smallest driving wheel. Since the potentiometer is not rotating, the shear strain and shear strain rate should be zero. The measured shear strain values however change up to ± 0.03 in 300 s, which is equivalent to a virtual shear strain rate of $\pm 1 \cdot 10^{-4}$ s^{-1}. This is of the same order as the bulk shear strain rates that must be measured. The data must therefore be filtered to reduce the effects of noise on the shear rate measurements. A suitable Fourier-filtering routine was unavailable at the time of processing the data, so a simpler, moving-window linear least-squares interpolation routine was used (fig B.6).

A data-set will consist of N pairs of time - shear strain data. During a time interval, of length 2w, from t*-w to t*+w, the shear strain is assumed to change linearly with time, which implies that the shear strain rate is assumed to be constant. A linear least-squares best fit of the form:

$$\gamma = \gamma_0 + \dot{\gamma}(t^*-t) \qquad (B.1)$$

is made through all data available in the given time-window. Then $\gamma=\gamma_0$ at $t=t^*$, and the shear strain rate is $\dot{\gamma}$. t* is then incremented by Δt to calculate the shear strain and shear strain rate and the next point in time. The result is a set of time, shear strain and shear strain rate data. The choice of w and Δt depends on the time interval at which the data were recorded, the shear strain rate, the radii of the driving wheel and potentiometer wheel and the magnitude of the noise in the data-acquisition. To keep resolution as high as possible, w and Δt must be chosen as small as permitted by these factors. Figures A.5.b&c show the results of two choices of w, to process the data set of figure A.5.a. Δt was set to 5000 s and the window width was set at w=1000 s and w=25000 s. w=1000 reduces the variations in shear strain by a factor

4, and variations in the shear strain rate by a factor 10 ($\pm 10^{-5}$ s^{-1}). When w is chosen to be 25000 s, we see that the error in shear strain is reduced to less than ± 0.002 and the errors in shear strain rate are now less than $\pm 10^{-7}$ s^{-1}. For each experiment a minimum value for w was chosen such that the the resulting fluctuations in shear strain rate were on average about one order of magnitude less than the average shear strain rate. This means that variations in shear strain rate below a certain threshold in amplitude and wavelength can not be resolved. The threshold depends on the radius of the driving wheel, the potentiometer wheel and the frequency of data acquisition.

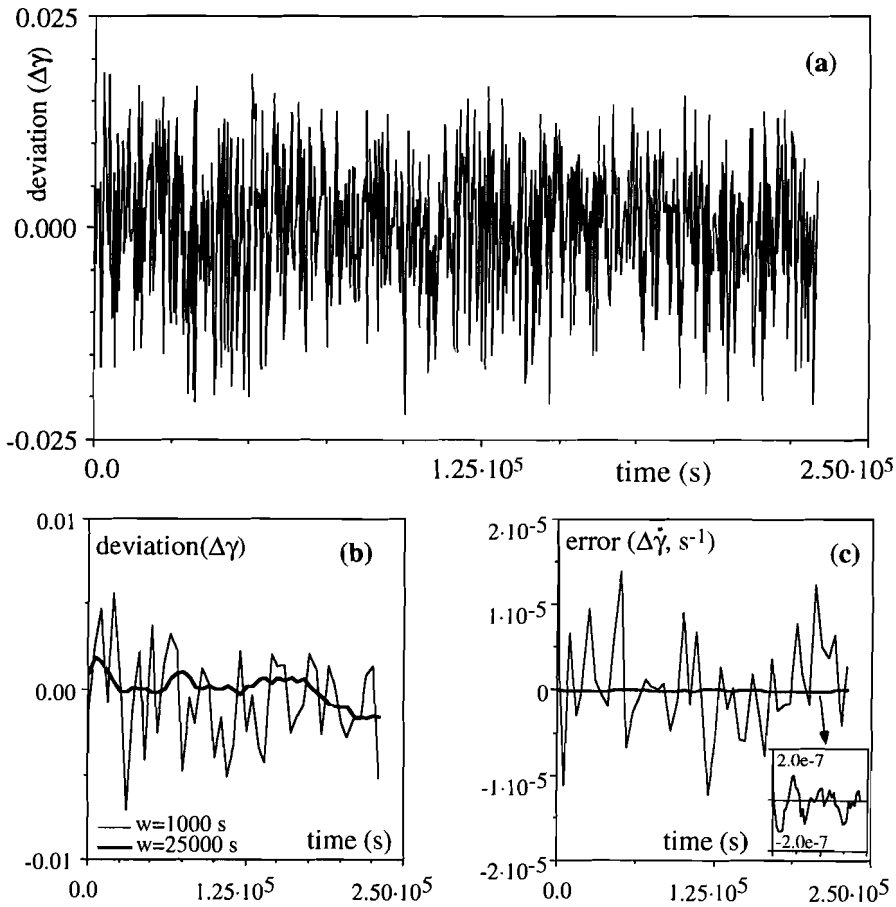

Fig B.5. *(a) The shear strain - time curve derived from the data shown in figure B.4. The potentiometer was not rotating, so the shear strain should be zero over the whole range. The deviations are caused by noise. (b) The same shear strain - time curve after moving-window linear least squares interpolation. (c) Shear strain rate calculated with the same filtering. With a moving-window width of w=25000 s, the error in shear strain rate determination from the data is reduced from $1 \cdot 10^{-4}$ s^{-1} to less than $1 \cdot 10^{-7}$ s^{-4} (inset). Δt=5000 s, w=1000 s (6-7 data points, thin line) and w=1000 s (167 data points, heavy line).*

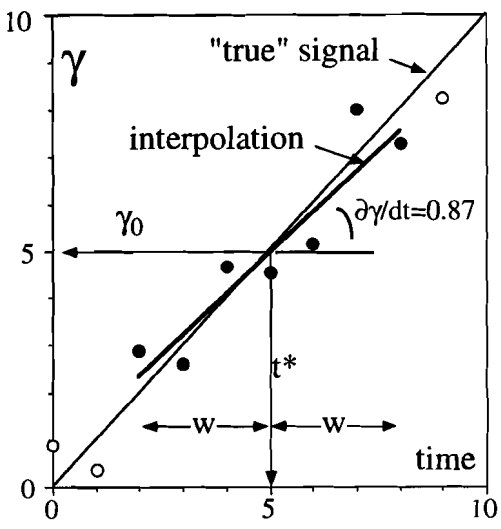

Fig B.6. Example of the linear moving-window least-squares interpolation routine. The graph shows a set of shear strain - time data, containing errors (because of noise). An estimate of the shear strain and shear strain rate at point $t=t^*$ (=5) is made by performing a best fit through all data available in the time window $t^*-w < t < t^*+w$ (7 data points shown black in example). The least-squares best fit obtained in this case (for $t^*=5$ and $w=3$) is $\gamma=0.67582+0.86675 \cdot t$. That means that the estimate for $t=5$ is $\gamma=0.501$ and $\dot{\gamma}=0.867$. The true values for $t=5$ are $\gamma=5.000$ and $\dot{\gamma}=1$. One can see that the estimate for the shear strain is quite accurate, even with a relative large error in the data, but the estimate for the shear strain rate is relatively larger.

Estimate of friction along the confining cylinders

One component of friction is the friction due to sticking of the deforming sample to the rigid inner and outer confining cylinders. The magnitude of this friction could not be determined in the short period of time that the apparatus has operated so far. This must certainly be done now the apparatus has proven its value.

An estimate of the magnitude of friction can be made by considering possible flow fields in the specimen that can arise because of sticking (fig. B.7.a). The velocity vectors of material particles must be parallel to the shear direction, so in the following analysis the velocity field in a section perpendicular to the shear direction is taken as a scalar field. Taking the flow plane as horizontal in the middle of the specimen, the vertical (y) velocity gradient is ideally independent of y (dashed lines in figure B.7.a). In the case of complete coupling between the confining cylinders and the specimen, the velocity will be zero at the contact and the velocity field will be distorted and resemble the curved contours in figure B.7.a.

We will now estimate the effect of the distorted flow field on the measured bulk shear rate (relative displacement rate of grips divided by sample thickness) at a certain shear stress applied on the grips. We will only consider one half of the section through the sample and use a square section through a straight shear zone for simplicity (fig. B.7.b). At the grips the velocity of material particles is the same as that of the grip: $v_{(y=0.5)} = 1$, whereas on the middle plane the velocity is the same as

that of the confining cylinders, taken as $v_{(y=0)} = 0$. The velocity profile at the contact with the confining cylinders (x=0 or 1) depends on the amount of adhesion at the interface. In the ideal case we have $v_{(x=0,1)} = y$, and in the worst case $v_{(x=0,1)} = 0$. The actual flow field inside the sample will depend on the adhesion at the interface and the flow properties of the sample material and the determination of it requires complicated computation. The simplified approach here is to assume a certain flow field as drawn in figures B.7.c (ideal case scenario) and B.7.d (worst case scenario). It is then determined what normalised shearstress (G^*) is needed to achieve a certain bulk shear rate (i.e. velocity at the grips). The normalisation is with respect to the ideal case where $G^*=1$. The integral for x=0 to 1 over de shear stresses in the material at y=0 is equal to the shear force applied on the grip. Divided by the area of the grip (unity here) this is equal to the shear stress applied on the grip:

$$\int_{x=0}^{x=1} G_{(x)}dx = G^* \tag{B.2}$$

The shear stress in the material is related to the velocity gradient with

$$G \propto \left(\frac{dv}{dy}\right)^{1/n} \tag{B.3}$$

Equations B.2 and B.3 were solved numerically for different values of n for the flow field shown in figure B.7.d (fig B.7.e). We now have an estimate of how much extra shear stress is needed to achieve a certain velocity at the grips, and thus a certain bulk shear rate, in the worst case. At a stress exponent of 1, one must apply more than 3 times as much shear stress to get the same bulk shear rate as would be the case when no sticking occurred at the confining cylinders. G^* is much lower for higher stress exponents

In the reality a shear stress is applied on the grips and the displacement rate of the grips is measured. The bulk shear strain rate ($\dot{\gamma}^*$) measured at a certain stress, relative to the shear strain rate that would occur at that stress in the ideal case can be estimated with:

$$\dot{\gamma}^* = \left(\frac{1}{G^*}\right)^n \tag{B.5}$$

In the worst case, the measured bulk shear rate ranges from 0.3 (n=1) to 0.4 (n>1) of the shear rate that would be measured in the ideal case (fig. B.7.e). Measured shear strain strain values in OCP and camphor may therefore be up to 60% to low. Observations of the deformed samples showed that the finite shear strain at the outside was of the same order as in the centre of the sample. From this one can infer that the actual flow field in the sample is far from the worst case scenario and that errors in the measured bulk shear rate are less than 60%. In case of strong localisation of shear near te grips, as observed in camphor, the shear rate values are less meaningfull.

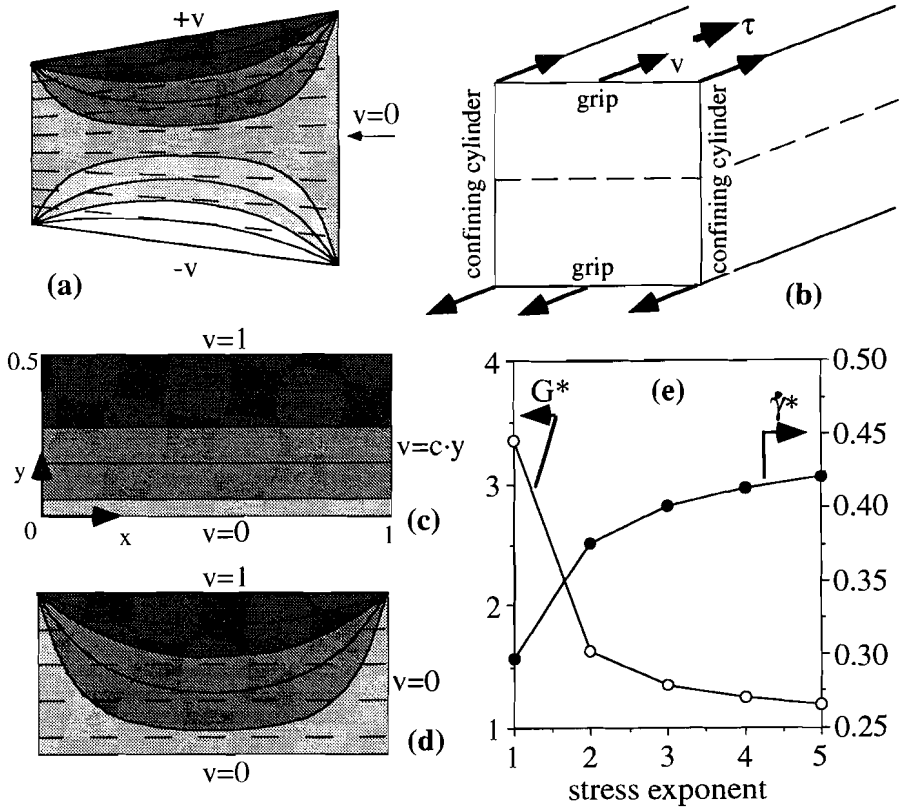

Fig B.7. (a) Possible flow fields in a section perpendicular to the shear direction, ideal situation (dashed lines) and worst case, where coupling between sample and confining cylinders is complete (shaded contours). (b) schematic explanation of the model to estimate the effect of sticking on the measured shear stress - bulk shear strain rate values. (c) Flow field in the ideal case, (d) flow field in the worst case. (e) graph of the relative measured shear stress (G^*) at a certain bulk shear strain rate (left axis) and the relative measured shear strain rate ($\dot{\gamma}^*$) at a certain bulk shear stress (right axis), both as a function of stress exponent for the worst case scenario.

Appendix C

List of symbols

Strain and deformation

$\mathbf{F}$	Position gradient tensor
$\mathbf{L}$	Velocity gradient tensor
D or $\dot{\varepsilon}_{ij}$	Strain rate tensor
$\overline{D}$	Average strain rate tensor of composite
$\boldsymbol{x}$	Position vector of material point before deformation increment
$\boldsymbol{x}'$	Position vector of material point after deformation increment
$\Delta\boldsymbol{x}$	Displacement vector of a material point
$\boldsymbol{v}$	Velocity vector of material point
$\boldsymbol{d}$	Rigid body translation vector
$\boldsymbol{l}$	Rigid body velocity vector
$\dot{\gamma}$	Shear strain rate
$\dot{\varepsilon}$	Shortening rate
γ	(bulk) Finite shear strain
ε	Finite strain
W	Vorticity (Means et al 1980)
S	Spin
W_k	Kinematic vorticity number (Truesdell 1953)

Stress and forces

Σ or σ_{ij}	Stress tensor
Σ_D or τ_{ij}	Deviatoric stress tensor
Σ_H	Hydrostatic stress tensor
$\overline{\Sigma}$	Average stress tensor of composite
$\boldsymbol{t}$	Traction vector
P	Pressure = mean normal stress
T_{II}	Second invariant of deviatoric stress tensor
g	Gravitational acceleration

Axisymmetric gas apparatus and bulk ring shear apparatus

T	Torque applied on grip in ring shear apparatus
M	Mass of dead weight
r	Radius
r_w	Radius of driving wheel
r_s	Radius of sample
r_p	Radius of potentio-meter wheel
r_0, r_1	Inner and outer radius of sample
P'	Applied confining pressure in axisymmetric gas apparatus
σ	Applied vertical compressive stress in axisymmetric gas apparatus
h	Height of sample
G	Applied shear stress
ω	Rotation angle of upper grip
u	Displacement or unwinding distance of wire
ω_p	Rotation angle of upper grip
V_p	Output voltage of potentio-meter
k	Number of full rotation cycles of potentio-meter
V_t	Voltage for one full cycle of potentio-meter
t^*	Time for which linear least square interpolation is made
w	Half width of time window for least square interpolation
G^*	Actual shear stress at a certain applied shear strain rate
$\dot{\gamma}^*$	Actual shear strain rate at a certain applied shear stress

Material properties, modelling and two-phase materials etc.

P	(Mechanical) Properties
A	Pre-exponential factor in power law equation
Q	Activation enthalpy in poer law stress-strain rate equation
R	Gas constant
B	Pre-exponential factor, inclusing temperature dependency
n	Stress exponent
η	Viscosity
η^V	Viscosity at Voigt bound
η^R	Viscosity at Reuss bound
$[\eta]$	Intrinsic viscosity
E	Young's modulus

E_c	(Normalised) Young's modulus of the composite
R^E	Ratio of Young's moduli of the two components ($R^E \geq 1$)
R^B	Ratio of pre-exponential coefficients for composites of power-law creep materials
n	Poisson's ratio
μ	Coefficient for interaction between matrix and inclusion or stress concentration factor
H	Relative horizontal distance between Reuss and Voigt bounds
F	Fraction
c	(subscript for) composite
0	(subscript for) matrix/reference phase
p	(subscript for) porosity
w,s	(subscript for) soft/weak phase,
h	(subscript for) hard/strong phase
V	(superscript for) Voigt bound
R	(superscript for) Reuss bound
F^t	Transition fraction
$F_{Reuss(E_c)}$	Fraction (at given E_c) on Reuss boundary
$F_{Voigt(E_c)}$	Fraction (at given E_c) on Voight boundary
P	Chance ($0 \leq P \leq 1$)
P^c	Percolation threshold
$P^{c(hor)}$, $P^{c(ver)}$	Orientation dependent percolation threshold (horizontal, vertical)
$El^{(hor)}$, $El^{(ver)}$	Elonagation (horizontal, vertical)
ϕ	angle defining shape of percolating cluster in directed percolation
L	Mesh size
I	Identity tensor or Kronecker delta δ_{ij}
n	Normal vector
t	Time
c	Polynomial coefficient
N	Polynomial order
T	Temperature
S	Area

Grain growth

R	Grain size
R_0	Initial grain size
$\dot{R}$	Relative growth rate
k, c	Constants
n	Growth exponent
d	Dimension parameter
M	Mobility of grain boundary
P	Driving force on grain boundary
g	Grain boundary surface energy
n	Number of sides of a grain
$\mu 2$	Second moment of n-sided grains distribution
A	Average grain area
Nn	Number of n-sided grains
Nt	Total number of grains
L	Maximum distance between nodes
$\boldsymbol{g}$	Position vector of the centre of a grain before displacement
$\boldsymbol{g}'$	Position vector of the centre of a grain after displacement
Ra	Average grain shape aspect ratio

References

Anderson M.P. 1988. *Simulation of grain growth in two and three dimensions.* in: Annealing Processes - Recovery, Recrystallization and Grain Growth, (edited by Hansen, N. Juul Jensen, D. Leffers, T., Ralph, B). Risø National Laboratory, Roskilde, Denmark, 15-34.

Anderson M.P., Grest G.S. & Srolovitz D.J. 1985. Grain growth in three dimensions: a lattice model. *Script. Metall.* 19, 225-230.

Anderson M.P., Srolovitz D.J., Grest G.S. & Sahni, P.S. 1984. Computer simulation of grain growth - I. Kinetics. *Act. Metall.* 32, (5), 783-791.

Ashby M.F. & Centamore R.M.A. 1968. The dragging of small oxide particles by migrating grain boundaries in copper. *Acta Metall.* 16, 1082-1092.

Ashby M.F. & Verrall R.A. 1973. Diffusion accommodated flow and superplasticity. *Acta Metal.* 21, 149-163.

Ball R. & Richmond P. 1980. Dynamics of colloidal suspensions. *J. Phys. Chem. Liquids.* 9, 99-116.

Barnes H.A., Hutton J.F. & Walters K. 1989. *An Introduction to Rheology.* Elsevier, Amsterdam.

Barr T.D. & Houseman G.A. 1992a. Distribution of deformation around a fault in a non-linear ductile medium. *Geophys. Res. Lett.* 19, 1145-1148.

Barr T.D. & Housemann G.A. 1992b. Deformation fields around a fault embedded in a non-linear ductile medium. *J. Geophys. Res.* in prep.

Benveniste Y., Dvorak G.J. & Chen T. 1991. On diagonal and elastic symmetry of the approximate effective stiffness tensor of heterogeneous media. *J. Mech. Phys. Solids.* 39, (7), 927-946.

Blumenfeld P.R. & Wilson C.J.L. 1991. Boundary migration and kinking in sheared naphtalene. *J. Struct. Geol.* 13, (4), 471-483.

Borradaile G.J. & McArthur J. 1990. Experimental calcite fabrics in a synthetic weaker aggregate by coaxial and non-coaxial deformation. *J. Struct. Geol.* 12, (3), 351-363.

Burg J.P. & Wilson C.J.L. 1987. Deformation of two phase systems with contrasting rheologies. *Tectonophysics.* 135, 199-205.

Carter N.L. & Tsenn M.C. 1987. Flow properties of continental lithosphere. *Tectonophysics.* 136, 27-63.

Ceppi E.A. & Nasello O.B. 1984. Computer simulation of bidimensional grain growth. *Scr. Met.* 18, 1221-1225.

Cleary M.P., Chen I.W. & Lee S.M. 1980. Self-consistent techniques for heterogeneous media. *J. Eng. Mech. Div.* 106, 861-887.

Cobbold P.R. 1983. Kinematic and mechanical continuity at a coherent interface. *J. Struct. Geol.* 5, 341-349.

Corson P.B. 1974a. Correlation functions for predicting properties of heterogeneous materials. I. Experimental measurement of spatial correlation functions in multiphase solids. *J. Appl. Phys.* 45, (7), 3159-3164.

Corson P.B. 1974b. Correlation functions for predicting properties of heterogeneous materials. II. Empirical construction of spatial correlation functions for two-phase solids. *J. Appl. Phys.* 45, (7), 3165-3170.

Cox S.J.D. & Paterson L. 1990. Damage development during rupture of heterogeneous brittle materials: A numerical study. *Spec. Publ. Geol. Soc. London.* 54, 57-62.

Cox S.J.D. & Paterson L. 1993. The effect of finite element mesh topology on simulating mechanical breakdown in solids. *Num. Meth. Eng.* submitted.

Dell'Angelo L. & Tullis J. 1982. Textural strain softening in experimentally deformed aplite. *EOS.* 63, (18), 438.

Dell'Angelo L. & Tullis J. 1989. Fabric development in experimentally sheared quartzites. *Tectonophysics.* 169, 1-21.

Desai C.S. & Abel J.F. 1972. *Introduction to the Finite Element Method. Appendix 1.* Van Nostrand Reinhold, New York.

Detert K. 1978. Secondary recrystallization, ch 5, p 97-109. In: *Recrystallization of metallic materials* (edited by F. Haessner), Rieder Verlag, Stuttgart, 293 pp.

Dipple G.M. & Ferry J.M. 1992. Metasomatism and fluid flow in ductile fault zones. *Contrib. Mineral. Petrol.* 112, 149-164.

Einstein A. 1906. Eine neue Bestimmung der Moleküldimensionen. *Ann. Phys. Leibzig.* 19, 289-306.

Eshelby J.D. 1957. The determination of the elastic field of an ellipsoidal inclusion, and related problems. *Proc. R. Soc. (London).* A241, 376-396.

Eudier M. 1962. The mechanical properties of sintered low-alloy steels. *Powder Metall.* 5, 278-290.

Fontein W.F. 1990. Analogue materials. *unpubl. report, Utrecht University.* 52 pp.

Fradkov V.E., Shvindlerman L.S. & Udler D.G. 1985. Computer simulation of grain growth in two dimensions. *Scr. Met.* 19, 1285-1290.

Franssen R.C.M.W. & Spiers C.J. 1990. Deformation of polycrystalline salt in compression and in shear at 250-350°C. In: *Deformation Mechanisms, Rheology and Tectonics*, (Knipe R.J. & Rutter E.H. eds) Geological Society Special Publications 54, 201-213.

Frost H.J. & Ashby M.F. 1982. *Deformation-mechanism maps.* Pergamon Press, Oxford.

Gapais D. & White S.H. 1982. Ductile shear bands in a naturally deformed quartzite. *Textures and Microstructures.* 5, 1-17.

Gerding H. & Rijnders G.W.A. 1946. The Raman spectra of a number of polychloro compounds. *Rec. des Trav. Chim. des Pays-Bas.* 65, p 145.

Giesekus H. 1983. Disperse systems: dependence of rheological properties on the type of flow with implications for food rheology. In: *Physical properties of food* (edited by Jowitt *et al.*).Applied Science Publisher, ch. 13.

Gladman T. 1966. On the theory of the effect of precipitate particles on grain growth in metals. *Proc. Roy. Soc.* A294, 298-309.

Glazier J.A., Gross S.P. & Stavans J. 1987. Dynamics of two dimensional soap froths. *Phys. Rev. A.* 36, (1), 306-312.

Gleiter H. 1969a. The mechanism of grain boundary migration. *Acta Metall.* 17, 565-573.

Gleiter H. 1969b. Theory of grain boundary migration rate. *Acta Metall.* 17, 853-862.

Gray G.W. & Winsor P.A. 1974. *Liquid Crystals & Plastic Crystals, Volume 1.* John Wiley & Sons, New York.

Grest G.S., Srolovitz D.J. & Anderson, M.P. 1985. Computer simulation of grain growth - IV. Anisotropic grain boundary energies. *Act. Metall.* 33, (3), 509-520.

Haggert K., Cox S.J.D. & Jessell M.W. 1992. Observation of fault gouge development in laboratory see-through experiments. *Tectonophysics.* 204, 123-136.

Handin J., Higgs D.V. & O'Brien J.K. 1960. Torsion of Yule marble under confining pressure. *Geol. Soc. Am. Mem.* 79, 245-274.

Handy M.R. 1989. The solid-state flow of polymineralic rocks. *J. Geoph. Res.* 95, (B6), 8647-8661.

Handy M.R. 1992. Correction and addition to "The solid-state flow of polymineralic rocks". *J. Geoph. Res.* 97, (B12), 1897-1899.

Harris L.B. & Cobbold P.R. 1984. Development of conjugate shear bands during bulk simple shearing. *J. Struct. geol.* 7, (1), 37-44.

Hashin Z. & Strickman A. 1963. A variational approach to the elastic behavior of multiphase materials. *J. Mech. Phys. Solids.* 11, 127-140.

Hill R. 1963. Elastic properties of reinforced solids: some theoretical principles. *J. Mech. Phys. Solids.* 11, 357-372.

Hill R. 1965a. Continuum micro-mechanics of elastoplastic polycrystals. *J. Mech. Phys. Solids.* 13, 89-101.

Hill R. 1965b. Theory of mechanical properties of fibre-strengthened materials - III. Self-consistent model. *J. Mech. Phys. Solids.* 13, 189-198.

Hirschhorn J.S. 1969. *Introduction to powder metallurgy.* American Powder Metallurgy Institute, New York. 341 pp.

Hobbs B.E., Means W.D. & Williams P.F. 1976. *An Outline of Structural Geology.* John Wiley and Sons, 571 pp.

Horowitz F.G., Tullis T.E., Kronenberg A., Tullis J. & Needleman A. 1981. Finite element model of polyphase flow. *EOS.* 62, (17), 396-397.

Hubbert M.K. 1937. Theory of scale models as applied to the study of geological structures. *Bull. Geol. Soc. Am.* 48, 1459-1520.

Hudleston P.J. 1973. An analysis of "single-layer" folds developed experimentally in viscous media. *Tectonophysics.* 16, 189-214.

Hudleston P.J. & Lan L. 1993. Information from fold shapes. *J. Struct. Geol.* 15, (3-5), 253-264.

Ildefonse B., Launeau P. & Bouchez J.L. 1992. Effect of mechanical interactions on the development of shape preferred orientations: a two-dimensional experimental approach. *J. Struct. Geol.* 14, (1), 73-83.

Ishii K. 1992. Partitioning of non-coaxiality in deforming layered rock masses. *Tectonophysics.* 210, 33-43.

Janssen Ch., Bankwitz E, Bankwitz P. & Harnisch G. 1991. Application of digital image analysis in modelling recrystallization processes. *J. Struct. Geol.* 13 (7), 851-858.

Jessell M.W. 1986a. *Dynamic grain boundary migration and fabric development: observations, experiments and simulations.* (PhD-thesis), State University of New York at Albany, 269 pp.

Jessell M.W. 1986b. Grain boundary migration and fabric development in experimentally deformed octachloropropane. *J. Struct. Geol.* 8, (5), 527-542.

Jessell M.W. & Lister G.S. 1991. Strain localization behaviour in experimental shear zones. *PAGEOPH.* 137, (4), 421-438.

Jordan P.G. 1987. The deformational behaviour of bimineralic limestone-halite aggregates. *Tectonophysics.* 135, 185-197.

Jordan P.G. 1988. The rheology of polymineralic rocks - an approach. *Geol. Rundsch.* 77, (1), 285-294.

Jordan P.G. 1986. *Gefüge-Entwicklung und mechanische Eigenschaften von Zwei-Phase-Aggregaten (Kalk-Halit) bei experimenteller Deformation.* (PhD-thesis), ETH, Zürich,

Karato S.I. & Masuda T. 1989. Anisotropic grain growth in quartz aggregates under stress and its implication for foliation development. *Geology.* 17, 695-698.

Kesten H. 1982. *Percolation theory for mathematicians*. Birkhäuser, Boston, 423 pp.

Kinzel W. 1983. Directed percolation. *Ann. Isr. Phys. Soc.* 5, Percolation Structures and Processes, 425-445.

Kirby S.H. & Kronenberg A.K. 1987. Rheology of the lithosphere: selected topics. *Rev. Geoph.* 25, (6), 1219-1244.

Knipe R.J. & Law R.D. 1987. The influence of crystallographic orientation and grain boundary migration on microstructural and textural evolution in an S-C mylonite. *Tectonophysics*. 135, 155-169.

Kosheleva (Geiro) A.A. 1983. Multipole expansion method in mechanics of matrix composites. *Mekhanika Kompozinykh Materialov*. N3, 416-422.

Krieger I.M. & Dougherty T.J. 1959. A mechanism for non-Newtonian flow in suspensions of rigid spheres. *Trans. Soc. Rheol.* 3, 137-152.

Lee B.J. & Mear M.E. 1991a. Effect of inclusion shape on stiffness of isotropic and transversely isotropic two-phase composites. *Int. J. Solids Structures*. 28, (8), 975-1001.

Lee B.J. & Mear M.E. 1991b. Effect of inclusion shape on the stiffness of nonlinear two-phase composites. *J. Mech. Phys. Solids*. 39, (5), 627-649.

Lister G.S. & Williams P.F. 1983. The partitioning of deformation in flowing rock masses. *Tectonophysics*. 92, 1-33.

Mancktelow N.S. 1991. The analysis of progressive deformation from an inscribed grid. *J. Struct. Geol.* 13, (7), 859-864.

Mandal N. & Karmakar S. 1989. Boudinage in homogeneous foliated rocks. *Tectonophysics*. 170, 151-158.

Mandal N. & Khan D. 1991. Rotation, offset and separation of oblique-fracture (rhombic) boudins: theory and experiments under layer-normal compression. *J. Struct. geol.* 13, (3), 349-356.

Masuda T. & Ando S. 1988. Viscous flow around a rigid spherical body: a hudrodynamic approach. *Tectonophysics*. 148, 337-346.

Mawer C.K. & Williams P.F. 1991. Progressive folding and foliation development in a sheared, coticule-bearing phyllite. *J. Struct. Geol.* 13, (5), 539-555.

McCrone W.C. 1949. Boundary migration and grain growth. *Disc. Faraday Soc.* 5, (?), 158-166.

McCrone W.C. & Cheng P.T. 1949. Grain growth in octachloropropane. *J. Appl. Phys.* 20, 230-231.

McKenzie D. 1979. Finite deformation during fluid flow. *Geophys. J. Astr. Soc.* 58, 689-715.

Means W.D. 1977. A deformation experiment in transmitted light. *Earth & Plan. Sci. Letters*. 35, 169-177.

Means W.D. 1980. High temperature simple shearing fabrics: a new experimental approach. *J. Struct. Geol.* 2, (1/2), 197-202.

Means W.D. 1983. Microstructure and micromotion in recrystallization flow of octachloropropane: a first look. *Geol. Rundsch.* 72, (2), 511-528.

Means W.D. 1986. Three microstructural exercises for students. *J. Geol. Education* 34, 224-230.

Means W.D. 1989a. Stretching faults. *Geology*. 17, 893-896.

Means W.D. 1989b. Synkinematic microscopy of transparent polycrystals. *J. Struct. Geol.* 11, (1/2), 163-174.

Means W.D. 1990. Kinematics, stress, deformation, and material behaviour. *J. Struct. Geol.* 12, (8), 953-971.

Means W.D., Hobbs B.E., Lister G.S. & Williams P.F. 1980. Vorticity and non-coaxiality in progressive deformations. *J. Struct. Geol.* 2, (3), 371-378.

Means W.D. & Ree J.H. 1988. Seven types of subgrain boundaries in octachloro-propane. *J. Struct. Geol.* 10, (7), 765-770.

Means W.D. & Xia Z.G. 1981. Deformation of crystalline materials in thinsection. *Geol.* 9, 538-543.

Molinari A., Canova G.R. & Ahzi S. 1987. A self consistent approach of the large deformation polycrystal viscoplasticity. *Act. Met.* 35, (12), 2983-2994.

Nicolas A. & Poirier J.P. 1976. *Crystalline plasticity and solid state flow in metamorphic rocks.* Wiley,New York.

O'Hara K. 1990. State of strain in mylonites from the western Blue Ridge province, southern Appalachians: the role of volume loss. *J. Struct. Geol.* 12, (4), 419-430.

Olgaard D.L. & Evans B. 1986. Effect of second phase particles on grain growth in calcite. *J. of the ACS.* 69, C272-277.

Olgaard D.L. & Evans B. 1988. Grain growth in synthetic marbles with added mica and water. *Contr. to Min. and Petr.* 100, 246-260.

Panozzo R. 1983. Two-dimensional analysis of shape-fabric using projections of digitized lines in a plane. *Tectonophysics.* 95, 279-294.

Panozzo R. 1984. Two-dimensional strain from the orientation of lines in a plane. *J. Struct. Geol.* 6, (1/2), 215-221.

Passchier C.W. 1986. Flow in natural shear zones - the consequences of spinning flow regimes. *Earth Planet. Sci. Lett.* 77, 70-80.

Passchier C.W. 1987. Efficient use of the velocity gradients tensor in flow modelling. *Tectonophysics.* 136, 159-136.

Passchier C.W. 1988. Analysis of deformation paths in shear zones. *Geol. Rundsch.* 77, (1), 309-318.

Passchier C.W. & Simpson C. 1986. Porphyroclast systems as kinematic indicators. *J. Struct. Geol.* 8, 831-844.

Passchier C.W. & Sokoutis D. 1993a. Experimental modelling of mantled porphyroclasts. *J. Struct. Geol.* 15, in press.

Passchier C.W., ten Brink C.E., Bons P.D. & Sokoutis D. 1993b. Stair stepping as a natural gauge for the strain-rate sensitivity of stress in deformed rocks. *Erath. & Plan. Sc. Lett.*. submitted.

Paterson M.S. 1987. Problems in the extrapolation of laboratory rheological data. *Tectonophysics.* 133, 33-43.

Pohl D. 1969. On the fatigue strength of sintered iron. *Powder metall. Int.* 1, 26-28.

Poirier J.-P. 1985. *Creep of crystals. High temperature deformation processes in metals, ceramics and minerals.* Cambridge University Press, Cambridge, 260 pp.

Ponte Canstañeda P. 1991. The effective Mechanical properties of nonlinear isotropic composites. *J. Mech. Phys. Solids.* 39, (1), 45-71.

Price G.P. & Torok P.A. 1989. A new simple shear deformation apparatus for rocks and soils. *Tectonophysics.* 158, 291-309.

Price R.H. 1982. Effects of anhydrite and pressure on the mechanical behavior of synthetic rocksalt. *Geoph. Res. Let.* 9, (2), 1029-1032.

Ray S.K. 1991. Significance of forelimb folds in the Shumar allochton, Lesser Himalaya, eastern Buthan. *J. Struct. Geol.* 13, (4), 411-418.

Ree J.H. 1990. High temperature deformation of octachloropropane: dynamic grain growth and lattice reorientation. In: *Deformation Mechanisms, Rheology and Tectonics* (Knipe R.J. & Rutter E.H. eds.) Geol. Soc. Spec. Publ. 54, 363-368.

Ree J.H. 1991. An experimental steady-state foliation. *J. Struct. Geol.* 13, (9), 1001-1011.

Ree J.H. 1992. Grain boundary deformation and development of grain boundary openings in experimentally deformed octachloropropane. *J. Struct. Geol.* in press.

Reuss A. 1929. Berechnung der Fliessgrenze von Mischkristallen auf Grund der Plastizitätsbedingung für Einkristalle. *Z. Angew. Math. Mech.* 9, 49-58.

Ross J.H., Bauer S.J. & Hansen F.D. 1987. Textural evolution of synthetic anhydrite-halite mylonites. *Tectonophysics*. 140, 307-326.

Rykkelid E. & Fossen, H. 1992. Composite fabrics in mid-crustal gneisses: observations from the Øysgarden Complex, West Norway Caledonides. *J. Struct. Geol.* 14, (1), 1-9.

Saada A.S. & Townsend F.C. 1981. *State of the art: laboratory strength testing of soils.* American Society for Testing and Materials,

Schmid S.M., Panozzo R. & Bauer S. 1987. Simple shear experiments on calcite rocks: rheology and microfabrics. *J. Struct. Geol.* 9, 747-778.

Schmid S.M., Patterson M.S. & Boland J.N. 1980. High temperature flow and dynamic recrystallization in Carrara Marble. *Tectonophysics*. 65, (3-4), 245-280.

Shea W.T. & Kronenberg A.K. 1993. Strength and anisotropy of foliated rocks with varied mica contents. *J. Struct. Geol.* (J. Christie Vol.), submitted.

Smith C.S. 1964. Some elementary principles of polycrystalline microstructure. *Met. Rev.* 9, (33), 1-48.

Soares A., Ferro A.C. & Fortes M.A. 1985. Computer simulation of grain growth in a bimodal polycrystal. *Script. Metall.* 19, 1491-1496.

Spencer A.J.M. 1980. *Continuum mechanics.* Longman,London.

Srolovitz D.J., Anderson M.P., Grest, G.S. & Sahni P.S. 1984a. Computer simulation of grain growth - III. Influence of particle dispersion. *Act. Metall.* 32, (9), 1429-1438.

Srolovitz D.J., Anderson M.P., Sahni P.S. & Grest G.S. 1984b. Computer simulation of grain growth - II. Grain size distribution, topology, and local dynamics. *Act. Metall.* 32, (5), 793-802.

Srolovitz D.J., Grest G.S. & Anderson M.P. 1986. Computer simulation of recrystallization - I. Homogeneous nucleation and growth. *Act. Metall.* 34, (9), 1833-1845.

Stauffer D. 1985. *Introduction to percolation theory.* Taylor and Francis, London.

Stavans J. & Glazier J.A. 1989. Soap froth revisited: dynamic scaling in the two-dimensional froth. *Phys. Rev. Letters.* 62, (11), 1318-1321.

Stüwe H.P. 1978. Driving and dragging forces in recrystallization, ch 2, p 11-21. In: *Recrystallization of metallic materials* (edited by F. Haessner), Rieder Verlag, Stuttgart, 293.

Suery M. & Baudelet B. 1978. Rheological and metallurgical discussion of superplastic behaviour. *Rev. Phys. Appliquee.* 13, 53-66.

ten Brink C.E. & Passchier C.W. 1992. *T.S.G. Ann Meeting, Abstr.*

ten Brink C.E. & Passchier, C.W. 1993. Modelling of mantled porphyroclasts using rock analogue materials. *J. Struct. Geol.* submitted,

ter Haar J., Urai J.L. & Oostra A. 1987. *EUG IV Conf., Abstr*

Tharp T.M. 1981. Sintered, porous, powder metal (PPM) and the high-temperature rheology of certain two phase rocks. *EOS.* 62, (17), 397.

Tharp T.M. 1983. Analogies between the high-temperature deformation of polyphase rocks and the mechanical behavior of porous metal. *Tectonophysics.* 96, T1-T11.

Tóth L.S., Molinari A. & Bons P.D. 1993. Self consistent modelling of the creep behavior of twophase organic rock analogs. *Act. Metal. et Mat.* submitted,

Treagus S.H. 1988. Strain refraction in layered systems. *J. Struct. geol.* 10, (5), 517-527.

Treagus S.H. & Sokoutis D. 1992. Laboratory modelling of strain variation across rheological boundaries. *J. Struct. Geol.* 14, (4), 405-424.

Truesdell C. 1953. Two measures of vorticity. *J. Rotational Mech. Anal.* 2, 173-217.

Tullis J. & Yund R.A. 1977. Experimental deformation of dry Westerly Granite. *J. Geoph. Res.* 82, (36), 5705-5718.

Tullis J. & Yund R.A. 1981. Grain growth kinetics of quartz and calcite aggregates. *J. of Geol.* 90, 301-318.

Tullis T.E., Horowitz F.G. & Tullis J. 1991. Flow laws of polyphase aggregates from endmember flow laws. *J.G.R.* 96, (B5), 8081-8096.

Tullis T.E. & Tullis J. 1986a. Experimental rock deformation techniques. *Geoph. Monograph.* 36, 297-324.

Tullis T.E. & Weeks D. 1986b. Constitutive behavior and stability of frictional sliding of granite. *PAGEOPH.* 124, (3)

Tungatt P.D. & Humphreys F.J. 1984. The plastic deformation and dynamic recrystallization of polycrystalline sodium nitrate. *Acta Metall.* 32, (10), 1625-1635.

Urai J.L. 1983. Deformation of wet salt rocks: an investigation into the interaction between mechanical properties and microstructural processes during deformation of polycrystalline carnallite and bischofite in the presence of a pore fluid. *PhD-thesis, Utrecht Univ.* 223 pp.

Urai J.L. 1985. Water-enhanced dynamic recrystallization and solution transfer in experiemntally deformed carnallite. *Tectonophysics.* 120, 285-317.

Urai J.L. 1987. Development of microstructure during deformation of carnallite and bischofite in transmitted light. *Tectonophysics.* 135, 251-263.

Urai J.L. & Humphreys F.J. 1981. The development of shear zones in polycrystalline camphor. *Tectonophysics.* 78, 677-685.

Urai J.L., Humphreys F.J. & Burows S.E. 1980. In-situ studies of the deformation and dynamic recrystallization of rhombohedral camphor. *J. Mat Sc.* 15, 1231-1240.

Urai J.L., Means W.D. & Lister G.S. 1986. Dynamic recrystallization of minerals. *Geoph. Monograph.* 36, 161-199.

Van Den Driessche J. & Brun J.-P. 1987. Rolling structures at large shear strain. *J. Struct. Geol.* 9, (5/6), 691-704.

Voigt W. 1928. *Lehrbuch der Kristallphysik.* Teubner, Leibzig.

Von Neumann J. 1952. Written discussion on grain topology and the relationship to growth kinetics. In: *Metal Interfaces* 108-113.

Watt J.P., Davies G.F. & O'Connell R.J. 1976. The elastic properties of composite materials. *Rev. Geoph. Space Phys.* 14, (4), 541-563.

Weaire D. & Kermode J.P. 1983. Computer simulation of a two-dimensional soap froth I. Method and motivation. *Phil. Mag. B.* 48, (3), 245-259.

Weaire D. & Kermode J.P. 1984a. Computer simulation of a two-dimensional soap froth II. Analysis of results. *Phil. Mag. B.* 50, (3), 379-395.

Weaire D. & Rivier N. 1984b. Soap, Cells and Statistics - Random Patterns in Two Dimensions. *Contemp. Phys.* 25, (1), 59-99.

Weijermars R. 1986. Flow behaviour and physical chemistry of bouncing putties and related polymers in view of tectonic laboratory applications. *Tectonophysics.* 124, 325-358.

Weijermars R. 1992. Progressive deformation in anisotropic rocks. *J. Struct. Geol.* 14, (6), 723-742.

Weijermars R. & Schmeling H. 1986. Scaling of Newtonian and non-Newtonian fluid dynamics without inertia for quantitative modelling of rock flow due to gravity (inclusing the concept of rheologic similarity). *Phys. Earth Planet. Inter.* 43, 316-330.

Wejchert J., Weaire D. & Kermode J.P. 1986. Monte Carlo simulation of the evolution of a two-dimensional soap froth. *Phil. Mag. B.* 53, (1), 15-24.

Weng G.J. 1990. The overall elastoplastic stress-strain relations of dual-phase metals. *J. Mech. Phys. Solids.* 38, (3), 419-441.

Wenk H.-R., Canova G., Molinari A. & Mecking H. 1989. Texture development in halite: comparison of Taylor model and self consistent theory. *Acta metall.* 37, 2017-2029.

Wenk H.-R., Bennett K., Canova G.R. & Molinari A. 1991. Modelling plastic deformation of peridotite with the self-consistent theory. *J. Geoph. Res.* 96, (B5), 8337-8349.

Wheeler J. 1992. Importance of pressure solution and Coble creep in the deformation of polymineralic rocks. *J. Geoph. Res.* 97, (B4), 4579-4586.

Willis J.R. 1991. On methods for bounding the overall properties of nonlinear composites. *J. Mech. Phys. Solids.* 39, (1), 73-86.

Wilson C.J.L. 1986. Deformation induced recrystallization of ice: the application of in situ experiments. *Geoph. Monograph.* 36, 213-232.

Winsor P.A. 1974. Non-amphiphilic Cubic Mesophases. Plastic Crystals. In: *Liquid Crystals & Plastic Crystals, Volume 1* (edited by G. W. Gray, & P. A. Winsor). *Ellis Horwood Series in Physical Chemistry.* 1, 48-59.

Wu T.T. 1966. The effect of inclusion shape on the elastic moduli of a two-phase material. *Int. J. Solids Structures.* 2, 1-8.

Wu X. & Chen I.-W. 1992. Exaggerated texture and grain growth in a superplastic SiAlON. *J. Am. Ceram. Soc.* 75, (10), 2733-2741.

Yoon C.K. & Chen I.-W. 1990. Superplastic flow of Two-phase ceramics containing rigid inclusions - zirconia/mullie composites. *J. A. Ceram. Soc.* 73, (6), 1555-1565.

Zienkiewicz O.C. 1977. *The finite element method.* McGraw-Hill, London.

Acknowledgements

After four and a half years it is a difficult but pleasent task to acknowledge the many persons who in some way contributed to the completion of my PhD-project. I wish to express my gratitude to all these persons before proceeding to mention those whose contribution and involvement deserve special attention.

I am greatly indebted to Janos Urai, Cees Passchier and Prof Henk Zwart for creating the PhD-project, which enabled me to achieve my degree on a very interesting subject. Janos Urai was my first advisor whose never failing enthousiasm was most encouraging. I thank him for sharing with me his experience with rock analogues and experimental techniques, his suggestions, criticism, ideas, comments and for helping me through the final stages of this project. Cees Passchier was the second advisor and I thank him for his help and guidance. Allthough not involved from the beginning of the project, Mark Jessell has played an indispensible role in this project. During the one and a half year that I spent in his laboratory in Melbourne he was an allways available advisor, who tought me programming in "C", with whom I had many interesting discussions and who did his best to organise the facilities I needed. I thank him and the Department of Earth Sciences, Monash University, for their hospitality. I thank Prof Stan White for taking me as his PhD-student when I needed a promotor.

Next I want to mention Coen ten Brink, my closest colleague, and thank him for our many discussions, his questions and suggestions and his help during the last stages of finishing this thesis. It was great to have someone to share my problems with and I wish him succes with the completion of his own PhD-research.

Prof Win Means I thank for his interest in my work and for the discussions we had in Albany from which I learned a lot.

A considerable part of this thesis exists thanks to Simon Cox and Terence Barr, who both volunteered to modify their software packages for my research and thus introduced me into the field of finite element modelling. Simon Cox pointed the importance of percolation theory out to me.

I am gratefull for the technical support by Richard Clarke, Arnoud van der Gon Netscher, Eimert de Graaff, Gert Kastelein, Peter van Krieken, Bill Manley and Chris Pierson. Gert and Aarnoud did a great job in building the ring shear creep apparatus, which worked straight away. Next I want to acknowledge Steve Morton, Brigitta Benders (photography), Magda Martens, Margret Beckers, Pam Hermansen and Eileen Lynch (administration).

I thank AWON/NWO for the financial support of myself and my research and for providing travel funds.

Many persons remain to be mentioned because they contributed to the accomplishment of this project, by their comments, the discussions we had, their hospitality during the my travels, their help or by other means. I can only attempt to mention them all: Rebecca Askew, Anton-Jan Bons, Ronald Bakker, Bas den Brok, Mirjam and Tirza van Daalen, Willem Fontein, Gijsbrecht, Mark Handy, Marco Herwegh, Linda Jessell, Leo Kriegsman, Prof Gordon Lister, "Bear" MacPhail, Shigeru Otoh, Siese de Meer, Boudewijn van Milligen, Nick Oliver, my parents, Young-Do Park, Alice Post, Jin Han and Bok-Nam Ree, Pjotr Skotnicki, Francis d'Souza, Chris Spiers, Rian Visser, Julie Vry, Trudy Wassenaar and especially Marlina Elburg.

Curriculum vitae

Place and date of birth:	Sydney, Australia, February 20, 1964
High school education:	1976 - 1982. V.W.O. at the Christelijk Lyceum Dr W.A. Visser 't Hooft, Leiden
University education	1982 - 1987. Faculty of Geology and Geophysics, University of Utrecht. Main subject: Structural and Applied Geology; second subject: Exploration Geophysics
Post graduate experience:	1987 - 1989. Military service, first training and posting as seconded officer at the Bureau for Military Geography of the Intelligence Section of the Staff of the First Netherlands Army Corps, Apeldoorn 1989 - 1993. PhD-research as "Onderzoeker in Opleiding"

The research presented in this thesis was conducted at:

Institute of Earth Sciences
University of Utrecht
P.O. Box 80.021, 3508 TA Utrecht
THE NETHERLANDS

Department of Earth Sciences
Monash University
Clayton, VIC 3168
AUSTRALIA